CHARACTERIZATION AND MODELING OF STRAINED LAYERS GROWN ON V-GROOVED SUBSTRATES

By

ARCHANA GUPTA, B.TECH., M.SC.

A Thesis

Submitted to the School of Graduate Studies

in Partial Fulfillment of the Requirements

for the Degree

Doctor of Philosophy

McMaster University

CHARACTERIZATION AND MODELING OF STRAINED LAYERS GROWN ON V-GROOVED SUBSTRATES

DOCTOR OF PHILOSOPHY (1997) McMaster University
(Materials Science and Engineering) Hamilton, Ontario

TITLE: Characterization and Modeling of Strained Layers Grown on V-Grooved Substrates.

AUTHOR: Archana Gupta, B.Tech. (Indian Institute of Technology, Kanpur, India), M.Sc. (University of Manitoba, Winnipeg, Canada).

SUPERVISOR: Professor George C. Weatherly

NUMBER OF PAGES: xviii, 202

To my parents

ABSTRACT

Growth of superlattices on V-grooved substrates has become a popular method of producing quantum wires. The success of this technique to date has been limited to the lattice-matched AlGaAs/GaAs system. The unpredictability of the morphology and defects found in lattice-mismatched systems has been a major hindrance in their development. Additionally, the misfit stresses in lattice mismatched systems may play an important role in determining the properties of the laser. In V-grooves, the singular points at the corners of the groove produce a stress distribution completely different from the case of layers grown on a planar substrate. Accurate knowledge of the stress distribution is hence necessary because a stress can affect the optoelectronic properties and lead to defects, limiting the life of the laser.

The aim of the project was two fold: first to characterize the InGaAs/InP growth on (211)A and (111)B grooves using molecular beam epitaxy in terms of faceting, thickness variation, and composition variation; second to obtain an analytical and numerical stress distribution for the case of a layer with uniform composition and thickness grown on a sharp V-groove. The characterization was performed using transmission electron microscope and degree of polarization methods. Composition analysis was done with a high resolution scanning transmission electron microscope. Numerical simulation was done using a commercial finite element program, 'ABAQUS'.

The results showed a clearly distinct morphology for layers grown on faceted (211)A and (111)B substrates. The differences observed in faceting, thickness variations, and composition variations in the (211)A and (111)B grooves suggest that the lower incorporation rate of group III atoms on (111)B surfaces leads to increased interfacet diffusion compared to (211)A grooves, where a higher incorporation rate produces layers with uniform composition and thickness. Furthermore, the 46.5% increase in In content

found at the bottom of (111)B grooves indicates that the mean diffusion length of In is much higher than Ga for the growth conditions used in this study. The large variation in composition in (111)B grooves produced extensive defects at the bottom of the groove and at certain locations of the sidewall where the misfit exceeds the critical limit.

The analytical and numerical solution of the stress distribution were in good agreement with experimental results. The stress fields obtained by these methods would be useful in helping to predict the optoelectronic properties of the quantum wire. Furthermore these models are useful in determing the composition and thickness of the layers which need to be grown to obtain specific optical properties.

ACKNOWLEDGEMENTS

I would like to sincerely thank my supervisor, Dr. G.C.Weatherly, for his help and guidance during the course of this work. In particular, I am grateful for his ready availability and for the time he spent with me on the microscope. I would like to thank my committee members, Dr. D.T.Cassidy and Dr. G.R.Purdy, for their help and suggestions during the course of this thesis. I appreciate the suggestions of Dr. J.D.Embury and Dr. D.R Wilkinson in modeling the problem. I am also thankful to Dr. D.A.Thompson, Dr. B.J. Robinson. and Nick Bulitka for providing the samples and Doug Bruce for performing the DOP analysis.

I would like to thank Fred Pearson and Andy Duft for helping me on the electron microscope, and Dr. R. Sowerby for allowing me to use the ABAQUS software.

I would like to thank all my friends at McMaster who have helped me in a myriad of ways. Lastly, I would like to thank my parents and my husband, Kalyan, for their support and encouragement.

CONTENTS

FIGURES

TABLES

1. INTRODUCTION

1.1 INTRODUCTION TO QUANTUM WIRES

In the past two decades strained layer superlattices have made a big impact on the optoelectronics community. These materials offer a wide range of flexibility in tailoring the properties according to the application. However this flexibility becomes constrained for lattice mismatched systems where dislocations and other growth related problems arise after critical limits of thickness or composition are exceeded. A large volume of work in the literature deals with the characterization of defects in superlattice structures grown on planar substrates, the so called quantum well structures. Theoretical treatment of the stress distribution has also helped in understanding the process of defect formation and devising ways to circumvent them.

In the last decade work on development of lasers with 2D and 3D confinement of carriers is underway. The additional degrees of confinement generate lasers which are more efficient and have better optical properties. One of the more popular ways of generating 2D structures, known as quantum wires, is to grow quantum wells on a V-grooved substrate. The AlGaAs/GaAs system grown on (111)A V-grooves has been quite successful in achieving this goal. However to develop greater flexibility in altering the properties of the laser, as in the case of quantum wells, one needs to grow lattice mismatched systems. Growths using these systems have been largely unsuccessful, because the presence of adjoining facets in the groove which complicates the growth process, leading to unpredictable growth patterns. Part of the problem lies in the sensitivity of the morphology to slight changes in the growth parameters. If the generation of defect free quantum wires is to become a standard procedure, it is important

that the effect of different parameters on the growth process is understood, and models developed which can closely predict the final outcome in terms of morphology and properties of quantum wires.

1.2 RESEARCH GOAL

The aim of the present thesis was to try to gain some understanding of the growth process of the lattice mismatched system InGaAs/InP on (111)B and (211)A V-grooves. The difference in interaction of atoms with different surfaces gives rise to a difference in growth morphology. Success in generating quantum wires depends on understanding the process better and then exploiting it to tailor the growth according to the need. The importance of strain as a degree of freedom in designing laser structures has been realized in the case of quantum wells. Although it is known that the properties of quantum wires would also be affected by strain, no model exists which would predict the stress distribution. Hence another aim of this thesis was to develop such a model using both analytical and numerical techniques.

1.3 THESIS OUTLINE

This thesis has been divided into seven chapters. The second chapter gives a background to the subject in terms of relevant definitions and related work in the literature. The third chapter gives details of the experimental techniques used in this project. These were transmission electron microscopy (TEM), scanning transmission electron microscopy (STEM) and degree of polarization (DOP) techniques. The results have been divided into three categories and put into three self contained chapters. Chapter 4 deals with the general characterization of the samples using TEM. The results in this chapter have been discussed using existing data in the literature. Chapter 5 deals with the

composition analysis of growths on both (111)B and (211)A V-grooves using STEM. These results have been compared with the compositions obtained using cathodoluminescence (CL) and other techniques in the literature. In chapter 6 a comparison of the stress distribution obtained using experimental techniques with analytical and numerical simulation methods has been discussed. The importance of developing such simulations has been emphasized, given the effect of stress on the optical properties. In the last chapter a list of conclusions based on the present experiments is given, as well as suggestions for the future direction of this research are presented.

2. LITERATURE REVIEW

2.1 GROWTH ON PLANAR SUBSTRATES

The purpose of growing thin layers on planar substrates can be seen in the context of many applications such as for protective coatings, or for magnetic, superconducting or optoelectronic devices. This research focuses on optoelectronic applications. The significance of thin layers for optoelectronic applications was realized when Esaki and Tsu (1970) proposed a superlattice, that consisted of alternating layers of two different semiconducting materials grown on bulk substrates, which would generate a quantum well structure. The substrate is a single crystal and the layers are grown epitaxially, i.e. the crystal structure of the layer, which might have a different lattice parameter or atom positions compared to the substrate, is forced to match with the substrate crystal structure.

The superlattice proposal of Esaki and Tsu(1970) was realized experimentally in the 1970's (Matthews and Blakeslee, 1977). This success spawned a large body of research work in the area of quantum wells and the study of various aspects of their behavior. These can be divided into two categories: electronic and optical properties; and material and growth properties. This research will mainly focus on the latter category. In this category efforts were made to improve the quality of the interface, to reduce defects, to understand strain related effects, to understand the growth mechanisms and to come up with better growth techniques to improve upon the existing methods. Research in all these areas has considerably improved our understanding but there are still areas such as

composition control, surface undulations and faceting, and diffusion at the interface which are not properly understood.

Initially all the efforts were directed towards growing lattice matched systems: systems in which the lattice parameters of the layer and the substrate are identical. AlGaAs/GaAs is the only system, consisting of layers of two different compositions, whose lattice parameters are within 0.2% over the entire Al composition range. By varying the composition and thickness of the AlGaAs layer, the bandgap, and hence the electronic and optical properties could be varied. However, the wavelengths needed by different applications could not be achieved with the AlGaAs/GaAs system; hence this need could only be satisfied with systems such as InGaAs/GaAs, InGaAsP/ InP, Si-Ge/Si etc. In these systems for certain compositions the mismatch was enough to generate dislocations, but for compositions for which dislocations were absent, it was found that strain changed the optoelectronic properties. This provided a new degree of freedom to tailor the properties of optoelectronic materials.

Structure of the surfaces, on which growth of superlattices occurs, plays an important role in determining the quality of growth. III-V compounds consist of two different atoms joined by partially ionic bonds, which are directional, hence some surfaces are polar. In the next section, the terminology used to refer to a particular arrangement of these surfaces, is defined.

2.1.1 Polar Surfaces

Elemental semiconductors like Si and Ge have diamond cubic crystal structure with each atom having four symmetrically placed valence bonds. This crystal structure has the translational symmetry of the F.C.C Bravais lattice and hence for each lattice point of

the F.C.C structure it has a basis of two atoms, one at 000 and the other at 1/4 1/4 1/4. However, many compounds of the III-V and II-VI type have the zincblende or sphalerite structure. Sphalerite differs from diamond in that the two F.C.C sublattices are decorated by different atomic species (Zn and S in the case of sphalerite).

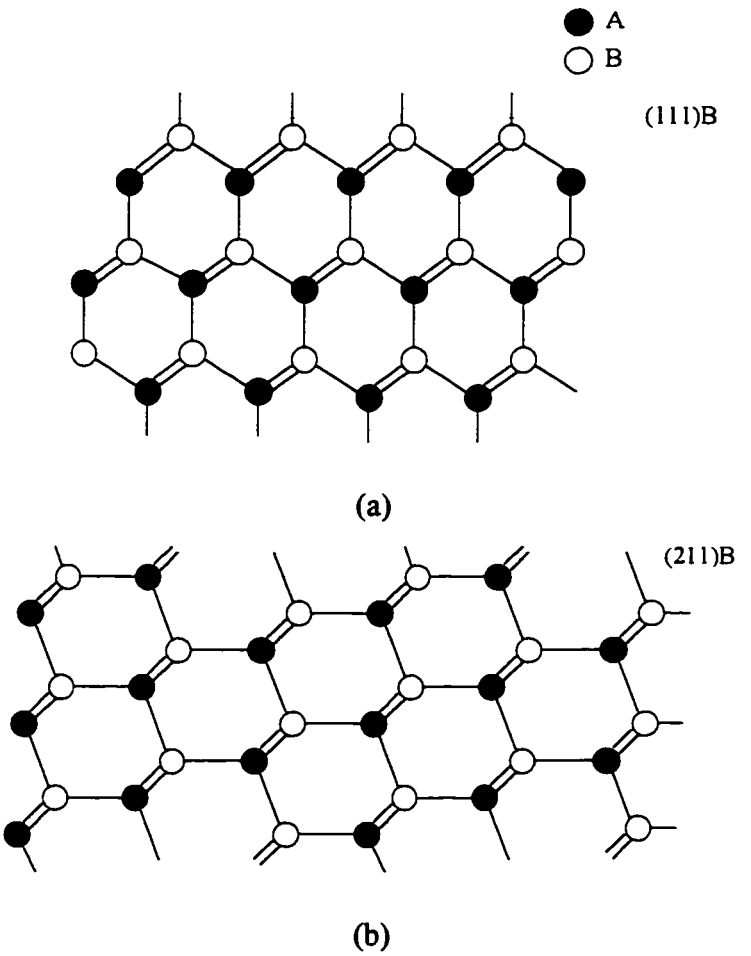

Fig. 2.1 Atomic arrangement on {111} and {211} planes (a) (111)A and (111)B (b) (211)A and (211)B

In the sphalerite structure there is no center of inversion and hence a (111)A plane is composed of all Zn atoms while the (111)B plane is composed of S. In

the case of III-V compounds the group III atom is labeled A and the group V atom is labeled B. Thus a (111) plane of A atoms is labeled (111)A and a (111) plane of B atoms is labeled (111)B (Fig. 2.1a). In case of the (211) planes the distinction is not so easy as it is terminated by both A and B atoms. However in one case for every A atom which has two dangling bonds there are two B atoms with a single dangling bond (Fig. 2.1b). This configuration is labeled (211)A. The case where there are two A atoms for every B atom is labeled (211)B.

2.1.2 Molecular Beam Epitaxy (MBE)

2.1.2.1 Introduction

MBE is an advanced growth technique in which the growth occurs under ultrahigh vacuum condition(10^{-10} Torr.) and growth can be controlled down to the atomic level. The MBE setup used at McMaster is shown in Fig.2.2. A series of effusion cells known as Knudsen cells surround the substrate. The substrate sits on a heating block which controls the temperature. The substrate wafer is rotated at a given speed during growth to allow uniformity of the growth. The Knudsen cells are provided with shutters which allows one to control the composition. The composition of the beam incident on the substrate is controlled by the temperature of the individual effusion cells. The growth rate in MBE is slow and is of the order of 1μm/hr. But the growth rate is fast enough for the growth to be kinetically controlled. This makes it possible to grow metastable layers. Metastability can be achieved by growing at temperatures where surface diffusion is appreciable, but volume diffusion is negligible.

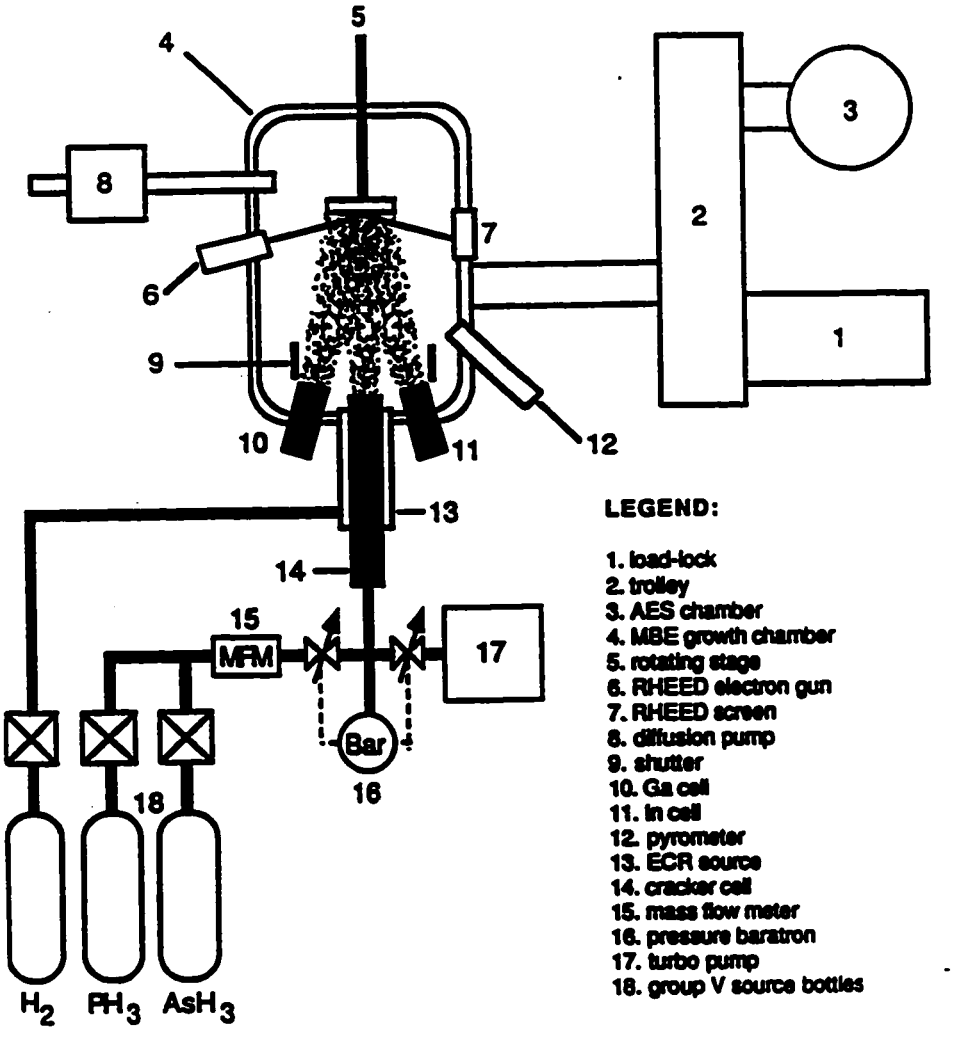

Fig. 2.2 Setup of the MBE system used at McMaster

The group III beam is always composed of monoatomic species whereas the beam of the group V atom can be either diatomic when generated by incongruent evaporation of the III-V compound itself or tetratomic when generated from the elemental sources (Ploog,1981). Stoichiometry of the compounds formed depends on the sticking coefficients, which in turn depends on the temperature and orientation of the substrate. MBE growth involves three basic steps: in the first step the incident flux is formed in the Knudsen cells; in the second step physisorption and diffusion to the lowest energy site occurs; and finally incorporation of the elements occurs by chemical absorption.

2.1.2.2 Factors Affecting MBE Growth

One of the important parameters that determines the quality of growth is the nature of the exposed surface of the substrate on which the growth takes place. If a covalently bonded solid is cleaved the atomic arrangement at the surface may be different from the bulk. To minimize the excess energy associated with dangling bonds there is a driving force causing the atoms to reconfigure (Williams and Bartelt, 1991). This leads to surface-reconstruction, that has been observed using a number of techniques (Biegelsen et al., 1990). Surface reconstruction depends on the temperature, the plane and the stoichiometry (Bachrach et al. 1981; Daweritz and Hey, 1990). To determine the atomic arrangement techniques such as low energy electron diffraction (LEED) or reflected high energy electron diffraction (RHEED), incorporated in the MBE system for the continuous monitoring of surfaces, may be used.

Before loading a sample in the growth chamber, the surface is cleaned to remove any contaminants or surface oxides. This can be done by a variety of methods including evaporation, cleavage under high vacuum, heat treatment, ion bombardment, or annealing and etching. Cleavage under high vacuum prevents the formation of any contaminating

film whereas the other methods are used to eliminate an already formed layer of oxide. Ion sputtering is not normally used for III-V compounds because it causes surface damage and is a time consuming procedure. Furthermore, if it is not conducted properly, impurities can be added to the surface.

For III-V compounds chemical treatments are used to produce a surface free of metallic and organic impurities and protected from atmospheric contamination by a thin passivating oxide layer. After loading into the MBE system the compounds are heated to desorb the surface oxide. At this point the substrate should be nearly atomically clean and ready for epitaxial growth.

Once the substrate is ready for deposition, the other factors to consider are the temperature and the incoming flux. Incorporation of the elements requires surface diffusion to a kink site on a surface step. Since the elements are incorporated at step sites, one way to increase the density of steps is by growing on offcut surfaces (Kroemer, 1987). The rate of diffusion is determined by the temperature; the higher the temperature the faster is the growth. However a higher temperature also implies that low melting point elements may be desorbed, thus a compromise has to be made (Dryburgh, 1988; Dryburgh, 1993; Fawcett et al., 1994). The temperature also determines the surface reconstruction and the sticking coefficient (Gonda and Matshushima, 1976; Yoo et al., 1993). Since the sticking coefficient depends on temperature the fluxes need to be closely controlled for growth of a particular composition (Chang et al., 1977). In addition the temperature cannot be too low otherwise an amorphous product is formed (Zeindl et al., 1987).

If all of the factors are carefully taken care of one can get layers with exactly defined composition and abrupt interfaces. The degree of control one can exercise in MBE is impressive and this has led to remarkable advances in device growth.

Once the substrate is ready for growth two types of deposition can be considered. In the first the composition of the film is the same as the substrate. This is known as homoepitaxy. The second possibility is a layer with a composition different from the substrate. This is known as heteroepitaxy.

2.1.3 Homoepitaxy

Homoepitaxy is defined as the growth of a layer on a substrate with the same composition and orientation. Such growths are done mainly to improve the surface quality of the substrate before heteroepitaxy and to understand the process of growth. In the case of growth on (001) substrates homoepitaxial growth maintains a planar surface and there are no growth related defects. But in case of growth on (111) substrates extensive defect formation has been reported (Rajkumar et al., 1991; Zeindl et al., 1987). Rajkumar et al. (1991) attribute these defects to the presence of a single dangling bond on the surface. An atom adsorbed to a single dangling bond has three unsatisfied bonds. This makes it possible for the bonds to rotate about the single bond joining the adatom to the surface and hence change the position of the next atoms to be adsorbed. This can result in twinning (Zeindl et al., 1987; Rajkumar et al., 1991) because the adsorbed atoms on a (111) surface have the possibility to occupy right or wrong crystallographic positions.

Sangster (1962) proposed a mechanism of nucleation on (111) planes. Since (111) planes are composed either by all A or all B atoms, all atoms bonding to the surface should be of the same type. Let us consider growth on a (111)B plane. Since the adatom(A) is joined to the substrate with one bond there are three dangling bonds. A

second A atom must attach itself to the existing layer as a second nearest neighbor of the first, again with a net increase of two dangling bonds. This is not an energetically favorable process. Then an atom of the opposite type(B) bonds to these two previous adatoms without any increase in the number of dangling bonds. To complete the triangular island an adatom of the first type(A) forms bonds with these B atoms and the original (111)B surface without any increase in dangling bonds. The surface is thus covered by a number of triangular deposits which later coalesce to give a 2D layer. The energy barrier to the formation of these islands makes the nucleation on (111) surface difficult.

Other studies involving growth on slightly misoriented (111) substrates reported defect free growths (Zeindl et al., 1987; Hou and Tu, 1993). The reason for this drastic change seems to be that in offcut substrates there are more steps and hence growth proceeds by step propagation rather than by nucleation and growth.

Subbanna et al. (1986) studied the growth of GaAs layers on (211)A and (211)B oriented GaAs substrates. They demonstrated that (211)A substrates yielded growth morphologies and photoluminescence linewidths comparable to (100) growths; (211)B growths were also excellent. Electron diffraction showed some submicroscopic faceting on the (211)B substrate but not on the (211)A substrate. Subbanna et al. (1986) did not give any explanation for this difference in the behavior of (211)B and (211)A surfaces.

Table 2.1 Growth Factor Comparisons of Crystallization on Basic Surfaces (Sangster, 1962)

Surface Orientation	Growth Factor			
	Nucleation	**Surface Stoichiometry**	**Surface Packing**	**Surface Planarity**
{100}	Very good	Poor	Fair	Very poor
{110}	Poor	Perfect	Very poor	Good
{111}	Very poor	Good	Very good	Very good

Sangster (1962) proposed a qualitative growth model based on the density of dangling atomic bonds. Table 2.1 gives his predictions for growths on three basic surface orientations. He defined surface packing as the number of atoms per unit area, surface stoichiometry as the ideal configuration of A and B atoms, and surface planarity as the geometrical plane on the atomic scale. All surfaces with higher Miller indices can be resolved on an atomic scale into stepped structures built from combinations of {100}, {110} and {111} planes. Hence, since a {311} surface is made up of {100} treads and {111} risers, it should have the optimum growth properties because the desirable nucleation properties of {100} dominate. Nucleation on (100) plane is easier because there is no change in the number of unsatisfied bonds at any stage. Similarly any surface can be broken up into a combination of these basic planes and hence its growth properties worked out. The {n11} surfaces are all a combination of {100} treads and {111} risers. With n>5 the growth axes becomes indistinguishable from <100>. Sangster concluded that the optimum growth direction is probably <n11> with n between three and five because (100) planes dominate and nucleation becomes easier.

2.1.4 Heteroepitaxy

In heteroepitaxial growth the layer and the substrate are of different composition. They may or may not have the same lattice constant. In the case of growth of a layer whose composition is different from the substrate there are many aspects which become important. First is the relative bond strength of the A-A, B-B and A-B bonds which can give rise to different growth modes (Bauer,1958). Second is the misfit strain which can lead to the formation of defects. These two factors determine which type of growth predominates.

2.1.4.1 Types of Growth

Bauer(1958) divided growth into three categories (Fig 2.3): in the first category the conditions are such that the growth occurs in layer by layer or two dimensional form. This is also referred to as Frank-Van der Merwe (FM) type of growth and is the one most desired in fabrication of devices (Fig. 2.3a). The second category is the three-dimensional growth or Volmer-Weber (VW) type of growth (Fig. 2.3b). Here a series of islands nucleate, which after some growth merge together and form a continuous layer. The third category is a mixed type of growth which is also known as Stranski-Krastonov (SK) type of growth (Fig. 2.3c). Initially there is layer by layer growth but it reverts to a three-dimensional form to minimize the extra energy due to strain.

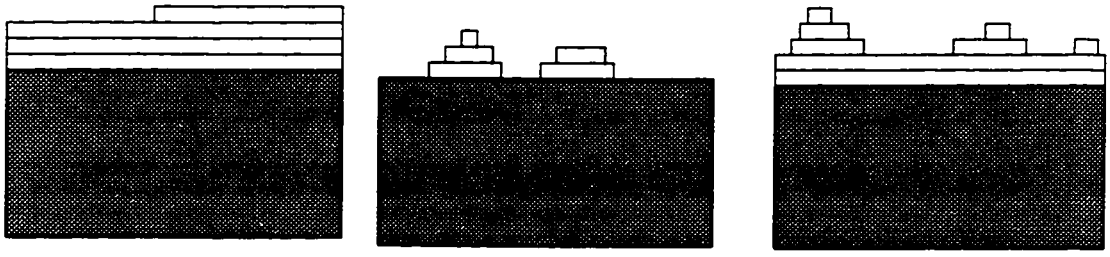

Fig. 2.3 Three types of growth (a) FM (b) VW (c) SK.

The law which governs which type of growth dominates is based on interfacial energies and the strain energy built into the film. Fig.2.4 gives a schematic representation of an assumed spherical-cap like deposit on a substrate. If σ_{sv} , σ_{xs} , and σ_{xv} are the free energies of the substrate-vapor, deposit-substrate, and deposit-vapor interfaces and θ is the contact angle (Matthews, 1975), then at equilibrium

$$\sigma_{sv} = \sigma_{xs} + \sigma_{xv}\cos\theta$$

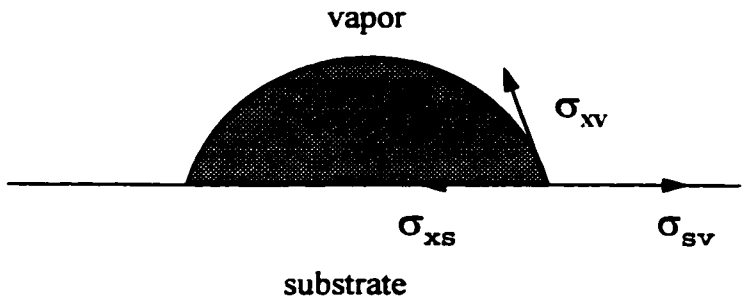

Fig. 2.4 Schematic diagram of a spherical-cap type deposit.

If $\theta = 0$ then $\sigma_{sv} = \sigma_{xs} + \sigma_{xv}$; this implies that the deposit completely wets the substrate and hence growth would be in the layer by layer form.

When θ is finite then $\sigma_{sv} < \sigma_{xs} + \sigma_{xv}$; this condition leads to three dimensional growth. Here the particles formed by three dimensional growth eventually agglomerate and form a continuous film.

For the case when $\sigma_{sv} > \sigma_{xs} + \sigma_{xv}$, the deposit-substrate binding is stronger than that within the deposit. In this case a continuous two dimensional layer first forms, followed by the formation of three dimensional islands.

In most cases although the layer starts out with a layer by layer growth mode it reverts to SK mode. The first monolayer is in direct contact with the substrate and hence if the bonding between the layer and substrate atoms is strong it would lead to two dimensional growth but after the first monolayer there is no direct contact between the layer and the substrate and the Bauer criteria cannot be applicable. There are other factors like intermixing at the interfaces, lattice mismatch, anisotropy of atom migration, and supersaturation which need to be taken into account (Van der Merwe, 1984). The effect of strain was worked out by Grabow and Gilmer (1988). According to their model if the cluster forms on a few layers of a uniform film then cluster formation will be independent of the strength of film-substrate interaction. So cluster nucleation will depend on the

misfit and the temperature. As in the Bauer model they assumed a cap shaped deposit but now the pertinent interfaces were those of the strained-film/vacuum, cluster/vacuum, and strained film/ cluster interfaces. Their molecular dynamics computer simulations showed that a uniform film is never the equilibrium state for film thicknesses greater than several layers of atoms and for a misfit of several percent or more. According to Grabow and Gilmer (1988), although uniform films are rarely possible under equilibrium condition they may persist in a metastable state because of the large nucleation barrier for islanding.

If there is a misfit strain in the layer then it provides the driving force for the formation of islands. In the next section, the misfit strain in the layers and their effect on the quality of growth, will be discussed.

2.1.4.2 Misfit Strain

Misfit strain is a very important factor in the growth of a layer with a lattice parameter different from the substrate. Its importance arises from the fact that if the misfit exceeds a critical limit dislocations or surface morphological instabilities may be generated. Secondly, since strain modifies the bandgap, it can be used as an additional degree of freedom for designing devices with novel properties. Both these factors are critical for device design. Hence it is important to get qualitative and quantitative information about the stress distribution in the device. For the case of planar growth the misfit stress distribution can be worked out using two different models (Perovic et al., 1991). This knowledge has been used for designing devices with novel properties.

2.1.4.2.1 Elastic Stress Analysis

The simplest geometry, for which stress distribution has been worked out analytically, is a thin misfitting layer grown on a large substrate (Frank and van der Merwe, 1949). The model makes the following five assumptions: (1) the layers are thin

compared to the substrate; hence, all stresses are assumed to be concentrated in the layer (Fig.2.5). If this is not the case, a stress distribution that alternates in sign between the substrate and the layer must be considered; (2) there is no bending of the layers; (3) the lateral extension of the layers is infinite so that any edge effects can be neglected; (4) the interfaces are sharp i.e there is no interdiffusion of elements at the interface; and (5) the material is isotropic and the layer and the substrate have the same elastic constants.

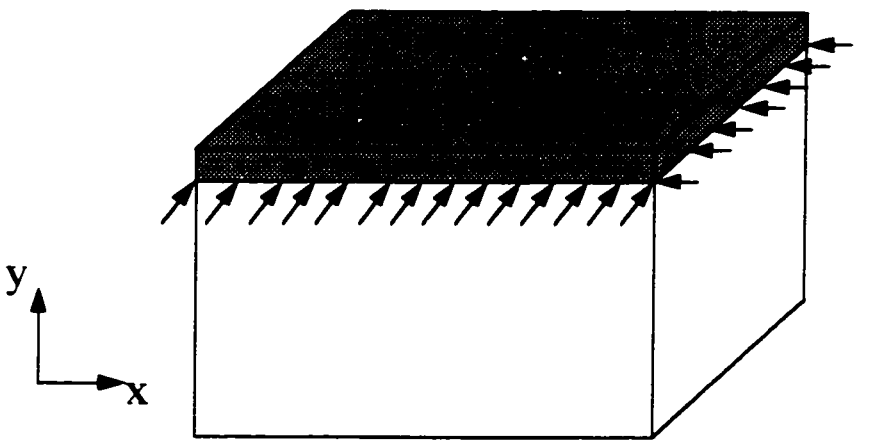

Fig. 2.5 Schematic diagram showing misfit stresses in a thin epitaxial strained layer

According to the model of Frank and Van der Merwe (1949), if the lattice parameters of the substrate and the layer are a_s and a_l , then the misfit at the interface is defined as follows:

$$f = \frac{a_s - a_l}{a_l} \qquad \text{.....(1)}$$

Since the interface is constrained in the growth plane but is free to relax in the growth direction there is a tetragonal distortion of the layer. Solution of the planar stress situation results in the in-plane strains, ε_{xx} and ε_{yy}.

$$\varepsilon_{xx} = \varepsilon_{yy} = \varepsilon = \frac{a_s - a_l}{a_l} \qquad \text{.....(2)}$$

Since the layer is free to relax in the growth direction, the strain in the perpendicular direction z, due to the Poisson effect is given by,

$$\varepsilon_{zz} = -\frac{2\upsilon}{(1-\upsilon)}\varepsilon \quad \text{.....(3)}$$

The stresses in the growth plane are equal and are given by

$$\sigma_{xx} = \sigma_{yy} = \sigma = \frac{E}{(1-\upsilon)}\varepsilon \quad \text{.....(4)}$$

where E is the Young's Modulus and υ is Poisson's ratio.

In the case of a superlattice if the thickness of the two layers are given by h_1 and h_2, then the net misfit strain is given by

$$\varepsilon = \frac{h_1\varepsilon_1 + h_2\varepsilon_2}{h_1 + h_2} \quad \text{.....(5)}$$

where ε_1 and ε_2 are the strains in the two layers with respect to the substrate.

2.1.4.2.2 Critical Thickness

The critical thickness can be defined as the thickness at the transition point, in going from a fully elastic to a partially relaxed state. It is an important parameter as it needs to be taken into account if one wants to design lasers with long and reliable life.

Strained layers give an extra degree of freedom in the manipulation of the properties of a device. But there has to be a compromise between how much strain one can build in to get the desired properties and the limit at which the structure will relax, generating defects. Even though the amount of strain is such as to maintain coherency at the interface, as the thickness of the layer increases the strain energy builds up proportionately. Thus there comes a point when the layers relax. For a given thickness there is a critical composition and for a given composition there is a critical thickness above which the layers relax. These critical points can be worked out from a strain energy approach.

The elastic energy stored in a fully coherent, isotropic, elastically strained layer of thickness h is given by (Matthews, 1975):

$$E_\varepsilon = \frac{2G(1+\upsilon)}{(1-\upsilon)}\varepsilon^2 h \quad \text{.....(6)}$$

where E_ε is the elastic strain energy, G is the shear modulus, and ε is the strain.

Once it exceeds a critical limit, the misfit strain energy in the layer can lead to two different effects :

1. the formation of dislocations, and
2. morphological instabilities.

In this section, we concentrate on the critical thickness at which the layers relax by the formation of dislocations. The total misfit f, defined in the earlier section can now be broken into two parts:

$$f = \varepsilon + \delta \ ;$$

where ε is the elastic strain in the epilayer, and δ is the plastic strain.

The energy per unit area of a square grid of two perpendicular and noninteracting arrays of mixed dislocations of <110> type, is (Fitzgerald, 1991):

$$E_\delta = D\left(\frac{b}{b_{eff}}\right)(1-\upsilon\cos^2\alpha)(f-\varepsilon)\left(\ln\frac{R}{b}+1\right) \quad \text{.....(7)}$$

where, E_δ is the dislocation energy, b is the burgers vector of the dislocation, b_{eff} is the effective Burger's vector (i.e. the interface-plane component of the Burgers vector in the direction of dislocation spacing), R is the outer cut-off radius of the dislocation energy, α is the angle between b and the dislocation line, and D is an average shear modulus of the interface given by the following equation:

$$D = \frac{G_l G_s b}{\pi(G_l + G_s)(1-\upsilon)} \quad \text{.....(8)}$$

where, G_l is the shear modulus of the layer and G_s is the shear modulus of the substrate.

The value of ε which minimizes $E_\varepsilon + E_\delta$ is

$$\varepsilon^* = \frac{D(1-\upsilon\cos^2\alpha)(b/b_{eff})}{2Yh}\left(\ln\frac{R}{b}+1\right) \quad \text{.....(9)}$$

where, $Y = \frac{2G(1+\upsilon)}{(1-\upsilon)}$.

The value of R depends on the dislocation density. If half the interface dislocation spacing is greater than the thickness of the film, h, then R=h. If it is less than h then $R=b_{eff}/2(f-\varepsilon)$ and this value should be inserted in Eq.(7) before taking derivatives. To find the critical thickness h_c, at which it is energetically favorable to introduce misfit dislocations, f is substituted for ε^* in eq.(9) which gives:

$$h_c = \frac{D(1-\upsilon\cos^2\alpha)(b/b_{eff})}{2Yf}\left(\ln\frac{h_c}{b}+1\right) \quad \text{.....(10)}$$

Van der Merwe(1993) showed that strain release by dislocation generation may cause a transition to SK growth.

2.1.4.2.3 Morphological Instabilities

Stress relaxation by dislocations was discussed in the previous section. There is another mode by which the elastic strain energy of a strained layer can relax i.e. by creating surface instabilities. This mode of relaxation has been observed only when there is compressive stress in the layers. Thus thin films have been shown to demonstrate an asymmetry with respect to the sign of the strain: films under compression roughen by forming coherent islands while those under tension remain relatively smooth (Roland, 1996).

Surface undulations only occur when the decrease in strain energy due to relaxation outweighs the increase in surface energy due to the increase in surface area. Thus there is a critical thickness for a given misfit strain beyond which the layer is unstable with respect to morphological instabilities. This critical thickness is found by considering the increase in surface energy and decrease in elastic strain energy that occurs by surface roughening.

If the growth rate of the film is appreciable (Roland, 1996) or the temperature of growth is decreased (Spencer et al., 1991), then the instability may be postponed to a larger thickness because of a kinetic stabilization of the growing film.

Surface instabilities can take many forms such as surface ripples or undulations, facets, and three dimensional islands. For undulations as the growth proceeds there is diffusion on the surface due to the stress gradient. This surface stress gradient results because the formation of ripples on a compressively strained layer produces crests that are elastically stress-relieved, while at the intervening troughs there is an additional local compression (Cullis, 1996). This can lead to the development of a cusp like morphology. The sharp cusps serve as dislocation sources. Similarly facets and islands may eventually lead to formation of dislocations due to stress concentration effects at corners or cusps.

2.2 GROWTH ON PATTERNED V-GROOVED SUBSTRATES

2.2.1 Introduction

Growth of quantum wells on planar substrates leads to one dimensional(1D) confinement of electrons and holes. Although the variables one can tailor (composition and thickness of the layer) to meet the requirements give enough flexibility in terms of

designing devices with specific wavelengths, the theoretical possibility of achieving greater speed, mobility and efficiency by confining the carrier motion in 2D and 3D has been explored. 2D and 3D quantum confinement lead to the terms quantum "wires" and quantum "dots" respectively. To obtain carrier confinement in more than one direction one should be in a position to vary certain properties such as refractive index and bandgap in the lateral direction in addition to the growth direction. This can be achieved by varying the composition or thickness in the lateral direction. In order to obtain a lateral variation of the crystal properties, additional processing is required. In the following section, the different growth methods for obtaining quantum wires, will be compared.

2.2.2 Different Techniques of Fabricating Quantum Wires

Control of the lateral variation of composition has led to the fabrication of quantum wires and quantum dots, with 2D and 3D confinement of carriers, respectively. Techniques such as selective ion implantation, application of strong magnetic field, etching and regrowth, growth on vicinal substrates, and growth on patterned substrates can be used. The success of these techniques can be attributed in part to advanced growth techniques such as molecular beam epitaxy (MBE) and metal-organic chemical vapor deposition (MOCVD) and hence have added a new dimension to the power of these methods (Hoenk et al., 1989). Selective disordering of layers induced by implanted or diffused impurities is one of the techniques for patterning the bandgap and refractive index of devices. Although this method avoids direct regrowth on etched surfaces, it can result in the introduction of defects due to high energy implantation or contamination associated with the incorporation of impurities (Kapon, 1994). Simulation of quantum wires by strong magnetic fields results in effective 2D confinement of carriers in the plane normal to

the field axis but this method does not afford much flexibility in terms of the design of quantum structures and their potential applications (Kapon, 1992a). Etching and regrowth are not foolproof against damage generated at the interfaces during the etching process and this can severely degrade the luminescence efficiency, particularly for lateral dimensions below 100nm for which multidimensional quantum size effects are expected to emerge (Kapon, 1992a). Growth on vicinal substrates can be used for fabricating quantum wire arrays of sub-10nm lateral dimensions without the use of lithography (Kapon, 1992a). This method does not involve post growth processing steps and thus yields QWR structures of high interface quality. Furthermore the lateral dimensions obtainable are beyond the capabilities of most lithography methods in current use. These advantages make this technique quite attractive but its application requires preparation of vicinal surfaces with regular monatomic steps and control of growth rate with extremely high accuracy. Also the resulting lateral bandgap modulation can be limited by diffusion effects which might prevent complete segregation of group III atoms (Kapon, 1992a). This summary of some of the current techniques of generating QWRs helps us in understanding the significance of growth on patterned substrates.

Compared to all the techniques discussed above growth on patterned substrates has proved to be the most successful and widely used technique for generating quantum wires. It not only provides clean interfaces but is easily reproducible. The growth on patterned substrates on which V-grooves have been etched, leads to a lateral variation in properties such as the bandgap and refractive index. Variations in the properties of epilayers grown on nonplanar substrates occur as a result of an orientation dependence of surface kinetics during the growth. In the following sections some of the results reported in the literature will be discussed.

2.2.3 Growth of AlGaAs/GaAs on Patterned V-Grooved Substrates

Growth on V-grooves was first demonstrated by Kapon, Tamargo, and Hwang (1987). They used the AlGaAs/GaAs system that has negligible misfit stresses and hence the formation of strain related defects can be suppressed. Growth on V-grooves was successful in generating wires because the thickness of the layer at the bottom of the groove was more than three times that at the sides. A schematic diagram of an ideal growth is shown in Fig. 2.6 and the schematic of the proposal of Kapon et al. (1987) explaining the formation of quantum wires in a V-groove is shown in Fig. 2.7. The change in thickness led to a lateral confinement of carriers in addition to the confinement in the perpendicular or growth direction due to a change in composition. Although as noted before, other techniques were available to generate quantum wires, growth on patterned substrates offered certain advantages over these other methods. The in-situ formation of wires yielded damage free interfaces, free from nonradiative interface recombination effects, which resulted in long carrier lifetimes and high quantum efficiency. A second advantage of this method was the formation of quantum well regions (Fig. 2.6) which were connected to the quantum wires and provided 2D channels that facilitated excess carrier capture into the extremely narrow and thin crescent shaped wires. This crescent shape leads to broadening of the subband gaps (Kapon et al., 1992b).

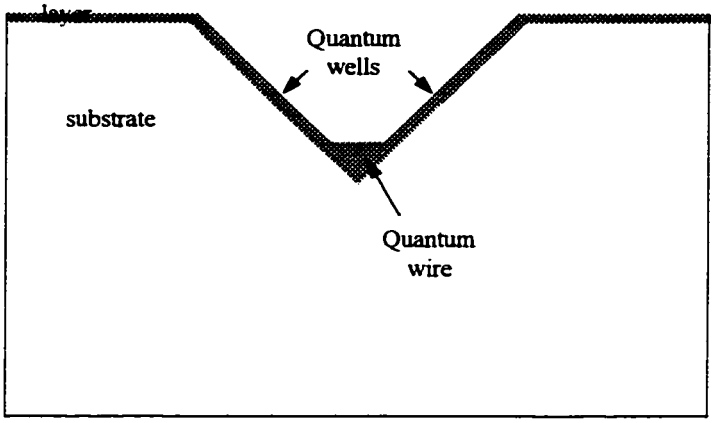

Fig. 2.6 Schematic diagram of an ideal quantum wire growth on V-grooves.

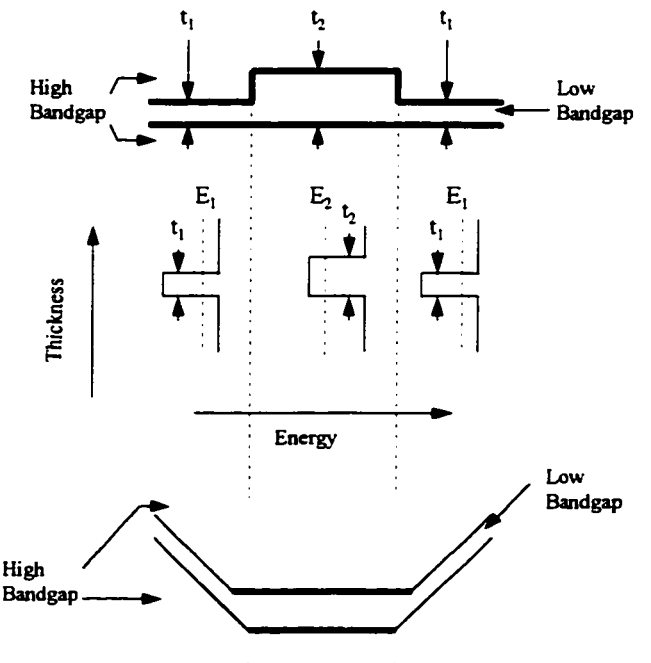

Fig. 2.7 Carrier confinement induced by quantum well thickness variations(a) Quantum well heterostructure with lateral thickness variations. (b) Lateral variations in the energy of the two dimensional bound state. Carriers can be confined in the center region, where they have the lowest energy. (c) Possible realization of the structure in (a) by growth of a quantum well heterostructure in a groove (after Kapon et al., 1987).

As mentioned before one of the desirable characteristic of growing layers on V-grooves is a change in thickness at the bottom of the groove compared to the sides. The orientation of the planes with respect to the incoming flux only explains part of the changes often observed at the bottom of V-grooves. The difference in sticking coefficients on different planes and difference in diffusion rates of group III elements also contribute to thickness variations.

Hata et al.'s (1990) study provided evidence that different diffusion rates are important for generation of quantum wires. They studied the growth behavior of GaAs on <110> etched GaAs mesa structures. The mesa structure consisted of (111)A faces in $[1\,\bar{1}\,0]$ direction and $(1\,\bar{1}\,1)$B faces in the [110] direction, with a (001) plane at the bottom. From the edge of the (111) planes the growth rate varied in an exponential manner on the (001) plane, with an increase on the surface near the junction with (111)A and a decrease in growth rate near the junction with $(1\,\bar{1}\,1)$B surfaces. They concluded that the surface diffusion length was 8 times smaller along [110] than $[\bar{1}\,10]$ at 560°C.

Pan et al. (1995) found similar results for $Al_xGa_{1-x}As$/GaAs grown on patterned V-grooved GaAs substrates with (111)A sidewalls. They observed that the growth rate on the top (100) plane was dependent on the migration characteristics of group III atoms from the neighboring sidewalls. The migration behavior determines the facet development and is dependent on the temperature. Hence the study of Pan et al. (1996) done at different temperatures showed how a change in diffusion length changed the facet development. They studied AlGaAs/GaAs grown on (111)A V-grooved GaAs substrates at 600°C, 650°C, and 700°C. The sidewalls subtended an angle of 70° to start with, but during growth these sidewalls deviated from (111)A planes to higher index planes (n11)A (n>1). The structure grown at 600°C subtended an angle of 86° corresponding to (433)A sideplanes, while those grown at 650°C and 700°C subtended an angle of 94°

corresponding to (322)A sidewalls. A measurement of the growth rates showed that at 600°C the growth rate on the top (100) surface was slower than that on the sidewall, at 650°C the growth rate on the top (100) surface was comparable to the sidewall, while at 700°C the growth rate on the (100) surface was much faster than that on the sidewall. These results showed that at higher temperatures more Ga and Al atoms diffuse from the sidewalls to the top (100) planes, leading to a higher growth rate on the (100) surface at 700°C. Similar growths on planar (100) GaAs substrates with growth temperature in the range 550°C to 750°C did not show any variation in growth rates. Thus Pan et al. (1996) concluded that the sidewall orientation that develops is determined by three factors: growth rate differences between the top (100) plane and the sidewall; the growth temperature, and the Al content since the diffusion length of Al and Ga are different. The Al content distribution was found to vary in the sequence, x_{Al} (the sidewall) > x_{Al} (top(100)) > x_{Al} (edge-facet) > x_{Al} (bottom-intersection).

The variation in composition along the groove sides occurs because near a facet boundary the population of surface atoms may be altered by transfer of atoms to an adjacent facet. Hoenk et al. (1989) observed this composition variation using spectrally resolved cathodoluminescence (CL). They suggested that there is another important factor involved in producing composition changes: the different sticking coefficients of aluminum and gallium (a sticking coefficient is defined on infinite surfaces as the ratio of the number of atoms incorporated into the surface to the composition of the incident flux). Hoenk et al. (1989) suggested that both the sticking coefficients and diffusion lengths must be strongly dependent on facet orientation to account for their results. Kapon et al. (1992d) observed that in samples grown on $[0\,1\,\bar{1}]$ oriented grooves on (100) substrates, CL images displayed uniform emission along the axis of the wires and across the array of wires. From this they concluded that the diffusion mechanism which gives rise to the

crescent shaped wires occurs uniformly along the wire axis. These crescent shaped wires are also a result of the difference in diffusion and incorporation rates of Ga and Al.

The growth depends on the orientation of the substrate; hence it becomes important to understand the effect of different orientations on the growth rate and morphology of the layer. Kim et al. (1994) studied the growth of $Al_{0.5}Ga_{0.5}As$/GaAs on GaAs grooves etched out of high index planes such as (13 11)A, (511)A, (311)A, and (211)A. These growths were done using metal organic vapor phase epitaxy (MOVPE). The profile of the groove or ridge was dependent on the etching method, the direction of the stripe ([011] or $[0\bar{1}1]$), the stripe width, and substrate orientation. All of these factors affect the growth properties. After growth the sides of the grooves consisted of (433)A type planes for all $[0\bar{1}1]$ oriented grooves although the as-etched structure contained (111)A sidewalls. The reason for this change from the as-etched state to the initial stage of growth was attributed to the nucleation problem. Kim et al. (1994) argued that nucleation is easier on a plane having steps or kink sites than on an atomically flat {111}A surface; hence the etching and the growth mechanisms are quite different. As the growth progressed on these grooves a (100) orientation was finally attained irrespective of the initial substrate orientation. The reason given for the evolution of the (100) facet was the lower surface energy of {100} planes. The planarization of V-grooves oriented along $[0\bar{1}1]$ for AlGaAs/GaAs was also reported by Colas et al. (1990b). Planarization of grooves was attributed to the differences in the surface mobilities of group III atoms on different planes, dependent on the growth temperature.

The growth rate of epilayers was also shown to depend strongly on the substrate temperature and the As/Ga flux ratio in addition to the direction of growth (Hoenk et al., 1989; Sogawa et al., 1994). Sogawa et al. (1994) showed that the shape of the groove can be controlled by changing the V/III flux ratio and temperature. Increasing the

temperature and decreasing the As/Ga flux ratio both increase the surface mobility of group III atoms and hence these methods can also be used to control the composition at the bottom of the groove (Vermeire et al., 1992; Hersee et al., 1986).

In terms of optical properties AlGaAs/GaAs grown on V-grooves gave a photoluminescence (PL) intensity peak corresponding to a single QWR (Kapon et al., 1989b) or multiple quantum wires (Walther et al., 1992). In the case of multiple quantum wires a small difference in crescent size and shape in successive layers caused a slight inhomogeneous broadening of the PL intensity peak (Simhony et al., 1991). Simhony et al. (1991) proposed that increasing the effective Al mole fraction in the barrier layers and using thicker barriers would lead to a more complete recovery of the V-groove shape and therefore to smaller differences in the wire sizes. Other criteria which need to be satisfied to get efficient quantum wire structures are: (a) lateral dimensions should be in the 10nm range to resolve the energy subbands, (b) a low or zero defect density to reduce nonradiative recombination processes and (c) a high density of wires to maintain high interaction with incident light (Jouneau et al., 1995).

2.2.4 Misfit Layers Grown on Patterned V-Grooved Substrates

The AlGaAs/GaAs system is lattice matched over the whole composition range but there have been other studies involving systems such as InGaAs/GaAs, and InGaAs/InP where the misfit changes with composition. The interest in these systems arises due to the need to develop lasers with a wavelength of 1.3 or 1.55microns for optical communication systems. In addition, compressive strain is expected to be beneficial for lowering the heavy hole effective mass and increasing the separation of the valence subbands, thus leading to a more effective 2D confinement in the valence band (Kapon et al., 1992b). The

growth of misfit layers on patterned V-groove substrates has proved to be a much bigger challenge since composition variation along the groove sometimes exceeds the critical thickness limit and generates dislocations (Bhat et al., 1990).

One of the earliest attempts at growing lattice mismatched systems on V-grooves was by Bhat et al. (1990). They investigated InGaAs and InGaAsP layers grown on InP substrates with $[01\bar{1}]$ oriented grooves on (100) plane. The sidewall planes in these grooves were close to {211}A. They observed large deviations from lattice matched compositions on the sidewalls of the groove and they attributed this to the difference in sticking coefficients of the various growth species for different crystal orientations. According to these authors when different crystal faces are nearest neighbors, the incident atoms can diffuse to more favorable sites by surface diffusion or by a desorption-adsorption process. Thus the variation in composition may lead to defects in areas where the misfit energy exceeds the critical limit for dislocation formation.

In their investigation of InGaAs/InP and InAlAs/InP systems grown on {211} type grooves aligned along $[1\bar{1}0]$, Turco et al. (1990) observed that the surface mobilities of the species over the different facets make a more important contribution to lateral thickness variation than in AlGaAs/GaAs. Compositional variations occur in InAlAs and InGaAs grown on InP, resulting in lateral inhomogeneous strain, and eventually to dislocation formation. The diffusion and sticking coefficients on the various planes in the groove must be known in order to grow layers with sufficient thickness variations for carrier confinement without the formation of any defects. They concluded that the preferential diffusion from the sidewall to the bottom of the groove changes the In concentration at the bottom of the groove.

The growth of mismatched layers on grooved substrates can also be affected by the strain field, presumably through a change in the surface chemical potential of the atoms as a function of the elastic strain field (Chu, 1993). Chu (1993) noted that such effects are not observed in the InP spacer layers where the growth surface planarizes quickly. A similar observation was made by Hartmann et al. (1995) who studied the growth of SiGe/Si layers on patterned Si substrates. The sides of the groove consisted of {111} planes. According to these authors the formation of quantum wires is not simply a result of different growth rates on different planes but also is a consequence of differences in growth behavior of SiGe and Si. The local growth rate of SiGe in convex corners of the grooves was at least ten times higher than on the (001) planes, whereas the growth rate of Si was unaffected. They suggested that the lattice mismatch strain must be the driving force for the increased growth rate of SiGe in the corners as already noted by Chu (1993). This increase in growth rate was shown to be a result of diffusion of Ge from the sides to the bottom of the groove during growth.

The investigation of Bhat et al. (1991) of InGaAs/InGaAsP growth on (211)A grooves showed that the thickness of the layers at the bottom of the groove in the central region of the crescent was 50% greater than that on the edge of the (311)A plane. This enhancement occurred only after the first few layers were deposited. Thus, although there was a crescent shaped region similar to AlGaAs/GaAs at the bottom of the groove, the large variation in the shape and size of the crescent-shaped regions with successive layers led to inhomogeneous broadening of the PL peak. Extensive dislocation formation at the sides of the groove also led to nonradiative carrier recombination and optical absorption by defects. Thus these structures did not lase.

Bhat et al. (1990) also studied InGaAs and InGaAsP layers grown on InP grooves oriented along $[01\bar{1}]$ on (100) plane. These growths showed faceting of the {111}A type

sidewalls. The facets consisted of {311}A and {111}A type planes. These facets also appeared even when only InP was grown in the grooves. In another study Bhat et al. (1991) concluded that defect free InGaAsP layers can be grown without any composition deviation if the facets are {h11}A oriented, where $h \geq 3$. Growth of InP on V-grooves with {111}A sidewalls created {311}A facets at the bottom of the groove. Growing InGaAsP on these grooves after growing a thick layer of InP resulted in a crescent shaped layer at the bottom of the groove with little growth on the sidewalls.

The major cause of dislocations in the growth of misfit layers on V-grooves seems to be related to the different diffusion lengths and incorporation rates of the growth species. Since surface diffusion may be controlled by changing the temperature or V/III ratio, getting a better understanding of the growth process can lead to defect free growth. Nishioka et al. (1992) reported the successful fabrication of thin $In_{0.1}Ga_{0.9}As$ strained quantum wires grown on patterned GaAs substrate by MOCVD. The sidewalls of the groove were (111)A type. Kapon et al. (1992b) also obtained defect free $In_{0.2}Ga_{0.8}As$ strained layers on patterned GaAs substrates with grooves containing (111)A sidewalls. Moreover darker contrast patterns observed by TEM below and above the InGaAs crescents signified the presence of strains. The strain was expected to be beneficial for lowering the heavy hole effective mass and increasing the separation of the valence subbands.

Most growths reported so far in AlGaAs/GaAs and in lattice mismatched systems have been conducted on grooves with (111)A sidewalls. The reason for (111)B not being a popular growth plane is the deterioration of growth quality on these planes. Thrush et al. (1993) compared growth on {111}A with {111}B and found that nucleation on {111}A type facets occurred more readily than on {111}B type facets. Similar results were obtained by Hersee et al. (1986) and Lee et al. (1993). The difference in growth behavior

of the two surfaces may arise because {111}B surface is group V dominated and has two free valence electrons per atom at the surface whereas {111}A surface is group III dominated and has no free valence electrons (Dilger et al., 1994).

This section showed the important role played by strain in determining the quality of growth. Hence the need for a suitable model that gives the strain distribution of layers grown on V-grooves is critical for further development of quantum wires.

2.2.5 Stress Distribution in Quantum Wires Grown on V-Grooves

In the case of growth on planar substrates the development of models giving the strain distribution progressed at the same time as devices were being developed. The knowledge of strain distribution allowed researchers to develop better devices because they could use the strain to tailor the properties of the laser without endangering the life of the device (O'Reilly, 1989). So the importance of models which give the strain distribution and critical elastic energy cannot be overemphasized. But surprisingly as far as growth on V-grooves goes, development of these models are lagging far behind the progress in device fabrication. Growth on patterned substrates started about ten years ago. As we saw in the previous section the growth of strained layers on patterned substrates has not developed to a stage where one can predictably obtain defect-free growths. These defects are a result of strain exceeding the critical limit in certain parts of the groove although the "intended" composition often corresponded to the lattice matched case in planar growths. This deviation in composition (and hence strain) is caused by many factors such as sticking coefficients, diffusion, orientation, temperature and III/V flux ratio. Although our understanding is still incomplete as to how they affect growth, simple models assuming uniform composition have been developed.

Freund and Gosling (1995) have calculated the critical thickness condition for the growth of strained quantum wires on V-grooved substrates. They studied an "idealized" quantum wire of triangular cross section (Fig.2.8) grown epitaxially in a V-shaped groove on a patterned (100) surface of a cubic substrate. The sides of the groove were {111} planes and the wire extended along a <110> direction.

Their calculation of the critical thickness followed the Matthews-Blakeslee (1974) approach, taking into account both the free surface effect and the mismatch strain effect

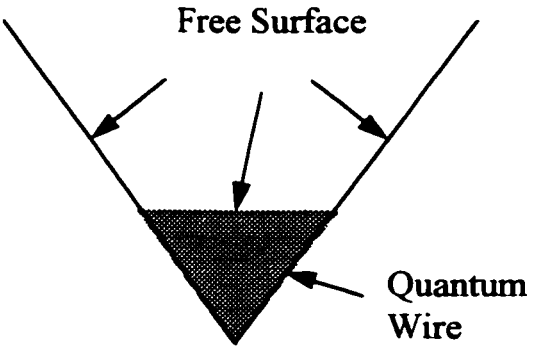

Fig. 2.8 Assumed geometry of the wire in Freund and Gosling's model (after Freund and Gosling, 1995)

The assumptions in Freund and Gosling's analysis were:

1. The spacing between the wires and the depth of the V-grooves were large enough to model each wire as being an isolated feature in a deep groove.
2. The apex of the groove was sharp and the wire cross section was triangular with a flat top surface.

On comparing their theoretical results with the experiments of Arakawa and coworkers (1993) they found a good match. Thus they were able to establish a condition

of critical thickness in the form of a relationship between wire size and the smallest mismatch strain for which the wire remains stable against the formation of misfit dislocations.

In an earlier paper Gosling and Willis (1995) calculated the stress distribution associated with a periodic array of misfitting inclusions in an infinite body. These inclusions simulated buried arrays of $[1\bar{1}0]$ oriented wires. They developed a critical mismatch condition for this geometry following the Matthews and Blakeslee (1974) condition and showed that these quantum wire structures were extremely stable in the postgrowth processing stages provided they were spaced at a distance more than four times the wire dimension. They also demonstrated that a strain induced band gap shift is the same for quantum wires and quantum wells with the same mismatch.

Grundmann et al. (1994) modeled the strain distribution, in and around the quantum wire grown on V-grooves, using finite element analysis. Their analysis showed that, in addition to lateral thickness variations, strain effects may also appreciably modify the confinement in these quantum wires. The geometry that Grundmann et al. (1994) used was closer to the experimental situation than the geometry of Fig.2.8 but they also assumed a uniform composition in the layer. In Secs. 2.2.3 and 2.2.4 the experimental results showed that the difference in diffusion and incorporation rates of group III species causes a composition variation along the groove. Grundmann et al. (1994) used a 1.4% lattice mismatch in their calculations, that might lead to formation of dislocations in real growths. However, their study for the first time shows the effect of strain on the optical properties of quantum wires grown in V-grooves.

There is a need for a theory that gives the critical mismatch which leads to formation of dislocations. As noted above Freund and Gosling (1995) have provided such

a theory but for a simplified geometry of a triangular shaped quantum wire. However, a similar theory with a geometry that has a continuous layer on a V-groove, as in the study by Grundmann et al. (1994), needs to be developed.

2.2.6 Faceting of Layers Grown on Patterned V-Grooved Substrates

No complete theoretical treatment exists for faceting in the case of growth on V-grooves. The factors which determine faceting behavior of layers grown on V-grooved substrates include the orientation of the grooves, the temperature of growth, surface reconstruction, and sticking coefficients. The interplay between these factors and the kinetics of the process makes the modeling of faceting very difficult.

Faceting of layers grown on patterned V-grooved substrates is different from faceting of layers grown on planar substrates. In the former case faceting usually occurs for both homoepitaxial and heteroepitaxial growth. But in the case of layers grown on planar substrates, as we saw in an earlier section, faceting occurs only when the misfit strain energy exceeds a critical limit. So any explanation for faceting in the planar case may not be valid for V-grooves, and vice-versa.

Jones et al. (1991) proposed a technique to determine the shapes of GaAs epitaxial layers grown by OMCVD on patterned substrates. This technique is based on the Borgstrom construction, which is based on the same premise as the Wulff construction for finding the equilibrium shape of a body.

Using the Borgstrom construction the shape of a growing crystal on any type of starting surface morphology can be predicted if the growth rate on different planes and the geometrical relationship of the facets is known. According to this construction:

1. Given a concave surface ($180°<\theta<360°$, θ being the angle between the initial facets defined in Fig. 2.9a), with growth rates $h_2 > h_1 > 0$, if $h_1 < -h_2 \cos(\theta)$, then the faster growing facet will consume the slower growing facet. If $h_1 > -h_2 \cos(\theta)$, then both facets will diminish in area with time (Fig. 2.9b).

2. Given a convex surface ($0°<\theta<180°$), with growth rates $h_2 > h_1 > 0$, if $h_1 < -h_2 \cos(\theta)$ then the slower growing facet will consume the faster growing facet (Fig. 2.10a). If $h_1 > -h_2 \cos(\theta)$ then both facets will increase their relative area with time (Fig. 2.10b).

The Borgstrom construction assumes that the growth rates, for orientations between the neighboring facets, are linearly interpolated. This assumption can lead to incorrect results. Jones et al. (1991) proposed a slightly more complicated technique, based on the Wulff construction, that does not assume that the growth rate varies linearly with orientation. In this technique the orientation dependence of the growth rate must be known to some degree of accuracy. As in the Borgstrom construction, here also the interface shape is defined by:

Minimization of $\int$(growth rate)dA (convex).....(10)

Maximization of $\int$(growth rate)dA (concave).....(11)

Equations 10 and 11 imply that for a convex corner the interface region takes on the shape that minimizes the growth rate over the area of the convex contour and for concave corner the surface will have a shape that maximizes the growth rate over the area of the concave contour.

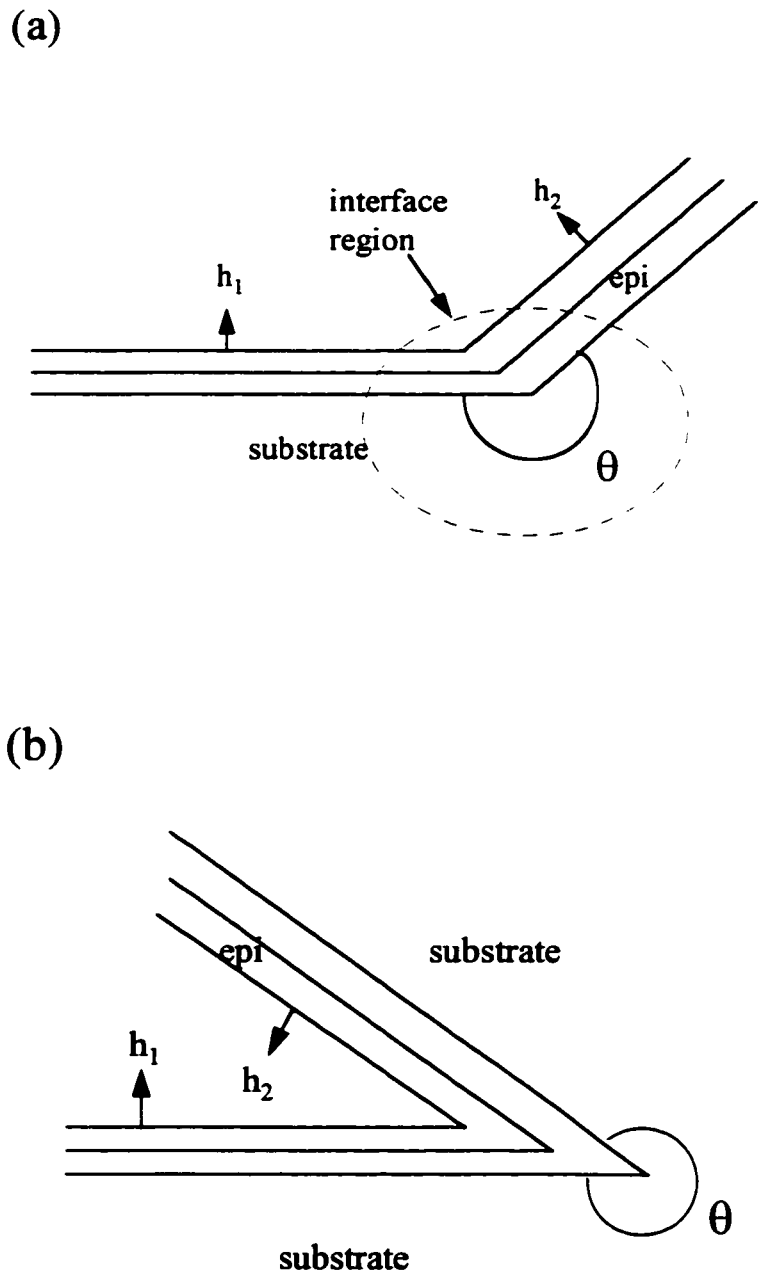

Fig. 2.9 Examples of Borgstrom constructions for concave surfaces ($h_2 > h_1$) (a) faster growing facet is consuming the slower growing facet. (b) both facets are being consumed for all h_1 and h_2 (after Jones et al., 1991).

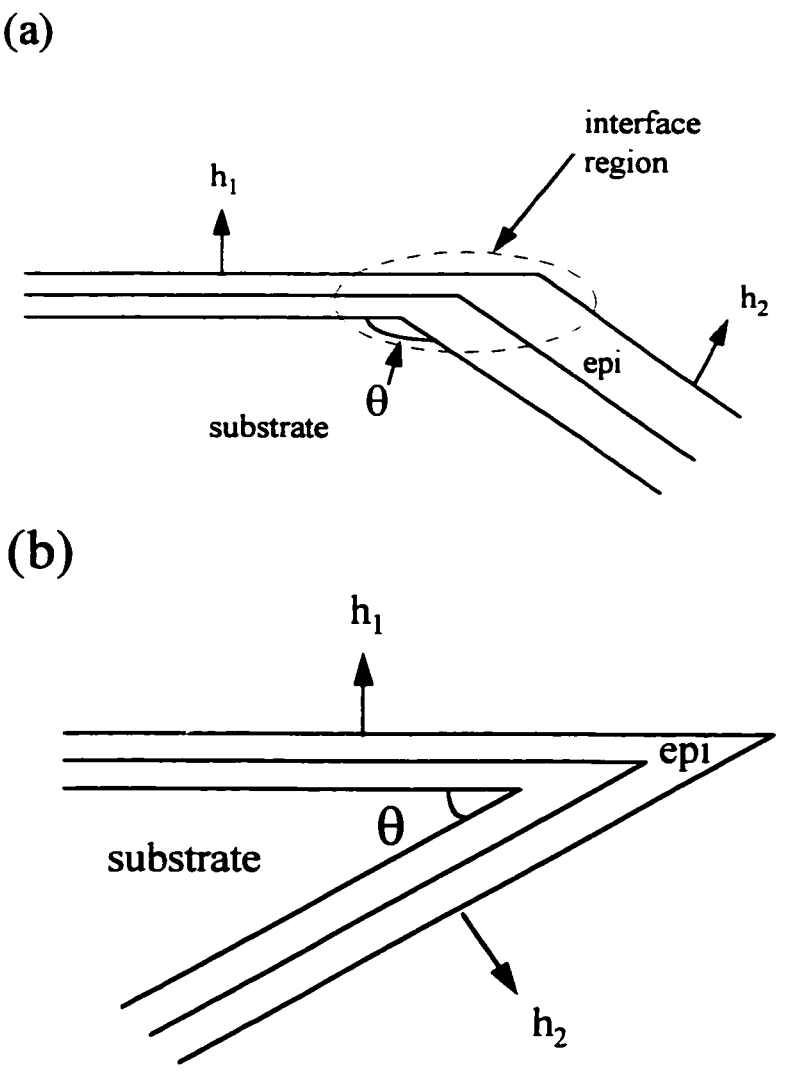

Fig. 2.10 Examples of Borgstrom constructions for convex surfaces. (a) slower growing facet is consuming faster growing facet. (b) neither facet is being consumed for all h_1 and h_2 (after Jones et al., 1991).

The original Wulff construction was based on the minimization of surface energy. This construction plots the surface energy as a polar diagram and one can determine the shape of the minimal surface for anisotropic cases. For etching of V-grooves the etch rate polar diagram predicts the profiles. Similarly an orientation dependence of growth rate

can be plotted as a polar diagram and will aid in predicting the resultant steady state crystal shapes. Both the Wulff and Borgstrom constructions predict the crystal shapes based on the geometrical constraints of crystal growth exemplified by eq. 10 and 11. Comparison of their theoretical prediction with experimental results for the case of GaAs grown using OMCVD showed that their construction technique can predict the general shape of the growth surface. However, this prediction is accurate only when the facet lengths are smaller than the surface diffusion lengths. In their construction Jones et al. assumed that the growth rate across any given facet is constant. They did not take into account the role played by interfacet migration and temperature in determining the morphology of growth on a nonplanar substrate.

Ozdemir and Zangwill (1992) proposed a different approach to faceting of layers grown on nonplanar substrates. They took into account kinetic processes of deposition, desorption, interfacet migration, adatom exchange between terraces and kink sites, and capillary driven mass transfer in their analysis. A major basis of their theory was based on the experiment of Geguzin and Ovcharenko (1961) that showed thermal planarization of nonplanar, faceted substrates by mass transport. Thus in a grooved substrate the chemical potential varies with the facet and hence even in the absence of a deposition flux, capillary forces will drive mass transfer (by surface diffusion) until planarization occurs and the chemical potential is uniform everywhere. In the example solutions that Ozdemir and Zangwill (1992) cited for different growth parameters, planarization eventually occurred in every single case they studied, although the morphological evolution and rate of planarization varied, depending on growth parameters.

One striking feature of growth on nonplanar substrates that has not been explained yet is the appearance and growth of entirely new facets not exposed by etching the original substrates. Although the construction of Jones et al. (1991) did generate new facets, they

did not explain how such facets nucleate in the first place. Many instances of faceting of layers grown on V-grooves have been reported in the literature. Faceting was observed for both homoepitaxial (Bhat et al., 1990; Kim et al., 1994) as well as heteroepitaxial growth (Turco et al., 1990; Colas et al., 1990; Dilger et al., 1994; Bhat et al., 1990; Bhat et al., 1991; Pan et al., 1996). In many growths, both homoepitaxial and heteroepitaxial, the facets on (n11) grooves gradually develop with increasing n such as to planarize the surface (Kim et al., 1994; Colas et al., 1990) as predicted by Ozdemir and Zangwill (1992). However the planarization behavior is not the same for the different compounds. Ga and In atoms are highly mobile and this leads to a rapid planarization of the V-grooves. On the other hand, the low mobility of Al atoms tends to preserve the shape of the grating (Jouneau et al., 1995). Jouneau et al. (1995) observed a difference for V-grooves oriented along [110] and [$1\bar{1}0$], other conditions remaining the same. Planarization was faster when the substrate was grooved along [$1\bar{1}0$]. This behavior can be explained by the difference in surface diffusion lengths along [110]and [$1\bar{1}0$] (Turco et al., 1990). In this case, to obtain well shaped wires the grooves should be oriented along [110].

2.3 TRANSMISSION ELECTRON MICROSCOPY(TEM)

2.3.1 Introduction

Electron microscopy plays an important role in the characterization of strained layers. It is used to check the quality of the interface, identify the type of dislocation formed, study the strain field, and in general determine the quality of crystals produced by a growth process.

Samples used for microscopy are very small and the thickness in the electron transparent region is only a few thousand Angstroms. At this thickness the results may

not be representative of bulk behavior. One has to be careful in interpreting the results. In strained epitaxial layers, an important factor contributing to the image is the relaxation of forces at the free surface. We will consider this factor in detail in the next section.

2.3.2 Elastic Relaxation Contrast at the Surface

The specimens used for TEM are thin and hence the constraints at the surface relax leading to a displacement of atoms near the surface. If this displacement changes with depth it can lead to contrast changes. This contrast can be qualitatively and quantitatively related to the strain field present.

One of the earliest studies which looked at surface effects was done by Ashby and Brown (1963) for coherent precipitates near a free surface. It was observed that most precipitates had a symmetrical strain field contrast with a line of no-contrast running perpendicular to $\vec{g}$ ($\vec{g}$ is a vector pointing towards the diffracted beam from the transmitted beam) under two beam diffracting conditions. But curiously the image of some precipitates displayed an anomalously large strain field and these were unsymmetrical i.e. they were dark on one side of the precipitate and bright on the other. Further, on reversing the sense of $\vec{g}$ the contrast reversed. The bright field and dark field contrast was complimentary for a particle at the bottom of the foil, but it was the same for a particle near the top of the foil. This behavior was linked to surface relaxation of the strain field of precipitates close to the either surface of the foil. The effect can be understood using the concept of anomalous absorption, first introduced by Hashimoto et al. (1962). This concept is based on the excitation of Bloch waves shown in Fig. 2.11.

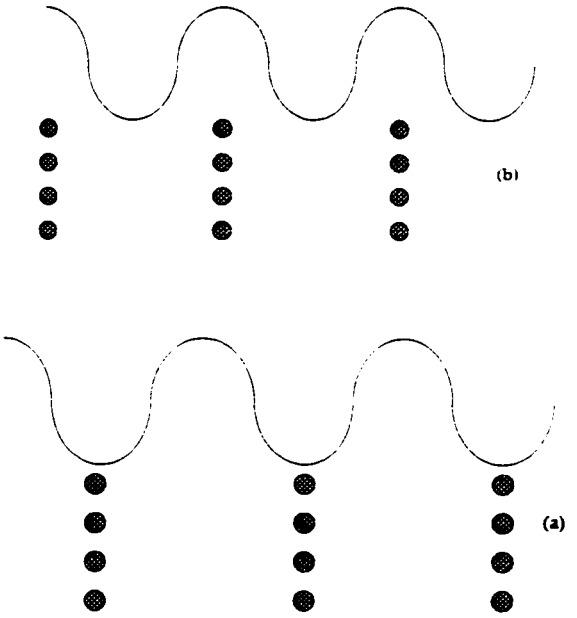

Fig. 2.11 Schematic diagram showing Bloch waves (a) Bloch wave I (b) Bloch wave II.

Bloch wave I is shown in Fig. 2.11a. This wave has peaks between the atoms and hence it is transmitted well but Bloch wave II which is shown in Fig. 2.11b has peaks at the atomic positions and hence is absorbed. Bloch wave II will be more heavily absorbed than Bloch wave I, since for the latter the current flow vector avoids the regions of high absorption whereas in the former it peaks at the absorbing regions. This situation is true at or close to the exact Bragg condition.

A phenomenological treatment of absorption was given by Hashimoto et al. (1962). They represented absorption in the dynamical theory by adding a periodic imaginary part to the crystal lattice potential. This imaginary part takes account of the inelastic scattering and gives rise to two additional parameters, the normal extinction distance ξ_o' and anomalous extinction distance ξ_g'. Taking into account absorption the dynamical two beam Howie-Whelan equations are given as follows:

$$\frac{dA_o}{dz} = -\frac{\pi}{\xi_o'} A_o + \pi\left(\frac{i}{\xi_g} - \frac{1}{\xi_g'}\right) A_g \qquad \text{.....(12)}$$

$$\frac{dA_g}{dz} = \pi\left(\frac{i}{\xi_g} - \frac{1}{\xi_g'}\right)A_o + \left(-\frac{\pi}{\xi_o'} + 2\pi i(s_g + \beta')\right)A_g \quad \text{.....(13)}$$

where, A_O is the amplitude of the transmitted beam and (A_g) is the amplitude of the diffracted beam as a function of depth z,

$$\beta' = \frac{d}{dz}(\vec{g}.\vec{u})$$

where, $\vec{u}$ is the displacement of the crystal, s_g is the deviation parameter, and ξ_g is the extinction distance. These equations have been used to derive the contrast from lattice plane bending at free surfaces, as discussed in the next section.

2.3.3 Strained-Layer Superlattices (SLSs)

Coherently strained, planar layered semiconductors have a biaxial stress distribution. Cross-sectional samples prepared from strained layer structures (Fig. 2.12) show a strong strain field which is related to the relaxation of one of the stress components at the free surface. By comparing the experimental results with theoretically calculated two-beam images one gets a calibration of the intensity which can be used to give quantitative information about the strain (and indirectly the composition of the sample).

A number of researchers have studied free surface stress relaxation at a misfitting interface (Cook and Howie, 1969; Auret, Ball, and Snyman, 1979; Treacy, Gibson and Howie, 1985; Treacy and Gibson, 1986; Perovic, Weatherly and Houghton, 1991).

Perovic et al. (1991) modeled the strained layers grown on a planar substrate using either a line-force or Fourier series solution to model stress relaxation. Both solutions gave good agreement with the experimental results. In the simplest case of a single strained layer, a broad, anomalous band of diffuse contrast was observed near the interface

(Fig. 2.12b). This contrast was symmetrical in bright field imaging but showed bright-dark contrast in thicker foils in dark field. From a theoretical treatment it was seen that the degree of plane bending (i.e. the effect responsible for the strain contrast) depended on the ratio of layer thickness to foil thickness. For a given layer thickness the magnitude of surface plane rotation decreased with increasing foil thickness (Fig.2.13a), while the maximum value of plane rotation lay further from the interface (Fig.2.13b).

As the thickness of the foil increased anomalous absorption effects became evident. Dark-field images exhibited asymmetric dark-bright contrast for foil thickness$\geq 4\xi_g$ whereas bright field images remained symmetrical. As in the case of coherent precipitates the asymmetry of dark field images for thicker regions of the foil can be used to determine the sign of the misfit.

In a multilayer structure the situation is more complicated as account has to be taken of the interaction between the layers. Perovic et al. (1991) observed that for layers spaced sufficiently closely together, the displacement field cancellation effects take over and the only significant contrast was from the first-layer-substrate interface. In such cases the effective misfit can be calculated by regarding the strained layer superlattice (SLS) as a large single strained layer.

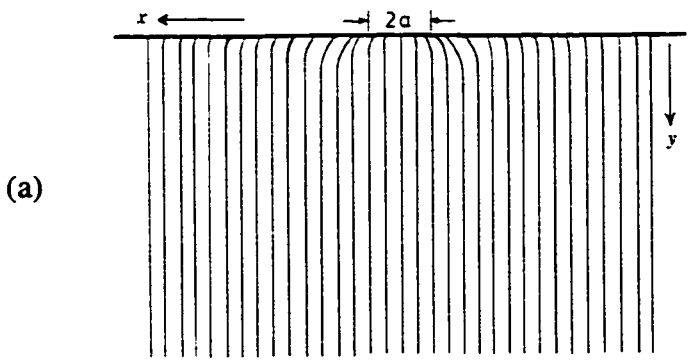

(a)

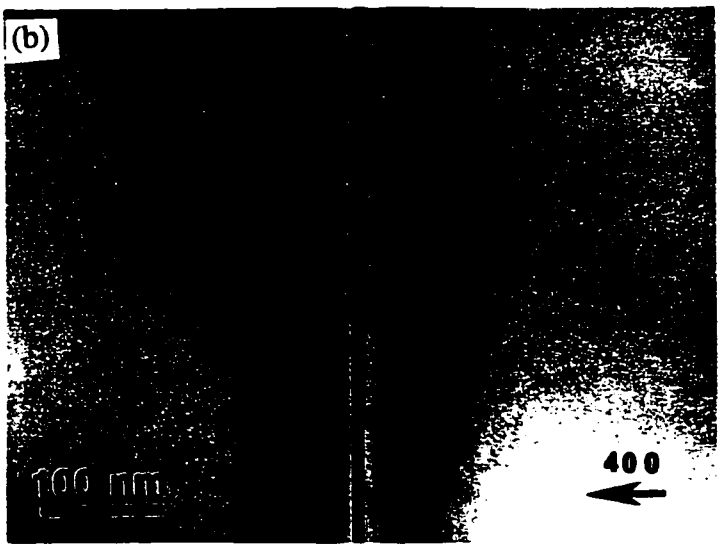

Fig. 2.12 Stress relaxation at the interfaces of layers grown on planar substrate (a) Two dimensional representation of surface lattice plane rotation. (b) $\vec{g} = 400$ bright field (BF) diffraction contrast image of a single, 10nm $Ge_{0.2}Si_{0.8}$ layer buried in Si. (after Perovic et al., 1991).

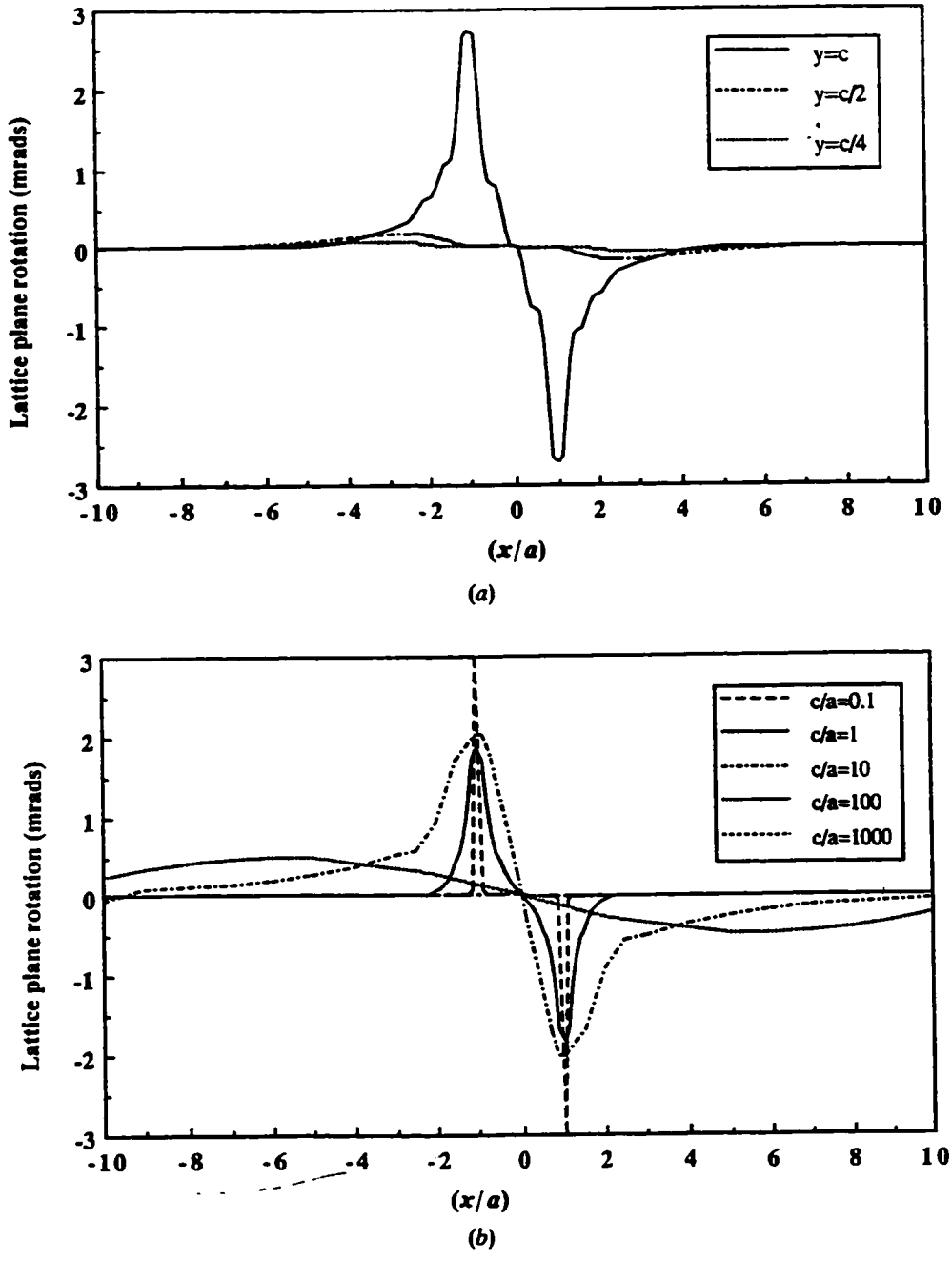

Fig. 2.13 Calculated lattice plane rotations as a function of distance x normal to the interfaces for a single strained layer of width 2a in a foil of thickness 2c; (a) variation of β' (lattice plane rotation) with c for the case c/a = 3 illustrating the localization of strain relaxation near the free surfaces; (b) dependence of β' at the surface (y = c) on the foil-to-layer thickness ratio (c/a). All values of β' are expressed in units of the unconstrained misfit strain (ε_0); the other parameters used in the calculation were: $\nu = 0.3$ and l/a = 1000 (after Perovic et al., 1991).

2.4 COMPOSITION ANALYSIS USING STEM

Energy dispersive X-Ray (EDX) analysis using a STEM is a powerful technique for doing composition analysis. The excellent spatial resolution obtainable on a electron microscope allows one to analyze compositions from extremely small volumes of a thin foil, e.g. a strained layer superlattice. It also offers a number of advantages over bulk chemical analysis. If the sample is quite thin and parallel sided then absorption and fluorescence corrections may be neglected, in contrast to the situation with bulk samples where ZAF (atomic number,absorption and fluorescence) corrections must be made. In practice, samples are not parallel sided but are wedge shaped (Fig. 2.14). In most cases they are not thin enough to neglect absorption effects and hence one needs to determine the thickness at each analysis point to get accurate results.

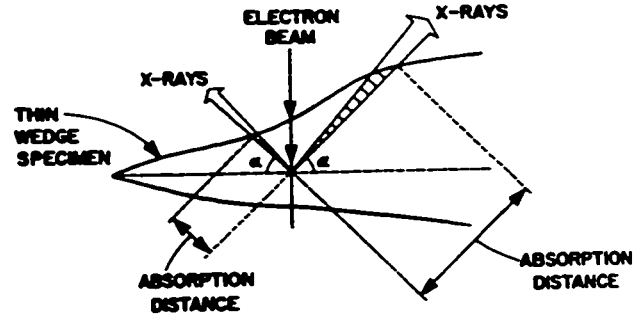

Fig. 2.14 Schematic of a wedge shaped TEM sample

The Cliff-Lorimer's (Cliff and Lorimer, 1975) ratio technique is the most widely used method for obtaining compositions. According to this method the ratio of concentrations of two elements is proportional to the ratio of their intensities. Thus,

$$\frac{C_A}{C_B} = k_{AB}\frac{I_A}{I_B} \qquad (14)$$

where C_A and C_B are the compositions of the two elements A and B, I_A and I_B are the corresponding intensities and k_{AB} is the proportionality constant which accounts for the

relative efficiency of X-ray production and detection. For a given voltage, if absorption and fluorescence can be neglected, k_{AB} is independent of specimen thickness and composition. k_{AB} can be determined either theoretically or experimentally. Although it is more appropriate to determine it experimentally, using standards studied under the same experimental conditions as the sample, consideration of thickness effects and other errors makes the analysis quite complicated.

A reliable criterion to determine whether for a given thickness absorption effects are important or not was given by Tixier and Philibert (1969). Their criterion states that absorption can be neglected if

$$\chi_A \rho t < 0.1 \quad \text{.....(15)}$$

where

$$\chi_A = \left(\frac{\mu}{\rho}\right)^A_{spec} \operatorname{cosec}(\alpha)$$

$\left(\frac{\mu}{\rho}\right)^A_{spec}$ is the mass absorption coefficient for the characteristic X-ray of element A in the specimen composed of A, B, C etc.

ρ is the density of the specimen, calculated using the relation

$$\frac{1}{\rho} = \sum \frac{C_i}{\rho_i}$$

where C_i is the concentration of element i, and ρ_i is the density of element i in the thin film, t is the thickness of the foil, and α is the take off angle between the specimen and the X-ray detector.

Specimen preparation techniques can give rise to certain problems. Ion beam thinning might form a surface layer which leads to variation of the composition ratio with

thickness. Another important consideration is the formation of carbon build up during analysis. These effects can be minimized by cleaning the sample thoroughly before analysis.

Beam broadening effects become important for cases where the analysis is being done close to an interface. To minimize this the sample should be quite thin, the beam voltage should be high and spot size should be kept to a minimum. The effects of beam broadening become an important consideration for small precipitates (Lorimer et al., 1984) and layered samples (McGibbon, 1989).

In the case of strained layer superlattices grown on patterned substrates very few studies of composition analysis using EDX have been reported, since it is a tedious technique which involves difficult sample preparation and careful analysis of the data. CL has been the most popular technique used for composition determination (Hoenk et al., 1989; Keller et al., 1994). Although composition analysis by CL is quick, it does not give the resolution achievable in a modern STEM (~1μ in CL compared to ~ 5-10Å in STEM).

Keller et al. (1994) used both CL and EDX to determine the composition of $In_{1-x}Ga_xAs/InP$ layers grown on nonplanar structures consisting of {111}A and {111}B faces. They used pure InAs and GaP binary alloys as the standards for EDX analysis with a scanning electron microscope (SEM). CL analysis showed that the composition of Ga varied as x_{Ga} (ridge)< x_{Ga} (planar)< x_{Ga} (groove). EDX analysis conducted on the ridge structure gave a more detailed picture of the Ga variation. In the vicinity of the {111}A plane there was an enhancement of Ga concentration whereas in the vicinity of the {111}B plane there was a decrease in Ga concentration in the planar (001) area adjacent to the sidewalls. They observed similar Ga concentration profiles for groove structures with a corresponding orientation near the intersections of the groove bottoms(001) and

{111}sidewalls. In contrast to this, on top of the ridge structure, the (001) plane showed a Ga depletion in the immediate vicinity of both the {111}A and {111}B planes, relative to the ridge centres. They also compared the Ga compositions obtained on the {111} planes of the ridge structure with those obtained on the planar substrates and showed that they followed the same trend: i.e.

$$x_{planar}^{(001)} = 0.47 > x_{planar}^{\{111\}A} = 0.37 > x_{planar}^{\{111\}B} = 0.16$$

Turco et al.(1990) investigated InGaAs/InP and InAlAs/InP layers grown on {211}A type of grooves using EDX analysis. They showed surface migration in both cases occurs from the sidewall towards the bottom of the groove. The migration from the (211) to the top (100) plane appeared to terminate at the interface, thus preserving a [100] straight line at the top. The EDX measurements indicated that there was a small 5% variation in In composition for the InGaAs case from the top to the bottom of the groove. However, for the InAlAs case the variation in In content was around 30% from the top to the bottom.

2.5 PHOTOELASTICITY

Photoelasticity is an optical method of stress analysis. Consider first a plane stress (two dimensional stress) system. There are two planes at right angles to each other on which the shear stresses are zero. On these two planes the normal stresses are either a maximum or minimum; thus the planes are referred to as principal planes and the stresses are known as principal stresses. The principal stresses and strains deform the body in such a way as to alter the isotropic character of the body with reference to light (Frocht, 1941). As a consequence of the different deformation, a ray of light entering a point in a stressed transparent body will travel faster along one principal plane than along the other.

The photoelasticity method is based on double refraction. Each element of a stressed isotropic body behaves as a doubly refracting crystal. Thus a beam of plane-polarized light incident normally upon a stressed plate resolves into two components. In two dimensions, the relationship between temporary double refraction and the stresses and strains causing it, is given by the stress-optic law.

In a transparent isotropic plate in which the stresses are two dimensional and lie within the elastic limit, the phase difference or relative retardation R_t in wavelength between the rectangular wave components traveling through it and produced by temporary double refraction is given by

$$R_t = Ct(p-q) \quad \text{.....(16)}$$

where C is a constant known as the stress-optic coefficient, t is the thickness of the plate, and p and q are the principal stresses.

For some semiconductors a similar technique based on photoelasticity is available for determining the stress distribution. This is known as the degree of polarization (DOP) method. In an unstressed crystal the electron energy (E) versus wavevector magnitude (k) are identical along the x, y, and z axes. A strain causes the heavy hole and light hole bands to deform, so that they are no longer identical along the three axes. Hence the stresses change the isotropic character of the body and since luminescence is dependent on stress, it leads to a polarization of the luminescence. Luminescence in a semiconducting material can be excited by passage of a current or by excitation with photons. The former is termed electroluminescence(EL) and the latter is termed photoluminescence(PL). Polarization of EL due to stresses in a body was first shown experimentally by Cassidy and Adams (1989). Based on the success of this

technique Colbourne (1992) extended it to polarization resolved PL. Colbourne and Cassidy (1989) studied the distribution of stresses near a dislocation using this technique.

3. EXPERIMENTAL TECHNIQUES

3.1 ETCHING V-GROOVES INTO INP

Two different types of V-grooves were formed by etching : (111)B and (211)A. These grooves were etched using a 5:1(by volume) mixture of reagent-grade hydrochloric acid (37%) and phosphoric acid (85%). The InP substrate used for etching was a (100) face of a single crystal (Fig. 3.1). The etchant attacks certain planes more slowly than others; these slow etching planes determine the profile of the groove. For our case we observed that if the masks were oriented in $[0\,\bar{1}\,\bar{1}]$ then the slowest etching plane was $(1\,1\,\bar{1})$B and when the mask direction was $[0\,\bar{1}\,1]$ the groove was bounded by (211)A planes. The terminology here follows from the polar nature of these materials described in Sec. 2.1.1. (111)A implies that the plane from the {111} family of planes is terminated by In atoms, while (111)B planes would be terminated by all P atoms (Fig. 3.2a). As described in Sec. 2.1.1, a (211)A plane has two In atoms with a single dangling bond and one P atom with a double dangling bond (Fig. 3.2b).

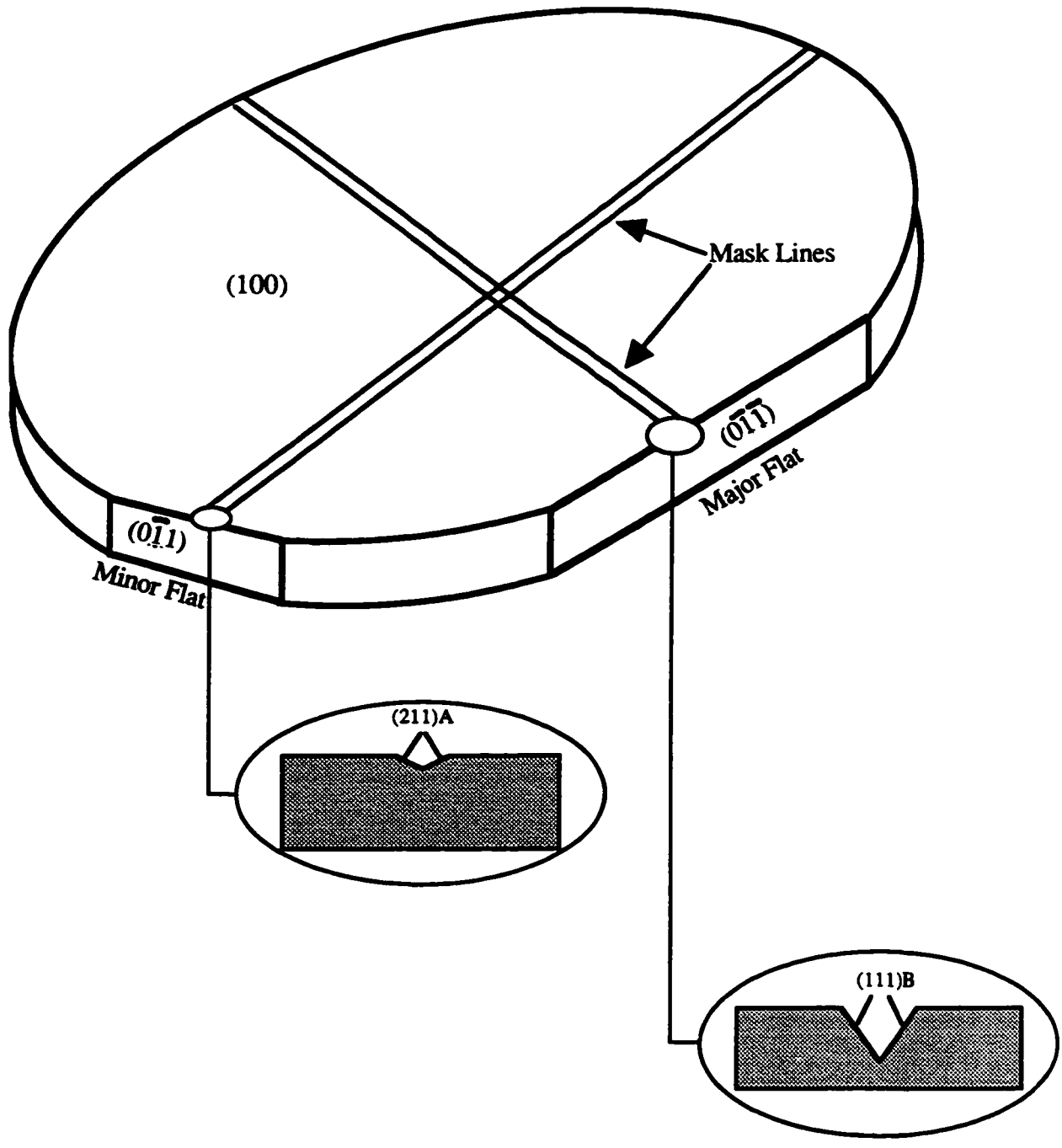

Fig. 3.1 Crystallographic orientation of the InP wafers based on SEMIOption 1 convention. The V-groove profiles corresponding to the mask lines in the [0 $\bar{1}$ 1] and [0 $\bar{1}$ $\bar{1}$] are also shown. These two directions were the ones used in all the experiments (after Bulitka, 1993).

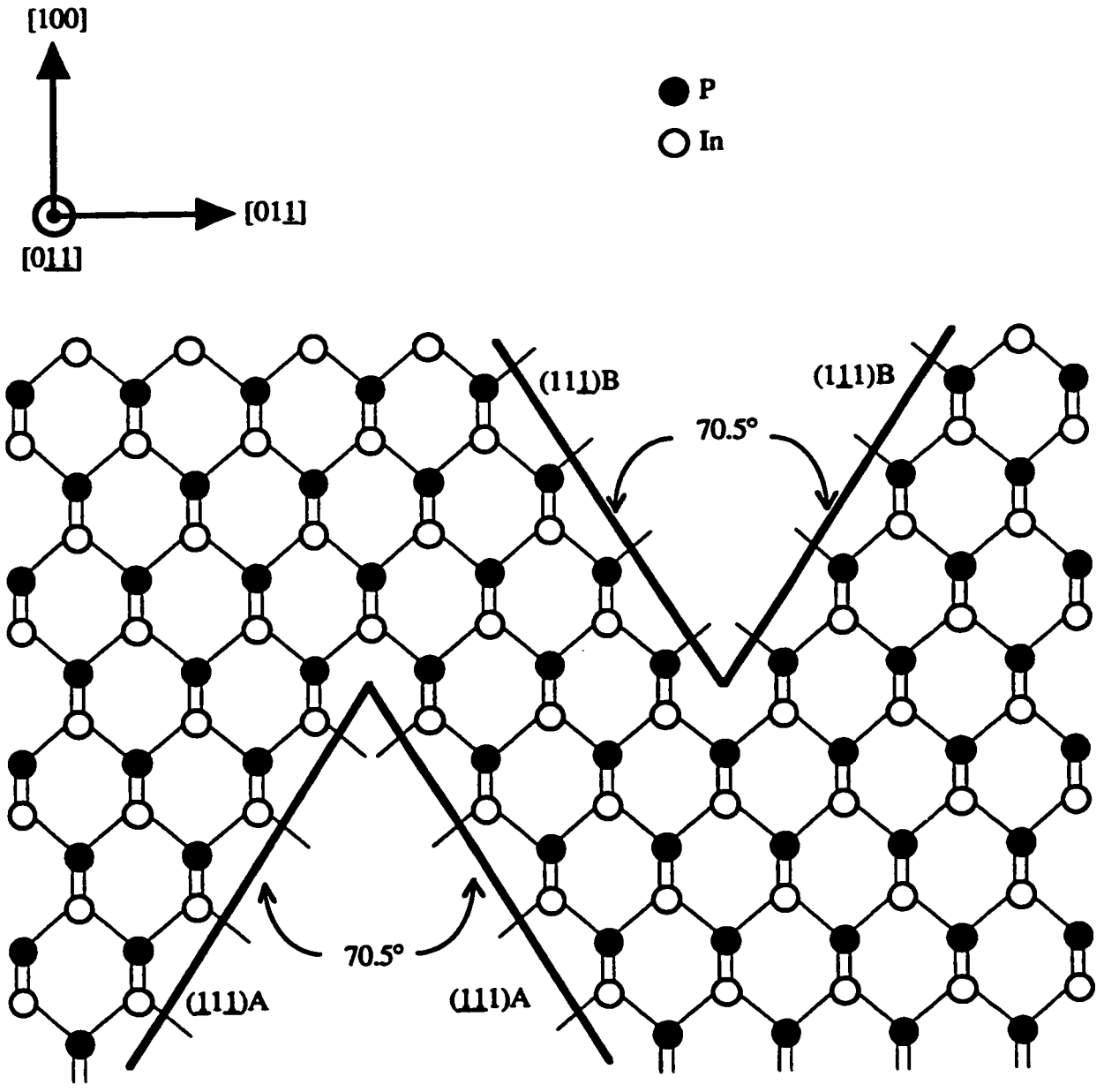

Fig. 3.2 Schematic diagram showing atom arrangement on polar {111} and {211} surfaces (a) (111)A and (111)B V-grooves etched into InP. Both planes are terminated by single dangling bonds. In case of (111)A it is terminated by In atoms and in case of (111)B it is terminated by P atoms.(angles are not to scale) (after Bulitka,1993).

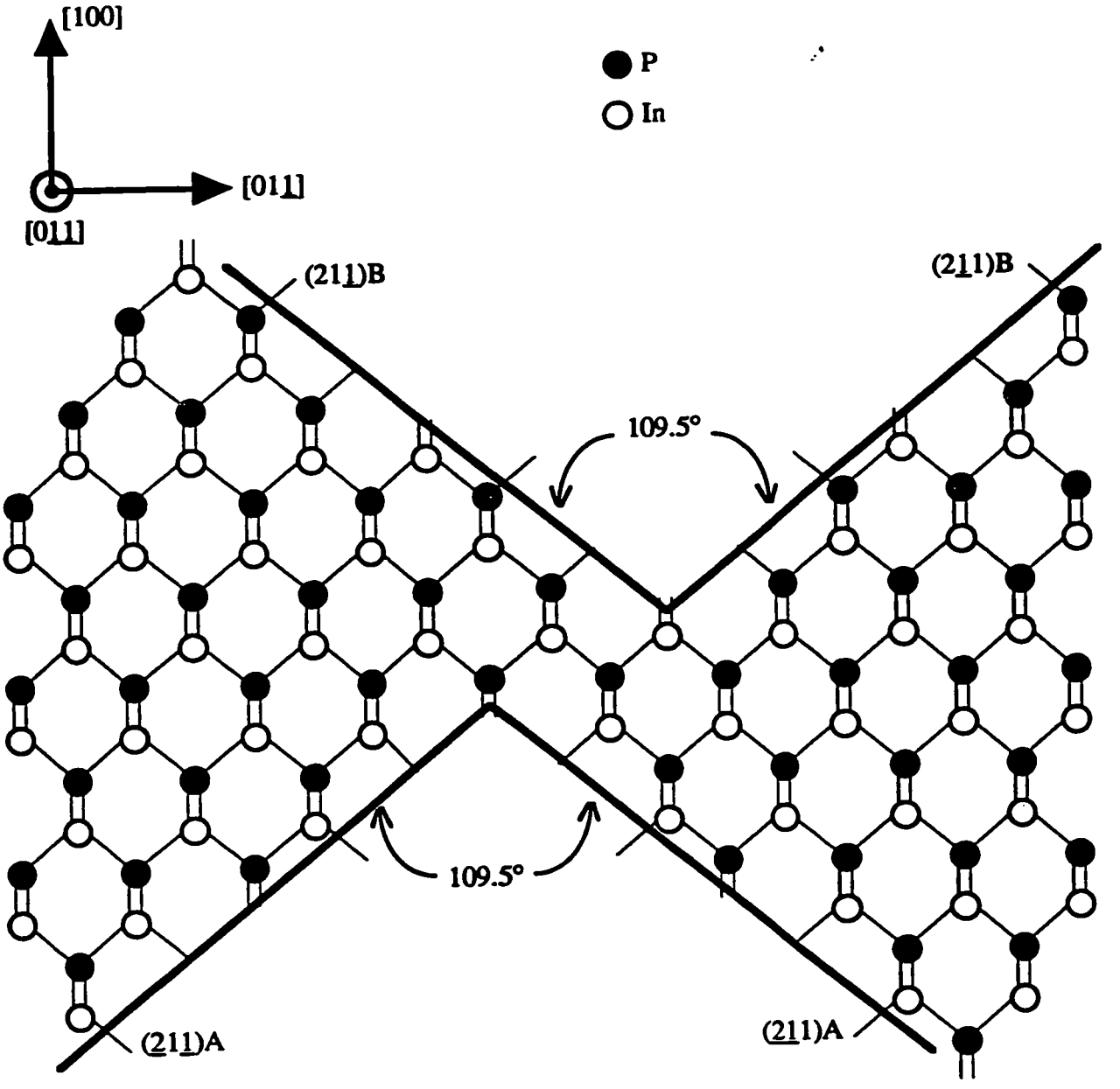

Fig. 3.2(b) (211)A and (211)B V-grooves etched into InP. In case of (211)A the In atoms have single dangling bonds and P atoms have double dangling bonds. The situation is reversed in case of (211)B planes. Angles are not drawn to scale (after Bulitka, 1993).

3.2 MOLECULAR BEAM EPITAXY (MBE)

All growths were done using the MBE set-up at McMaster University (Fig. 2.3). The system at McMaster is called a Gas Source MBE (GSMBE) because the group V atoms come from decomposition of gaseous hydrides (AsH_3 and PH_3). These are passed through a cracker cell containing a Rhenium catalyst heated to 1000°C to form the dimers As_2 and P_2. After impinging on the substrate these dimers dissociate and As and P are incorporated into the growing film. The group three atoms are generated from metallic Ga and In by evaporation. The effusion cells are heated to an appropriate temperature to generate the group III fluxes and the flow rate of fluxes are controlled by both the temperature and opening and closing of effusion cell shutters. Before loading the sample in the growth chamber it was degassed for 15min at 300°C. In the growth chamber the sample was heated to 470°C and subjected to a 2min electron cyclotron resonance(ECR) H_2 plasma to remove native oxides from the InP substrate (Bulitka, 1993). While at the growth temperature the sample was subjected to a P_2 overpressure to avoid decomposition of InP resulting from incongruent sublimation of In and P. At this stage the sample is ready for growth.

The growth rate was around 1μm/hr and the substrate temperature was ≈470°C for all growths unless otherwise stated. The sample was rotated at 10 rpm in some cases and 5rpm in the others, although the recommended speed is 60 rpm corresponding to approximately one revolution per monolayer. The speed was kept low because the rotating stage tended to bind (Bulitka,1993).

3.3 TEM SAMPLE PREPARATION

The following procedure was used for making cross-sectional TEM samples (Fig.3.3):

1. The sample (Fig. 3.3a) was cleaved into 2mm by 6mm slices along (011) planes. Similar slices were obtained from either InP, GaAs, or Si to serve as supporting material (Fig.3.3b).
2. The top faces(containing the layers) of the sample slices were joined using EPO-TEK H22S silver epoxy. Then slices from supporting material were added on to either side such that the two sample slices lay in the center of the sandwich (Fig. 3.3c).
3. This structure was held on a jig and heated to ~ 150°C to cure the epoxy.

This gave a 6mm by 10-12mm sample, about 2mm in thickness. The sample was then mechanically polished down to 200μm thickness and cut using an ultrasonic cutter, to give a 3mm disc (Fig. 3.3d). This disc was next dimpled to a thickness of 50μm at the center, and then put into the Gatan ion beam thinner for final polishing until perforated.

InP has been reported in the literature to give segregation of In (Chew and Cullis, 1987) on ion beam thinning, hence care has to be taken to minimize this and also to prevent amorphisation of surface layers. Liquid nitrogen was used to avoid sample heating. To reduce the intensity of the ion beam low beam angles ($< 10^{\circ}$) were used for most of the thinning process. Towards the end, the angle was increased to 15-20° to get a hole; then again a low angle was used for about 2-3hrs to get a sufficiently thin area around the hole.

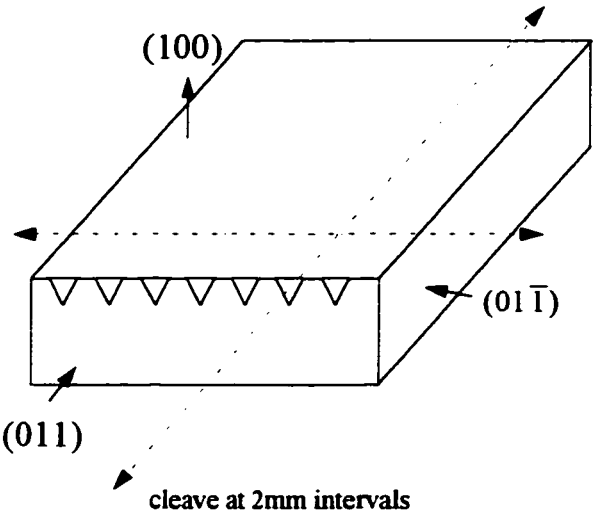

(a) Cleavage directions in the sample to obtain slices

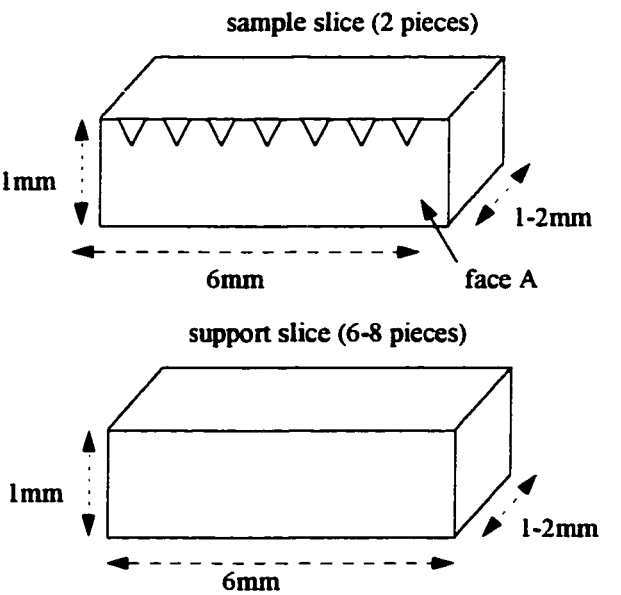

(b) Slices obtained after cleavage.

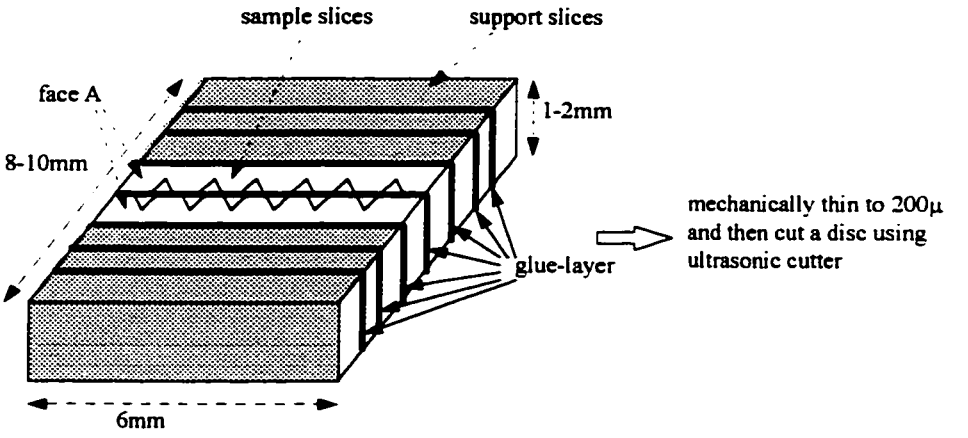

(c) After the slices have been glued together.

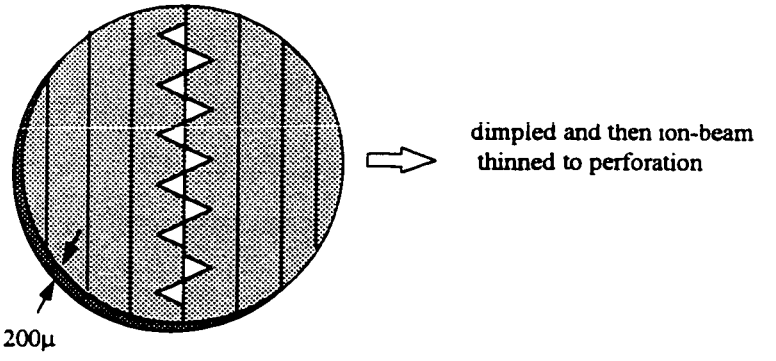

(d) ultrasonically cut 3mmX3mm disc

Fig. 3.3 Different stages in the preparation of TEM samples.

3.4 DEGREE OF POLARIZATION (DOP)

The DOP method is a non destructive technique which can be used for detecting dislocations and strain fields in III-V semiconductors. In this method, the measurements are based on stress induced changes in the degree of polarization of luminescence from III-V semiconductors. Fig. 3.4 shows the experimental set-up. A mechanically chopped HeNe laser is reflected off a cold mirror and focused on to the diode facet using a microscope objective. The luminescence from the facet is collected with the same objective in a confocal arrangement, and passes through the cold mirror to a polarizing beamsplitter cube. A filter removes any remaining HeNe light. The two polarizations are detected using two 200μm diameter Si n-p-n photodiodes (L_x, L_y) after an optical path length of 1.3m. Phase sensitive detectors (PSD's) are used to reject ambient light signals and reduce noise.

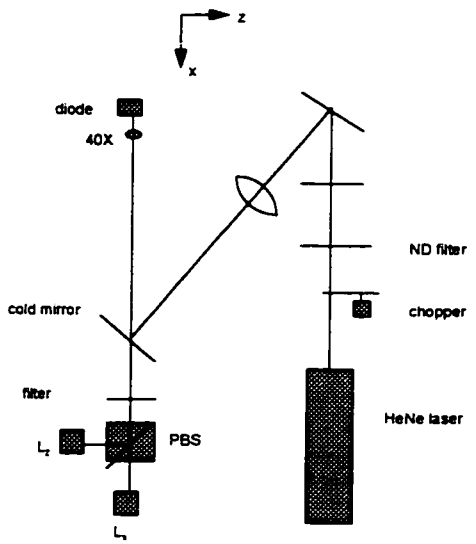

Fig. 3.4 DOP set-up used in this work (after Colbourne, 1991).

The DOP, ρ, is related to the luminescences in the x and y direction and can be expressed as,

$\rho = \frac{L_x - L_y}{L_x + L_y}$, where L_x and L_y are related to the stresses in the x and y direction. Thus, $\rho = K_\sigma(\sigma_{xx} - \sigma_{yy})$ where σ_{xx} and σ_{yy} are the stresses in the x and y direction respectively, and K_σ is the polarization constant.

The scanning of the diode is done under computer control. At each scan point values of L_x, L_y, and ρ are recorded. Scanning is done unidirectionally to eliminate hysteresis effects. The system allows positioning repeatability within about 0.1μm, while the smallest step size used was 0.5μm. Each data point requires about 2seconds. A 40X microscope objective gives a spatial resolution of about 0.9μm. A stress resolution of ±1.0MPa was obtained for GaAs and ±0.3MPa for InP based on the standard deviation of readings of ρ scans of nominally unstressed material. The better resolution for InP is due to its greater luminescence intensity, resulting in a greater signal to noise ratio. Repeatability of stress measurements between scans, with removal and replacement of the sample is about ±3.0MPa.

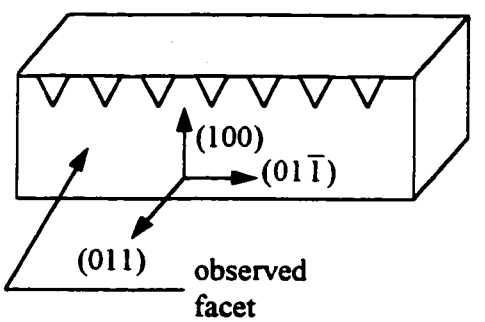

Fig. 3.5 Sample orientation with respect to the HeNe laser.

Fig. 3.5 shows the orientation of the V-grooved sample with respect to the HeNe laser. Here L_y corresponds to the growth direction <100> and L_x corresponds to the <011> direction perpendicular to the growth direction. The value of the constant K_σ was

determined by 3 point bending measurements (Colbourne, 1991). For InP a large anisotropy (2 times) was noticed in the [110] and [$\bar{1}$ 10] direction, hence an average value based on isotropic assumption was derived. Thus,

$K_\sigma = -(9.4\pm1.0) \times 10^{-11} cm^2/dyn.$

3.5 TRANSMISSION ELECTRON MICROSCOPY

The purpose of doing TEM was to assess the quality of growth and to study the stress-relaxation effects. A Phillips CM12 transmission electron microscope, operating at 120KV with a LaB6 electron source, was used for this purpose. The microscope was equipped with a double tilt stage, thus making it possible to achieve the required two beam conditions. As explained in the sample preparation section above, all samples were cross-sectional and hence were oriented in the <011> direction.

Structure factor contrast was best under (200) two beam conditions. Under this condition the interfaces are sharpest and the contrast between the layers and the substrate highest. A $\vec{g}$= (200) diffracting condition shows stress relaxation contrast at the interfaces for layers grown on a planar substrate.

3.6 SCANNING TRANSMISSION ELECTRON MICROSCOPE

STEM was used for doing composition analysis of layers grown on both (111)B and (211)A type of grooves. EDX analysis was done on a high resolution JEOL2010F. This is a 200kV scanning transmission electron microscope with a field emission gun. The minimum spot size which can be achieved under ideal conditions is around 0.5nm. The microscope with Link Si detector and super atmospheric thin window (ATW) for EDX analysis was capable of detecting low atomic weight (< carbon) elements.

In order to get optimum results from this technique, one has to be careful in setting the parameters which affect the analysis. The first concern is the sample alignment: it should not be too close to a channeling condition which causes strong absorption of the electron beam by the atoms. Once the sample orientation has been fixed, one has to consider whether the X-rays coming from the sample are properly detected. In the JEOL 2010F there are two options: optimum acquisition and best resolution. "Optimum acquisition" is a fast counting mode while the "best resolution" is used for light element detection. In our sample there are no light elements and hence we used the optimum acquisition mode.

The spectra were collected with an energy range of 0-20keV. Within this range, for InGaAs and InP, the peaks of interest were the Phosphorus Kα peak (2.015keV), the Gallium Kα peak (9.251keV), the Arsenic Kα peak(10.543keV), and the Indium Lα peak (3.287keV). After collecting the first spectrum it had to be calibrated with respect to the detection system. For this purpose any X-ray peak (energy greater than 5keV) can be chosen as the reference position. The As-Kα line was used in this study. The spectrum was collected for about 200 secs to get around 40,000 counts for gain calibration.

The following settings were used for collecting the EDX data:

560(211)A: Acquisition live time: 50 secs

Tilt: 8.5°, elevation angle: 25°, azimuth angle: 0°, entry angle:0°

570(111)B: Acquisition live time: 50secs

Tilt: 2.2° and 0.1°, elevation angle: 45°, azimuth angle: 0°, entry angle: 0°

Standard ($In_{0.54}Ga_{0.46}As$ layer grown on planar (100) InP): Acquisition ion angle: 45°, azimuth angle: 0°, entry angle: 0°

The angles are defined as follows:

Elevation angle: angle between the horizontal plane(i.e. the plane perpendicular to the electron beam) and a line drawn between the X-ray detector and the point where the incident beam meets the sample (it is equal to the take off angle when the sample is not tilted).

Azimuthal angle: angle between the direction of the sample tilt and a line drawn between the X-ray detector and the point where the incident beam meets the sample, viewed along the electron beam.

Entrance angle: angle between the X-ray detector axis and the X-rays entering the detector.

The ISIS software was used to do composition analysis from the data generated under the above conditions. Before doing quantitative analysis the peaks were identified and the gross integral of the peak was calculated by summing the counts in each channel in the window. Peaks could be identified either manually or automatically. The net integrals were calculated automatically during peak identification by summing the number of counts above a straight line drawn between the top of the first and last channel of the window i.e., they were calculated by linear interpolation. Once the net integrals were obtained, the value of parameters such as the density of the sample, the thickness of the sample, and the k-factors must be provided. To do quantitative analysis, these parameters can be either input manually or the computer uses the values from its database. The automatic values from the computer database were used in this work.

density: 4.787 g/cm^3

thickness: 1000Å

As Kα peak: k factor = 1.834 (k factors are defined with respect to Si)

Ga Kα peak: k factor = 1.609

In Lα peak: k factor = 1.822

P Kα peak: k factor = 1.0

For each area, analysis was done at more than ten points to determine the statistical accuracy of the data.

If the absorption effects are neglected then the thickness only affects composition due to beam broadening effect. As described in Chap.5, the geometry of the growth makes it possible to calculate the amount of signal picked up from the adjacent layers due to beam broadening. Any variation in thickness would only alter the amount of beam broadening and since it is possible to subtract these effects, thickness variations were not critical in calculating the composition. Also, it should be emphasized that in this thesis composition analysis was conducted to measure the variation in composition in layers grown on V-grooves and not to measure the absolute value of composition. Hence the exact knowledge of the sample thickness and k-factors is not necessary.

4. CHARACTERIZATION OF GROWTHS

4.1 GROWTHS ON (211)A V-GROOVES

(211)A grooves were obtained by etching (100) InP substrates in a $[01\bar{1}]$ direction. They were 2-3 microns in width and about 2 microns in depth. The angle made by the (211) sides at the apex was 109°. This angle is too wide for carrier confinement and hence any growths on these grooves are probably not useful from a device point of view. However, to get a basic understanding of the growth process, both heteroepitaxial and homoepitaxial growths on (211)A grooves as well as the growth behavior on (211)A planar substrates, were studied. The results from these investigations will be discussed by comparing the three growths.

4.1.1 Homoepitaxial Growth on (211)A V-Grooves

InP was grown on patterned InP substrates to assess the quality of the interface and the growth morphology, independent of composition. A 12000Å thick layer was grown at ~470°C. Also homoepitaxial layers of thickness 3000Å were grown at two different temperatures, 450°C and 490°C, to investigate the effect of temperature on the growth process.

For a temperature of 470°C it was observed that at a thickness of 12000Å the V-groove was mostly covered by (311)A and (111)A facets (Fig. 4.1). These facets started to form at some critical thickness and continue to grow. At a thickness of 12000Å the groove had almost "filled-up". The flattening of grooves probably leads to a thermodynamically low energy state which is achieved by the faceting of (n11) side planes, with n gradually increasing until a flat (100) configuration is reached. Scanning electron

microscopy of etched grooves showed that the initial (211)A faces have a rough surface. It is possible that this roughness is due to the fact that (211)A plane is made up of primary (100) and (111) planes (this should be true for any (n11) type plane).

Comparing growths in Figs. 4.2 and 4.3, where InP layers of the same thickness were grown at different temperatures, the facets which develop at the bottom of Fig. 4.2 have vanished at the higher temperature (490°C). Furthermore in all the homoepitaxial growths no defects were observed and the original surface could not be seen, suggesting that the layers were free of impurities or defects that can be detected by TEM techniques

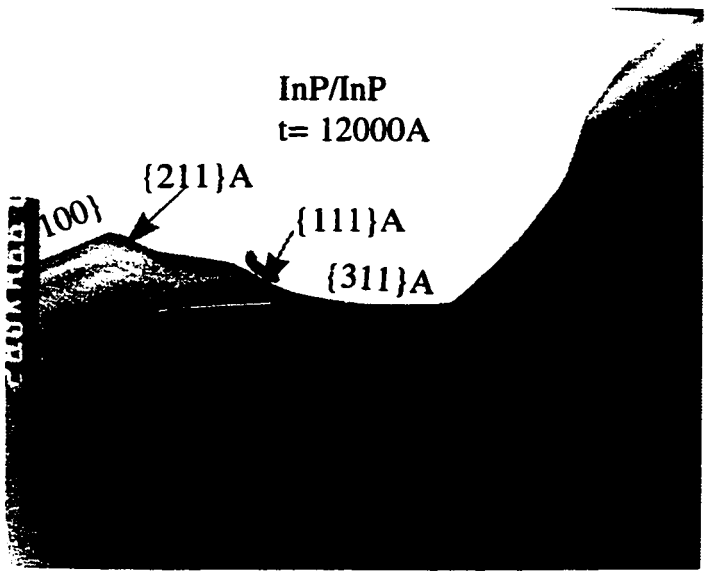

Fig. 4.1BF TEM image showing homoepitaxial growth on (211)A InP V-groove. Layer thickness= 12000Å, Temperature of growth= 470°C.

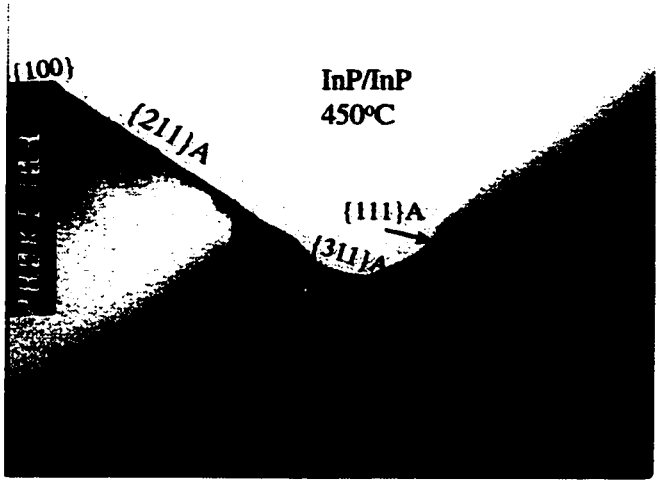

Fig. 4.2 BF TEM image showing homoepitaxial growth on (211)A InP V-groove. Layer thickness= 3000Å, Temperature of growth= 450°C.

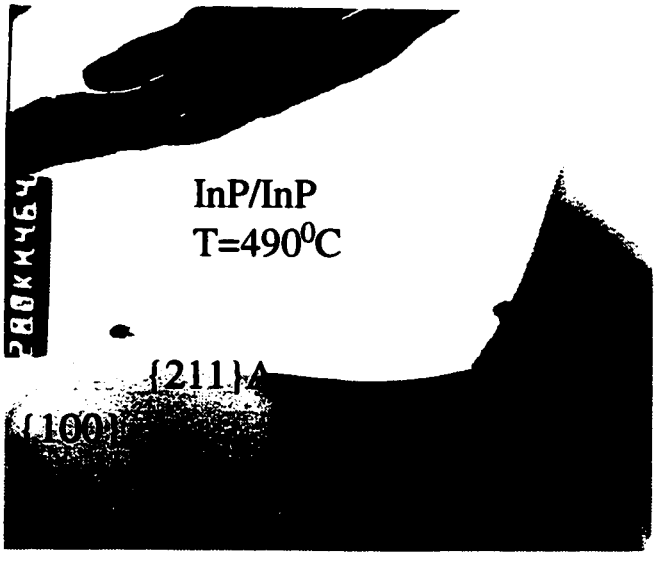

Fig. 4.3 BF TEM image showing homoepitaxial growth on (211)A InP V-groove. Layer thickness= 3000Å, Temperature of growth= 490°C.

4.1.2 Heteroepitaxial growths on (211)A V-grooves

The following growths were characterized for the (211)A case:

Sample 488A- Composition: 52.55%In*

Lattice parameter mismatch: +0.048%

Eight layers of InGaAs and InP each having a thickness of 300Å.

Sample 489A- Composition: 54.75%In*

Lattice parameter mismatch: -0.103%

Eight layers of InGaAs and InP each having a thickness of 300Å.

Sample 560A- Composition: 53.2%In*

Lattice matched

Eight layers of InGaAs and InP each having a thickness of 300Å.

Sample 577A- Composition: 53.2%In*

100Å InP buffer layer

75Å InGaAs lattice matched layer

1000Å InP capping layer

The first three experiments compare samples having the same geometry, but the layers are lattice-matched (Fig. 4.4), in compression (Fig. 4.5), and in tension (Fig. 4.6). In all three cases faceting was observed; since faceting was also found with homoepitaxial growth, this phenomenon appears to be independent of composition or strain. In Fig. 4.6, the etched groove in sample 488(211)A was smaller in size compared to 560(211)A (Fig. 4.4) and 489(211)A (Fig. 4.5). Hence after the growth, sample 488(211)A is mostly covered by (311)A and (111)A facets and (211)A has almost disappeared.

---

* These are all based on the compositions expected for deposition on planar (100) surfaces, and does not account for possible facet to facet variability.

Fig. 4.4 BF TEM image of sample 560(211)A (lattice matched layers).

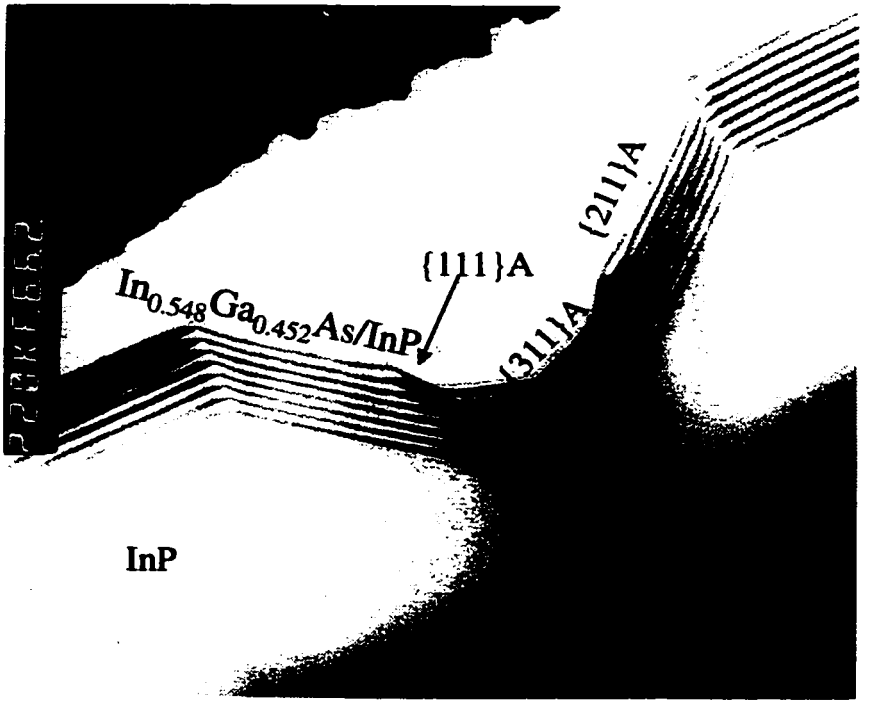

Fig. 4.5 BF TEM image of sample 489(211)A (layers in 0.103% compression).

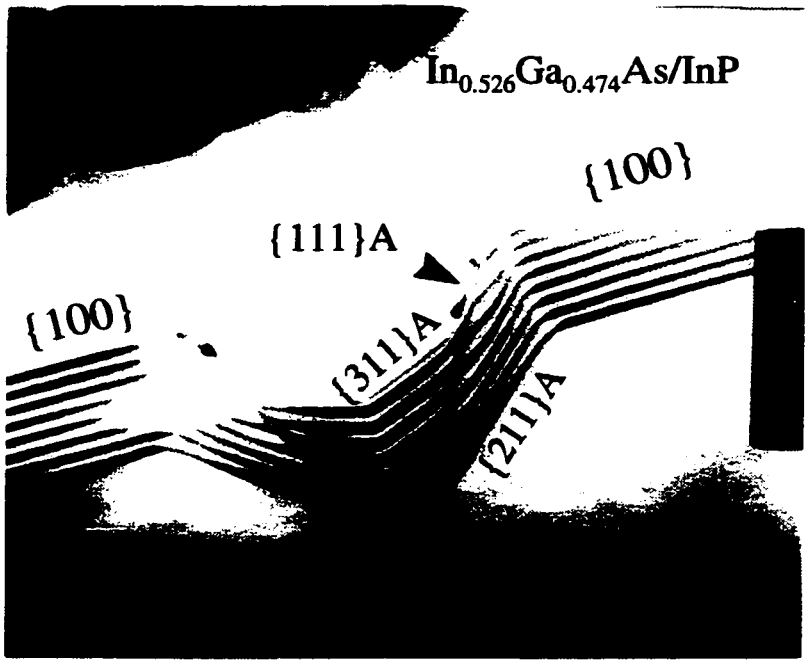

Fig. 4.6 BF TEM image of sample 488(211)A (layers in 0.048% tension).

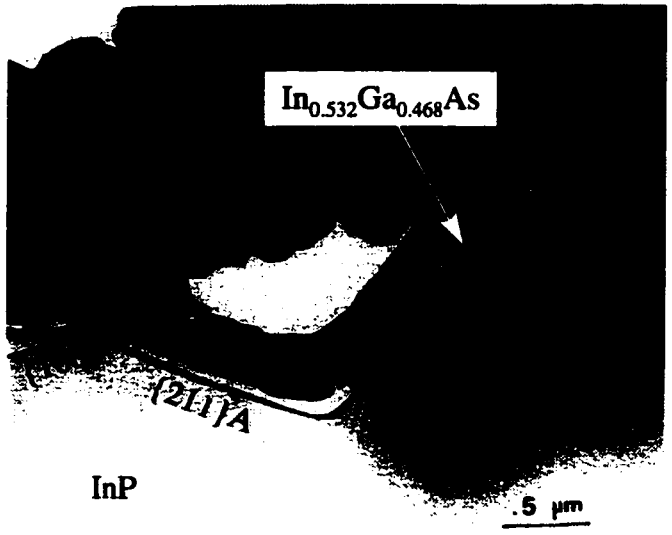

Fig. 4.7 BF TEM image of sample 577(211)A (lattice matched layers).

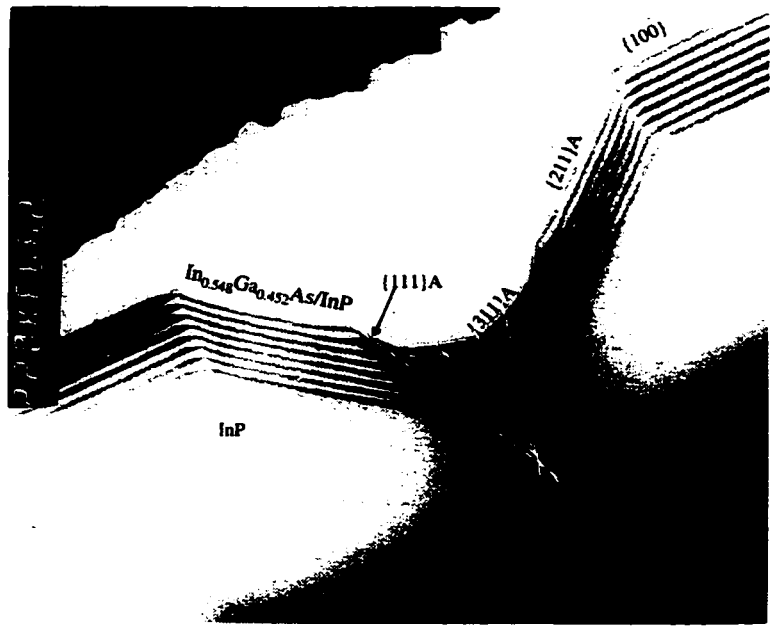

Fig. 4.8 Lines drawn through the midpoints of (311)A and (111)A facets in sample 489(211)A to show that they originate at one point.

The fourth sample had a 75Å InGaAs film deposited on a buffer layer (Fig. 4.7). No faceting was observed in this layer but after the growth of 1000Å of InP cap layer the sides have started to facet. This suggests that there is a critical thickness before facets start to develop. If a line is drawn through the midpoints of the different facets, in sample 489 (211)A, they all originate from a point; that is the facets form as a result of differences in the growth rates on different planes (Fig. 4.8).

No defects were observed in any of the growths that were studied. The thickness of the layers on the (311)A plane was about 1.5 times that on the (211)A plane. This thickness variation may be accounted for by the difference in orientation with respect to the incident flux. The absence of defects shows that the critical thickness for defect generation has not been reached for either the tensile or compressively strained layers.

These observations further suggest that we should not expect to find much composition variation along the sides of the groove.

Another feature of interest was evidence for a composition modulation shown by strain contrast effects in the TEM. Composition modulations have been reported in the literature for growth on planar substrates of ternary and quaternary layers (Mahajan et al., 1984; Chu et al., 1985). This is generally attributed to a surface decomposition phenomenon (Mahajan et al., 1984; Norman and Booker, 1985). For a particular range of composition and temperature, where the composition of the alloy lies within a miscibility gap, the layers may show modulations as a result of composition variations.

Composition modulations in layers grown on (100) show a coarse as well as a fine structure (Norman and Booker, 1985). Different explanations as to the source of the two types of modulations exist (Mahajan et al., 1984; Treacy et al., 1985; Glas et al., 1982). In Norman and Booker's (1985) study coarse contrast had a periodicity of 150nm whereas the fine contrast had a periodicity of 15nm. In the present set of experiments they were visible in each InGaAs layer but with a different periodicity (Fig. 4.9, Fig. 4.10). In all cases only fine modulations with a periodicity < 5nm were observed. The periodicity seems to be affected by small changes in the plane on which the growth occurs. One possible explanation of these observations might be the slightly different incorporation rates of the In and Ga atoms on these planes. One other interesting feature was the presence of strain relaxation contrast at the bottom of the grooves in the strained layers. This will be discussed in more detail in chapter 6.

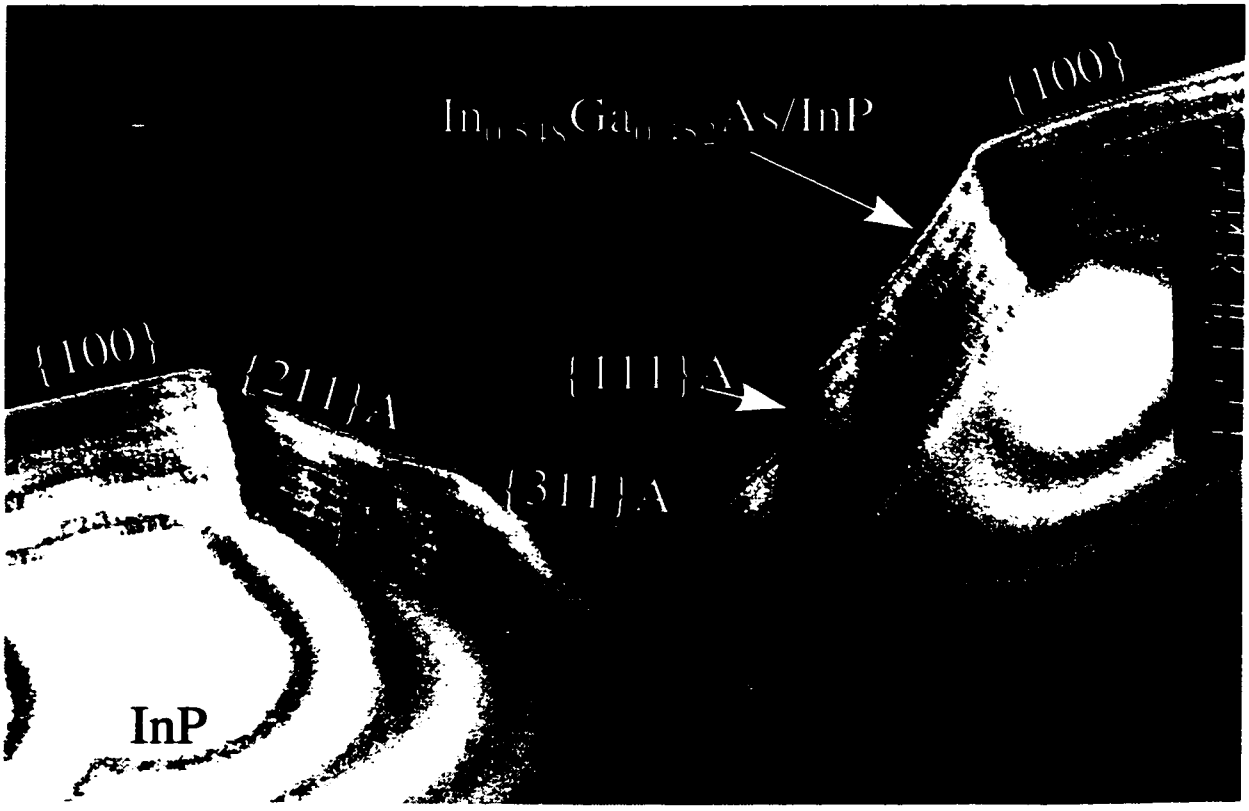

Fig. 4.9 BF TEM image showing composition modulations on different facets of sample 489(211)A.

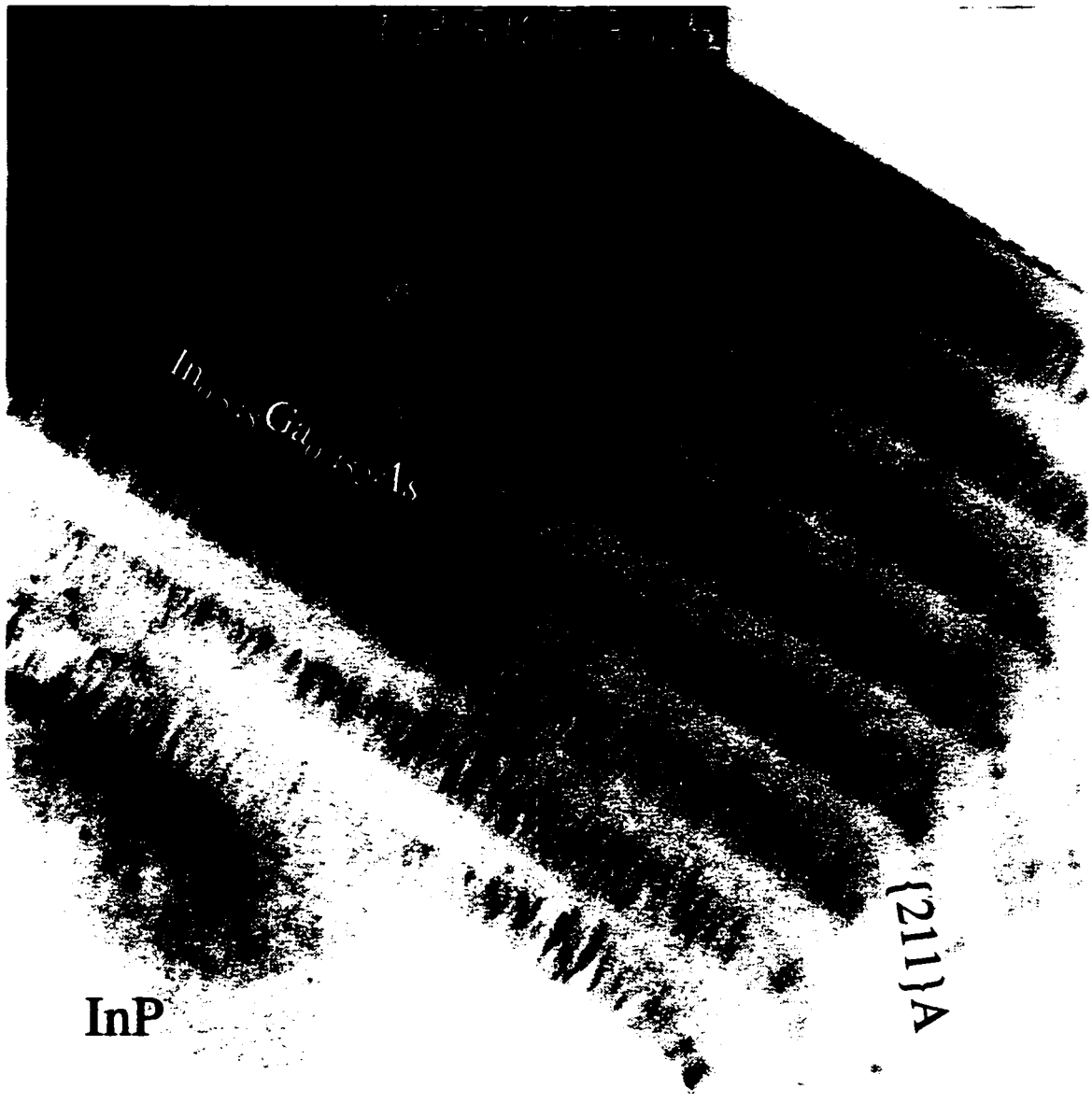

Fig. 4.10 BF TEM image showing composition modulations on the top (100) surface of sample 489(211)A.

4.1.3 Homoepitaxial Growth on Planar (211)A Substrates

The growth of InP on planar (211)A InP substrates did not show any features of interest. The growths were free of defects and there was no faceting. If we compare the planar growth with the V-groove growth behavior, one thing becomes quite clear- the faceting found with V-grooves must be related to the convexity of the V-shaped groove, and is not inherent to growth on (211) planar surfaces.

4.2 GROWTHS ON (111)B V-GROOVES

Most literature that is available describes heteroepitaxial growth on (111) grooves, but the understanding of the complex growth process on these surfaces is still limited. Growing homoepitaxial layers reduces one variable, that is the composition of the film. Homoepitaxial growth has been investigated to get a better understanding of the growth process. To explain the growth on V-grooves we have also studied homoepitaxial growth on planar {111}A and {111}B type InP substrates. At the end of the chapter, some important conclusions are drawn, based on a comparison of homoepitaxial and heteroepitaxial growth on V-grooves with the growth on planar substrates.

(111)B grooves etched on (100) InP substrate were about 6.0-7.5μm wide and subtended an angle of 70.5°. Both homoepitaxial and heteroepitaxial layers were deposited on these grooves. The surface quality of the grooves was checked first, using scanning electron microscope (SEM), before proceeding with the growths (Bulitka, 1993).

4.2.1 Homoepitaxial Growth on (111)B V-grooves

InP layers were grown on V-grooved InP substrates. Two different thicknesses, 12000Å and 30000Å, were grown at the same temperature (470°C) to see if the morphology of the film changed with thickness. To study the effect of temperature on growth, a 3000Å InP layer was grown at 450°C, 465°C and 490°C. All five growths were free of defects. This result is in accordance with the literature on AlGaAs/ GaAs growth on (111)A grooves ; as noted earlier these layers have negligible mismatch and were also free of defects irrespective of the growth technique, the growth temperature or the thickness of the layers.

Comparing the growth of layers with thicknesses 12000Å (Fig. 4.11) and 30000Å (Fig. 4.12), it is clear that as the growth proceeds the groove is slowly "filled in". From this trend it can be deduced that with continued growth the groove will planarize. At the bottom of the groove the thickness of the layer was about three times that at the top. The growth rate at the sides was much less than that at the top (100) planes and the apex of the groove. This shows that the sticking coefficient of In on the (111) planes is very small. In addition there might be some diffusion from the (111) plane to the bottom and the top (100) planes as shown by Hata et al.(1990) in their study of GaAs grown on <110> GaAs mesa structures. In the range of temperatures studied, the growth temperature did not seem to have any effect on the quality of the film or the morphology of growth. This can be seen in Figs. 4.13, 4.14, and 4.15 where a 3000Å thick layer was grown at three different temperatures, 450°C, 465°C, and 490° respectively.

Fig. 4.11 BF TEM image of homoepitaxial growth on (111)B InP V-groove. Thickness of layer= 12000Å, Temperature of growth= 470°C.

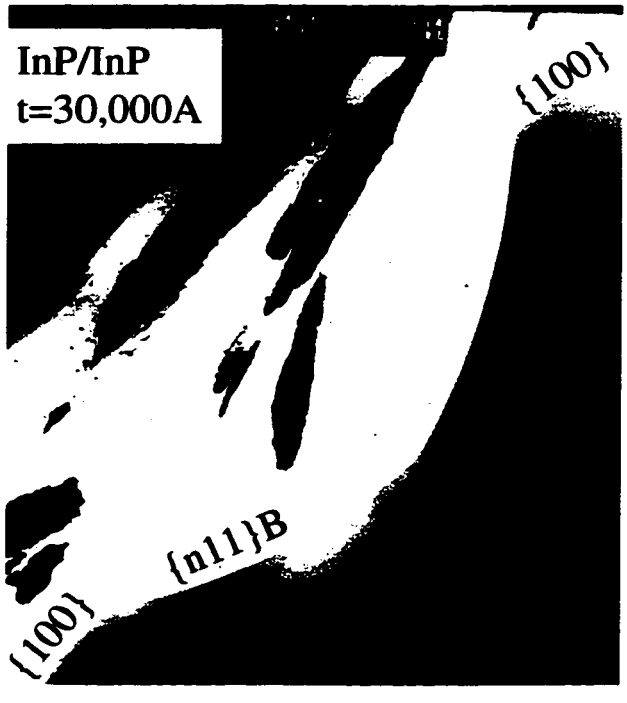

Fig. 4.12 BF TEM image of homoepitaxial growth on (111)B InP V-groove. Thickness of layer= 30000Å, Temperature of growth= 470°C.

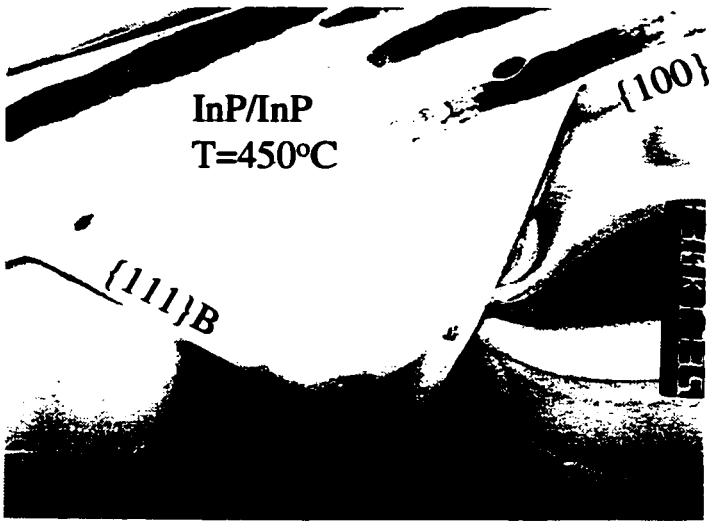

Fig. 4.13 BF TEM image of homoepitaxial growth on (111)B InP V-groove. Thickness of layer= 3000Å, Temperature of growth= 450°C.

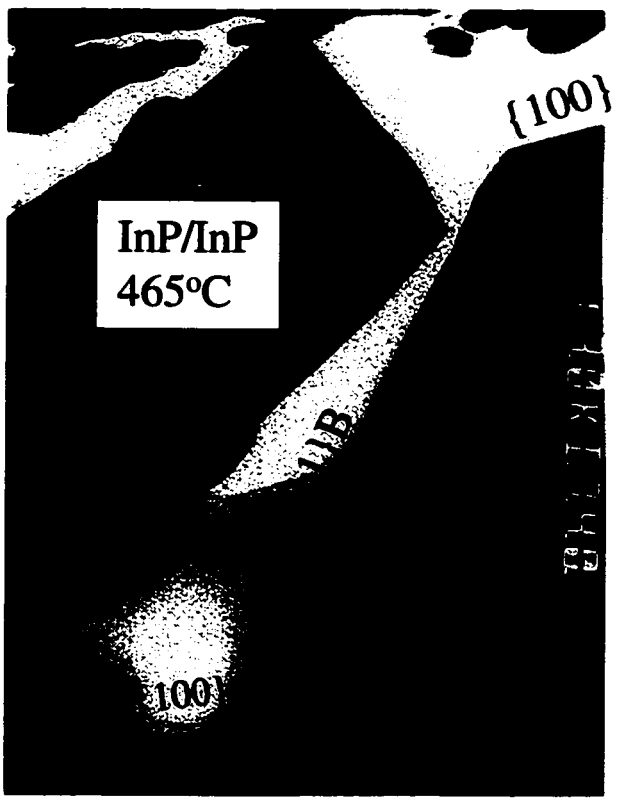

Fig. 4.14 BF TEM image of homoepitaxial growth on (111)B InP V-groove. Thickness of layer= 3000Å, Temperature of growth= 465°C.

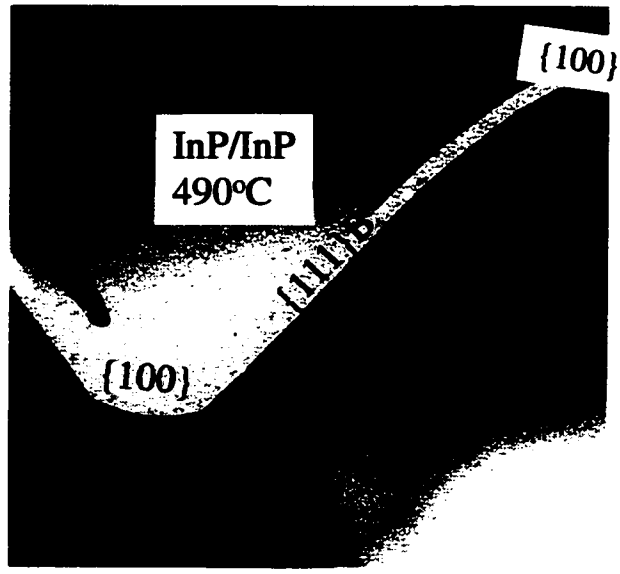

Fig. 4.15 BF TEM image of homoepitaxial growth on (111)B InP V-groove. Thickness of layer= 3000Å, Temperature of growth= 490°C.

4.2.2 Heteroepitaxial Growths on (111)B V-Grooves

The following growths were studied in the (111)B case:

Sample 555B- Composition: 50.45%In*
Lattice parameter mismatch: +0.194%
Eight layers of InGaAs and InP each having a thickness of 300Å

Sample 570B- Composition: 55.02%In*
Lattice parameter mismatch: -0.122%
Eight layers of InGaAs and InP each having a thickness of 300Å.

Sample 560B- Composition: 53.2%In*
Lattice matched composition
Eight layers of InGaAs and InP each having a thickness of 300Å.

Sample 645B- Composition: 53.2%In*
500Å InGaAs lattice matched layer
3000Å InP cap layer

---

* These are all based on the compositions expected for deposition on planar (100) surfaces, and does not account for possible facet to facet variability.

In contrast to the homoepitaxial growths, all the heteroepitaxial growths studied were full of defects such as twins, stacking faults, and dislocations. Since the size of the (111)B groove was 6-7μm, it was not possible to get a single sample thin enough throughout the groove for analysis. So different regions of the groove were examined from different parts of the TEM sample. A schematic diagram showing a composite picture of the growth is shown in Fig. 4.16. The defects were concentrated at the apex of the groove, region C, and at certain locations of the side layer, region E. Other portions of the sides of the groove were defect-free.

Fig. 4.17 shows the side (region E) of the groove where the defects were concentrated. Irrespective of the composition or the thickness of the layers these defects were observed in all the growths studied. Figs. 4.18, 4.19, 4.20, and 4.21 show the bottom region (C) in four different samples.

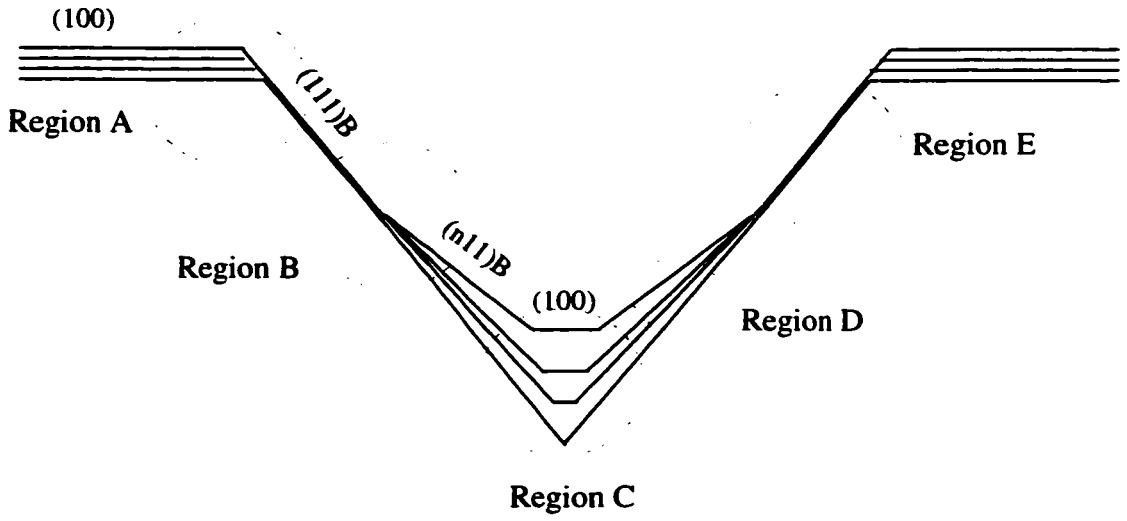

Fig. 4.16 Schematic diagram showing the growth morphology in a typical (111)B V-groove.

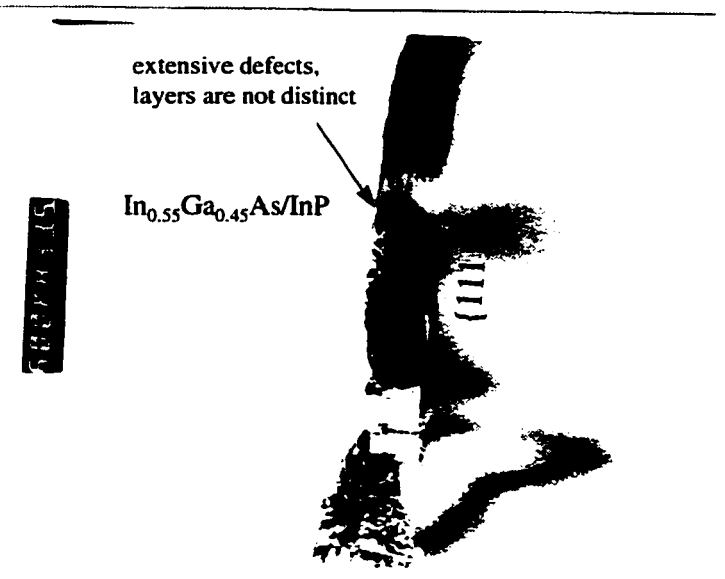

Fig. 4.17 BF TEM image showing the side (region E) of sample 570(111)B where the defects were concentrated.

Fig. 4.18 BF TEM image of sample 555(111)B showing region C (0.194% tension).

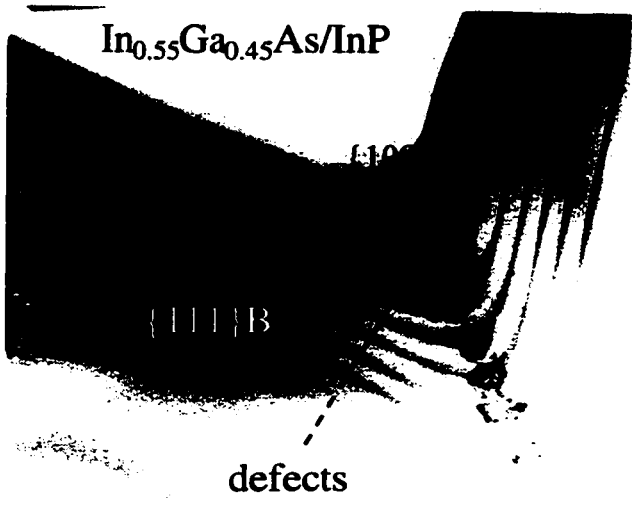

Fig. 4.19 BF TEM image of sample 570(111)B showing region C (0.122% compression).

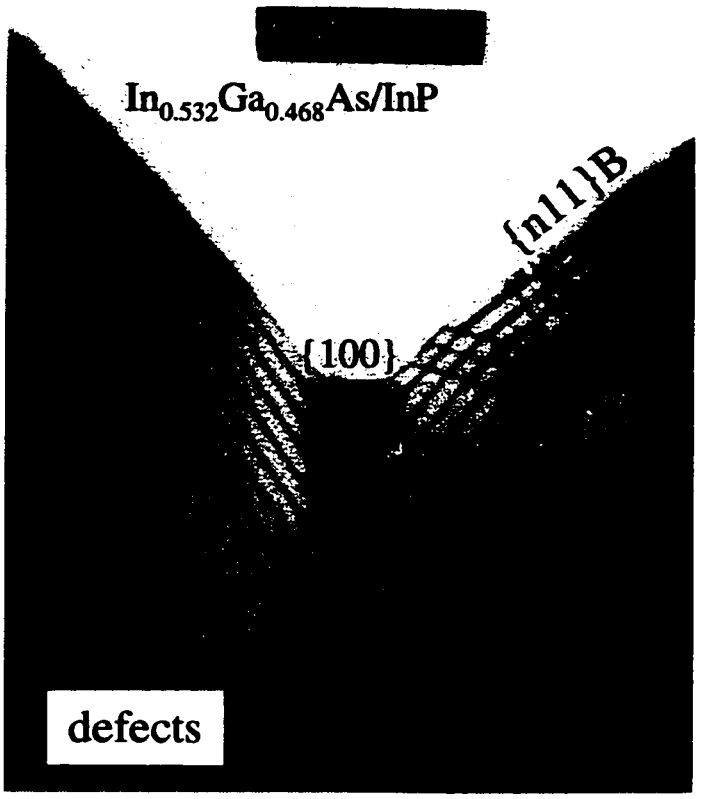

Fig. 4.20 BF TEM image of sample 560(111)B showing region C (layers are nominally lattice matched).

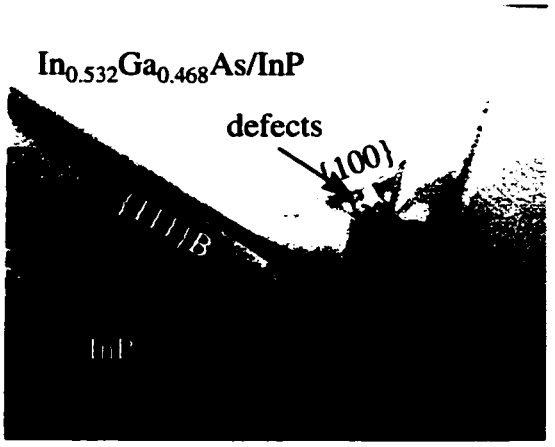

Fig. 4.21 BF TEM image of sample 645(111)B showing region C (nominally lattice matched layer).

Overall the growth morphology was identical to the behavior of the AlGaAs/GaAs system and the homoepitaxial growths i.e. the groove "filled up" as the growth proceeded. One of the more interesting features was the threefold increase observed in the thickness of the film at the bottom of the groove (region C). In addition to the sharpness of the groove this feature is very important for quantum wire applications. As mentioned earlier, an increase in thickness can lead to confinement of electrons in the lateral direction.

On the area of the side plane next to the top surface (region E) the individual layers could not be distinguished and were full of defects. Just below this region (D) the layers were again visible and their separation slowly increased. These changes imply that the growth plane gradually evolves and eventually the groove is "filled up". The thickness of the layers was reduced by about one third on average compared to the (100) surface. At the bottom of the groove a (100) type plane also developed and its width gradually increased with each successive layer. This behavior shows the complexity of the growth process in (111) heteroepitaxial experiments.

As in (211) heteroepitaxial growths a composition modulation was observed in layers grown on (111)B grooves (Fig. 4.22). Close to the apex of the groove (Fig. 4.22), the periodicity of these modulations was large enough to show distinct black and white strain field regions. To my knowledge this has not been observed before. Another feature of interest was that in the case of an eight period layered structure the periodicity of the modulations increased in successive InGaAs layers. This change in wavelength may come about because the plane on which the layers were growing is slowly changing orientation as growth proceeds. Since the wavelengths of composition modulations are probably determined by surface diffusion of Ga, a change in plane perhaps implies a change in the average diffusion length before incorporation as successive InGaAs layers are deposited.

The modulations observed on the top (100) plane had the same periodicity as in growths on planar (100) substrates (~ 5nm).

Fig. 4.22 BF TEM image of sample 570(111)B showing composition modulations on (111)B plane near the root of the groove (region C).

4.2.3 Homoepitaxial Growth on Planar (111)B and (111)A Substrates

Growth of InP layers on (111)A and (111)B planar substrates showed an extensive defect network (Figs. 4.23, 4.24). These defects consisted of twins, stacking faults, and dislocations. There appeared to be no difference between (111)A and (111)B in terms of the density of defects. The top surface of the layers was not flat but faceted, i.e. the growth proceeds by the nucleation and coalescence of 3D islands. The image obtained by Nomarski interference technique showed a 3D island type of growth (Fig. 4.25). These islands could be distinctly seen at the edges of the wafer. Sangster (1962) had predicted this type of growth mode from his model based on the atomic structure of the surfaces. The study of Rajkumar et al.(1991) showed similar defects on growths done on (111) A and (111)B type of surfaces. As noted in the literature review, the single dangling bond at the (111) surface leads to problems in nucleation and to the formation of defects. In the literature, there have been number of reports of the difference in growth behavior between (111)A and (111)B surfaces (Thrush et al., 1993; Hersee et al., 1986; Dilger et al., 1994; Lee et al., 1993). Lee et al. (1993) reported this difference in the case of InP growths. The growths in the present experiment did not show any marked differences in growth rate between the two surfaces. Galeuchet et al. (1988) also reported that the growth behavior of InGaAs/InP system on both (111)A and (111)B is similar. The reason for the different results of these studies is not understood at present.

In general the growth of defect free films on {111} surfaces has been a problem. Vina and Wang (1986) suggested that by growing layers on offcut (111)A planes one can minimize the defects and also obtain films with better optical properties. The steps

generated at the surface would lead to growth by step propagation rather than by 3D island nucleation (VW growth mode), thus reducing the defects.

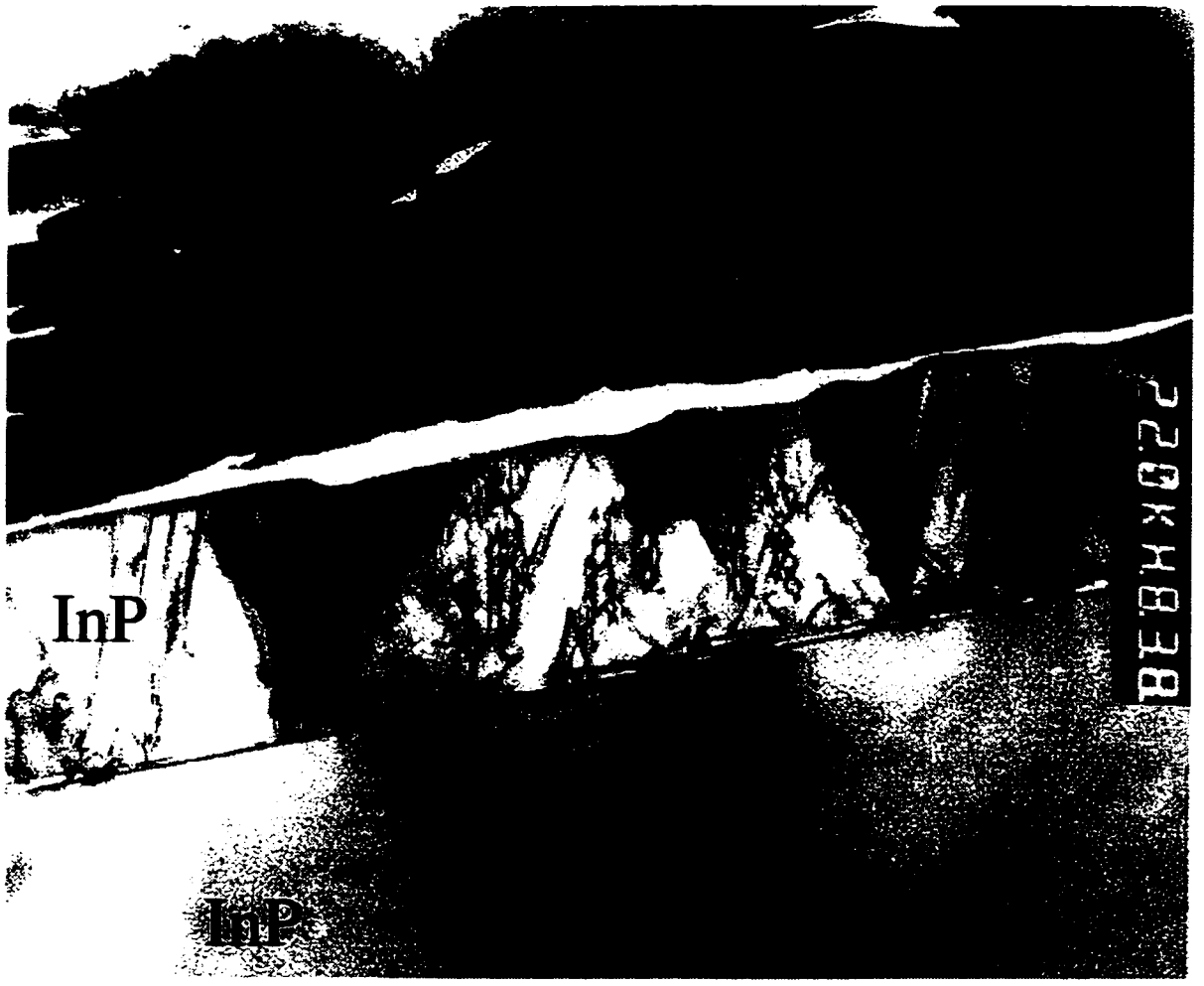

Fig. 4.23 BF TEM image of homoepitaxial growth of InP on (111)A planar substrate.

Fig. 4.24 BF TEM image of homoepitaxial growth of InP on (111)B planar substrate.

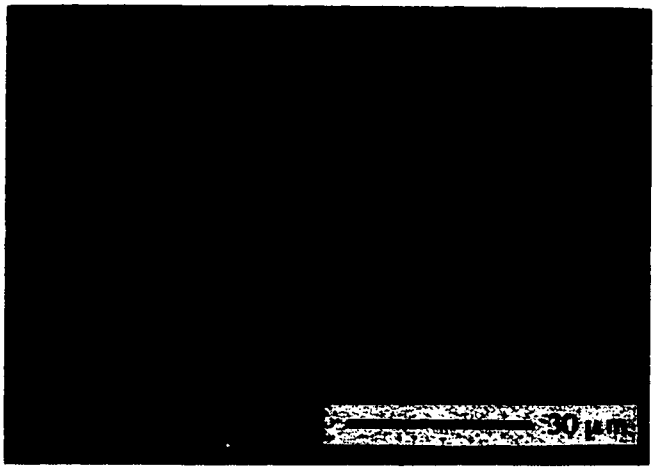

Fig. 4.25 Nomarski interference micrograph showing island type growth on (111)B planar substrate.(area of the sample corresponds to the edge of the wafer). Plane of the micrograph corresponds to (100) surface (after Lapierre, 1994). Arrow points to a triangular island.

4.3 COMPARISON OF GROWTH ON (211)A GROOVES AND (111)B GROOVES.

(211)A and (111)B grooves consist of surfaces which have very different atomic configurations. This difference in atomic arrangement leads to differences in growth characteristics. The major differences observed in the growth behavior on these two systems were:

1. All growths on (211)A were defect free whereas heteroepitaxial growths on (111)B were full of defects.
2. In the case of growth on (211)A grooves, there was little change in thickness of the layers on the different facets. There was about a threefold increase in thickness from the top to the bottom of the groove in the case of (111)B grooves. Such a large increase cannot be explained by orientation differences only. A more complex interplay between factors such as the sticking coefficient and the mean diffusion lengths on different facets must be considered.
3. Whereas faceting was observed with (211)A grooves and planes such as (311)A and (111)A appeared, as the thickness of the layer increased, there was no marked faceting for growth on (111)B grooves. On a macroscopic scale the groove appeared curved and gradually "filled up" as the growth proceeded. This implies that there was a continuous evolution of facets of the type (n11) with n increasing until the groove planarizes and attains a (100) orientation.
4. There was a significant difference in the wavelength of the composition modulations obtained in (211)A grooves and those obtained in (111)B grooves. In the case of (211)A grooves modulations were observed on all the planes. The periodicity of these modulations was close to that observed on (100) planes, i.e. ~5nm. A major change

took place in the (111)B growths. The wavelength increased to about 10nm and regions of varying composition could be distinctly observed.

4.4 DISCUSSION

{111} type grooves are ideal for quantum confinement of charge carriers because of the sharp groove angle (70.5°). In most studies (111)A V-grooves were used for growing quantum wires because of the better growth properties of (111)A compared to (111)B. All growths with the AlGaAs/GaAs system were reported to be defect free (see section 2.2.3). However, as discussed in section 2.2.4, success has been limited to date, with systems such as InGaAs/InP and InAlAs/InP, that involved lattice mismatch. The behavior of these systems (as discussed in section 2.2.4 of this thesis) illustrated the complexity associated with growths on V-grooves. A number of factors need to be understood before any progress in the design of lasers with an optimum performance can be made using V-groove systems.

In this study we have attempted to improve the understanding of the growth process by growing a series of homoepitaxial layers. In the case of homoepitaxy, the growths were defect-free for all the temperatures and thicknesses studied, for both (111)B and (211)A growths. However, for heteroepitaxial growth, the situation changed drastically. InGaAs growth on (111)B resulted in defects, for all compositions investigated, whereas similar growths on (211)A grooves were defect-free. The important differences in the two systems have been noted in a previous section. In this section we compare our results with those available in the literature. Four growth characteristics will be discussed: faceting, thickness variations, planarization, and defect formation. These characteristics will be compared between growths on (211)A grooves and (111)B grooves.

4.4.1 Faceting

Faceting is a common occurrence in growths on V-grooves but the nature of faceting is dependent on many factors. Foremost among them is the orientation of the sides of the groove. Most growths on (111)A V-grooves reported in the literature show a similar growth morphology, i.e. a development of (100) plane at the bottom of the groove while the sides develop an (n11) type orientation which is continuously changing. On the other hand grooves with (211) type orientation show development of well defined facets.

The few studies done on (211)A type of grooves using either InGaAs/InP or InGaAsP/InP have reported similar results to ours (Bhat et al., 1990, 1991). Bhat et al.(1990) reported faceting on (211) grooves, with the formation of (111)A and (311)A facets. We have observed similar faceting in this study for both homoepitaxial and heteroepitaxial growth. There was no faceting found for homoepitaxial growth on (211)A and (311)A planar substrates. Thus the faceting that develops in (211)A grooves seems to be a result of competition in growth rates between adjacent facets.

Based on their study of metal organic vapor phase epitaxy (MOVPE) of AlGaAs/GaAs on patterned substrates, Hersee et al. (1986) explained the faceting behavior of layers grown on patterned substrates. According to these authors, due to the finite but limited surface mobility of the arriving atoms, when several crystal facets exist within the range of the average diffusion length of atoms (before they are adsorbed or desorbed), the facets which lead to minimization of Gibbs energy will exhibit higher growth rates. However, for crystal facets separated by a distance larger than the average diffusion length, the arriving atoms are not able to travel far enough to minimize the free energy of the system and the growth rate is apparently independent of the substrate orientation. Jones et al. (1993) also arrived at the same explanation on comparing their

theoretical results with experiment. They did not take into account interfacet migration and hence predicted morphologies slightly different from the observed ones.

Jones et al.'s (1993) model of faceting is based on differences in growth rates of different planes. If a line is drawn through the midpoint of each facet formed on (211)A, they all meet at the same point (Fig. 4.8). This shows that the facets evolve due to a difference in growth rates. However, one point that remains unanswered is the appearance of (311)A planes. Before growth the facets were composed of (211)A planes, but as the growth proceeded (311)A facets appeared after some thickness (Fig. 4.26). For concave substrates Jones et al.'s model can predict the appearance of such facets based on a polar construction (Fig. 4.27). Measurements of thickness of the layers in sample 560(211)A showed that the thickness of the layers on the (311)A facet varies from 290±20Å near the edge close to (211)A planes to 417±20Å at the bottom corner. On the (211)A planes the thickness of the layers is 208±20Å, whereas on the (100) planes it is 290±20Å. Thus the development of the (311) facet is related to the inherent differences in growth rates on (211)A and (311)A surfaces. However the formation of a slow growing (111)A facet is unexpected, because slow growing facets are only expected to form at convex corners, not at concave junctions. Both (311) and (211) planes consist of (100) terraces and (111) risers according to Sangster (1962).

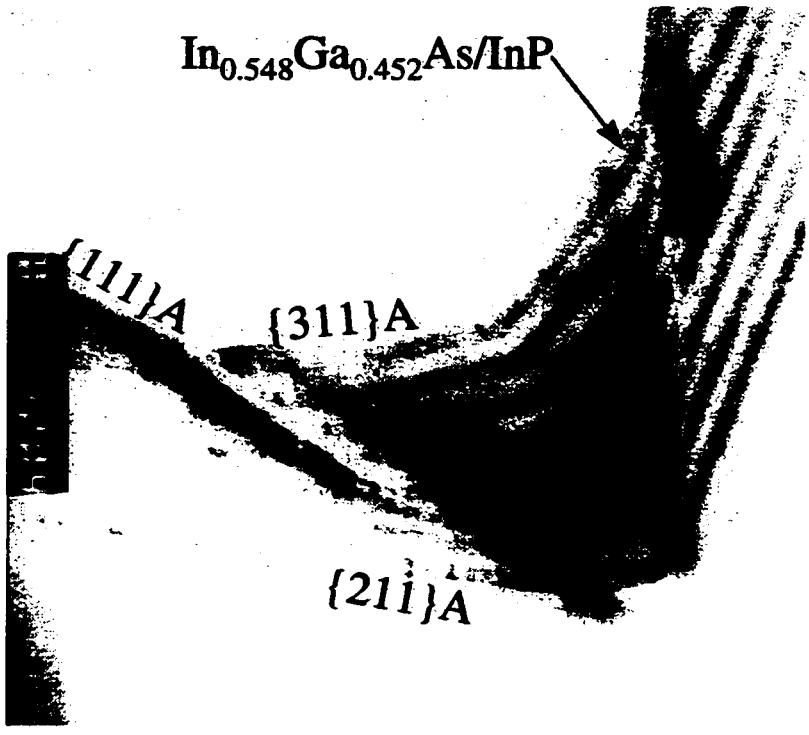

Fig. 4.26 BF TEM image of sample 489(211)A showing (311) facet evolution at the bottom of the groove.

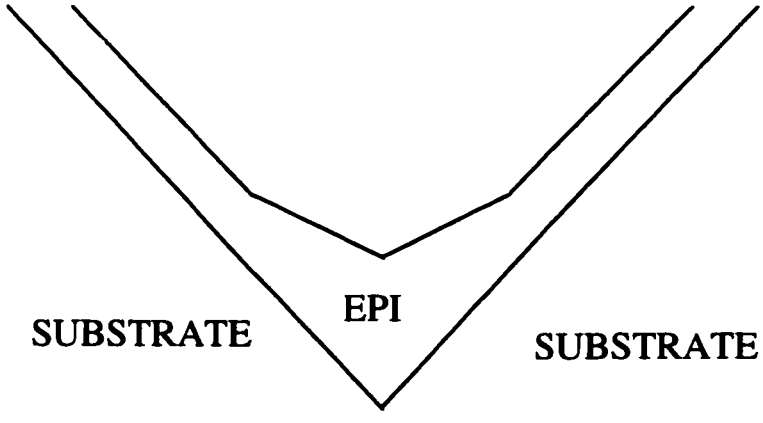

Fig. 4.27 Facet evolution at concave corners (after Jones et al., 1991).

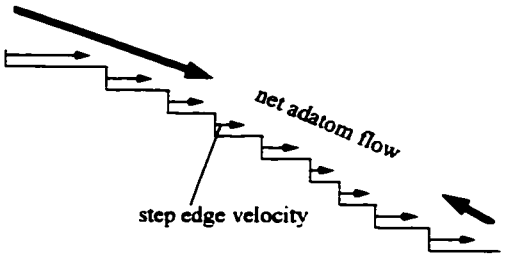

Fig. 4.28 Mechanism of step bunching (after Chalmers et al., 1993).

The difference in the growth rates on (211)A and (311)A may cause the (111) steps to bunch together forming a (111)A facet (Fig. 4.28). Step bunching occurs when adatoms that move predominantly down step edges cause the step edges on the left (see Fig. 4.28) to move faster than those on the right (Chalmers et al., 1993).

A new facet was also observed in the growth on (111)B grooves. In this case, at the bottom of the groove, a (100) plane appears and continues to expand with successive layers. These new facets always form at points on the surface where different facet planes meet. Possibly the same mechanism leads to the development of a (311)A/(411)A facet at the junction of (100) and (211)A planes near the top of the V-groove in the (211)A sample (Fig. 4.29). In the heteroepitaxial case, an interesting point to note, was that the (311)A facet only occurs at the corner of (100) and (211)A planes when InGaAs is grown, while the InP layer tries to restore the shape of the original sharp corner (Fig. 4.29). This does not happen at the bottom of the groove where InGaAs and InP exhibit similar growth rates (Fig. 4.26). The difference at the (100), (211)A junction arises due to the difference in growth rates of InGaAs and InP on (311)A and (100) InP. Measurements of the relative growth rates are also indicated in Fig. 4.29. It appears that the InGaAs growth rate on (311)A is much smaller compared to the (100) plane. Hence at a convex corner the slower growing plane expands at the expense of the faster growing plane, i.e. the (311)A

increases in size when InGaAs is deposited (Fig. 4.30). This trend reverses when the InP layer is deposited, as the growth rate on (311)A is now larger than that on (100). At a convex corner the faster growing plane gradually disappears. Hence InP effectively restores the original sharp corner geometry.

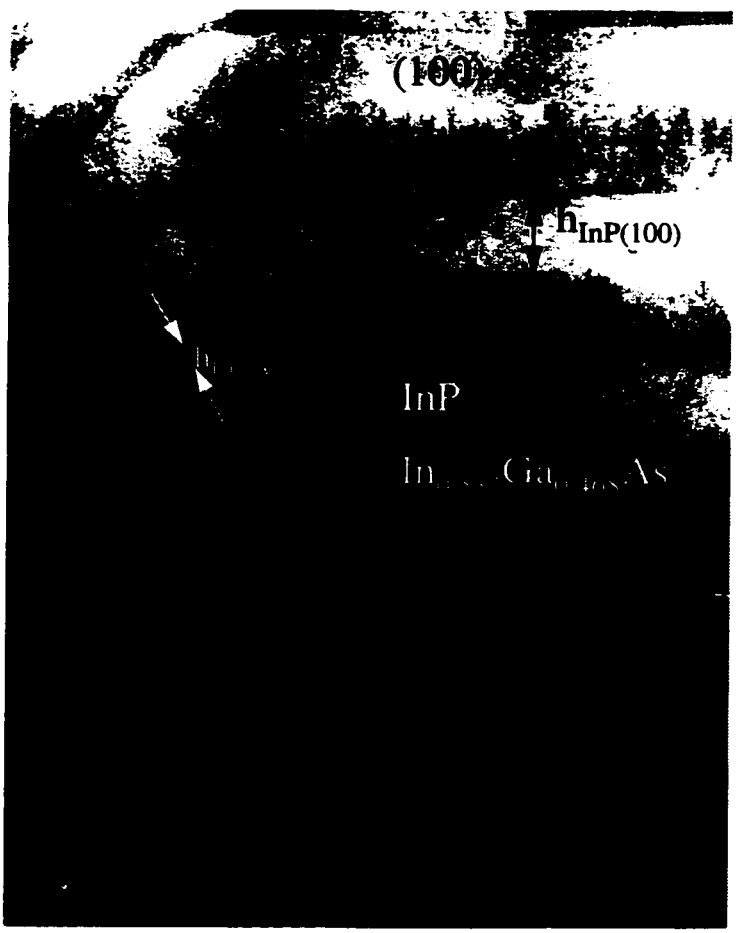

$h_{InP(100)}$: $h_{InP(311)}$= $v_{InP(100)}$: $v_{InP(311)}$= 0.592;
$h_{InGaAs(100)}$: $h_{InGaAs(311)}$= $v_{InGaAs(100)}$: $v_{InGaAs(311)}$= 3.0.
where h is the thickness of the layer and v is the growth rate.

Fig. 4.29 Measurements of the growth rate on the (311) facet near the top of the V-groove in sample 560(211)A.

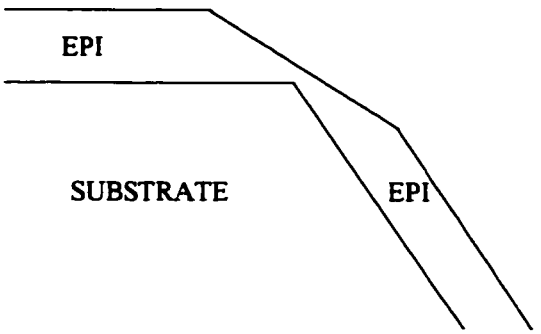

Fig. 4.30 Facet evolution at a convex corner (after Jones et al., 1991).

The difference in behavior observed at the bottom of the facet versus the convex surface, where (211)A and (100) meet, can be explained by the model proposed by Hersee et al. (1986), i.e. facet evolution can be influenced by the competition of growth rates between adjoining facets. This model is also supported by Tsang and Cho's (1977) and Shen et al.'s (1994) experimental observations. They studied AlGaAs/GaAs grown on (111)A type GaAs V-grooves. This growth also showed the development of (411)A facets at the junction of (111)A and (001) surfaces.

4.4.2 Thickness variation

The difference in growth rates on the facets constituting the groove leads to a thickness variation. In the case of (211)A grooves the thickness of both the InGaAs and InP layers on the (311)A plane at the root of the groove was about 1.5 times the thickness close to the edge of (211)A and on the (100) plane. Bhat et al.(1990, 1991) observed a similar increase in thickness in the central region of the V-groove compared to the edge. However Turco et al. (1990) found a decrease in thickness of layers on (311)A planes which evolved in growth done on (211)A grooves, and the V-groove developed a convex shape at the bottom of the groove. They explained the decrease on the basis of the difference in orientation of the planes with respect to the incident flux. A difference in

orientation will affect the growth rate to some extent but inherent differences in the growth behavior of different planes and interfacet migration of atoms plays a much larger role in determining the thicknesses. This becomes more evident in the case of (111)B grooves where the increase in thickness is threefold at the bottom of the groove with respect to the top surface. This increase cannot be explained by differences in orientation of the planes with respect to the fluxes. The difference between the experiment of Turco et al. (1990) and the present experiments might originate due to the InAlAs layers used in their study and the higher MBE growth temperature of 540°C.

Thickness variation may be aided by interfacet migration of the adatoms before incorporation. Support for the importance of facet dimensions, in the present set of experiments, comes from thickness measurements taken at the (100) surface close to the (211)/(100) corner (Fig. 4.31). For all the InGaAs layers the thickness is a maximum near the corner and decreases away from this location until the nominal value for growth on a flat (100) facet is reached. This probably is a result of group III atoms diffusing away from the (311) facet (lower growth rate) towards (100) (higher growth rate). The trend reverses in the case of the InP layer. Here the InP layer is thinnest near the corner and increases away from the corner till it reaches the flat (100) facet value.

On the other hand, at the bottom of the groove, the layer thickness for both InP and InGaAs on (311)A planes is the same. At this location, since there are no adjoining favorable planes (e.g. (100)), the atoms cannot diffuse away from or towards (311)A to accommodate the intrinsic differences in growth rates of different compositions.

Hartmann et al. (1994) and Chu (1993) attributed the difference in the growth rates of the layer and the substrate to the lattice mismatch strain, which they thought must be the driving force for the increased growth rate of SiGe and InGaAs at the corner. This explanation cannot explain the results of this study because lattice matched, compressive

and tensile layers all exhibited similar faceting and growth behavior. Thus the differences in growth rate are independent of lattice mismatch. In the case of samples grown on (111)B grooves, differences in the growth rates of InGaAs and InP at the bottom corner, similar to the results of Hartmann et al. (1994) and Chu (1993) were observed.

$h_{InP(1)}$: $h_{InP(2)}$: $h_{InP(3)}$= 0.9 : 1.0 : 1.15;

$h_{InGaAs(1)}$: $h_{InGaAs(2)}$: $h_{InGaAs(3)}$= 1.15 : 1.25 : 1.4.

Fig. 4.31 Micrograph showing a gradual variation in thickness of InGaAs and InP layers on the top (100) plane in sample 560(211)A.

It is likely that these differences in growth rates are a characteristic of the elements constituting the layer and their interaction with the atomic structure of the surface on which they are grown. Also, as this study has demonstrated, the development of facets

(i.e. the culmination of particular growth rates) is a strong function of the nature of adjoining facets and their size. Further support for this conjecture comes from the experiments of Shen et al. (1994). Their results suggest that facet development is mainly controlled by diffusion and incorporation of atoms on different planes. They studied $Al_{0.45}Ga_{0.55}As$, GaAs, and AlAs layers grown on (111)A V- grooved GaAs. The marked differences in morphology of the three growths led them to the conclusion that the difference in incorporation rates of Al and Ga on (111)A contributed to the observed changes.

The difference in incorporation rates of atoms on different surfaces and the consequent changes in diffusion behavior might be a possible explanation for the observed morphologies. An understanding of this can help in developing novel devices. As outlined in Chap.2, Pan et al. (1996) showed how the temperature changed the diffusion length, which in turn changed the facet development.

4.4.3 Planarization

In this study films grown on (111)B did not develop well defined facets but the groove slowly "filled-up". There was a gradual change in orientation of the sideplanes near the bottom of the groove and with the growth of each successive layer, the flat (100) plane at the bottom of the groove increased its width. On this plane the thickness increase was three times the thickness at the top (100) plane and hence gave the shape needed for quantum wires. However the size of successive "quantum wires" was not the same. This has been observed by other groups (Simhony et al., 1991) as well.

One similarity found in both systems was that the growth progresses such as to "fill-in" the grooves. In the case of (211)A this was achieved by forming well defined facets while in the case of (111)B there was a more gradual change in orientation. Kim et

al.(1994) suggested that planarization of grooves is a preferred low energy state which any growth on a nonplanar substrate tries to achieve. Planarization involves a gradual change in orientation and size of the planes, hence any attempt to grow quantum wire will lead to a change in size of these wires. In this study, this was evident in case of growths on (111)B at the bottom of the groove. Changes in the dimensions of successive quantum wires may be harmful to the properties of a device (Simhony et al., 1991) and hence needs to be controlled. Colas et al. (1990b) explained planarization based on a surface diffusion mechanism and suggested that planarization could be slowed down by reducing the temperature of growth. The factors that control the planarization of the grooves has been considered in a theoretical treatment of Ozdemir and Zangwill (1992). An understanding of these factors will allow one to grow quantum wires of uniform size and shape.

4.4.4 Defect formation

In the case of heteroepitaxial growth on (111)B grooves extensive defect formation was concentrated in certain areas of the groove, whereas the growths on (211)A were defect free. Defects in (111)B can be the result of one (or more) of three possible causes: (1) a composition variation; (2) atomic stacking "mistakes"; (3) misfit stresses exceeding the critical limit at the corners, given that the composition of the layer is uniform. One way to eliminate or confirm which of these might be the cause, was to compare homoepitaxial growth on (111)B grooves and (111)B planar substrates. Homoepitaxial growth would eliminate composition as a variable while growth on a planar substrate would show the effect of faults introduced by stacking "mistakes".

In the case of homoepitaxial growth on (111)B grooves, no defects were evident but, in the case of planar (111)B growths extensive defects were observed. The fact that defects have not been observed in the case of lattice matched AlGaAs/GaAs or in this

study with homoepitaxial growth on V-grooves suggests that a composition variation might be responsible for these defects. However, we have to explain why are there no defects observed in the case of homoepitaxial growth in (111)B grooves. One possible reason might be that the grooves are slightly misoriented from (111)B. Experiments on misoriented (111)B substrates have given defect free films (Vina and Wang, 1986). A defect-free growth would be produced in these experiments if a slight misorientation leads to an increase in the number of steps on the surface. Then growth initially proceeds by step propagation rather than by an island nucleation mechanism.

Since (111)B planes in the grooves may be slightly "offcut" and give perfect crystal for homoepitaxial growth we believe that the second possibility (that it might be a result of atomic stacking "mistakes") can be discounted. For a growth with uniform composition along the groove, lattice-matched growth (560(111)B) should not have any misfit stresses and hence no relaxation. Contrary to this, as shown in Fig.4.20, there are defects concentration at the bottom of the groove. Thus, it can be concluded that the defects observed in heteroepitaxial growth are a result of compositional variations. A composition analysis (to be reported in Chap.5) confirms this. As noted above, homoepitaxial growth on (111)B and (111)A planar substrates showed extensive defects such as twins, dislocations and stacking faults. In the literature these defects have been attributed to atomic stacking "mistakes"(Rajkumar et al., 1991) or "nucleation problems" (Sangster, 1962).

An increase in misfit energy can occur by diffusion from adjacent regions, locally changing the composition. The reason why defects were not seen in AlGaAs/GaAs is that this system is essentially lattice-matched over the entire composition range. Composition analysis has shown that there can be a significant change in composition along the sides of the grooves in this system (see Sec. 2.2.4). The uniform composition of layers (as shown

in Chapter 5) for growths on (211)A grooves may be a possible reason for defect-free growth in these systems.

Apart from the defects, the morphology of the growths on (111)B type of grooves is that needed for obtaining quantum wires, although the variation in the size of the wire (i.e. an increase in the curvature with successive wires) is undesirable. Some ways of preventing this size variation have been suggested (Simhony et al., 1991). By understanding the composition variation one hopes to be able to design better lasers by exploiting the vast resource of lattice-mismatched systems without affecting the quality or lifetime of the laser.

5. COMPOSITION ANALYSIS USING EDX ON STEM

5.1 INTRODUCTION

In studies of the growth pattern on V-grooves, it has been demonstrated that the generation of quantum wires is possible due to thickness variations of the heteroepitaxial layer, as discussed earlier in section 2.2.3. This thickness variation can be caused by three factors: a difference in orientation of the various facet planes with respect to the incident flux, a difference in sticking coefficients, and a difference in diffusion rates of the group three atoms. The latter two factors may also lead to a variation of composition. The extent of this variation will depend on the planes constituting the sides of the groove and the overall composition of the layer. It has been reported that the difference in composition between the top (100) plane and the bottom of the groove is more pronounced in the case of mismatched layers such as InGaAs/InP and InAlAs/InP than in lattice matched layers such as AlGaAs/GaAs (Turco et al., 1990). Hence it was proposed that in the case of lattice mismatched layers the strain plays a role in promoting diffusion (Hartmann et al., 1994; Chu, 1993). In the previous chapter (section 4.4.2) we showed that in this work, this explanation does not hold. The difference in growth rates is a characteristic of the atoms constituting the layer and their interaction with the plane on which they are growing. It was also strongly dependent on the growth behavior of adjoining planes and the facet dimensions.

For AlGaAs/GaAs layers a composition variation may not have any serious consequences on the lifetime of a device because the lattice misfit does not exceed the

critical limit (Sec. 2.2.3). But in the case of lattice mismatched systems, misfit is of paramount importance because it can lead to defects and hence limit the performance or lifetime of a laser. The only way one can control this variation is by understanding the process and by obtaining enough data to build a model which explains any composition variation. The first step is to do a detailed composition analysis of different layers grown on a patterned substrate. The best technique which can give such a detailed picture is EDX analysis using a STEM with a spatial resolution of around 5-10 Å (under optimum conditions). Most investigations on composition variation available in the literature have employed either CL (Pan et al., 1995; Hoenk et al., 1989), which has a resolution of about one micron, or EDX using a scanning electron microscope (Keller et al., 1994), which also has a resolution of about one micron. Although these techniques can show a gradient in composition as one goes from the top to bottom of a groove, the accuracy and detail of an EDX analysis in a STEM is missing. Our aim in doing composition analysis was to get a detailed composition analysis using EDX on a high resolution STEM.

Two types of grooves, (111)B and (211)A, were studied. As shown in earlier chapters, (211)A growths do not generate quantum wires because the change in thickness is negligibly small and the groove angle is too wide for quantum confinement effects. Nonetheless a compositional analysis is worthwhile in order to understand the growth behavior on different planes. In the case of (211)A growth, no defects were observed. One explanation for this may be that the composition is uniform along the groove. To verify this proposition composition analysis of layers grown on these grooves was performed.

For (111)B grooves the angle at the bottom of the groove was sharp enough to give quantum effects. There was also a large increase in thickness at the bottom of the groove, leading to a shape similar to that observed in AlGaAs/GaAs, and making it

potentially suitable for quantum wire applications. However, one obstacle to this goal is the large number of defects generated in growths of InGaAs/InP. As discussed in chapter 4 the reason for this is believed to be related to composition changes. Hence it becomes pertinent to do a composition analysis and to investigate how much migration is occurring for the growth conditions used in the present samples.

To determine the accuracy of the measurements on STEM, composition analysis was carried out on a standard sample. The statistical scatter of the data was also measured for all the samples.

5.2 STANDARD

For the standard a sample which consisted of a thick 2400Å single layer of $In_{0.54}Ga_{0.46}As$ on an InP (001) planar substrate was chosen. In addition to determining the accuracy of the EDX measurements we were also interested in finding out the maximum distance from the interface where beam broadening effects were still present. In analyzing layered materials in cross-section, compositions measured near an interface should be looked at carefully, as beam broadening of the electron beam can occur. This is a result of high angle elastic scattering of electrons, and hence the greater the thickness of the sample the greater is the broadening. Near an interface some of the X-rays may come from the adjacent region and not from the layer under analysis. The most effective way of reducing this effect is to analyze the compositions in a relatively thin region of the sample.

For InGaAs/InP samples, the analysis of the InGaAs layer often shows the presence of P. There are two possible sources of P. The P may actually be present in the layer close to the interface. During MBE a P_2 overpressure has to be maintained for depositing the InP layer because of preferential reevaporation of P. When depositing InGaAs, although the P source is inoperative, there is some residual P in the chamber

atmosphere which might be incorporated in the layer. Secondly the P may be detected due to beam broadening from the adjacent InP layer. It is also possible of course that any P detected is due to a combination of these two sources. For the first case since the P is actually incorporated in the layer, the amount of P detected would be independent of sample thickness. In the second case there would be a considerable difference in the amount of P detected in a thin region compared to a thicker region. A good test for ascertaining the source of P would be to do an analysis in relatively thick and thin regions of the sample. A thin region (< 100nm thick) corresponds to an area close to the hole while a thick region (200-400nm in thickness) to an area further away from the hole. It is also important to do the analysis at different distances from the interface in both the InGaAs and InP layers. This would show the extent of beam broadening for a given sample thickness. There should be no Ga or As incorporation in the InP layer during MBE growth. Hence any Ga or As present in InP comes solely due to beam broadening.

Table C1 in Appendix C lists all the data obtained from various regions of the InGaAs layer. The analysis was done at both "thick" and "thin" regions (as defined above) and at different distances from the interface. Thus the data represent the general conditions one encounters on a typical sample. In most of the data a P signal was detected. This probably comes from the adjacent InP substrate (Fig. 5.1). Assuming that this level of P originates from the InP layer an equivalent atomic amount of In should also be present in the spectrum, coming from the InP rather than the InGaAs. The data were corrected (as outlined in Appendix C) to get the actual In present in the InGaAs layer, and the compositions were recalculated.

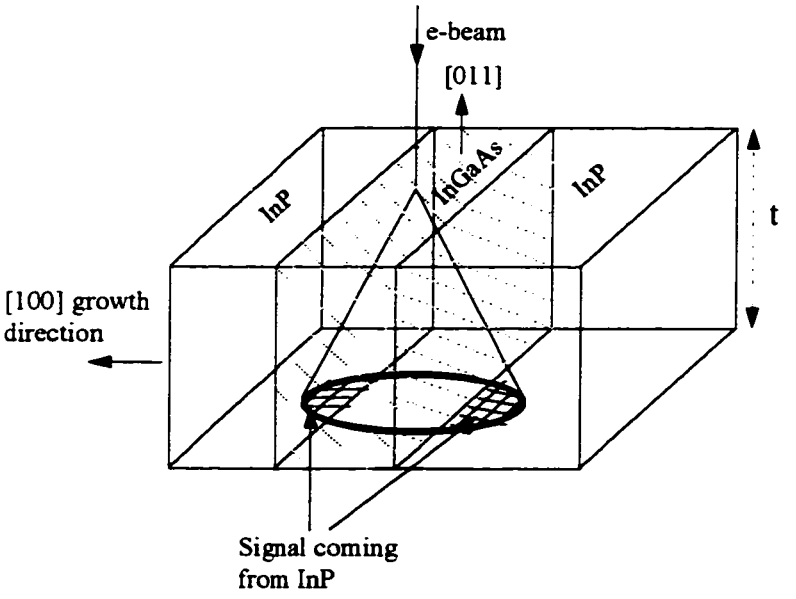

Fig. 5.1 Schematic diagram showing the beam broadening effect in TEM cross-sectional samples. Although the beam is concentrated in the InGaAs layer, it picks up signal from adjoining InP layer. The extent of broadening increases with foil thickness 't'.

Table 5.1 compares the data obtained in regions close to the hole and far from the hole, which represent thin and thick regions respectively. Micrograhs corresponding to Table 5.1a and 5.1b were taken at the same magnification. It was found that in the "thinner" region of the sample the amount of P picked up drops drastically compared to the one done at the same distance from the interface in the "thicker" region. This result shows that most of the P detected is due to beam broadening. In the thinner part there is a sharp decrease in the P signal as one goes away from the interface (point 4 to 5 in figure corresponding to Table 5.1a). Hence this confirms that in this study the apparent P signal is due to beam broadening. A further point of interest is the accuracy of the analysis in the corrected data (Table C1 in Append.C). This shows that small changes in the In/Ga ratio (of the order of 1%) should be detectable using EDX methods.

1	42.44	0.63	1.25	55.67
2	39.95	1.71	3.68	54.66
3	34.03	5.86	10.6	49.51
4	7.91	20.9	41.22	29.98
5	1.15	24.87	49.1	24.88
6	1.09	25.44	48.25	25.22
7	0.47	25.36	49.08	25.08
8	1.14	25.93	47.86	25.06
9	0	25.99	50.25	23.81
10	0.28	27.03	48.72	23.97

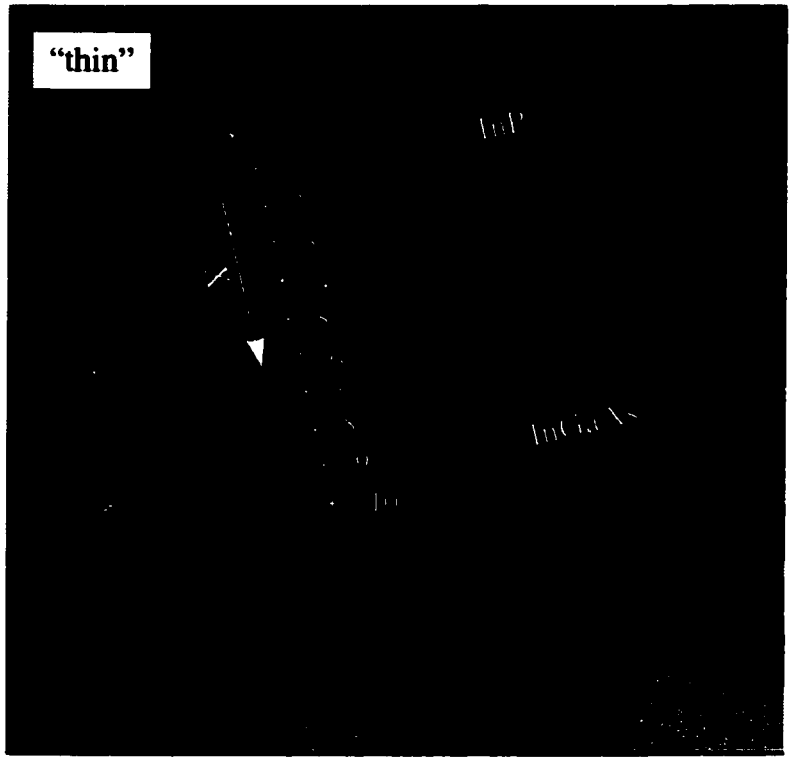

Table 5.1 Composition analysis across the substrate and layer interface in a "thick" and "thin" region of the sample.(a)Analysis in the area near the hole (Thin region).

1	39.42	1.07	2.46	57.05
2	36.47	3.43	6.95	53.15
3	36.21	3.88	7.38	52.53
4	31.18	6.45	13.14	49.23
5	19.54	14.6	27.24	38.63
6	9.52	20.53	40.03	29.92
7	2.75	24.73	47.58	24.94
8	0.91	25.16	49.79	24.14

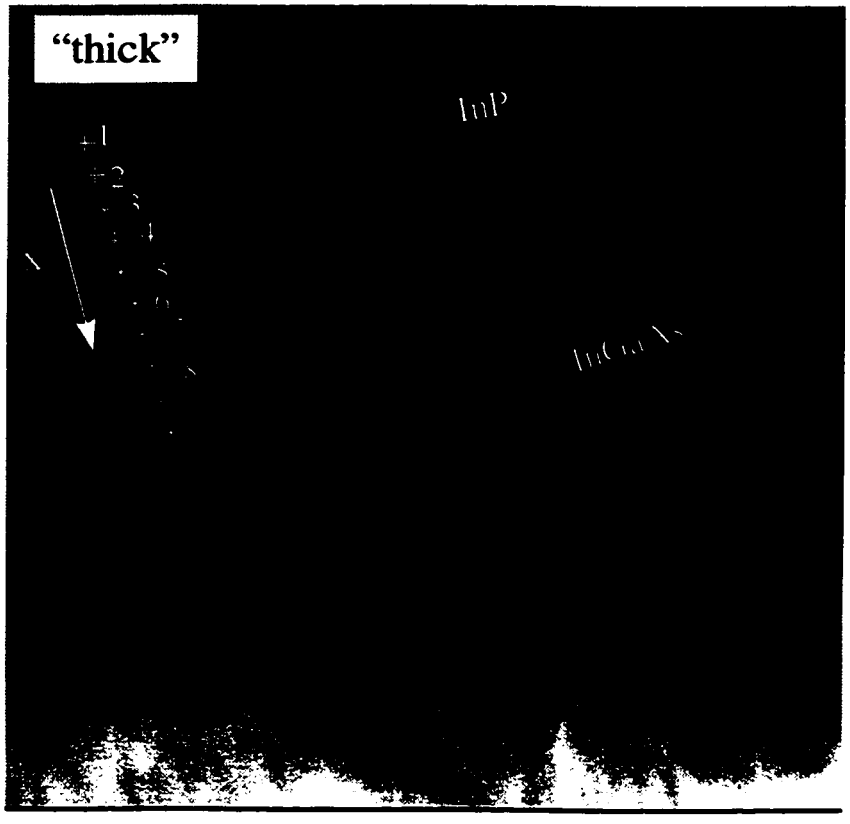

Table 5.1b: Analysis in an area far from the hole (thick region).

5.3 EDX ANALYSIS OF GROWTHS ON (211)A V-GROOVES

5.3.1 Results

Sample 560A, a (211)A growth, was analyzed using the JEOL 2010F. The areas that were analyzed were: the top (100) plane, the (211) sideplane, and the (311) bottom sideplane. Sample 560A consisted of 8 layers of $In_{0.532}Ga_{0.468}As$, 300Å thick, alternating with 300Å thick layers of InP. For layers of this thickness beam broadening effects become critical. Although the beam was always located in the centre of the layer, in all cases a certain level of P was detected. Problems due to specimen drift were also encountered. The beam track option was used to analyze several points in a given experiment. After the analysis was completed the carbon build-up, associated with beam-induced contamination, was sometimes found to be located close to the interface rather than in the center of the layer. Also in some cases carbon build-up occurred in the substrate, indicating substantial specimen drift. For these reasons only data which showed less than 10at% P were used in the analysis (Table C2 in Appendix C). The amount of P was subtracted from the apparent In signal and the compositions recalculated following the same procedure as described for the standard in Appendix C.

The data in Table 5.2 shows that within statistical error, defined by the standard deviation of the mean, the composition of the InGaAs layer is the same at the top (100) surface, the (211) facet and the bottommost (311) facet. This result agrees with our expectation because there were no defects in the sample and there was little (less than 50%) change in thickness of the layer in the groove with location.

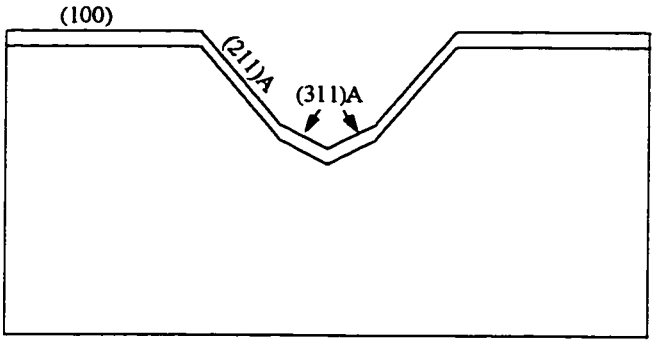

Fig. 5.2 Schematic representation of growth on (211)A Vgrooves.

Region	at% In ± std. dev.	at% Ga ± std. dev.	at% As ± std. dev.
Nominal	26.6	23.4	50.0
(100)	25.18±2.39	23.51±1.33	51.31±2.13
(211)A	25.59±2.03	23.24±2.24	51.17±1.79
(311)A	25.32±1.43	21.23±1.24	53.44±1.38

Table 5.2 Summary of the composition of the layers on different facets of sample 560(211)A.

5.3.2 Discussion

The negligible variation of composition along the groove sides suggests that the sticking coefficients are equal on (211)A and (311)A planes. Sangster (1962) had predicted good growths on (311)planes from his dangling bond model. His explanation was that (n11) planes with n≥3 consist of more (100) terraces than (111) steps and hence the better nucleation properties of the (100) surface dominate. In our case this also appears to be true for growth on (211) planes. Homoepitaxial growth on a planar (211)A substrate also showed good quality films.

The homogeneous composition found in the groove suggests very little difference in the diffusion rates of In and Ga on the planes constituting the groove. Bhat et al.(1991) concluded that defect free layers can be grown on {h11}A oriented planes without any composition variation for h≥3. Bhat et al.(1990) conducted another study using InGaAs/InGaAsP grown on (211)A InP grooves. In this latter study extensive defects were present on the sidewalls, suggesting a composition variation. The disagreement between our results and theirs may originate from the differences in compositions and/or growth conditions used in the two studies. Their sample consisted of lattice matched InGaAsP/InGaAs layers grown at 625°C using OMCVD. Turco et al.(1990) reported that there was ~5% In variation in lattice matched InGaAs layers and ~30% In variation in lattice matched InAlAs layer grown on similar {211}A patterned substrates. However the significance of this claim cannot be substantiated as no data were presented in the paper. This difference in In behavior in the two systems might arise from a difference in diffusion rates of the group III species, that is the difference in diffusion rates between In and Al is greater than that between In and Ga.

The difference in thickness values of InGaAs layers on (211)A grooves between the present study and that of Turco et al.'s (1990) was discussed in the last chapter. Increase in thickness of InGaAs layers on the (311)A facet and negligible composition variation in the layers, led Turco et al.(1990) to conclude that the thickness variation is mainly controlled by the orientation of the facets with respect to the flux. In the present experiments and in case of Bhat et al.'s (1991) growth, the increase in thickness on (311)A planes cannot be explained by a variation in orientation of the planes with respect to the flux. Only interfacet surface diffusion can explain this increase in thickness. The negligible composition variation in the (211)A groove suggests that at this particular

growth temperature the mean diffusion lengths on this surface of In and Ga (prior to their incorporation) are similar.

In the previous chapter it was shown that the thickness on the top (100) facets varies near the edge of the V-groove in order to accommodate the difference in growth rates of InGaAs and InP on the small (311)A facet at the junction of (100) and (211)A facets. However, the composition analysis did not reveal any variation in composition in this region.

5.4 EDX ANALYSIS OF GROWTHS ON (111)B V-GROOVES

5.4.1 Results

In the literature, most experiments have been done on (111)A grooves. The reason for this is the sharper groove which leads to a better confinement of electrons, often accompanied by a threefold increase in thickness at the bottom of the groove. A major factor leading to this increase in thickness was the difference in diffusion lengths of the group three atoms before incorporation. In all the reports of ternary or quaternary growths, the composition varied along the sides of the grooves (Keller et al., 1994; Hoenk et al., 1989; Pan et al., 1995). The extent of variation depended on the elements and their relative diffusion lengths.

Sample 570B which consisted of eight 300Å thick layers of $In_{0.55}Ga_{0.45}As$ with 300Å InP spacer layers was analyzed in depth. In this sample there were extensive defects at the side of the groove close to the top surface where the layers were indistinguishable. Below this region the layers start to "flare out"; the thickness of individual InGaAs layer reduces to around 100Å whereas the thickness of InP increases gradually. In this region the plane of growth is changing continuously. Although at the

onset of growth a relatively sharp groove at the bottom of the V-groove is present, as successive layers are grown the corner starts to flatten out and expand. In this region the thickness of InGaAs has increased about threefold compared to the top. Although this region is full of defects such as twins and dislocations, the layers are distinct.

The composition at each region specified above was analyzed at about 10-15 locations (Table C3 in Appendix C). Only data with less than 10at% P were usually considered, although in some cases data with more than 10at% P were included in the analysis. The criteria for including data with more than 10at% P was that the As amount should be close to 50±2at% after all the corrections for beam broadening have been made. Most data with P> 10at% gave an As content which was quite low, and were excluded from further analysis. The amount of As should remain unaffected by beam broadening effects because there is no As in the substrate. Hence it is a safe criteria for excluding incorrect data. After all the corrections were made, the results show a significant variation in composition with position (Table 5.3). As reported in the literature (Keller et al., 1994) we have also observed an increase in In content at the bottom of the groove corresponding to region 5 (Fig. 5.3). Also on the top (100) surface as one moves from region 2 to region 1 (Fig. 5.3) there is an increase in In content (Table 5.3). These observations suggest that In migrates to more favorable planes, in this case the (100) plane.

The layer thickness on (100) planes was 300Å but on the sides of the groove it was reduced to 100Å. Also since the groove was 6-7μm deep, it is likely that the foil used for TEM would be thicker near the bottom of the groove than at the top. These two factors would lead to more broadening of the electron beam at the sides of the TEM sample than at the top. As shown in Fig. 5.1 beam broadening leads to signals coming from both the InP and InGaAs layers. So even though the analysis is being done in the InGaAs layer

some P is picked up. A correction for this effect was done using the same procedures already described for the standard in Appendix C.

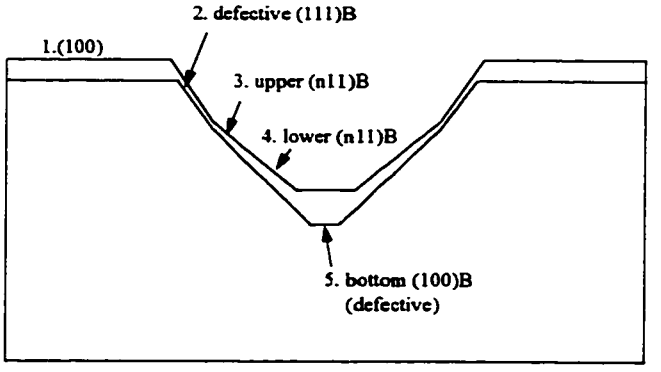

Fig. 5.3 Schematic representation of growth on (111)B V-groove.

Region	at% In ± std. dev.	at% Ga ± std. dev.	at% As ± std. dev.
Nominal	27.5	22.5	50.0
1. (100) top	26.54 ± 1.12	20.41 ± 1.12	53.05 ± 0.53
2. (111)B defective	23.23 ± 2.06	26.61 ± 1.53	50.16 ± 0.76
3. (n11)B upper	30.86 ± 2.90	18.87 ± 1.09	50.28 ± 2.10
4. (n11)B lower	32.76 ± 3.79	15.80 ± 3.89	51.43 ± 2.74
5. (100) bottom	36.26 ± 2.40	11.11 ± 1.98	52.64 ± 2.10

Table 5.3 Summary of composition analysis in different regions of sample 570(111)B.

5.4.2 Discussion

Sangster's (1962) model predicted nucleation problems on (111) planes. We have observed extensive defects both on layers grown on planar (homoepitaxial) and patterned (heteroepitaxial) growths. However, homoepitaxial growths on (111)B grooves did not

show any defects, probably, as discussed in Chap.4, because the sides of the groove are slightly misoriented from an exact (111) orientation. Thus the growth will proceed by step propagation. This suggests that the presence of defects in the heteroepitaxial case arises due to composition variation. Our data confirms that there is a composition change at different locations along the groove. This change in composition can be due to a difference in diffusion lengths of In and Ga atoms on {111} planes.

Table 5.3 summarizes the average composition measured in various regions of the groove. Although the nominal composition was 27.5at% In, on the top (100) layer the In composition was found to be (26.5±1.1)at%. In the defective region 2 on (111)B plane the composition of indium was lowest, which means that In has a low incorporation rate on this plane and hence is diffusing out towards the more favorable (in terms of growth) top (100) and bottom (100) facets. This suggestion is confirmed by the observed increase in In just below the defective region to (30.9±2.9)at%. In region 4 the In level again increased to (32.7±3.8)at% while on the (100) plane at the bottom (or the quantum wire region) it was (36.2±2.4)at%. The defects which were discussed in chapter 4 were concentrated in the bottom (100) plane and the sideplane (111)B near the top of the groove, that correspond to the highest and the lowest In concentration respectively. Thus the bottom (100) layer is under tension while the top region of the (111)B side plane is under compression. Both these regions contained defects (twins, stacking faults, and dislocations), but whereas on the (111) sideplane near the top (100) surface the growth rate was extremely slow, such as to make the layers indistinguishable, the growth rate on the bottom (111) plane was appreciable and the layers were distinct.

The spectrally and spatially resolved CL measurements of composition in different regions of the $Al_xGa_{1-x}As$ layers grown on (111)A GaAs V-grooves by Pan et al. (1996) showed that the composition varied as $x_{Al(1)} > x_{Al(2)} > x_{Al(3)} > x_{Al(4)}$ (see Fig. 5.4a). The Al

diffusion length is much smaller than the Ga diffusion length. The study of Pan et al. (1996) measured the composition variation at different temperatures and found that the Al content at the bottom of the groove was temperature dependent. The diffusion length of Ga atoms becomes much larger than that of Al atoms with increasing growth temperature and hence the Al content decreased at the groove bottom with increasing growth temperature. In the present experiment the variation of In showed a trend similar to Ga in case of AlGaAs/GaAs but the resolution of the STEM system allowed composition analysis with greater precision. An average of the data was taken at five different locations in the groove and the $In_xGa_{1-x}As$ composition varied as $x_{In(1)} < x_{In(2)} < x_{In(3)} < x_{In(4)} < x_{In(5)}$ (Fig. 5.4b). In this case In has a higher diffusion length than Ga and the In content at the bottom of the groove is the highest. In both examples it seems that the group III incorporation rate is lower on (111)A and (111)B surfaces, hence the group III atoms migrate to adjoining (100) planes which are more favorable. Since the diffusion length of In is higher than Ga, the In content at the bottom of the groove increases.

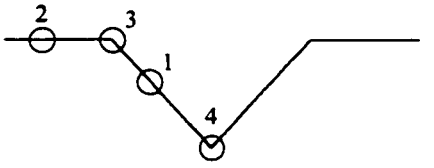

(a) AlGaAs/GaAs grown on (111)A V-groove

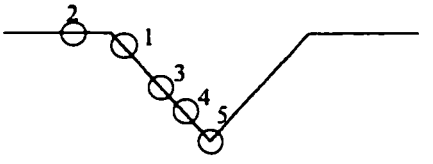

(b) InGaAs/InP grown on (111)B V-groove

Fig. 5.4 Comparison of composition variation in (a) AlGaAs/GaAs layers grown on (111)A V-groove (from Pan et al., 1996) and (b) InGaAs/InP layers grown on (111)B V-groove (from this study).

In is diffusing both to the top (100) plane and the bottom (100) plane from the (111)B side plane: further evidence for this comes from thickness measurements near the edge of (111)B and (100) plane on the (100) plane (Fig. 5.5a). The InGaAs layers are thickest near the edge and decrease in thickness away from the edge until they attain the thickness value of the flat (100) plane (Fig. 5.5b). An exponential decrease in thickness away from the edge on the (100) plane was also reported by Galeuchet et al. (1988) and Hata et al. (1990).

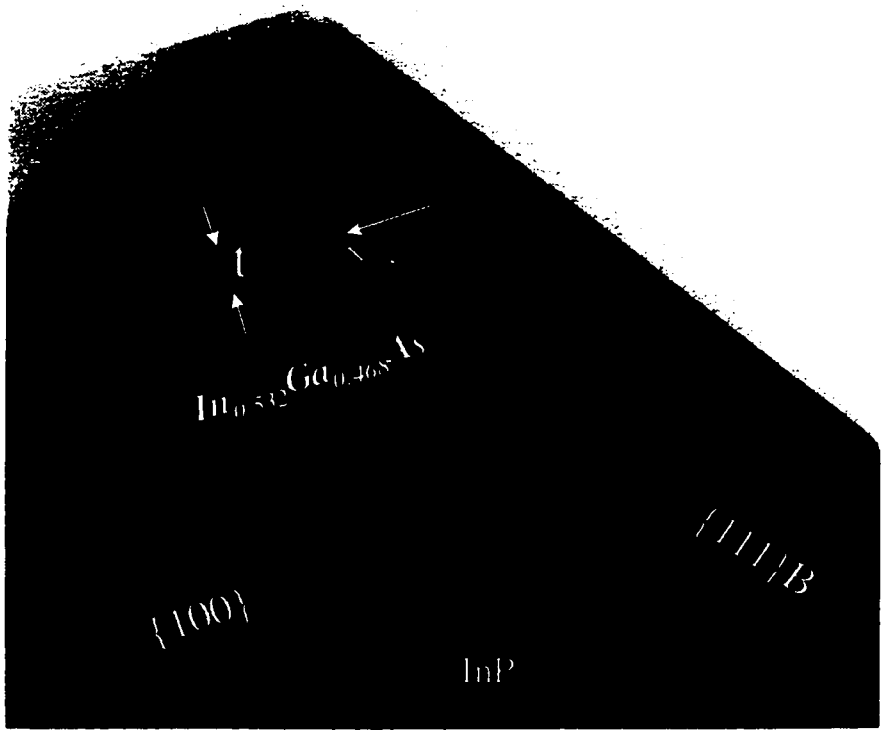

(a)

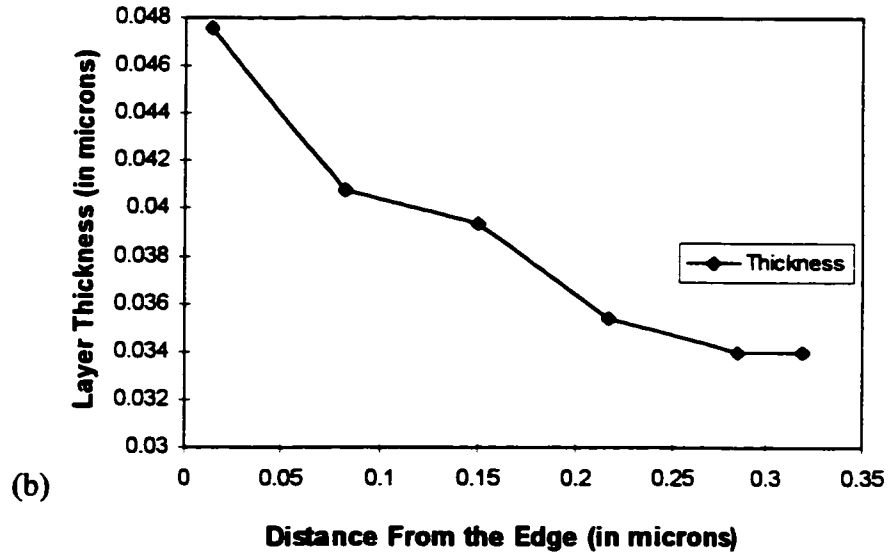

(b)

Fig. 5.5 Thickness variation near the edge on (100) layers. (a) BF TEM image showing the area (b) Thickness(t) variation as a function of distance away from the edge.

The data obtained by EDX showed a gradual change in composition along the sides of the groove. This disproves the observation of Hoenk et al. (1989) that the composition change from one facet to the other is abrupt. They arrived at this conclusion from CL measurements, which has a low spatial resolution.

The change in composition leads to local areas where the misfit exceeds the critical limit and gives rise to dislocations. In the present study these regions correspond to the portion of the sidewall near the intersection of the (111)B sidewall and (100) surface and the bottom of the groove. These regions correspond to the lowest and highest In content respectively. If it is assumed that the growth morphology at the bottom of the groove is triangular in shape, then the lower and upper limits of the misfit strain for generating defects in quantum wires for the 570(111)B sample can be calculated using Gosling and Freund's model (1996). The dimensions of the first layer were taken for the calculation because it gives the sharpest angle at the bottom of the groove. The thickness of the individual layers on the top (100) plane was 300Å, on the sideplane near the groove

bottom it was 125Å, and on the bottom quantum wire region it was 1560Å. The composition analysis from EDX gives a misfit strain of about ~0.013 in the quantum wire region. Gosling and Freund (1996) assumed that the strain relaxation in the wire occurs via 60° dislocation formation, with a {111} glide plane and <110>/2 Burger's vector ($\vec{b}$). If the lattice parameter of InP is taken to be 5.869Å then the magnitude of $\vec{b}$ would be 4.15Å. Since Gosling and Freund assumed the layer and the substrate to be isotropic and have the same elastic constants, the Voigt average elastic constants for InP can be used, with Poisson's ratio, $\nu = 0.284$.

According to Gosling and Freund the critical mismatch lies somewhere between lower (f_{lb}) and upper (f_{ub}) bounds of misfit strain, given by

$$f_{lb} = \frac{0.0589b}{(1+\upsilon)h}\left[(4-\upsilon)\ln\left(\frac{h}{q}\right) - 0.660 + 0.0709(1-\upsilon) + \frac{1+2\upsilon}{4(1-\upsilon)}\right]$$

$$f_{ub} = \frac{0.0589b}{(1+\upsilon)h}\left[(4-\upsilon)\ln\left(\frac{1.4h}{q}\right) - 0.614 + 0.101(1-\upsilon) + \frac{1+2\upsilon}{4(1-\upsilon)}\right]$$

where h is the height of the quantum wire and q is the core radius of the dislocation.

For h/b = 375.9 (assuming q=b), the lower and upper lattice misfit are, f_{lb}= 0.003 and f_{ub}= 0.0032 respectively.

From the composition analyzed using EDX, the misfit strain in this region of the film was 0.013, considerably greater than the critical values calculated above. Hence to achieve defect free growth either the thickness should be lowered such that h/b= 50 (i.e. h= 207.5Å) for a misfit strain of 0.013, or for an h/b of 375.9 the misfit strain should be lowered to 0.003. This gives some idea as to the measures one would have to take to prevent dislocations.

A final observation was that for the same growth conditions, while there was only a slight thickness change and negligible composition change for (211)A growths, for the (111)B growths the thickness change was threefold and there was a ~ 36.6% increase in In content at the bottom of the V-groove. These differences in growth behavior must be related to the incorporation rates of group III atoms on (211)A and (111)B planes. Nucleation problems (Sangster, 1962) on (111)B leads to a lower incorporation rate on these planes and hence more adatoms are available to diffuse to adjoining, more favorable planes. The better growth characteristics of (n11) planes result in a higher sticking coefficient on (211)A planes and hence fewer atoms are available to diffuse from one facet to another. The fact that the growths on (211)A grooves showed a variation in the thickness of layers near the intersection of (211)A and (100) planes (see section 4.4.1) but still did not show any variation in composition might be a result of similar diffusion lengths of In and Ga at 470°C in this situation. Turco et al.(1990) observed a 5% change in composition for InGaAs growths done on (211)A InP V-grooves at 625°C.

6. STRAIN DISTRIBUTION IN LAYERS GROWN ON V-GROOVES

6.1 INTRODUCTION

The growth of strained layers on V-grooves gives rise to a stress distribution which is different from that at layers grown on planar substrates. This difference arises due to the geometry of the V-groove and the presence of singular points at the corners of the groove. Since the quantum wire forms at the bottom of the groove it becomes important that the stress distribution is known at these locations. Freund and Gosling (1995) were the first workers to tackle this subject, but their model only deals with the critical dimensions and critical compositions of the quantum wire. No model exists to my knowledge which gives the stress distribution for a quantum wire grown within the critical limit i.e. without defect generation. The relevance of such a model arises because the optical and electrical properties of the quantum wire will be influenced by this stress distribution.

The experimental measurements were made using two techniques, TEM and DOP. However one has to be careful in interpreting the data, given the limitations of the two techniques. Only the data from the TEM and DOP measurements on the (211)A groove will be compared in a quantitative way with analytical and finite element simulations of the strain field. Although these models did not take faceting into account, (211)A grooves were considered for comparison because these grooves are defect free and the layers are quite uniform in thickness and composition.

6.2 TEM STRAIN RELAXATION CONTRAST

In TEM there are two types of contrast, structure-factor (amplitude) or phase difference, which can be used to extract information from the sample. In the case of strained layers grown on planar substrates it is important that one is able to distinguish between layers of different compositions and structure factor contrast becomes important in being able to do this. If the interfaces are sharp, the quality of the interface can be assessed and layer thicknesses measured. Cross-sectional {011} type TEM samples of strained layer superlattices have been shown to exhibit the best contrast under the {200} or {400} type two beam conditions for assessing interface sharpness and layer width (Petroff, 1977). For this orientation, the interfaces are edge on with respect to the electron beam, hence the layer thickness can be accurately measured. In addition to the information regarding the quality of the interfaces, TEM is also useful for providing information related to atomic displacements. The only constraint to this approach is that the displacements should be in a direction perpendicular to the electron beam and for diffraction contrast should vary in the direction of the beam. As shown in the literature review, stress relaxation contrast meets these requirements and hence surface strains can be measured to a reasonably high degree of accuracy. For strained layers grown on planar (100) surfaces, the surface displacement due to stress relaxation is in the growth direction lying in the free surface, perpendicular to the layers. Hence (200) and (400) $\vec{g}$ vectors show stress relaxation contrast while an (022) $\vec{g}$ vector does not (Perovic et al., 1991) in [01 $\bar{1}$] cross-sectional samples.

For the growths on V-grooves, the quality of the growth was assessed with $\vec{g}$ = 200 (Fig. 6.1). This diffraction condition showed good contrast between the layers and

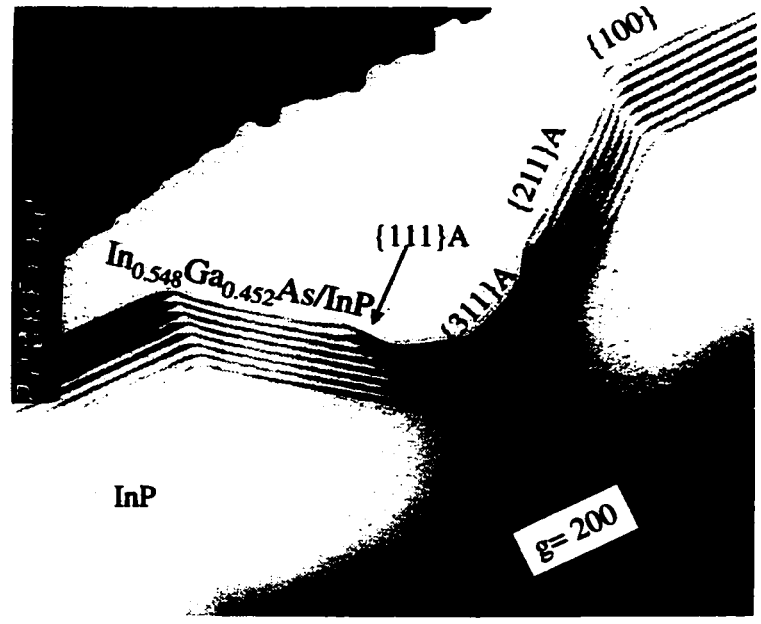

(a)

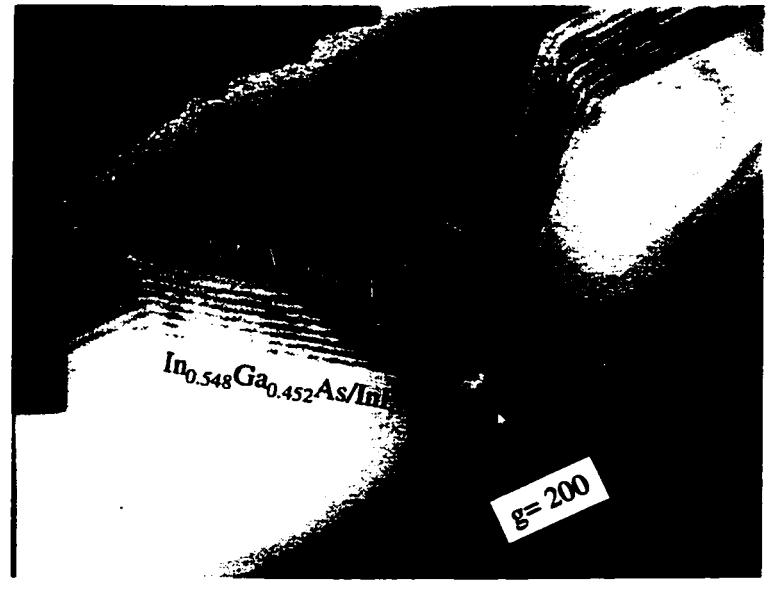

(b)

Fig. 6.1 TEM image of sample 489(211)A with $\vec{g}$ =(200). (a) BF image (b) DF image.

the substrate. The layers were uniform all along the groove. The other details of the growth have already been discussed in Chapters 4 and 5. Here we will concentrate on the stress relaxation contrast observed in the microscope.

In sample 489(211) the layers were grown with a 0.103% compressive strain. To verify whether the stress relaxation contrast is visible near the top (100) interfaces, similar to that observed for planar samples (Perovic et al., 1991), the sample was observed under (200) bright-field (BF) and dark field (DF) conditions. A strong contrast all along the (100) interface was observed (Fig. 6.2). This contrast terminated at the edge of the groove. For the case of a multilayer grown on planar substrates, Perovic et al. (1991) did not see any contrast between the layers but only at the interface between substrate and the first layer. A similar observation was made for sample 489 (211)A which consisted of multilayers. This contrast did not however continue along the interfaces of the side facet planes for sample 489(211)A (Fig. 6.1). A possible explanation for this observation is that the surface displacement due to stress relaxation in the V-groove has a relatively weak component (less than the minimum detectable limit in TEM) in the (200) direction. The situation at the root of the V-groove is different because of the symmetry; hence it was expected that relaxation contrast under (200) and (400) diffracting conditions might be visible there. This turned out to be true: stress relaxation contrast was visible at the bottom of the groove under (200) and (400) diffracting conditions. This contrast was observed under both bright field (BF) and dark field (DF) conditions (Fig. 6.1); as expected, the contrast changed from dark to bright in DF when the sense of the operating reflection $\vec{g}$ was reversed. The layers were under compression, hence for a $\vec{g}$ vector directed towards the free surface, the contrast is dark at the bottom of the groove in BF.

The visibility of stress relaxation contrast at the bottom of the groove under a (200) diffracting condition suggests that the stress relaxation occurs all along the groove

at the interfaces, but it shows up only when a component of the diffraction vector is in the direction of the displacement due to surface relaxation at the free surface.

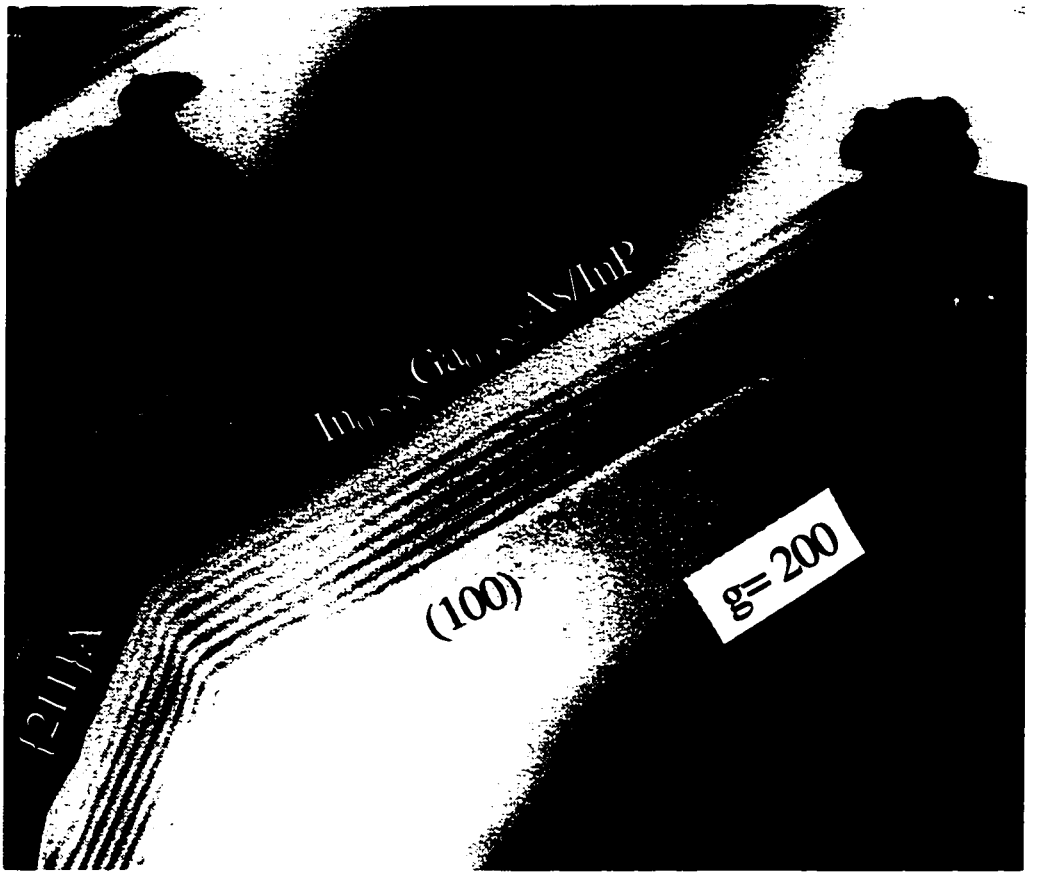

Fig. 6.2 DF TEM image of sample 489(211)A with $\vec{g}$=200 showing (100) top surface in-between two grooves.

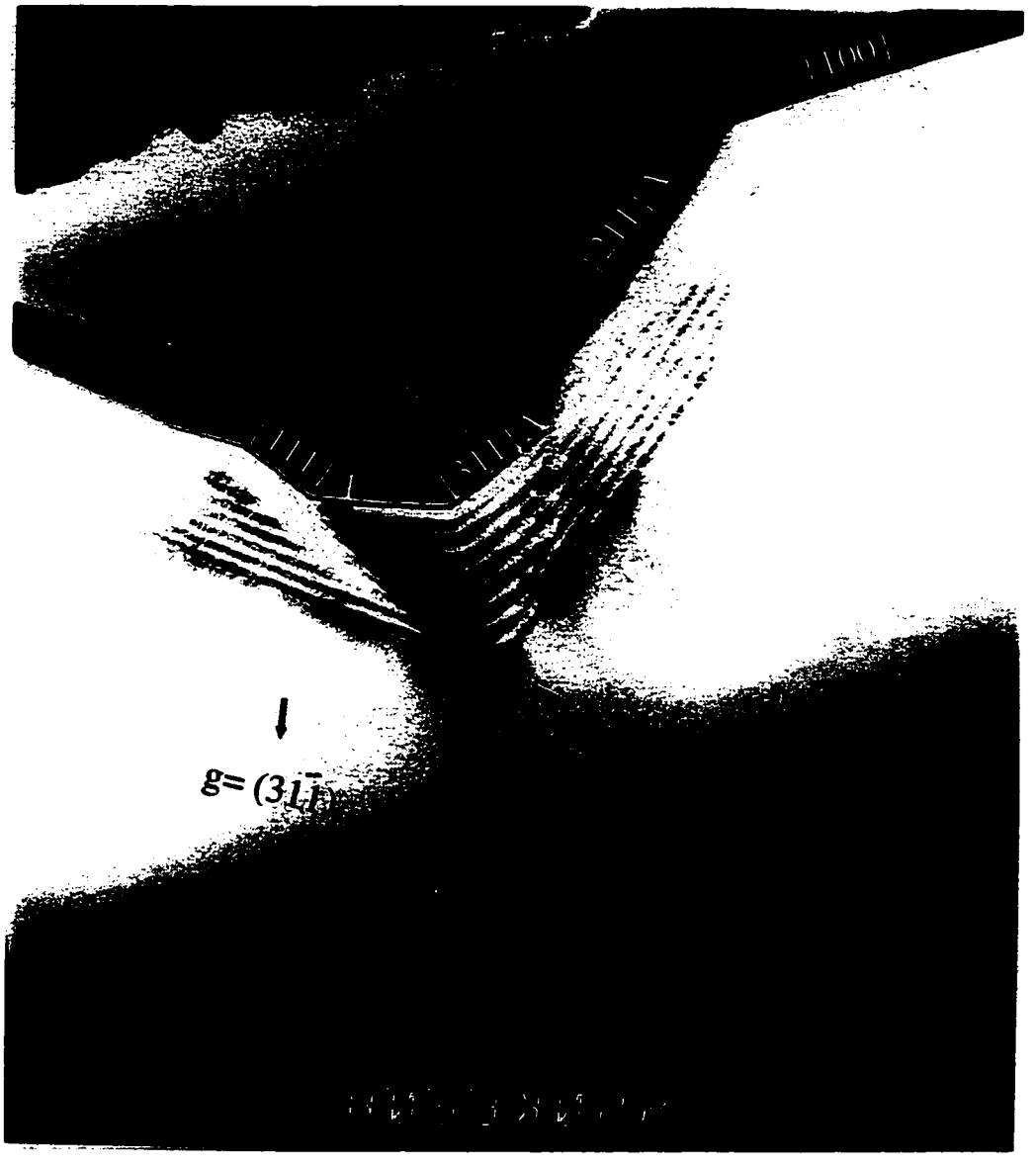

Fig. 6.3 DF TEM image of sample 489(211)A with $\vec{g} = 31\bar{1}$.

With $\vec{g}=(31\bar{1})$ the relaxation contrast was observed only on one side of the groove, as shown in Fig. 6.3. With $\vec{g}=(022)$ a black and white contrast was observed with a line of no contrast running at the centre along the axis of symmetry of the groove and perpendicular to $\vec{g}$ (Fig. 6.4).

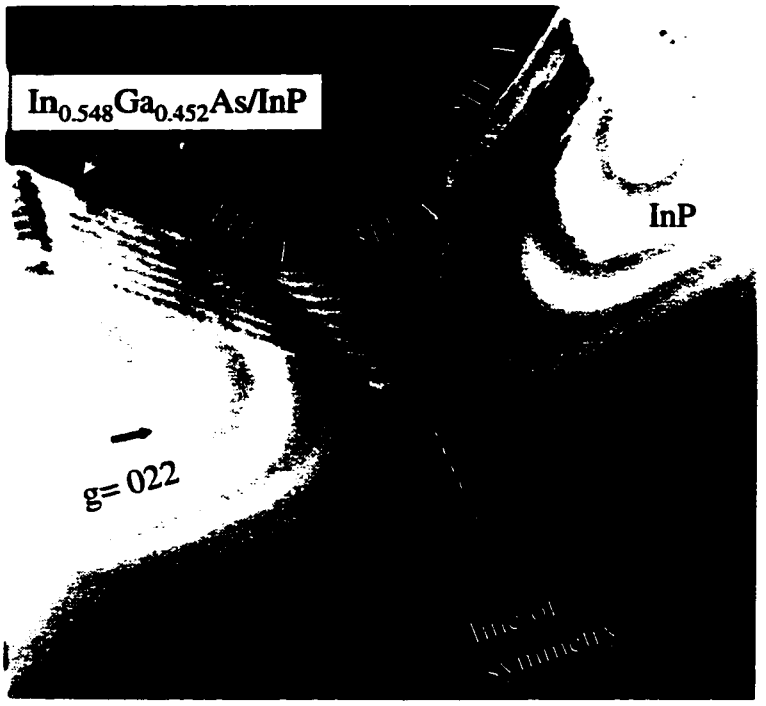

Fig. 6.4 DF TEM image of sample 489(211)A (layers in 0.103% compression) with $\vec{g}$ = 022.

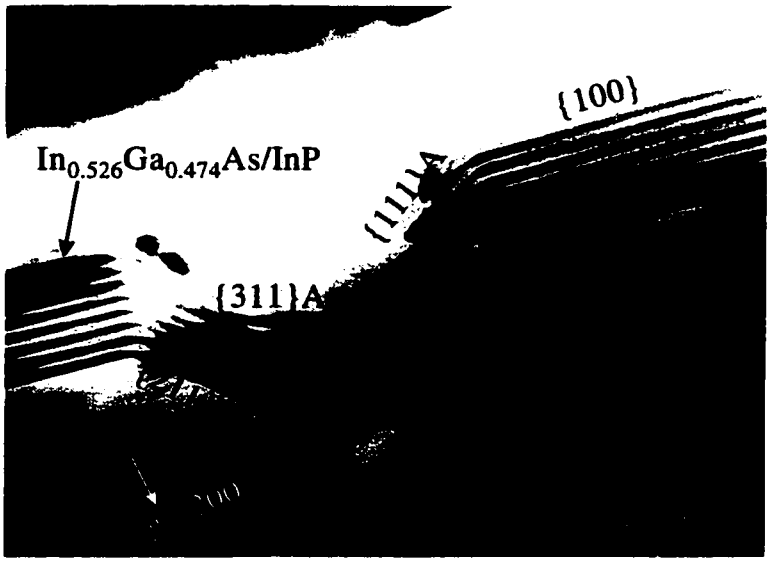

Fig. 6.5 DF TEM image of sample 488(211)A (layers in 0.048% tension) with $\vec{g} = \bar{2}\,00$. Arrows point to the stress relaxation contrast.

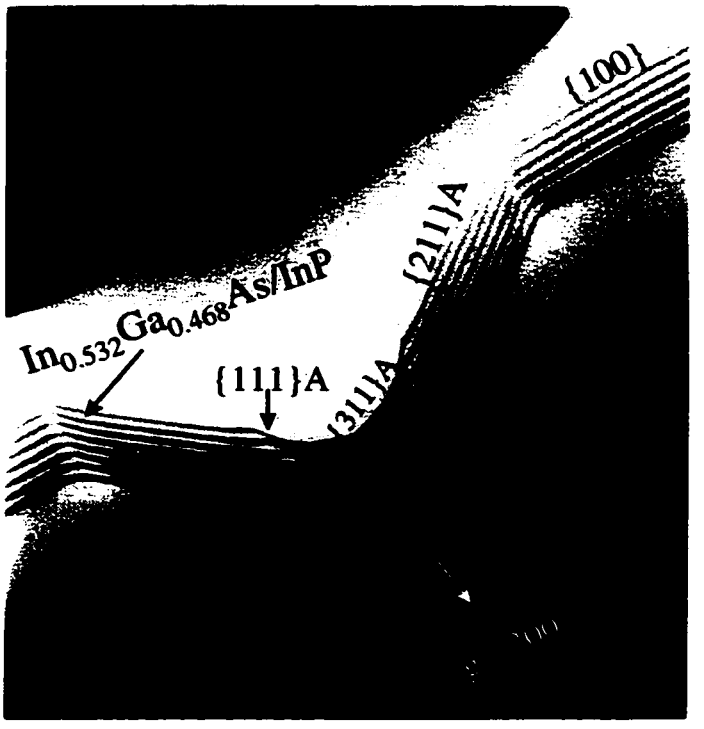

Fig. 6.6 DF TEM image of sample 560(211)A (lattice matched layers) with $\vec{g} = \bar{2}00$.

The black and white lobes present on either side of the line of no contrast, for $\vec{g}$=(022), show that the planes are bending in opposite directions along <022> direction. A line of no contrast runs along the axis of symmetry of the groove where the displacements are only in the [100] direction. This is evident from the shape of the V-grooves, where all the planes tend to relax in the direction of the free surface. Hence, the displacements of the (022) planes near the surface will occur in opposite senses on the two sides of the groove (Fig. 6.7). Contrary to this the (200) planes relax in only one direction i.e. towards [100] and hence all surface displacements in these planes detected by strain contrast occur along y direction (Fig. 6.8).

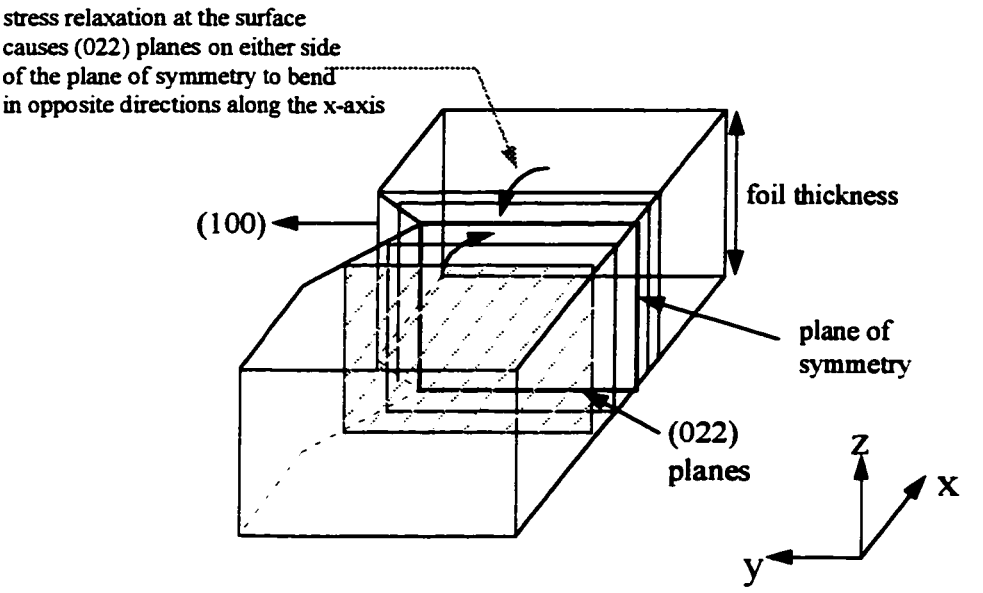

Fig. 6.7 Schematic diagram of the surface bending of the (022) planes in the x direction due to surface relaxation of built-in stresses.

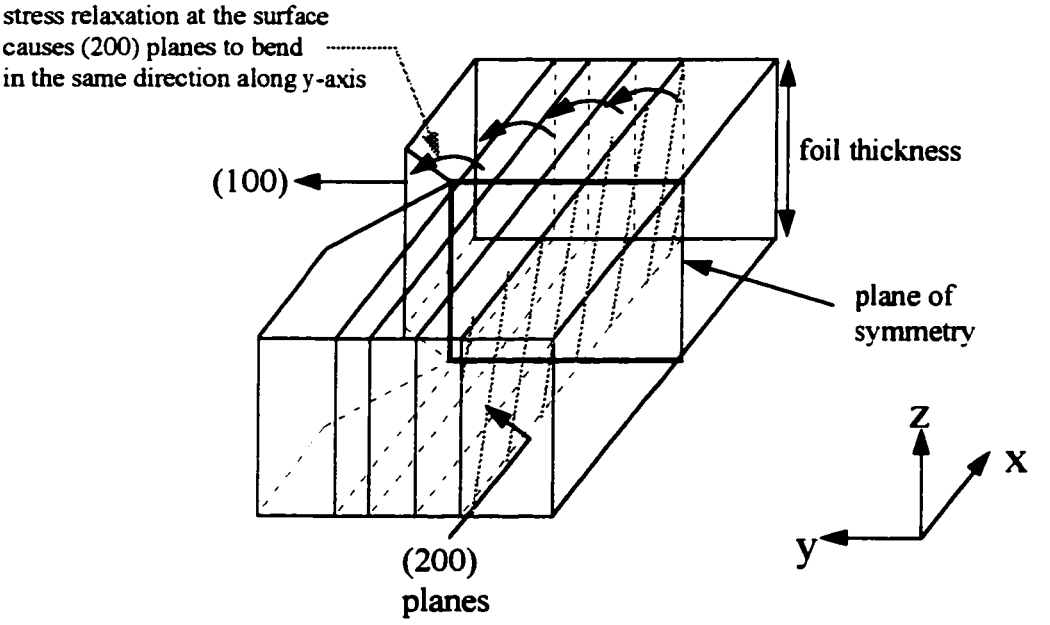

Fig. 6.8 Schematic diagram of the surface bending of (200) planes due to surface relaxation of built-in stresses.

Sample 488 (211)A was also observed under (200) two beam diffracting conditions. It also showed a strong symmetrical contrast at the bottom of the groove (Fig. 6.5). Since the layers in 488A are under 0.048% tension the contrast was opposite of that in 489A under the same diffracting conditions. A change in sign of strain from negative to positive causes the strain contrast to remain the same in the DF image of 489(211)A (Fig. 6.1b) and the DF image of 488(211)A (Fig. 6.5) when $\vec{g}$ is changed from (200) to ($\bar{2}$ 00). A smaller strain (magnitude) in the layers for sample 488(211)A causes the contrast at the bottom of the groove to be weaker compared to 489(211)A. For sample 560(211)A which consisted of lattice matched layers, no diffraction contrast was observed at any location of the V-groove (Fig. 6.6).

The contrast at the bottom of the groove with $\vec{g} = 022$ (Fig. 6.4) is similar to that observed at coherent precipitates close to the free surface of a foil (Ashby and Brown, 1963). Ashby and Brown (1963) showed that for a coherent precipitate present near the surface (within one extinction distance), there is a black and white anomalous contrast with a line of no contrast running in the centre perpendicular to the $\vec{g}$. These wide anomalous images are caused by stress relaxation at the free surface. In BF this contrast changes sign depending on whether the precipitate is close to the top or bottom surface, whereas the DF maintains the same sense of asymmetry for a precipitate present near both top and bottom surfaces. For a precipitate present close to the top surface BF and DF images show the same sense of asymmetry. The sign of the asymmetry in DF depends only on the sign of the strain and $\vec{g}$ vector.

Furthermore, Ashby and Brown (1963) showed that the sign of the misfit can be determined by examining the sense of asymmetry in a positive print of DF anomalous images. If the image is dark on the side of positive $\vec{g}$ it is an "interstitial" inclusion. If the same argument is extended to the present experiment, examining Fig. 6.4 reveals that for

the DF image with $\vec{g}$=022, the dark lobe is on the side of positive $\vec{g}$. Hence the layer lattice parameter is larger than the substrate, i.e. the layer is in compression. This is true for 489(211)A in which the layers are in 0.103% compression.

6.3 DEGREE OF POLARIZATION (DOP)

As shown in chapter 3, the DOP technique can measure the difference in stress between the lateral direction and the growth direction for cross-sectional (011) samples. The as-etched (111)B V-grooved substrate without any growth, (211)A grooves with strained layers (-0.122%) and lattice matched layers, (111)B grooves with strained layers (-0.122%) and lattice matched layers, and a (111)B as-etched V-grooved substrate under three point bending, were studied.

6.3.1 As-etched (111)B V-grooved substrate

This sample was analyzed so that any surface effects due to the geometry of the groove itself can be assessed. The DOP scan for this sample is shown in Fig. 6.9. The regions of red contrast near the (100) top surface are due to a surface effect. Apart from this surface-related contrast, there are no stresses associated with the grooves.

6.3.2 Strained layers on (211)A grooves

Fig. 6.10 shows the DOP distribution around a series of (211)A grooves. Strained layers with -0.122% lattice mismatch were grown on these grooves (sample 570(211)A). The grooves themselves are not clearly visible in the figure because of the resolution of the system. Near the bottom of each groove, there are a series of lobes in the direction of

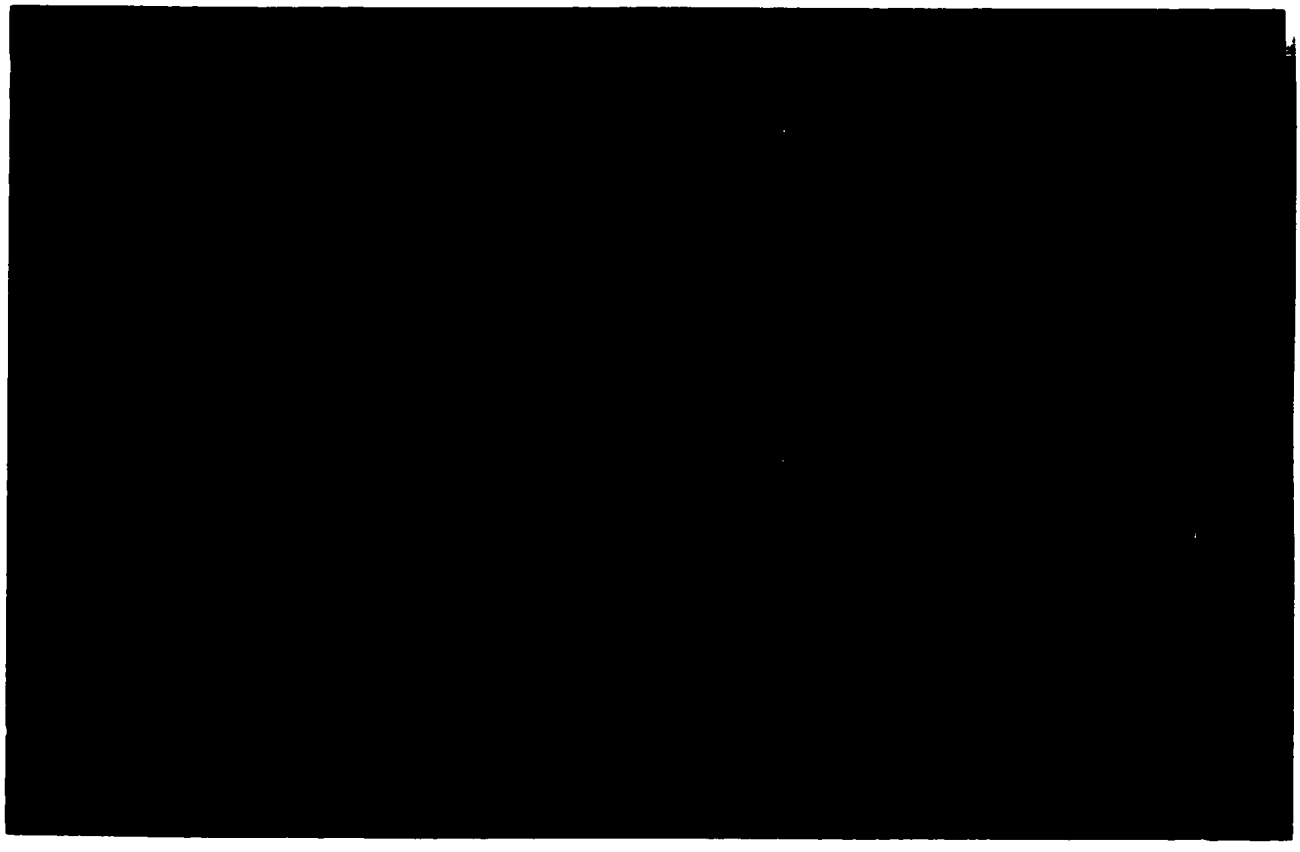

Fig. 6.9 DOP scan of an as-etched (111)B V-groove. 12X gain (+4.16% DOP for white to -4.16% DOP for black). Groove size is ~ 7μm.

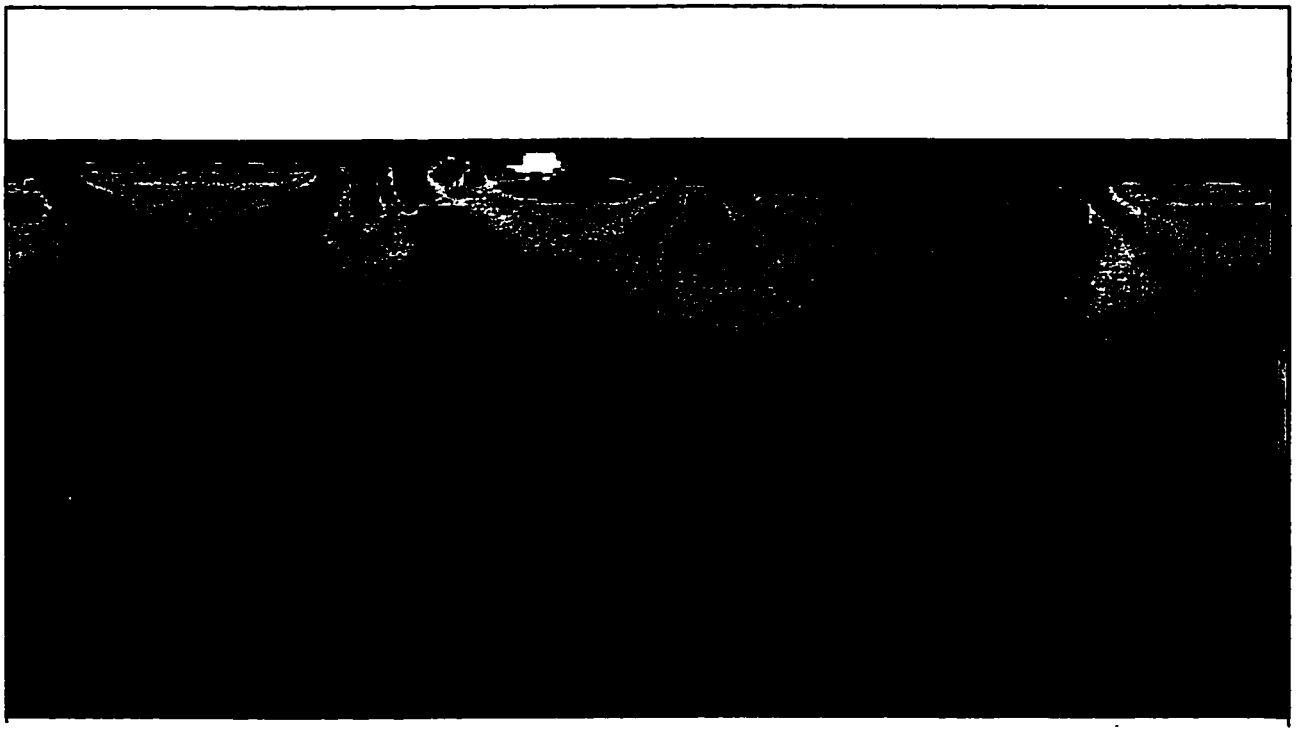

Fig. 6.10 DOP scan of sample 570(211)A containing $In_{0.55}Ga_{0.45}As$ layers in 0.122% compression. (a) showing a series of grooves. 30X gain (+1.67% DOP for white to -1.67% DOP for black). Groove size is ~ 2μm.

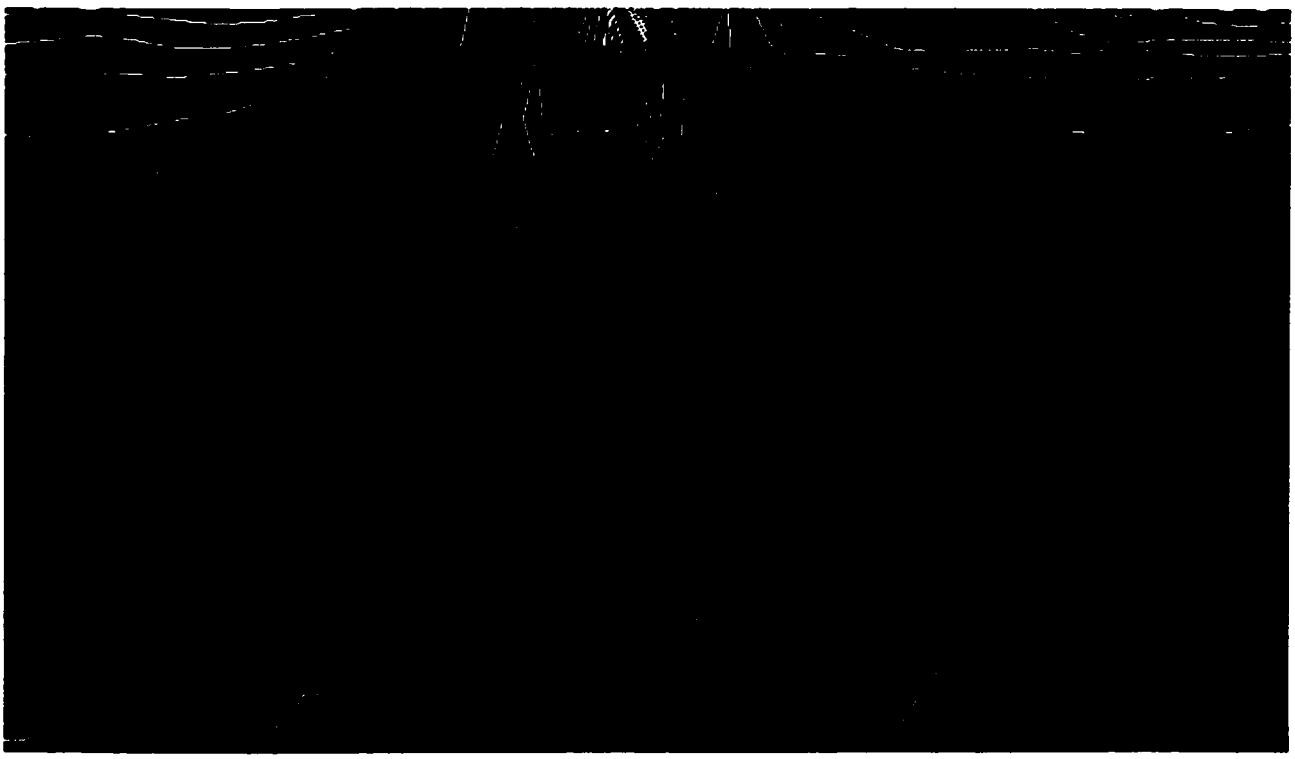

Fig. 6.10b a magnified image of a single groove showing contour lines.

the grooves. The magnitude of the DOP decreases as one moves away from the apex. On each side of the major lobes, that is on each side of the line of symmetry, there are a second set of minor lobes. Again the magnitude of DOP associated with this set of lobes decreases away from the V-groove. In between the grooves, on the (100) facets at the top surface of the sample, there are lobes spanning the length of each facet. The repeatability of the DOP pattern, from groove to groove, shows the reproducibility of these growths at each V-groove.

6.3.3 Lattice matched layers on (211)A grooves

Sample 560(211)A which consisted of eight layers of 300Å $In_{0.532}Ga_{0.468}As$ alternating with eight layers of 300Å InP. The purpose of studying this system was to confirm that no stress distribution is detected in this system because the layers were supposed to be lattice matched. As shown in Fig. 6.11, there was no significant DOP signal associated with these grooves, except (again) adjacent to the free surface.

6.3.4 Strained layers on (111)B grooves

Sample 570(111)B, which consists of layers with 0.122% compression, was studied. In Chap.4 TEM results showed that extensive defects were present at the root of the groove. The purpose of studying this sample was to investigate the effect of these defects. The DOP scan is shown in Fig. 6.12. The grooves are clearly seen here because their size is more than three times greater than that of the (211)A grooves. The DOP distribution is similar to that observed in the (211)A case. There are two sets of lobes, one below the root of the groove and the other associated with the side walls. The effect of the defects at the root of the groove does not seem very obvious.

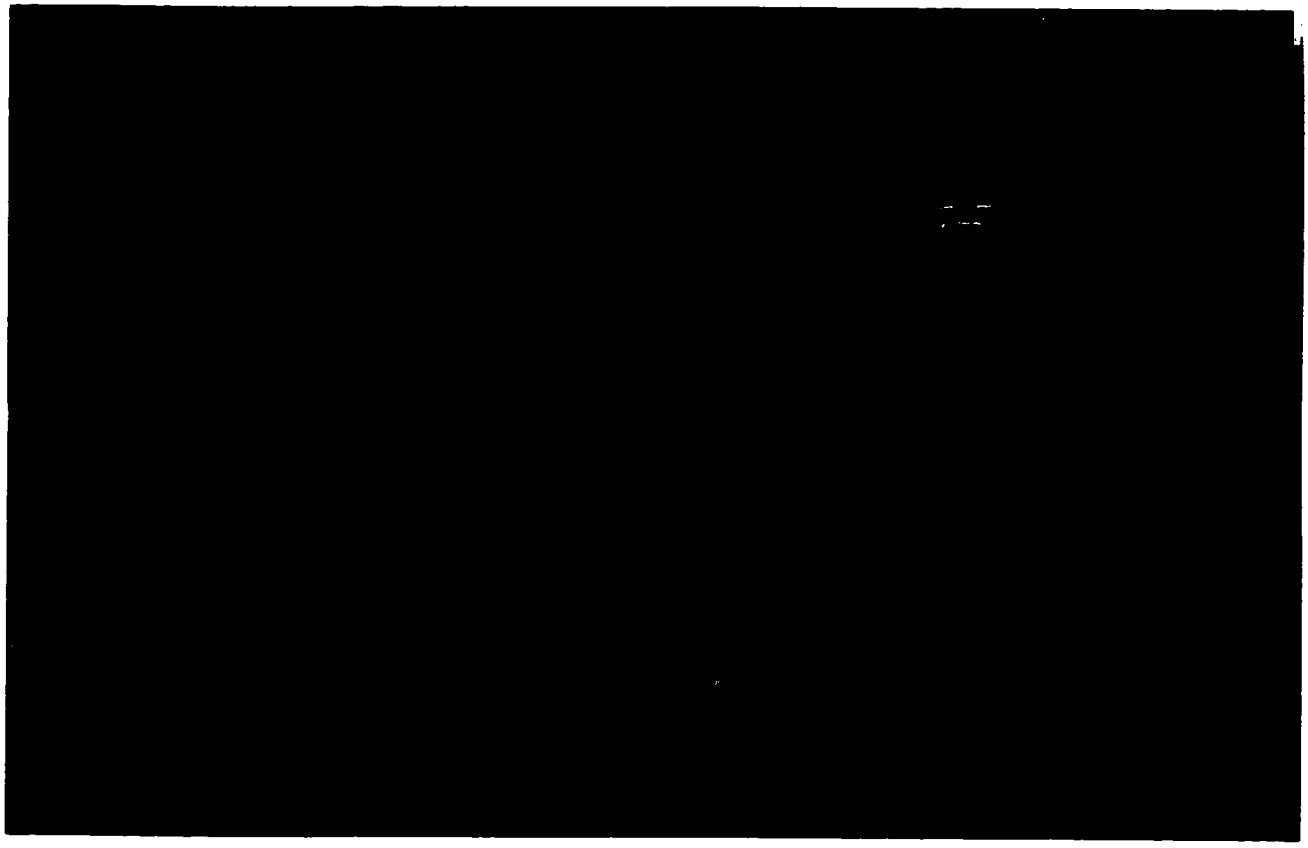

Fig. 6.11 DOP scan of sample 560(211)A containing lattice-matched $In_{0.532}Ga_{0.469}As$ layers. 30X gain (+1.67% DOP for white to -1.67% DOP for black). Groove size is ~ 2μm.

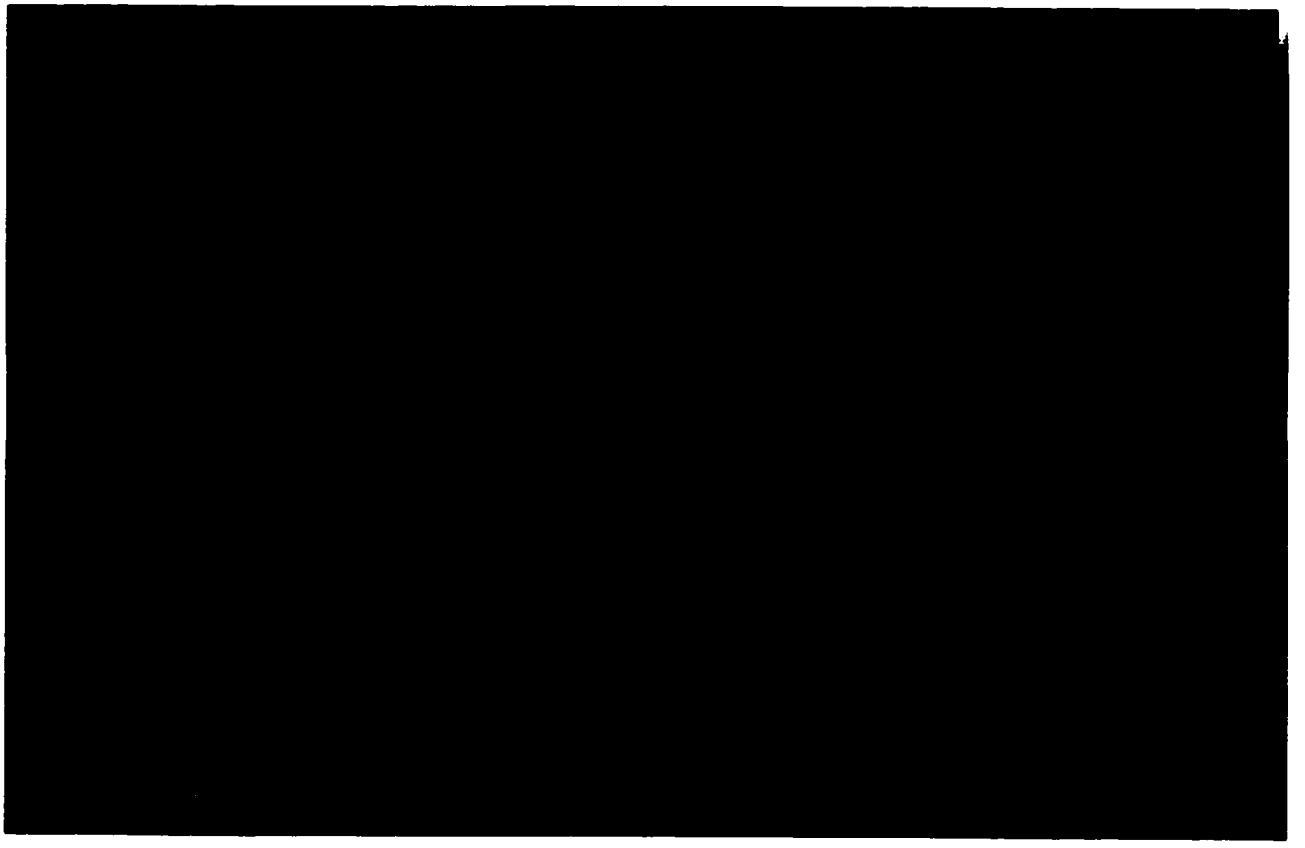

Fig. 6.12 DOP scan of sample 570(111)B containing $In_{0.55}Ga_{0.45}As$ layers in 0.122% compression. (a) Showing a series of grooves. 12X Gain (+4.16% DOP for white to -4.16% DOP for black). Groove size is ~ 7μm.

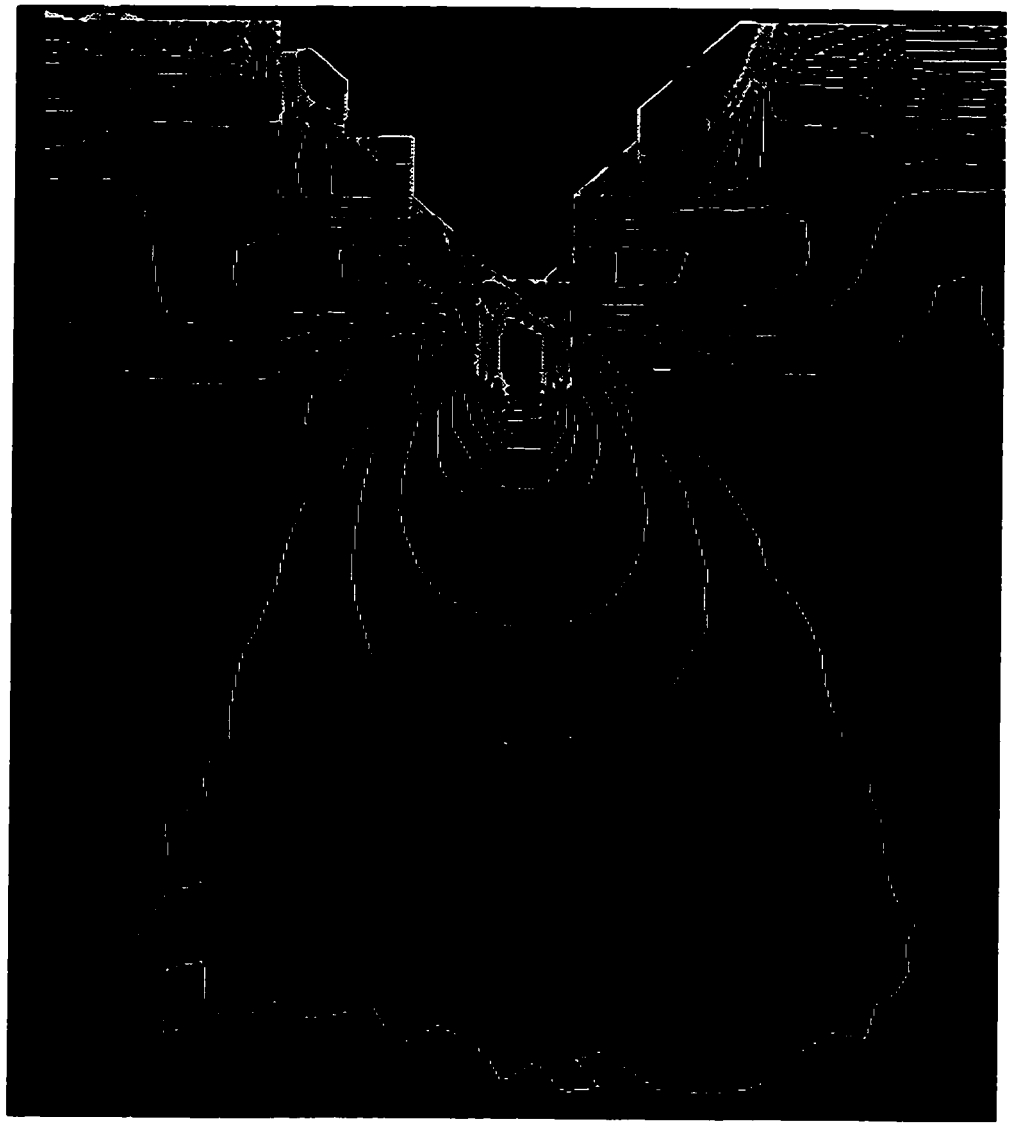

Fig. 6.12b a magnified image of a single groove showing contour lines.

6.3.5 Lattice matched layers on (111)B grooves

As seen in Chap.4, irrespective of the composition of the layers, the growths in (111)B had defect concentration at the root of the groove and some portion of the (111)B sidewall. This was true even for lattice-matched growth. In Chap.5, composition analysis showed that there was a large variation in composition along the groove. This variation in composition seems to be the most probable cause of these defects in lattice-matched growth.

Sample 560(111)B, which consisted of lattice matched layers, was studied using DOP. The purpose of this study was to investigate whether composition changes do produce a stress pattern in a growth which was nominally stress-free. As shown in Fig. 6.13 a prominent stress pattern was displayed by the DOP scan. Qualitatively the stress pattern did not differ from that of sample 570(111)B (Fig. 6.12).

6.3.6 As-etched (111)B grooves with 3-point bending

It is common knowledge that when a misfitting layer is grown on a substrate, it can lead to a pronounced bending of the wafer. This is most marked when the substrate thickness is not very different from the layer thickness, but occurs for all combinations of layer and substrate thickness. A bending test was done on an as-etched groove to ensure that the stress distribution obtained for layers grown on V-grooves was not simply due to the bending of the wafer.

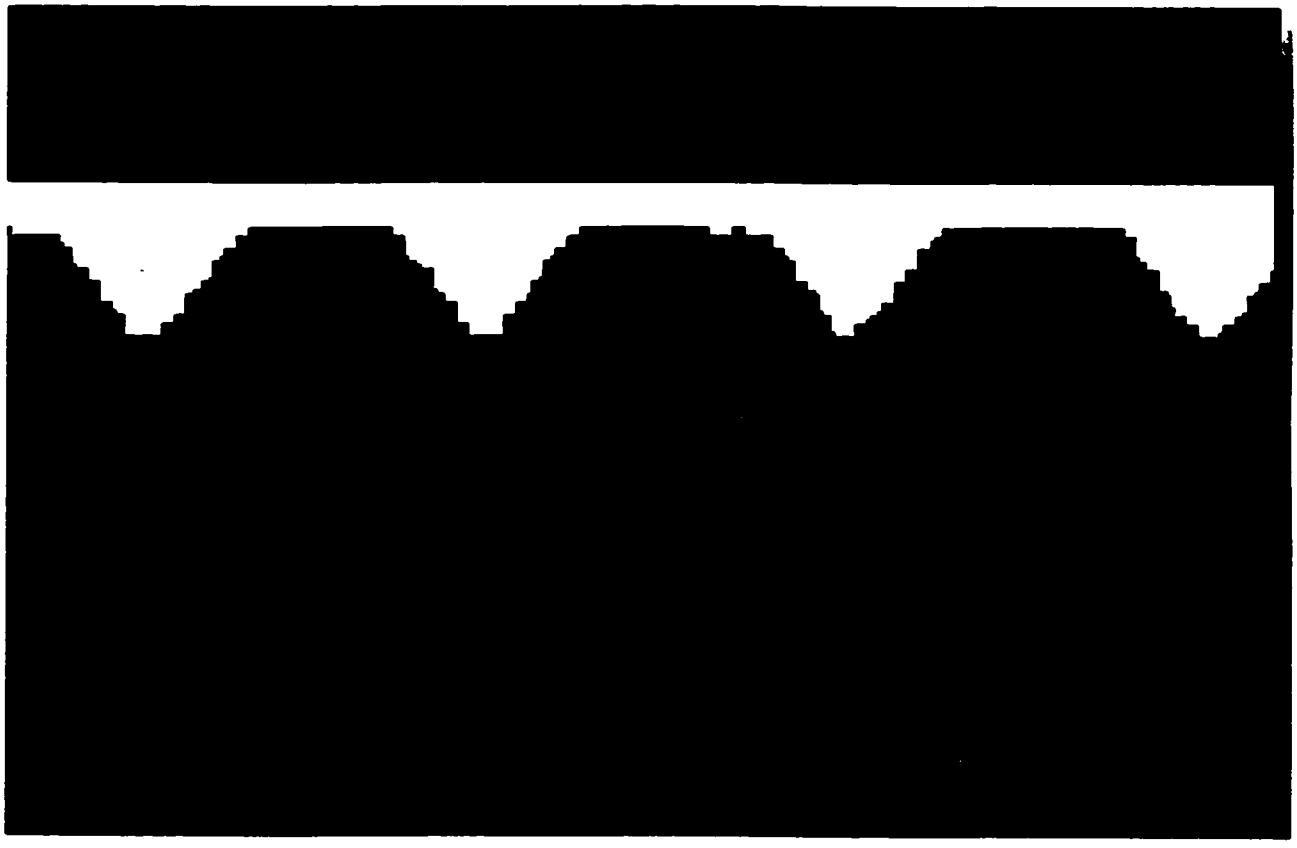

Fig. 6.13 DOP scan of sample 560(111)B containing lattice-matched $In_{0.532}Ga_{0.468}As$ layers. 12X Gain (+4.16% DOP for white to -4.16% DOP for black). Groove size is ~ 7μm.

The three-point bend test that was conducted on the wafer is shown schematically in Fig. 6.14. The bend test was performed for two different orientations of the wafer. In one case the V-groove was in tension (shown in Fig. 6.14) and in the other case the wafer was kept inverted such that the V-groove was in compression. The DOP images for these two cases are shown in Fig. 6.15. Fig 6.15(a) corresponds to the case where the V-groove is in tension while Fig 6.15(b) corresponds to the V-groove under compression. The sign of the DOP distribution changes from (a) to (b), as expected. These DOP patterns do not correspond in any way to the distribution seen for misfit layers grown on V-grooves.

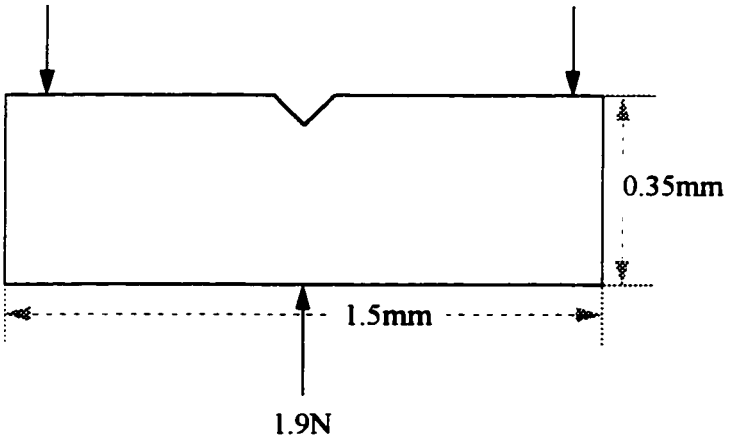

Fig. 6.14 Schematic diagram showing the three point bending test used in DOP experiment (grooves in tension).

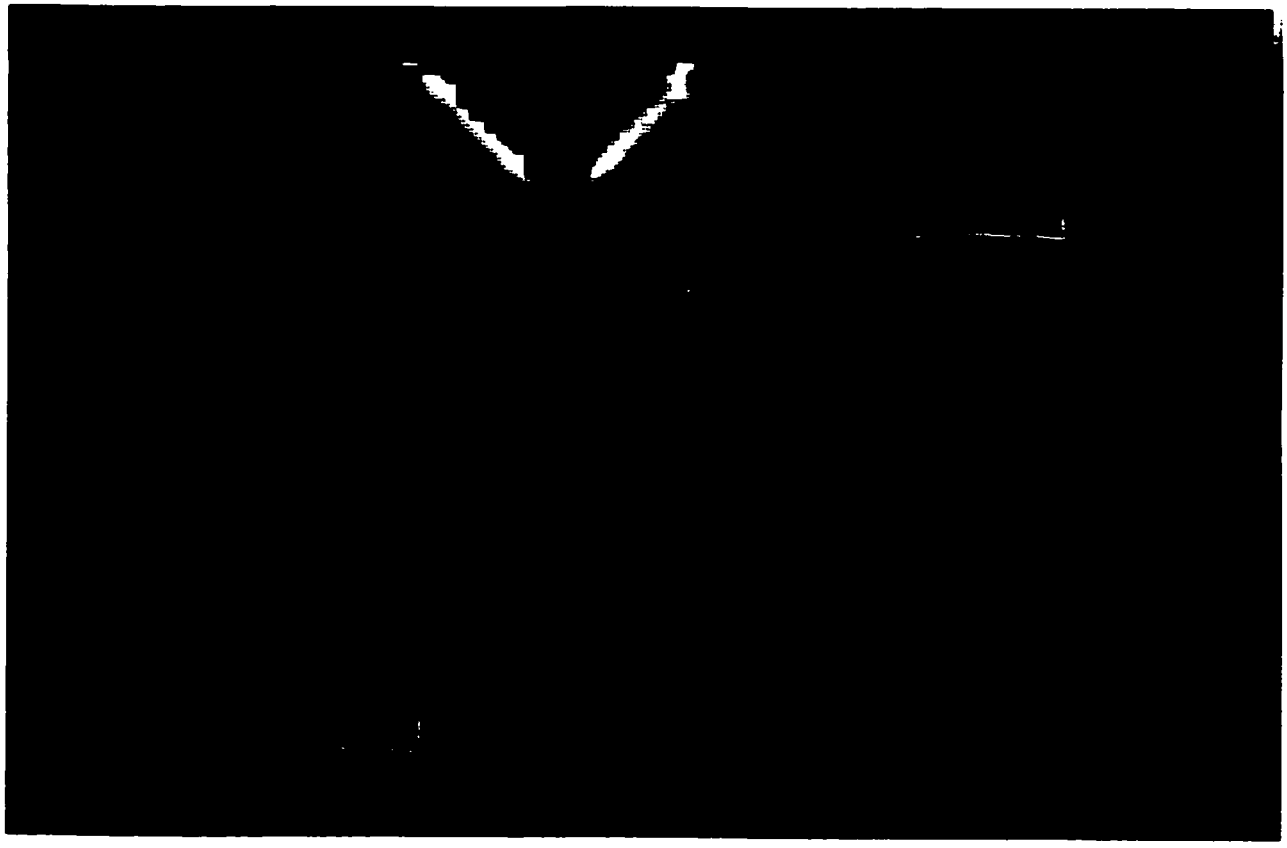

Fig. 6.15 DOP scan of the as-etched (111)B grooves under three point bending load. (a) a single V-groove in tension. 12X Gain (+4.16% DOP for white to -4.16% DOP for black). Groove size is ~ 7μm.

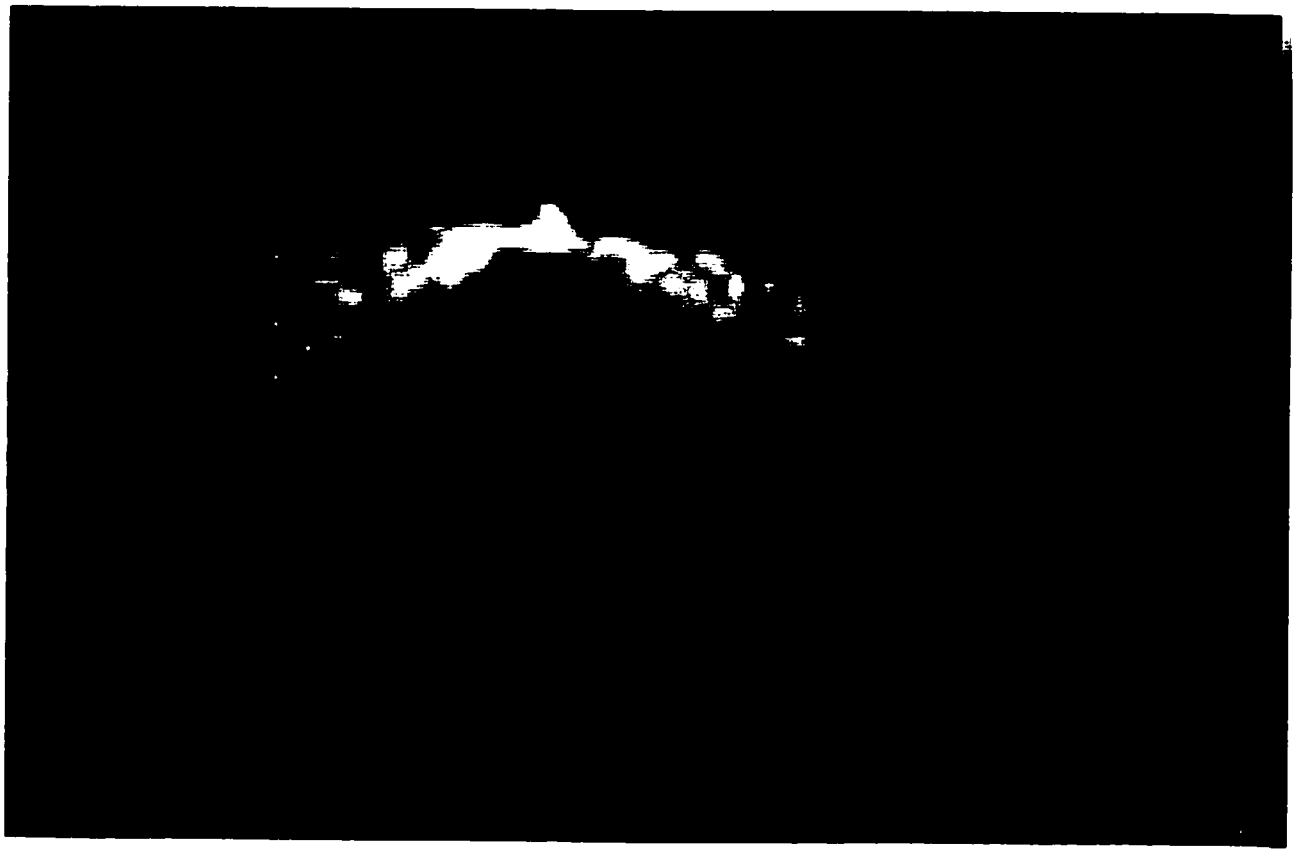

Fig. 6.15b a single V-groove in compression. 12X Gain (+4.16% DOP for white to -4.16% DOP for black). Groove size is ~ 7μm.

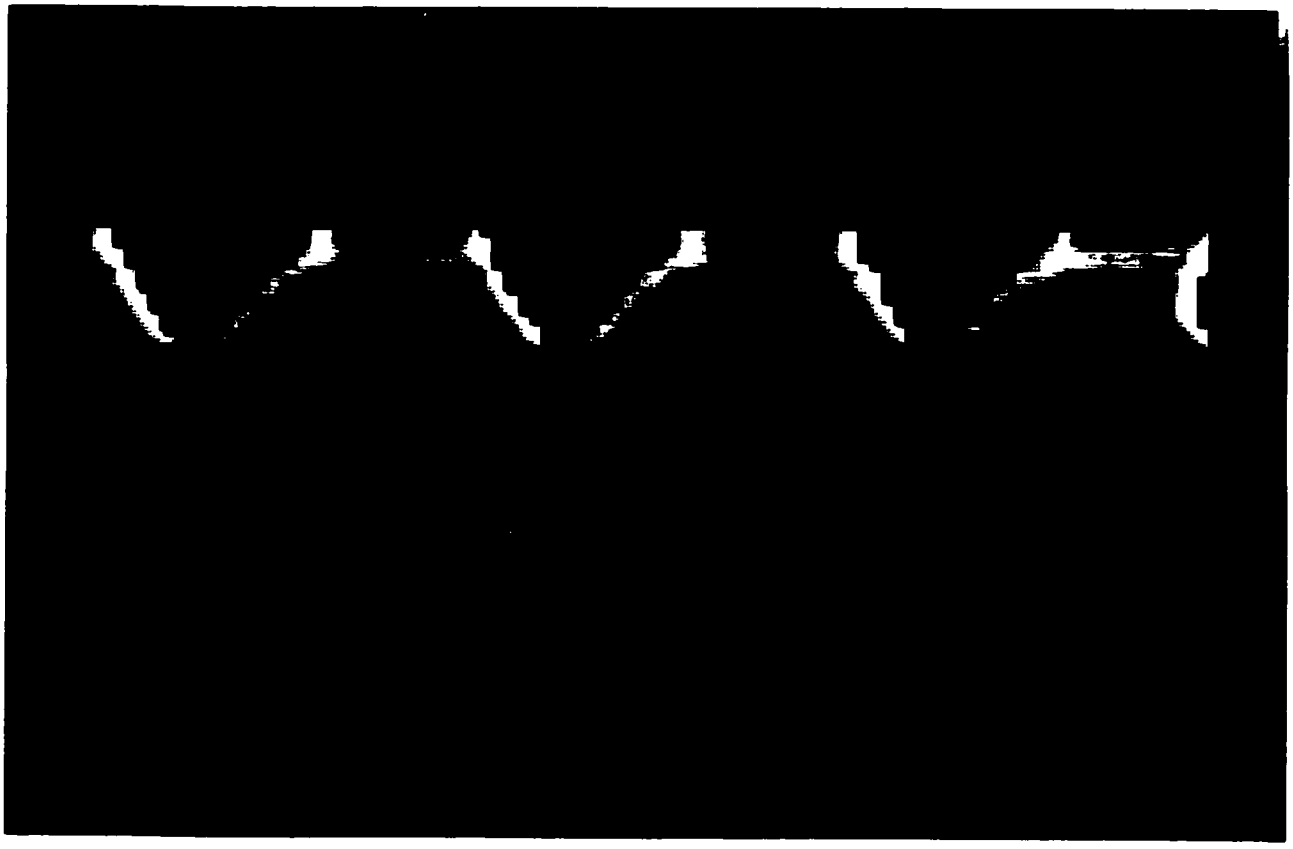

Fig. 6.15c a series of V-grooves in tension. 12X Gain (+4.16% DOP for white to -4.16% DOP for black). Groove size is ~ 7μm.

6.3.7 Discussion

In all the samples studied, the DOP patterns from strained layers grown on V-grooves are a result of misfit strain and do not arise from a simple macroscopic bending of the wafer. The experiments done with an unstressed V-grooved InP sample and the V-grooved InP sample under three point bending provide confirmation for this conclusion. Whereas the pure V-groove did not show any DOP, the groove under the 3 point bending test showed a DOP pattern that was quite different from the groove overgrown by strained layers.

Qualitatively, the strained layers grown on the (211)A groove showed a similar DOP to layers grown on (111)B. For (211)A grooves, the grooves were not clearly seen due to the resolution of the system, but the (111)B grooves were visible and displayed stress information along the length of the groove. However, in chapter 4, we saw that whereas the (111)B sample was full of defects for all heteroepitaxial growths (strained or lattice-matched), (211)A was defect free. Even in lattice matched growth on (111)B grooves (sample 560(111)B), the composition variation resulted in a stress concentration at the bottom of the groove, which produced defects. If the quantum wire at the root of the groove has a strain of ε, then if ε exceeds the critical limit the structure may relax by forming dislocations. In the (111)B V-groove if we assume that the strain relaxation occurs via 60° dislocations with a {111} glide plane and <110>/2 burger's vector ($\vec{b}$) (Freund and Gosling, 1993), then the magnitude of $\vec{b}$ for InP would be 4.15Å. In a simple analysis, the amount of strain relaxed plastically ε_p, can be expressed as $\varepsilon_p = b/d$, where d is the dislocation spacing. For the case of growth on (111)B grooves d was estimated to be 500Å, hence $\varepsilon_p = 0.0083$. In chap.5 for sample 570(111)B the strain in the quantum wire region was calculated to be ~ 0.013. Thus approximately 50% of the strain in this location is relaxed by defect formation. Hence the DOP from layers grown on

(111)B is due to the residual strain associated with the mismatched regions at the bottom and sidewalls, part of which has been relaxed by dislocations.

6.4 MODEL OF STRESS DISTRIBUTION IN V-GROOVES

To explain the experimental results, a model for the stress distribution in a V-groove has been developed. Such a model can be formulated by an extension of the planar model. For the layers grown on a V-groove the stress distribution is schematically illustrated in Fig. 6.16. As is obvious in the figure the in-plane stresses cancel out everywhere except at the corners. The resultant stress imbalance at these corners should give rise to a prominent strain distribution in the substrate at these locations.

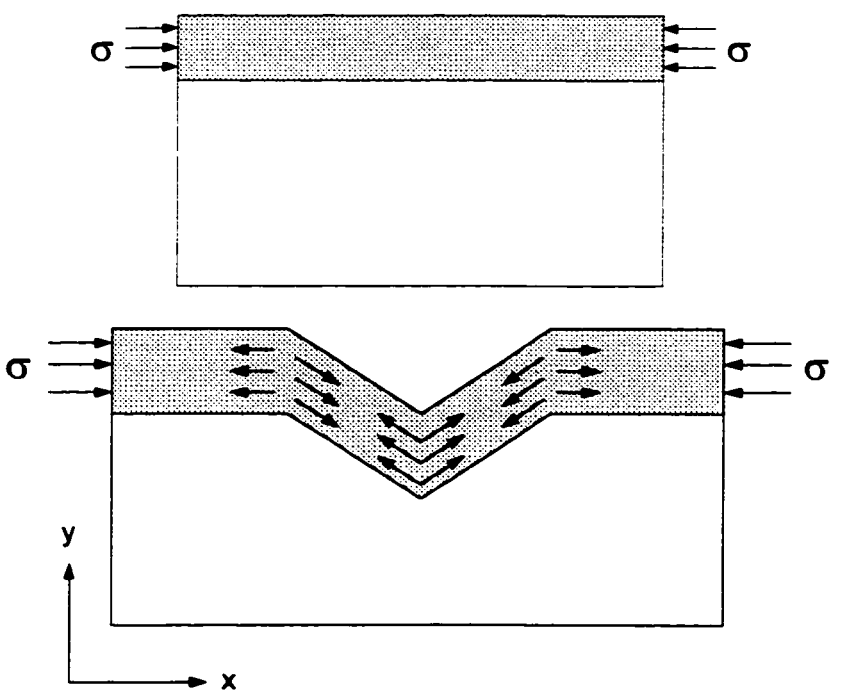

Fig. 6.16 Schematic diagram showing the models of strained layers (a) in the case of growth on planar substrates (b) extension of the planar model to growths on V-grooves.

6.5 ANALYTICAL SOLUTION

To solve the above model use was made of potential theory. If we assume that instead of the layer we have a uniform unit charge distribution, while the substrate is the space surrounding the charge distribution, standard potential theory can be employed to solve the elasticity problem. The relation between strains and potential has been derived for this situation by Eshelby (1957). The solution for the stress field for the geometry of the strained layer has been worked out in Appendix A.

The problem for a 2D case has been solved, assuming that the groove extends infinitely in the third dimension. The other assumptions made in solving the problem were:

- the groove on the substrate had a sharp V shape (faceting was ignored).
- the thickness and composition of the deposited layer were uniform all along the groove.
- the interface between the layer and substrate was sharp.
- the layer was embedded in an infinite substrate.
- the stresses in the substrate in the x and y direction were equal and opposite. This is a direct consequence of the fact that in the substrate the Laplacian $\nabla^2\varphi = 0$, where φ is the potential. Since $\sigma_{ii} \propto \frac{\partial^2\varphi}{\partial x_i^2}$, then $\sigma_{xx} = -\sigma_{yy}$. ($\sigma_{zz} = 0$ because the groove is assumed to extend infinitely in the z-direction).
- grooves were isolated enough so as not to influence each other.
- the deposited layer and the substrate were elastically isotropic, with the same elastic constants (those corresponding to InP were assumed, $\nu = 0.28$, $E = 1.0E+12$ dyne/cm^2).

With these assumptions, the two dimensional case (assuming the groove extends infinitely in the z-direction) has been solved using the Newtonian potential method. Using the solution given in appendix A the σ_{xx} contours are plotted in Fig. 6.17 and Fig. 6.18. Fig. 6.17 corresponds to a hypothetical case, assuming a unit charge distribution all along the groove, to illustrate the effect of geometry on the stress distribution in the groove.

The figure shows a variable stress pattern all along the groove. This pattern closely matches the DOP distribution for the case of strained layers grown on a (111)B groove (Fig. 6.12b). The (111)B groove was large enough to be seen clearly in the DOP scan and hence the stress distribution could be detected at each point of the groove. This made it possible to test the qualitative accuracy of the theoretical model. The parameters used in Fig. 6.18 correspond to the sample 570(211)A in which the layers were in 0.122 % compression with respect to the substrate. The groove angle was 109°, the groove depth was 2μm and there were 8 layers of 300Å $In_{0.55}Ga_{0.45}As$ alternating with 8 layers of 300Å InP. In the model these multilayers were simulated as a single layer with the ratio of the thickness of the layer to groove size being 0.24 and an average resultant strain of -0.061% with respect to the substrate. The stress contours in this case are confined to the bottom of the V-groove and at the V-groove-top surface intersection points. Since the angle is wider at the top corner, the concentration of stress is less compared to that at the bottom. These contours correspond well with those obtained from DOP of sample 570(211)A (Fig. 6.10b). There is one major difference between Fig. 6.17 and Fig. 6.18; the contours on the sides of the groove are missing in the case depicted in Fig. 6.18. Unfortunately this feature cannot be directly compared with the (211)A DOP results, as the groove itself does not show up in the DOP.

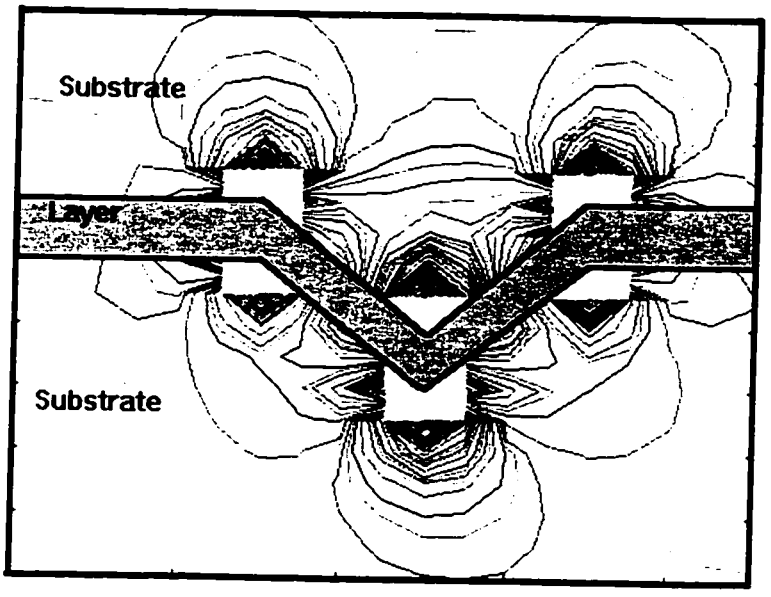

Fig. 6.17 Stress distribution using analytical solution for a hypothetical case.

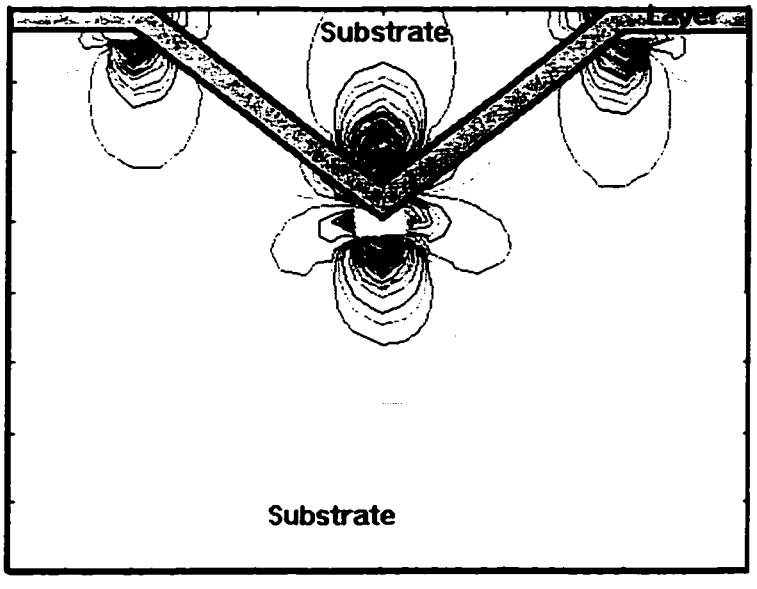

Fig. 6.18 Stress distribution using analytical solution with parameters similar to that in sample 570(211)A.

6.6 FINITE ELEMENT METHOD (FEM)

The analytical solution assumes that the strained layers are embedded in an infinite matrix. To account for the free surface of the V-groove and to get a three dimensional stress and strain distribution a finite element analysis is necessary. By doing this analysis we can compare the bulk case (with no surface relaxation) with the thin film case (surface relaxation). The sample used in the DOP experiments had a thickness of ~0.35mm in the z direction, and will be considered to be representative of the bulk stress distribution. However the TEM sample thickness is around 1000Å, much less than the groove dimensions, hence the relaxation of stresses at the free surfaces need to be taken into account. The details of the boundary conditions used in representing the two cases are given in Appendix B. In this section the results obtained on applying two different sets of boundary conditions are presented. The assumptions made in using this method were:

- a continuum body can be represented as a set of discrete elements.
- the layer and the substrate were isotropic with the same elastic constants (those of InP with ν= 0.28, and E= 1.0E+12 dyne/cm^2).
- the geometry of the groove corresponded to a single sharp V.
- the layers were uniform in thickness and composition.
- the interface between the layer and the substrate was sharp.
- grooves were isolated enough so as not to influence each other.

Fig.6.19 shows the σ_{xx} and σ_{yy} distribution obtained by applying bulk boundary conditions. The parameters used in the solution were the same as those chosen for sample 570(211)A. A single layer with a misfit strain of -0.061% and a thickness to groove size ratio of 0.28 was used. The thickness in the z direction was approximately the same as the

groove size. For simulating the DOP case the xy surfaces perpendicular to the z axis were constrained, whereas for simulating the TEM sample these surfaces were relaxed.

In the bulk case the magnitude of σ_{xx}-σ_{yy} obtained by FEM was compared with the DOP values. In the thin film case the x and y displacements of the nodes in the z direction were plotted at different points in the vicinity of the bottom of the groove to show if there was any surface relaxation. Fig. 6.20 shows some of these plots. Nodes close to the groove but away from the line of symmetry show surface relaxation in both the x and y directions (Fig. 6.20a). This is evident from the large displacement values at both the top and bottom surface nodes. The displacement in the x and y directions changes with depth, with a maximum magnitude in both cases occurring at the surfaces. At nodes on the line of symmetry there is no change in displacement along the z axis in the x direction, but there is a surface relaxation in the y direction (Fig. 6.20b). If the displacement values in the x and y directions are plotted along the nodes at the xy surface plane it shows that the maximum displacement value at the surface decreases away from the root of the groove (Fig. 6.20c and d). This is in agreement with the stress plots for the bulk case where the stress magnitude decreases away from the groove.

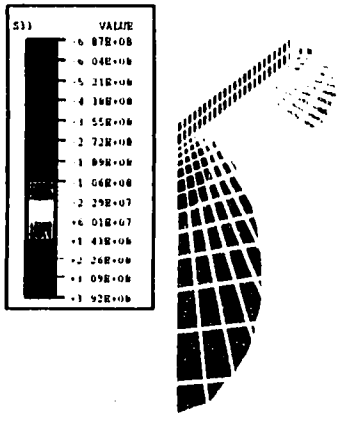

(a)

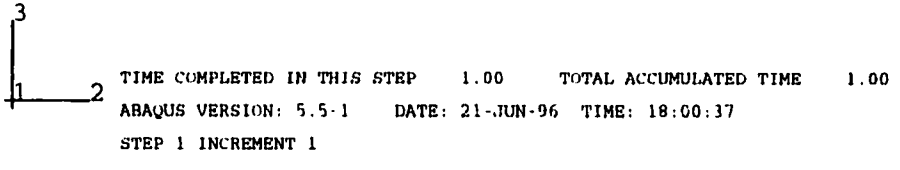

Fig. 6.19 Stress distribution using FEM (under bulk boundary conditions, BC I) (a) σ_{xx} (b) σ_{yy} .

ABAQUS

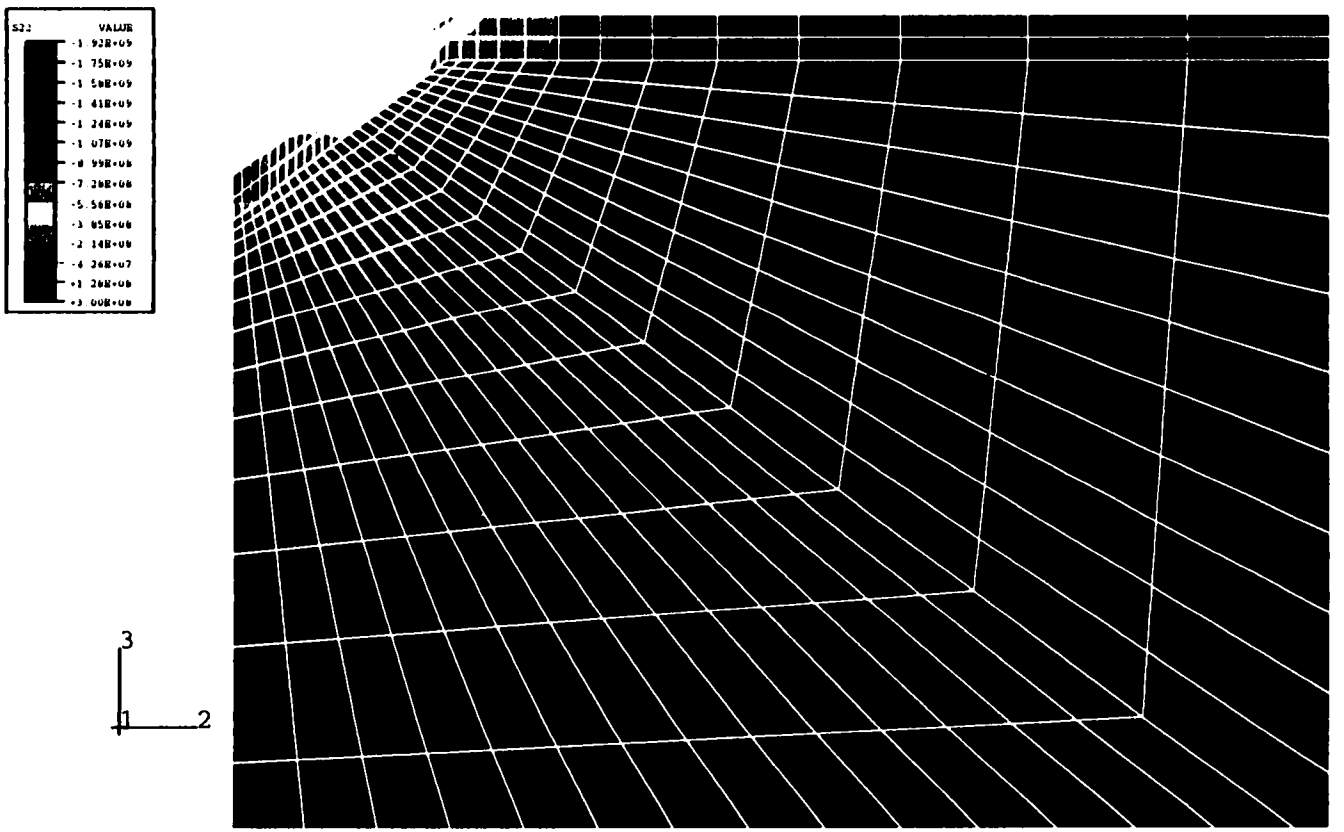

(b)

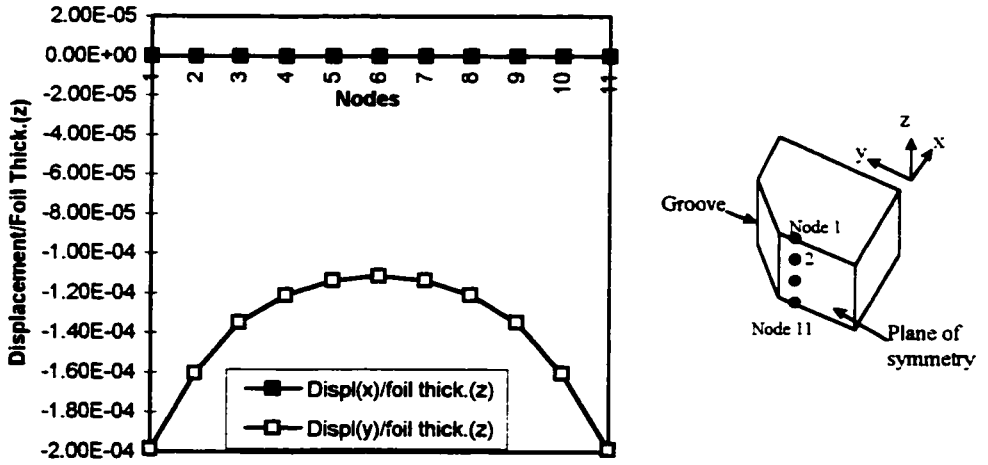

Fig. 6.20 Displacements of the nodes in the x and y direction as a function of depth in the z direction under thin film boundary conditions (a) At a node along the axis of symmetry

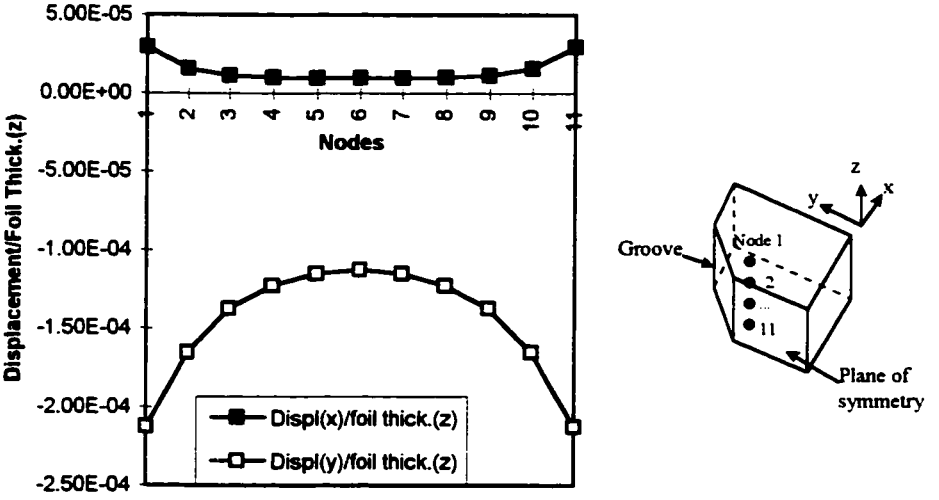

(b) on one side of the axis of symmetry.

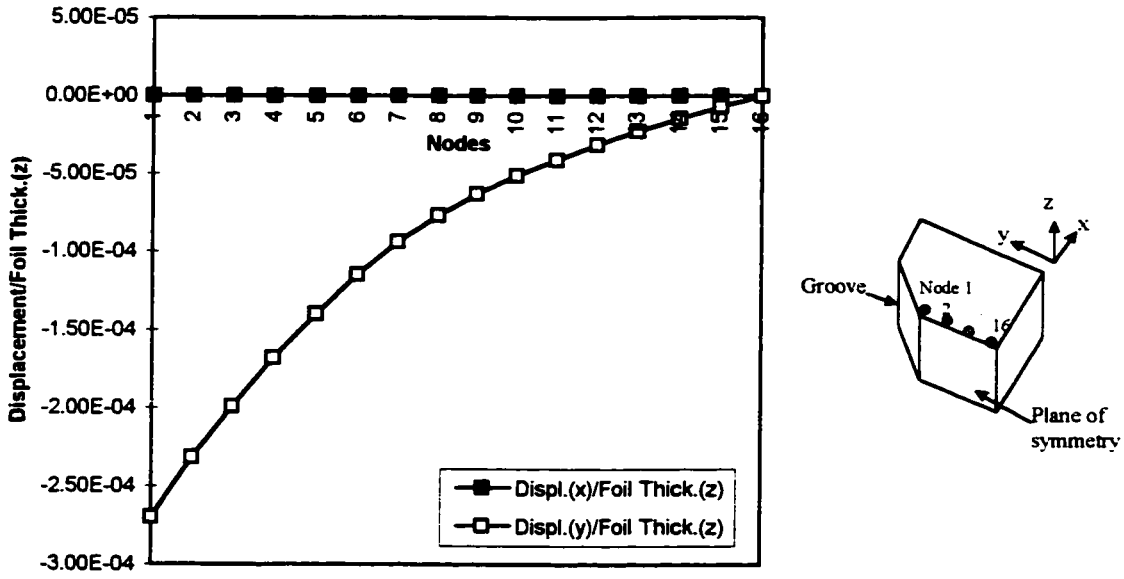

(c) Surface displacement in the x and y direction on the xy plane along the axis of symmetry away from the groove.

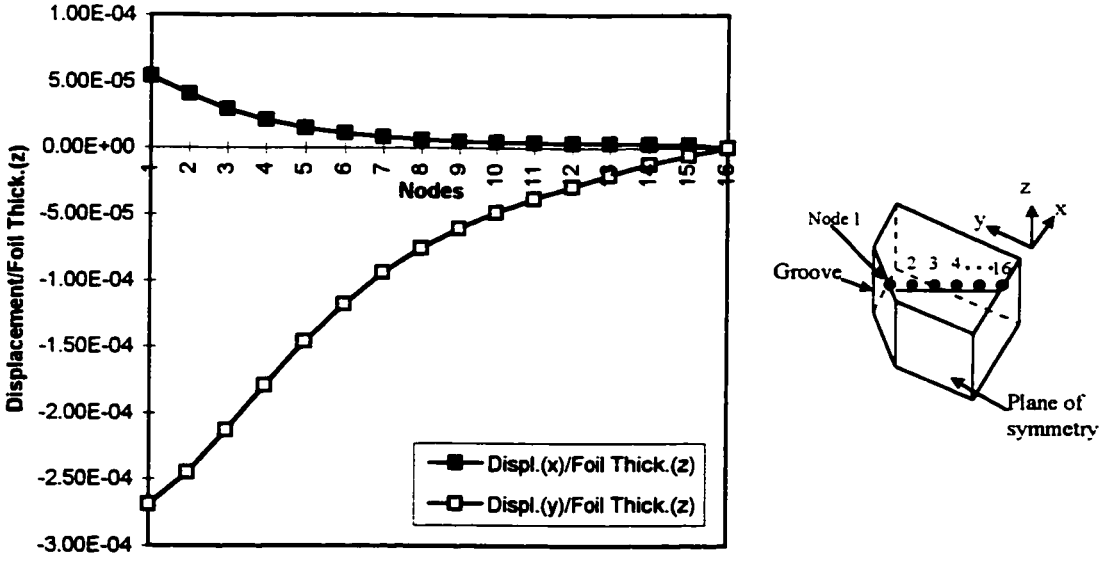

(d) Surface displacement in the x and y direction on the xy plane, along nodes on one side of the axis of symmetry, away from the groove.

6.7 DISCUSSION

Both solutions, analytical and numerical, simulate a growth which is defect-free. Hence we will compare these results only with layers grown on (211)A grooves. One further assumption made in the analysis was that the layers were uniform in thickness and composition. (211)A comes close to meeting this requirement: it has a small variation in thickness (maximum variation of 50%) and negligible variation in composition. However, growths on (211)A were faceted; this was not taken into account. We assumed a sharp groove in our simulations. This is true in the experimental case for the first layer/substrate interface. (311)A facets only start appearing after a certain critical thickness has been deposited on the (211)A V-groove.

Keeping these assumptions in mind, a comparison between the DOP contours obtained for sample 570(211)A (Fig. 6.12b) with the analytical solution (Fig. 6.18) and the FEM solution (Fig. 6.19), showed a good qualitative match in both cases. In ABAQUS it was not possible to plot the contours of the difference in stresses, hence they have been plotted separately. The σ_{xx} plots showed a side lobe whereas σ_{yy} showed the bottom lobe; hence it can be inferred that on subtracting the two, both sets of lobes would appear. One set of lobes (in the direction of the growth) should be observed at the bottom of the grooves, with two sets of side lobes. As noted earlier, however the side lobes were not seen by DOP for (211)A V-grooved samples because of the resolution of the DOP system, which averages over an area with a diameter of about a micron.

To compare the three results quantitatively, σ_{xx}-σ_{yy} was calculated as a function of the ratio of the distance from the root of the groove along the y-axis and the groove size (y/d). As shown in Fig. 6.21 the FEM and DOP results were in good agreement despite the assumptions made in the FEM analysis and the limited resolution of the DOP system. Since the resolution of the DOP system is 1 micron only the values beyond a distance to

groove size ratio of 0.5 should be considered (Fig. 6.21b). These values show an excellent match which suggests that the DOP gives an exact measure of the stress distribution, provided they are not measured too close to the bottom of the groove (within 1-2μm). The σ_{xx}-σ_{yy} values predicted by the analytical solution (Fig. 6.22) were an order of magnitude higher than the DOP and FEM values. It is thought that the main reason for this discrepancy was the boundary conditions used in the analytical solution. One of the assumptions made in arriving at the analytical solution was that the layer was embedded in an infinite substrate, i.e. the layers were not allowed to relax in the growth direction. However in the experimental situation the layers are free to relax in the growth direction (see Fig. B4 and B5 in Appendix B). This allows some of the misfit energy to relax. Since in the analytical case the layers are restrained in all three directions, the magnitude of misfit stresses which develops in the layer is quite large. The only way to compare the analytical results with an experiment would be to grow a thin layer on a V-groove and cover it with a thick capping layer.

(a)

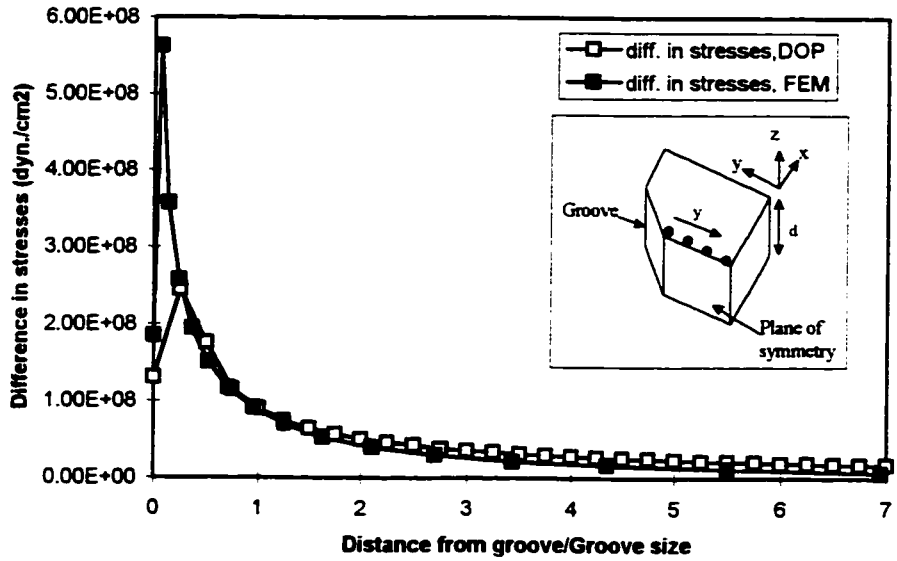

(b)

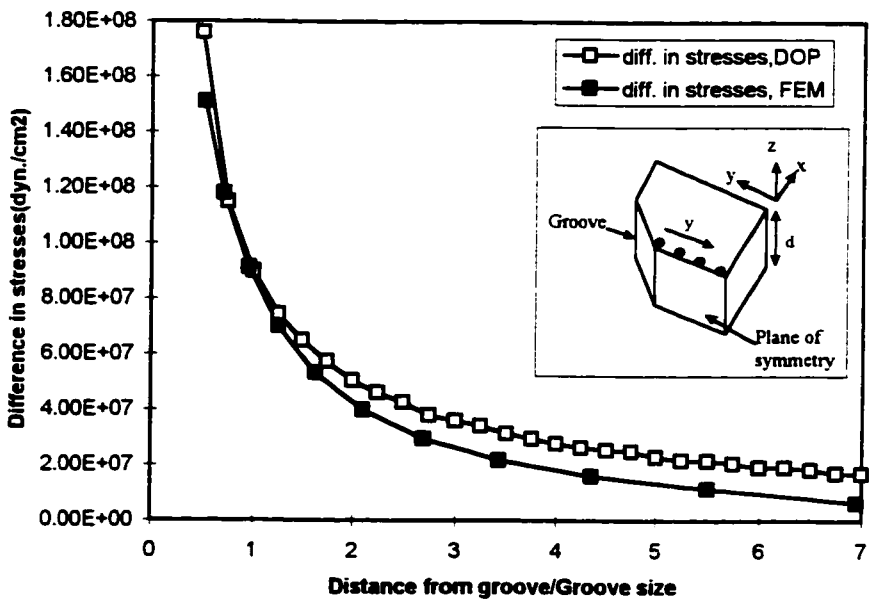

Fig. 6.21 A comparison of the FEM results with DOP results for sample 570(211)A of $(\sigma_{xx}-\sigma_{yy})$ vs (y/d) (a) Starting from the interface along the axis of symmetry. (b) Starting from a distance of 1 μm from the interface along the axis of symmetry.

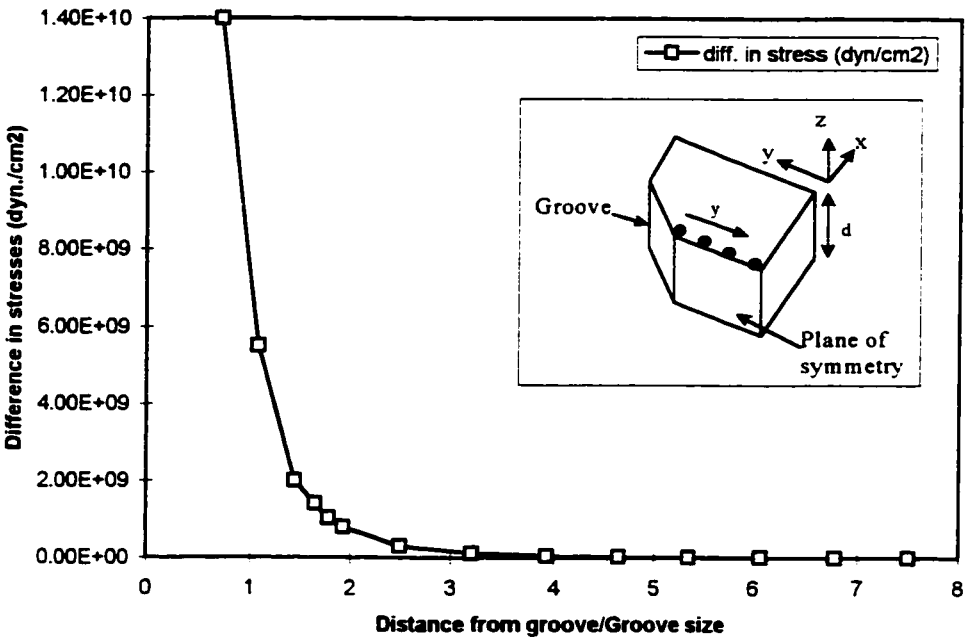

Fig. 6.22 Plot of σ_{xx}-σ_{yy}= $2\sigma_{xx}$ vs (y/d) along the axis of symmetry for the analytical results.

To compare the TEM contrast, the displacements at the surfaces perpendicular to the x-axis, in the y and z direction, must be compared. For this purpose a three dimensional solution is needed and hence only the FEM results can be used. The displacements in the y and x direction are shown schematically in Fig. 6.23b and c. This displacement varies.with depth z, with maximum values at the free surfaces. Qualitatively the sense of the displacements measured in the simulations are in full agreement with the diffraction contrast experiments described in section 6.2. The plane bending, in the y direction (Fig.6.23b) at the free surfaces, causes the anomalous absorption contrast seen with $\vec{g}$=200 (Fig. 6.1). Since the bending is in one direction the contrast is of same color for the given diffracting condition. FEM predicted the surface relaxation behavior quite accurately for B.C.II (Appendix B). In Fig. 6.20 the displacement in the x and y direction are plotted for two cases: in one the nodes are on the plane of symmetry (Fig. 6.20a) while in the other the nodes are away from the plane of symmetry (Fig. 6.20b). The displacements in the y-direction varies along the z-direction in both Fig. 6.20a and b. The magnitude of displacements is maximum at the xy free surfaces. This exactly corresponds to the schematic depicted in Fig. 6.23b. In Fig.6.23c however, the bending in x direction on the (022) plane is in opposite direction across the line of symmetry. The displacements in x direction also vary with z, maximum being at the free surfaces. TEM micrograph of Fig.6.4 depicts this situation, with $\vec{g}$=022 (when only (022) planes are in the Bragg diffracting condition), the figure shows a black and white lobe with a line of no contrast along the line of symmetry, at the root of the groove. The black and white lobes are a direct consequence of the fact that the planes are bending in opposite directions across the symmetry axis. Fig. 6.20a and b shows the displacements in the x direction for nodes on the symmetry plane and away from it, which corresponds to the schematic in Fig.6.23. For nodes on the plane of symmetry there is zero displacement in the x direction all along

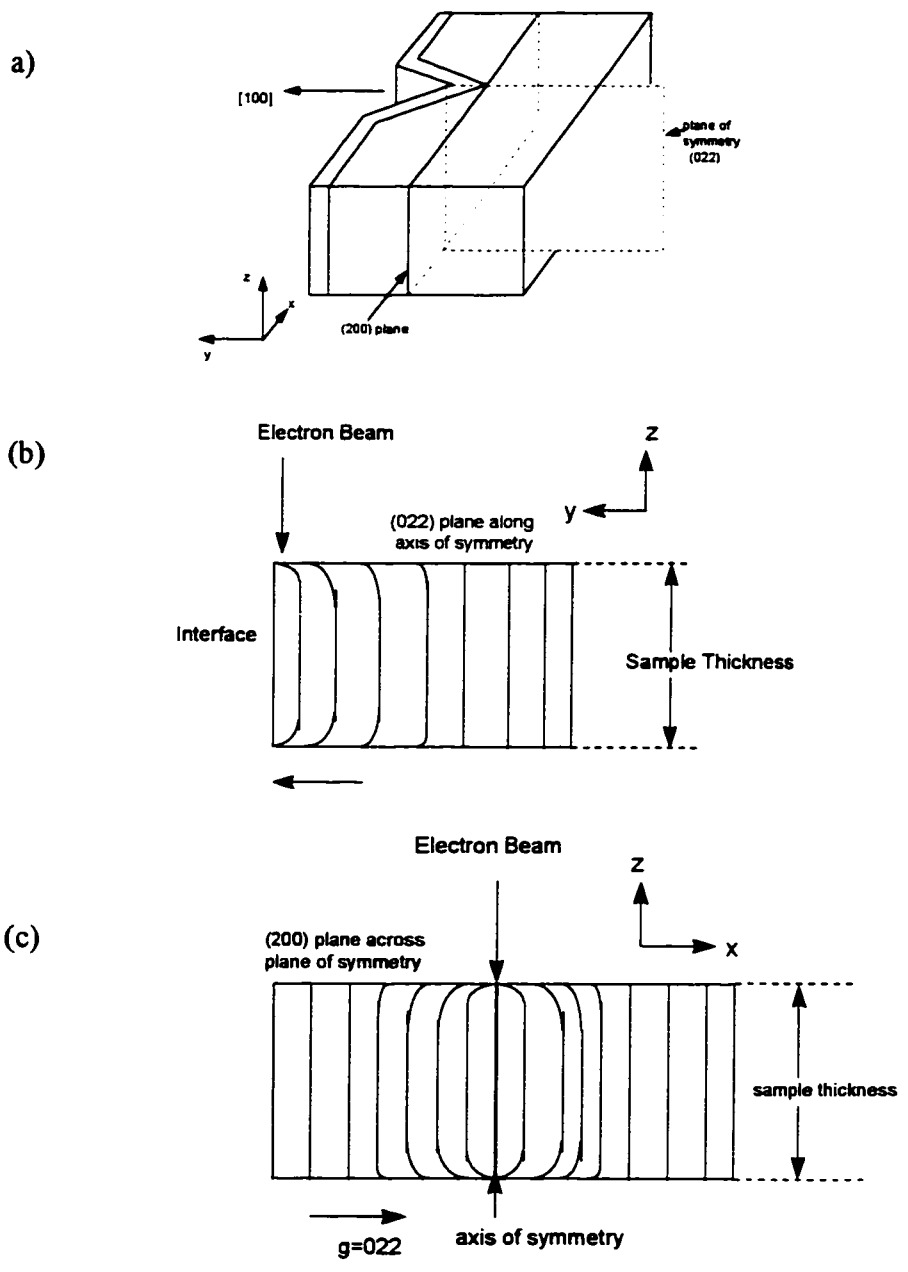

Fig. 6.23 Schematic showing the displacements as a result of plane bending at the surface, (a) position of the plane of symmetry in the groove (b) direction of plane bending with respect to $\vec{g}$=200 in a TEM foil (c) direction of plane bending with respect to $\vec{g}$= 022.the z direction (Fig.6.20a). This corresponds to the line of no contrast in the TEM micrograph along the axis of symmetry (Fig.6.4). However, away from the symmetry

plane the displacements in the x direction does change with z, maximum being at the xy free surfaces (Fig.6.20b). Since only half of the groove was considered in the FEM analysis we can only assume that, given the line of zero displacement at the symmetry axis, the displacements in the x direction on the other side of the groove will be in opposite direction of that in Fig.6.20b.

Fig. 6.20c and d show surface displacements in the xy plane in the x and y direction and their variation with distance away from the groove. Fig. 6.20c shows the displacements along nodes on the axis of symmetry. The displacement in the x direction is zero for all nodes on the symmetry axis but the magnitude of displacement in the y-direction decreases away from the interface. For nodes away from the symmetry axis (Fig.6.20d), both x and y displacements are experienced, with magnitudes decreasing away from the root of the groove. These results are in accordance with the bulk stress values (Fig.6.21) which decreases away from the groove.

The above discussion showed that the FEM results predict the bulk stresses (cooresponding to B.C.I in Appendix B) similar to the DOP results both qualitatively and quantitatively. However for the thin film case (B.C.II in Appendix B), even though the FEM gives a accurate qualitative prediction of surface displacements, since the mesh size is very coarse, the quantitative comparison of the amount of plane bending at the surface and the resulting TEM contrast, was not possible. Moreover the ratio of groove size to the thin foil thickness in the experimental case was ~ 20; not practical to depict using FEM if the mesh size is to be kept reasonable. However, the present model of thin film, with thickness of the foil comparable to the groove size, gives a satisfactory qualitative interpretation of the TEM relaxation contrast.

7. CONCLUSIONS AND FUTURE WORK

A summary of the conclusions obtained in this research is listed below:

1. There is a distinct difference in growth properties of InGaAs on (211)A and (111)B V-grooves etched in InP substrates. This difference arises due to the difference in interaction of In, Ga, and As with the different planes and the differences in diffusion lengths of In and Ga atoms under similar growth conditions.
2. Layers grown on (211)A are not suitable for quantum wire applications because the wide groove angle and negligible change in thickness of layers would not be successful in confining the carriers in the lateral direction.
3. Layers grown on (111)B would be suitable for quantum wire application provided that the defects could be eliminated. The threefold increase in thickness at the bottom and sharp groove angle are ideal for confining carriers in the lateral direction.
4. The wavelength of composition modulations depends on the surface on which layers are grown. A ten fold increase was observed in the wavelength in InGaAs layers grown on (111)B surfaces near the bottom of the groove compared to (211)A, (311)A, and (100) facets.
5. Faceting on (211)A grooves is a result of differences in growth rates on various facets. The development of facets is aided by interfacet diffusion and hence does not occur in growths on planar samples.
6. Composition analysis results showed that the composition is constant along the different facets of the (211)A groove, whereas the composition (In/Ga ratio)

changes by about 36.6% at the bottom of the (111)B groove compared to the top (100) plane.

7. Freund and Gosling's model shows that the misfit at the bottom of the (111)B groove is above the critical value for defect formation, in agreement with the observations. Application of their model showed that defects can be eliminated by lowering the thickness to 207.5Å for a misfit strain of -0.013 (with respect to the substrate) or to lower the misfit strain to -0.003 for a thickness of 1560Å.

8. TEM showed a strong surface relaxation contrast at the bottom of the (211)A grooves. This contrast is a result of a modified stress distribution at the bottom of the groove. DOP also showed a concentration of stresses at the bottom of the groove.

9. Analytical and numerical simulation of the stress distribution was performed and the results compared to the experimental results obtained from DOP and TEM. There was a good quantitative match with the DOP results. There was an order of magnitude difference between the analytical solution and the FEM, when they were compared with the DOP results. It is thought that this is due to the fact that in the analytical model, a layer buried in an infinite substrate was considered.

10. The surface relaxation contrast observed in the TEM was simulated by FEM; this analysis showed that the displacement in the z direction varies with depth. The magnitude of the displacement was a maximum at the surfaces in agreement with the observation that the free surfaces must be relaxed.

Based on the results of this work there are many possibilities which open up for future work. Some suggestions for future work are:

1. Growing lattice mismatched layers on (111)B with different thicknesses and compositions to see if defect free growth, as predicted by Freund and Gosling's model, could be achieved.
2. Extending the FEM simulation to a case closer to reality, i.e. incorporating thickness, profile, and composition variations in the model and obtaining a stress distribution for this situation.
3. Growing a thin misfit layer on a V-groove covered with a thick cap layer. DOP of this sample could then be compared to the analytical solution worked out in this thesis.
4. A complete understanding of the diffusion behavior of atoms on faceted surfaces would help to exploit this method for generating novel devices based on quantum wires. Hence a study could be done using the nominal composition of the layers, growth temperature, and orientation of sideplanes as variables for layers grown on V-grooves. A composition analysis would reveal the effects on changing these variables and a model for diffusion and incorporation of the different atomic species on faceted substrates could be developed.
5. The wavelength of composition modulations was observed to change with orientation. The composition, and hence strain might also be a factor in determining the wavelength of these modulations. It would be interesting to study these modulations under different growth conditions and attempt to explain their origin.

8. REFERENCES

Arakawa, T., Tsukamoto, S., Nagamune, Y., Nishioka, M., Lee, Jin-Hee, and Arakawa, Y., Fabrication of InGaAs strained quantum wire structures using selective-area metal-organic chemical vapor deposition growth, *Jpn. J. Appl. Phys.*, Vol.32, 1993, L1377-L1379.

Ashby M.F., and Brown, L.M, Diffraction contrast from spherically symmetrical coherency strains, *Phil.Mag.*, 1963, 1083-1103.

Auret, F.D., Ball, C.A.B., and Snyman, H.C., The transmission electron microscope image contrast of epitaxial interfaces with small misfits, *Thin Solid Films*, Vol.61, 1979, 289-295.

Bachrach, R.Z., Bauer, R.S., Chiaradia, P., and Hansson, G.V., Reconstructions of GaAs and AlAs surfaces as a function of metal to As ratio, *J. Vac. Sci. Technol.*, No.3, Vol.19, 1981, 335-343.

Bachrach, R.Z., Semiconductor surface and crystal physics studied by MBE, *Prog. Crystal Growth and Characterization*, Vol.2, 1979, 115-144.

Bauer, V.E., Phänomenologische Theorie der Kristallabscheidung an Oberflächen.I, *Z. Kristallographie*, Vol.110, 1958, 372-394.

Bhat, R., Kapon, E., Simhony, S., Colas, E., Hwang, D.M., Stoffel, N.G., and Koza, M.A., Quantum wire lasers by OMCVD growth on nonplanar substrates, *J. Crystal Growth*, Vol.107, 1991, 716-723.

Bhat, R., Kapon, E., Werner, J., Hwang, D.M., Stoffel, N.G., and Koza, M.A., Organometallic chemical vapor deposition of InP/InGaAsP on nonplanar InP substrates: Application to multiple quantum well lasers, *Appl. Phys. Lett.*, No.9, Vol.56, 1990, 863-865.

Biegelsen, D.K., Bringans, R.D., Northrup, J.E., and Swartz, L.-E., Surface reconstructions of GaAs(100) observed by scanning tunneling microscopy, *Physical Review B*, No.9, Vol.41, 1990, 5701-5706.

Bulitka, N.J., V-groove patterned substrate epitaxy using InGaAs/InP, *M.Eng. thesis*, McMaster University, 1993.

Cassidy, D.T., and Adams, C.S., Polarization of the output of InGaAsP semiconductor diode lasers, *IEEE J. Quantum Electronics*, Vol.25, 1989, 1156-1160.

Chalmers, S.A., Tsao, J.Y., and Gossard, A.C., Terrace width evolution during step-flow growth with multiterrace adatom migration, J. Appl. Phys., No.11, Vol.73, 1993, 7351-7357.

Chang, Chin-An, Ludeke, R., Chang, L.L., and Esaki, L., Molecular-beam epitaxy of $In_xGa_{1-x}As$ and $GaSb_{1-y}As_y$, *Applied Physics Letters*, No.11, Vol.31, 1977, 759-761.

Chew, N.G., and Cullis, A.G., The preparation of transmission electron microscope specimens from compound semiconductors by ion milling, *Ultramicroscopy*, Vol.23, 1987, 175-198.

Chu, S.N.G., et al., *J. Appl. Phys.*, No.10, Vol.57, 1985, 4610-4615.

Chu, S.N.G., Long wavelength laser diode reliability and lattice imperfections, *MRS Bulletin*, Dec. 1993, 43-48.

Cliff, G., and Lorimer, G.W., The quantitative analysis of thin specimens, *J. Microscopy*, Vol.103, 1975, 203-207.

Colas, E., Shahar, A., and Tomlinson, W.J., Diffusion-enhanced epitaxial growth of thickness-modulated low-loss rib waveguides on patterned GaAs substrates, *Appl. Phys. Lett.*, No.10, Vol.56, 1990a, 955-957.

Colas, E., Simhony, S., Kapon, E., Bhat, R., Hwang, D.M., and Lin, P.S.D., Growth of GaAs quantum wire arrays by organometallic chemical vapor deposition on submicron gratings, *Appl. Phys. Lett.*, No.9, Vol.57, 1990b, 914-916.

Colbourne, P.D., and Cassidy, D.T., Imaging of stresses in GaAs diode lasers using polarization-resolved photoluminescence, *IEEE J. Quantum Electronics*, No.1, Vol.29, 1993

Colbourne, P.D., Measurement of stress in III-V semiconductors using the degree of polarization of luminescence, *Ph.D. Thesis*, McMaster University, 1992.

Cook, R.F., and Howie, A., Effect of elastic constraints on electron energy loss measurements in inhomogeneous alloys, *Phil. Mag.*, 1969, 641-645.

Cullis, A.G., Strain-induced modulations in the surface morphology of heteroepitaxial layers, *MRS bulletin*, Vol. 21, No.4, 1996, 21-26.

Dilger, M., Hohenstein, M., Phillipp, F., Eberl, K., Kurtenbach, A., Grambow, P., Lehmann, A., Heitmann, D., and von Klitzig, K., Transmission electron microscopy studies of GaAs/AlGaAs heterostructures regrown on patterned substrates, *Semiconductor Sci. Technol.*, Vol.9, 1994, 2258-2262.

Dryburgh, P.M., Further notes on the estimation of minimum temperature for crystal growth from a gas phase, *J. Crystal Growth*, Vol.130, 1993, 305-307.

Dryburgh, P.M., The estimation of minimum growth temperature for crystals grown from the gas phase, *J. Crystal Growth*, Vol.87, 1988, 397-407.

Däweritz, L., and Hey, R., Reconstruction and defect structure of vicinal GaAs(001) and $Al_xGa_{1-x}As(001)$ surfaces during MBE growth, *Surface Science*, Vol.236, 1990, 15-22.

Esaki, L., and Tsu, R., Superlattice and negative differential conductivity in semiconductors, *IBM J. Research and Development*, Jan.1970, 61-65.

Eshelby, J.D., The determination of the elastic field of an ellipsoidal inclusion, and related problems, *Proc. Royal Soc.*, A241, 1957, 376-396.

Fawcett, P.N., Neave, J.H., Zhang, J., and Joyce, B.A., Study of the epitaxial growth of GaAs(110) films by molecular beam epitaxy, *J. Vacuum Science and Technology*, No.4, Vol.12,1994, 1201-1203.

Fitzgerald, E.A., Dislocations in strained-layer epitaxy: theory, experiment, and applications, *Materials Science Reports*, Vol.7, 1991, 87-142.

Frank, F.C., and Van der Merwe, J.H., One dimensional dislocations. II. Misfitting monolayers, *Proc. Roy. Soc.*, A198, 1949, 216.

Freund, L.B., and Gosling, T.J., Critical thickness condition for growth of strained quantum wires in substrate V-grooves, *App. Phys. Lett.*, No.21, Vol.66, 1995, 2822-2824.

Frocht, M.M., *Photoelasticity*, Vol.I and II, John Wiley & Sons, 1941.

Galeuchet, Y.D., Roentgen, P., and Graf, V., Buried GaInAs/InP layers grown on nonplanar substrates by one-step low-pressure metalorganic vapor phase epitaxy, *Appl. Phys. Lett.*, No.26, Vol.53, 1988, 2638-2640.

Geguzin, Ya. E., and Ovcharenko, N.N., Study of surface phenomena of single crystals II. Mechanism and Kinetics of the leveling of defects on the surface of crystals with considerable anisotropy of the coefficient of surface tension, *Sov. Physics-Crystallography*, No.1, Vol.6, 1961, 75-82.

Gibson, J.M., and Treacy, M.M.J., The effect of elastic relaxation on the local structure of lattice-modulated thin films, *Ultramicroscopy*, Vol.14, 1984, 345-350.

Glas, F., et al., *J. de Physique Colloque*, No.5, Vol.43, 1982, 11.

Gonda, Shun-ichi, and Matsushima, Y., Effect of substrate temperature on composition ratio x in molecular-beam-epitaxial $GaAs_{1-x}P_x$, *J. Appl. Phys.*, No.9, Vol.47, 1976, 4198-4200.

Gosling, T.J., and Freund, L.B., A critical thickness condition for triangular strained quantum wires grown in V-grooves on a patterned substrate, *Acta Metall.*, No.1, Vol.44, 1996, 1-13.

Gosling, T.J., and Willis, J.R., Mechanical stability and electronic properties of buried strained quantum wire arrays, *J. Appl. Phys.*, No. 11, Vol.77, 1995, 5601-5610.

Grabow, M.H., and Gilmer, G. H., Thin film growth modes, wetting and cluster nucleation, *Surface Science*, Vol.194, 1988, 333-346.

Grundmann, M., Stier, O., Christen, J., and Bimberg, D., Pseudomorphic quantum wires: Symmetry breaking due to structural, strain, and piezoelectric field induced confinement, *Superlattices and Microstructures*, No.3, Vol.16, 1994, 249-251.

Hartmann, A., Vescan, L., Dieker, C., and Lüth, H., Growth of SiGe quantum wires and dots on patterned Si substrates, *J. Appl. Phys.*, No.5, Vol.77, 1995, 1959-1963.

Hashimoto, H., Howie, A., and Whelan, M.J., Anomalous electron absorption effects in metal foils: theory and comparison with experiement, *Phil. Mag.*,1962, 80-103.

Hata, M., Isu, T., Watanabe, A., and Katayama, Y., Distributions of growth rates on patterned surfaces measured by scanning microprobe reflection high-energy electron diffraction, *J. Vac. Sci. Technol.*, No.4, Vol.B8, 1990, 692-696.

Hersee, S.D., Barbier, E., and Blondeau, R., A study of the orientation dependence of Ga(Al)As growth by MOVPE, *J. Crystal Growth*, Vol.77, 1986, 310-320.

Hoenk, M.E., Chen, H. Z., Yariv, A., Morkoc, H., and Vahala, K.J., Cathodoluminescence measurement of an orientation dependent aluminium concentration in $Al_xGa_{1-x}As$ epilayers grown by molecular beam epitaxy on a nonplanar substrate, *Appl. Phys. Lett.*, No.14, Vol.54, 1989, 1347-1349.

Holt, D.B., Surface polarity and symmetry in semiconducting compounds, *J. Mats. Sci.*, Vol.23, 1988, 1131-1136.

Hou, H.Q., and Tu, C.W., Homoepitaxial growth of InP on (111)B substrates by gas-source molecular beam epitaxy, *Appl. Phys. Lett.*, No. 3, Vol. 62, 1993, 281-283.

Jones, S.H., Seidel, L.K., Lau, K.M., and Harold, M., Patterned substrate epitaxy surface shapes, *Journal of Crystal Growth*, Vol.108, 1991, 73-88.

Jouneau, P.-H., Bobard, F., Marti, U., Robadey, J., Filipowitz, F., Martin, D., MorierGenoud, F., Silva, P.C., Magnenat, Y., and Reinhart, F.K., Fabrication and TEM characterization of V-groove InGaAs quantum wires, *Institute of Physics conference series*, Oxford, March, 1995.

Kapon E., Hwang, D.M., and Bhat, R., Stimulated emission in semiconductor quantum wire heterostructures, *Physical Review Letters*, No.4, Vol.63, 1989a, 430-433.

Kapon E., Quantum wire lasers, *Proceedings of the IEEE*, No.3, Vol.80, 1992a, 398-410.

Kapon E., Simhony, S., Bhat, R., and Hwang, D.M., Single quantum wire semiconductor lasers, *Appl. Phys. Lett.*, No.26, Vol.55, 1989b, 2715-2717.

Kapon E., Two dimensional quantum confinement in multiple quantum wire lasers grown by OMCVD on V-grooved substrates, *Surface Science*, Vol.267, 1992c, 593-600.

Kapon, E., Kash, K., Clausen Jr., E.M., Hwang, D.M., and Colas, E., Luminescence characteristics of quantum wires grown by organometallic chemical vapor deposition on nonplanar substrates, *Appl. Phys. Lett.*, No.4, Vol.60, 1992d, 477-479.

Kapon, E., Lateral patterning of quantum well heterostructures by growth on nonplanar substrates, *Semiconductors and Semimetals*, Vol.40, 1994, 259-336.

Kapon, E., Tamargo, M.C., and Hwang, D.M., Molecular beam epitaxy of GaAs/AlGaAs superlattice heterostructures on nonplanar substrates, *Appl. Phys. Lett.*, No.6, Vol.50, 1987, 347-349.

Kapon, E., Walther, M., Christen, J., Grundmann, M., Caneau, C., Hwang, D.M., Colas, E., Bhat, R., Song, G.H., and Bimberg, D., Quantum wire heterostructures for optoelectronic applications, *Superlattices and Microstructures*, No.4, 12, 1992b, 491-499.

Keller, B.P., Keller, S., Herrnberger, H., Lenzner, J., Nilsson, S., and Seifert, W., Compositional gradients in $Ga_xIn_{1-x}As$ on patterned InP substrates grown by atmospheric-pressure metalorganic vapor phase epitaxy, *J. Crystal Growth*, Vol.40, 1994, 33-40.

Kim, M., Kim, Y., Lee, M., Park, Y.J., Kim, S., and Kim, S., The facet evolution during metalorganic vapor phase epitaxial growth on V-grooved high miller index GaAs substrates, *J. Crystal Growth*, Vol.139, 1994, 231-237.

Kroemer, H., Polar-on-nonpolar epitaxy, *J. Crystal Growth*, Vol.81, 1987, 193-204.

LaPierre, R.R., *M. Eng. Thesis*, McMaster University, 1994.

Lee, B.-T, Logan, R.A., and Chu, S.N.G., Observation of growth patterns during atmospheric pressure metalorganic vapor phase epitaxy regrowth of InP around etched mesas, *J. Crystal Growth*, Vol.130, 1993, 287-294.

Lorimer, G.W., Cliff, G., Champness, P.E., Dickinson, C., Hasan, F., and Kenway, P., In situ X-ray microanalysis of second-phase particles in thin foils, *Analytical Electron Microscopy*, eds. D.B.Williams and D.C. Joy, San Francisco Press Inc., 1984, 153-156.

Mahajan, S., Dutt, B.V., Temkin, H., Cava, R.J., and Bonner, W.A., Spinodal decomposition in InGaAsP epitaxial layers, *J. Crystal Growth*, Vol.68, 1984, 589-595.

Matthews, J.W., and Blakeslee, A.E., Almost perfect epitaxial multilayers, *J. Vac. Sci. Technol.*, No.4, Vol.14, 1977, 989-991.

Matthews, J.W., and Blakeslee, A.E., Defects in epitaxial multilayers I. misfit dislocations, *J. Crystal Growth*, Vol.27, 1974, 118-125.

Matthews, J.W., Defects associated with the accomodation of misfit between crystals, *J. Vac. Sci. and Tech.*, No. 1, Vol.12, 1975,126-133.

McDevitt, T. L., Mahajan, S., Laughlin, D.E., Bonner, W.A., and Keramidas, V.G., Effects of annealing on phase separated microstructures in InGaAsP epitaxial layers, *Inst. Phys. Conf. Series*, No.117, 1991, 477-483.

McGibbon, A.J., High spatial resolution microanalysis of semiconductor interfaces, *Ph.D. Thesis*, University of Glasgow, 1989.

Nishida, T., Sugiura, H., Notomi, M., and Tamamura, T., InGaAs/InP quantum wires selectively grown by chemical beam epitaxy, *J. Crystal Growth*, Vol.132, 1993, 91-98.

Nishioka, M., Tsukamoto, S., Nagamune, Y., Tanaka, T., and Arakawa, Y., Fabrication of InGaAs strained quantum wires using selective MOCVD growth on SiO_2-patterned GaAs substrate, *J. Crystal Growth*, Vol.124, 1992, 502-506.

Norman, A.G., and Booker, G.R., Transmission electron microscope and transmission electron diffraction observations of alloy clustering in liquid phase epitaxial (001) GaInAsP layers, *J. Appl. Phys.*, No.10, Vol.57, 1985, 4715-4720.

O'Reilly, E.P., Valence band engineering in strained-layer structures, *Semicond. Sci. Technol.*, Vol.4, 1989, 121-137.

Ozdemir, M., and Zangwill, A., Theory of epitaxial growth onto nonplanar substrates, *J. Vac. Sci. Technol. A*, No.4, Vol.10, 1992, 684-690.

Pan, W., Yaguchi, H., Onabe, K., Shiraki, Y., and Ito, R., Growth temperature dependence of AlGaAs spontaneous vertical quantum wells on V-grooved substrates by low-pressure metalorganic vapor phase epitaxy, *J. Crystal Growth*, Vol.158, 1996, 205-209.

Perovic, D.D., Weatherly, G.C., and Houghton, D.C., On the electron diffraction contrast of coherently strained semiconductor layers, *Philosophical Mag.A*, No.1, Vol.64, 1991, 1-28.

Petroff, P.M., Transmission electron microscopy of interfaces in III-V compond semiconductors, *J. Vac. Sci. Technol.*, No.4, Vol.14, 1977, 973-978.

Ploog, K., *Ann. Rev. Mater. Sci.*, 11, 1981, 171-210.

Rajkumar, K.C., Chen, P., and Madhukar, A., A transmission electron microscope study of twin structure in GaAs/GaAs (111)B grown via molecular beam epitaxy, *J. Appl. Physics*, No.4, Vol.69, 1991, 2219-2230.

Roland, C., Effects of stress on step energies and surface roughness, *MRS bulletin*, Vol. 21, No.4, 1996, pp 27-30.

Sangster, R.C., Model studies of crystal growth phenomena in the III-V semiconducting compounds, *Compound Semiconductors*, Vol.1, Reinhold, NewYork, 1962, 241-253.

Shen, X.Q., Tanaka, M., Wada, K., and Nishinaga, T., Molecular beam epitaxial growth of GaAs, AlAs, and $Al_{0.45}Ga_{0.55}As$ on (111)A-(001) V-grooved substrates, *J. Crystal Growth*, Vol.135, 1994, 85-96.

Simhony, S., Kapon, E., Colas, E., Hwang, D.M., Stoffel, N.G., and Worland, P., Vertically stacked multiple-quantum-wire semiconductor diode lasers, *Applied Physics Letters*, No.18, Vol.59, 1991, 2225-2227.

Sogawa, T., Ando, S., and Kanbe, H., Growth of GaAs/AlAs trench-buried multiple quantum wires by metalorganic chemical vapor deposition on V-grooved substrates, *Appl. Phys. Lett.*, No.24, Vol.64, 1994, 3299-3301.

Spencer, B.J., Voorhees, P.W., and Davis, S.H., Morphological instability in epitaxially strained dislocation free solid films, *Physical Rev. Lett.*, No.26, Vol. 67, 1991, 3696-3699.

Stellini, E.M., Cheng, K.Y., Pearah, P.J., Chen, A.C., Moy, A.M., and Hsieh, K.C., AlGaInP multiple-quantum-wire lasers grown by gas source molecular beam epitaxy, *App. Phys. Lett.*, No.5, Vol.62, 1993, 458-460.

Subbana, S., Kroemer, H., and Merz, J.L., Molecular-beam-epitaxial growth and selected properties of GaAs layers and GaAs/(Al,Ga)As superlattices with the (211) orientation, *J. Appl. Phys.*, No.2, Vol.59, 1986, 488-494.

Thrush, E.L., Stagg, J.P., Gibbon, M.A., Mallard, R.E., Hamilton, B., Jowett, J.M., and Allen, E.M., Selective and non-planar epitaxy of InP/GaInAs(P) by MOCVD, *Materials Sci. and Eng.*, Vol.B21, 1993, 130-146.

Tixier, R., and Philibert, J., Analyse quantitative d'echantillons minces, G. Möllenstedt and K.H. Gaukler, Eds., *Proc. 5th Intern. Cong. On X-Ray Optics And Microanalysis*, Berlin, Springer-Verlag, 1969.

Treacy, M.M.J., and Gibson, J.M., The effects of elastic relaxation on transmission electron microscopy studies of thinned composition-modulated materials, *J. Vaccum Science and Tech.B*, No.6, Vol.4, 1986,1458-1466.

Treacy, M.M.J., Gibson, J.M., and Howie, A., On elastic relaxation and long wavelength microstructures in spinodally decomposed $In_xGa_{1-x}As_yP_{1-y}$ epitaxial layers , *Phil. Mag. A*, Vol.51, 1985, 389-417.

Tsang, W.T., and Cho, A.Y., Growth of GaAs-$Ga_{1-x}Al_xAs$ over preferentially etched channels by MBE: A technique for two-dimensional thin-film definition, *Appl. Phys. Lett.*, No.6, Vol.30, 1977, 293-296.

Turco, F.S., Tamargo, M.C., Hwang, D.M., Nahory, R.E., Werner, J., Kash, K., and Kapon, E., Growth of InGaAs/InAlAs quantum wells on InP patterned substrates by molecular beam epitaxy, *Appl. Phys. Lett.*, No.1, Vol.56, 1990, 72-74.

Van der Merwe, J.H., Recent developments in the theory of epitaxy, *Chemistry and physics of solid surfaces*, Vol.5, edited by R. Vanselow and R. Howe, Springer, Berlin, 1984, 365-401.

Van der Merwe, J.H., Theoretical considerations in growing uniform epilayers, *Interface Science*, Vol.1, 1993, 77-86.

Van Mieghem, P., Jain, S.C., Nijs, J., and Van Overstraeten, R., Stress relaxation in laterally small strained semiconductor epilayers, *J. Appl. Phys.*, No.1, Vol.75, 1994, 666-668.

Vermeire, G., Yu, Z.Q., Vermaerke, F., Buydens, L., Van Daele, P., and Demeester, P., Anisotropic photoluminescence behavior of vertical AlGaAs structures grown on gratings, *J. Crystal Growth*, Vol.124, 1992, 513-518.

Vina, L., and Wang, W.I., AlGaAs/GaAs (111) heterostructures grown by molecular beam epitaxy, *Appl. Phys. Lett.*, No.1, Vol.48, 1986, 36-37.

Walther, M., Kapon, E., Hwang, D.M., Colas, E., and Nunes, L., Observation of electronic subbands in dense arrays of quantum wires grown by organometallic-chemical-vapor deposition on nonplanar substrates, *Phy. Rev. B*, No.11, Vol.45, 1992, 6333-6336.

Wang, W.I., Novel crystal growth of AlGaAs/GaAs heterostructures on polar surfaces, *Surface Sciences*, Vol.174, 1986, 31-37.

Williams, E.D., and Bartelt, N.C., Thermodynamics of surface morphology, *Science*, Vol.251, 1991, 393-400.

Yoo, H.M., Ohuchi, F.S., and Stoebe, T.G., Influence of substrate temperature on the growth of InGaAs layers on (111)B GaAs, *J.Vac. Sci. and Technology*, No.3, 11, 1993, 542-545.

Zeindl, H.P., Fuenzalida, V., Messarosch, J., and Eisele, I., Influence of substrate misorientation and temperature on MBE-grown Si, *J. Crystal Growth*, Vol.81, 1987, 231-236.

9. APPENDICES

9.1 APPENDIX A- ANALYTICAL SOLUTION FOR STRAIN DISTRIBUTION OF A STRAINED LAYER ON PATTERNED SUBSTRATES

9.1.1 Potential Method

Eshelby(1957), in his classic paper, worked out the elastic field of an ellipsoidal inclusion. In this appendix his method is followed to solve the strain field of a coherent strained layer at a faceted(patterned) surface.

We assume that the geometry is such that the "particle" is infinite in one direction(z-direction), with singular points at the corners(Fig.A1). The geometry of the strained layers is made of several straight segments joined at the corners. The contribution due to each segment can be added to arrive at the complete solution of the problem, using the principle of superposition.

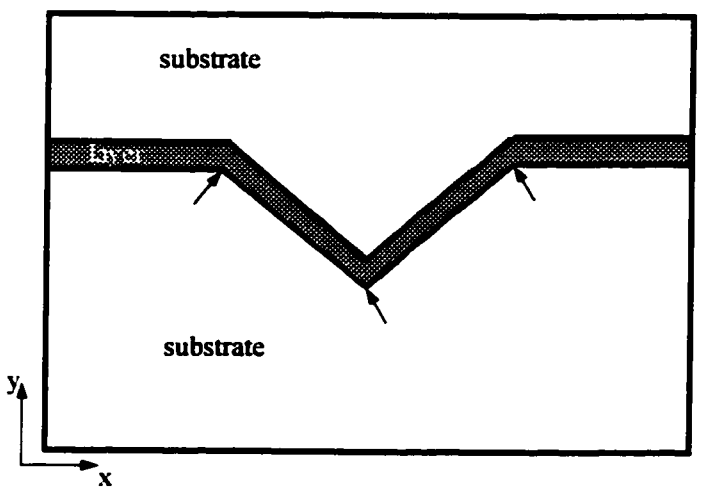

Fig.A1: Schematic diagram of a V-shaped strained layer buried in an infinite substrate. Arrows point to the singular points.

The problem can be solved using the Eshelby approach, so the first step is to calculate the Newtonian potential of each segment, followed by differentiating twice to get the stress field.

The Newtonian potential ϕ is defined as,

$$\varphi = \oint_V \frac{dV}{|\vec{r} - \vec{r}'|} \quad \text{.....(A1)}$$

where dV is the infinitesimal volume of the body and $|\vec{r} - \vec{r}'|$ is the magnitude of the distance of the observed point from the potential source.

The strain is defined as (Eshelby, 1957),

$$e^c_{il} = -\frac{1}{12\pi}\frac{1+\upsilon}{1-\upsilon} e^T \varphi_{,il} \quad \text{.....(A2)}$$

where $\frac{1}{3} e^T \delta_{ij}$, is a pure dilatation, e^c_{il} is the constrained strain and $\varphi_{,il}$ is the differentiation of the potential with respect to the two parameters i and l. The assumption that the strained layers are infinitely extended in the z-direction reduces the problem to one of generalized plane strain, i.e. in the matrix outside the strained layer $\sigma^c_{zz} = 0$ and $\varepsilon^c_{ii} = 0$.

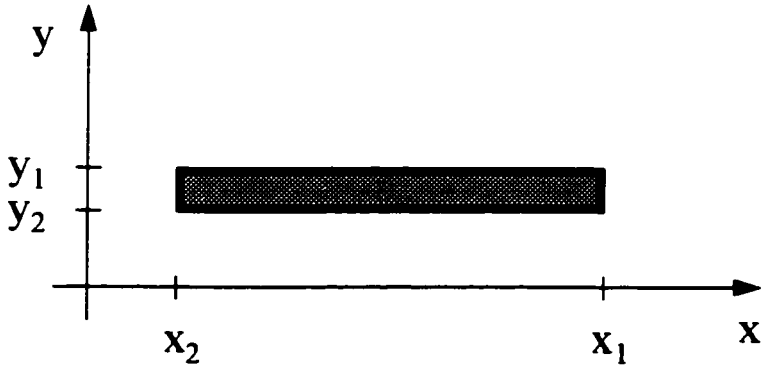

Fig.A2: Schematic diagram of a sheet infinite in z-direction.

If we take a sheet (fig. A2) which is infinite in the z-direction and has a width (x_1-x_2) in the x-direction and thickness (y_1-y_2) in the y-direction then the integral reduces to ,

$$\varphi = -\int_{x_2}^{x_1}\int_{y_2}^{y_1} \ln\sqrt{(x-x')^2+(y-y')^2}\,dy'\,dx' \quad \text{.....(A3)}$$

Solving this integral leads to the expression,

$$\begin{aligned}
\varphi = {} & -(x-x_1)(y-y_1)\ln\sqrt{(y-y_1)^2+(x-x_1)^2} + (x-x_1)(y-y_2)\ln\sqrt{(y-y_2)^2+(x-x_1)^2} \\
& +(x-x_2)(y-y_1)\ln\sqrt{(y-y_1)^2+(x-x_2)^2} - (x-x_2)(y-y_2)\ln\sqrt{(y-y_2)^2+(x-x_{21})^2} \\
& -(x-x_1)^2\tan^{-1}\left(\frac{y-y_1}{x-x_1}\right) + (x-x_1)^2\tan^{-1}\left(\frac{y-y_2}{x-x_1}\right) + (x-x_2)^2\tan^{-1}\left(\frac{y-y_1}{x-x_2}\right) - (x-x_2)^2\tan^{-1}\left(\frac{y-y_2}{x-x_2}\right) \\
& -\frac{1}{2}\left((y-y_1)^2+(x-x_1)^2\right)\cot^{-1}\left(\frac{y-y_1}{x-x_1}\right) + \frac{1}{2}\left((y-y_2)^2+(x-x_1)^2\right)\cot^{-1}\left(\frac{y-y_2}{x-x_1}\right) \\
& +\frac{1}{2}\left((y-y_1)^2+(x-x_2)^2\right)\cot^{-1}\left(\frac{y-y_1}{x-x_2}\right) - \frac{1}{2}\left((y-y_2)^2+(x-x_2)^2\right)\cot^{-1}\left(\frac{y-y_2}{x-x_2}\right) \\
& +\frac{1}{2}(x-x_1)(y-y_1) - \frac{1}{2}(x-x_1)(y-y_2) - \frac{1}{2}(x-x_2)(y-y_1) + \frac{1}{2}(x-x_2)(y-y_2) + (x_1-x_2)(y_2-y_1)
\end{aligned} \quad \text{..A4}$$

Eq.A2 shows that to get the constrained strains in the substrate Eq. A4 has to be differentiated twice. Since

$$e^c_{xx} = -\frac{1+\upsilon}{12\pi(1-\upsilon)}e^T\varphi_{,xx} \quad \text{.....A5}$$

we need to find,

$$\frac{\partial^2\varphi}{\partial x^2} = -\tan^{-1}\left(\frac{y-y_1}{x-x_2}\right) + \tan^{-1}\left(\frac{y-y_2}{x-x_2}\right) + \tan^{-1}\left(\frac{y-y_1}{x-x_1}\right) - \tan^{-1}\left(\frac{y-y_2}{x-x_1}\right) \quad \text{.....A6}$$

The above expression(Eq. A5) gives us the strain field in the x direction due to a thin misfitting layer deposited on a planar substrate.

In the substrate $\sigma_{xx} = -\sigma_{yy}$ since the Laplacian $\nabla^2\varphi = 0$ holds in the matrix.

Since at the sides of the groove, the layers are not rectangular but are rhombohedral in cross-section (Fig. A3) (in order to maintain continuity in the groove), the potential for a rhombus shape has to be found with y as a linear function of x.

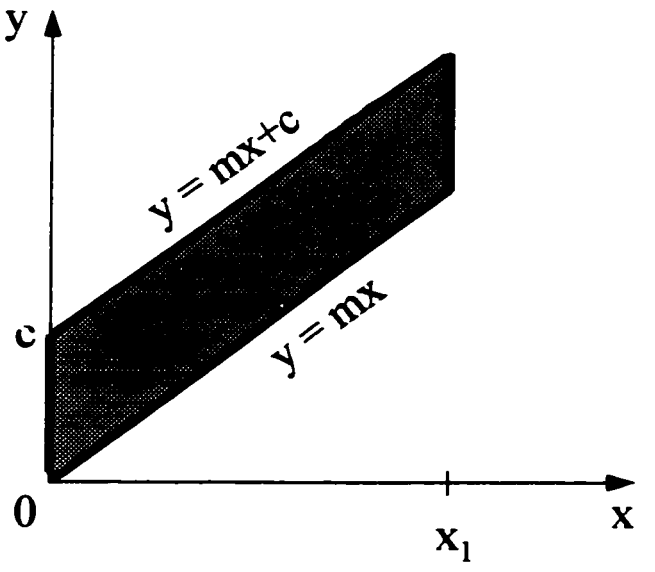

Fig.A3: Schematic diagram of the rhombus shaped sheet extending infinitely in the Z-direction.

The expression for φ now depends on

$$\int_{x_2}^{x_1}\int_{y_2}^{y_1} \ln\sqrt{(x-x')^2+(y-y')^2}\,dy'dx' \qquad \text{.....A7}$$

where both y_2 and y_1 are functions of x'. If we assume the thickness of the rhombus in the y-direction is c then,

$y_2=mx'$;

$y_1=mx'+c$;

To solve the double integral of Eq .A7 we first solve the inner integral which is a function of y',

$$\int_{y_2}^{y_1} \ln\sqrt{(x-x')^2+(y-y')^2}\,dy'$$

$$= (y-y_1)\ln\sqrt{(x-x')^2+(y-y_1)^2} - (y-y_1) + (x-x')\tan^{-1}\left(\frac{y-y_1}{x-x'}\right) -$$

$$(y-y_2)\ln\sqrt{(x-x')^2+(y-y_2)^2} + (y-y_2) - (x-x')\tan^{-1}\left(\frac{y-y_2}{x-x'}\right) \qquad \text{.....A8}$$

Substituting $y_2=mx'$ and $y_1=mx'+c$ in Eq.A8 gives the inner integral of Eq A7 in terms of the variable x' as,

$$(y-mx'-c)\ln\sqrt{(y-mx'-c)^2+(x-x')^2}+(y_1-y_2)+(x-x')\tan^{-1}\left(\frac{y-mx'-c}{x-x'}\right)- \quad \text{..A9}$$
$$(y-mx')\ln\sqrt{(y-mx')^2+(x-x')^2}+(y_1-y_2)-(x-x')\tan^{-1}\left(\frac{y-mx'}{x-x'}\right)$$

Eq. A9 is integrated again with respect to x'. This gives the potential for a rhombus ,

$$\varphi=\int_{x_2}^{x_1}\left((y-mx'-c)\ln\sqrt{(y-mx'-c)^2+(x-x')^2}+(y_1-y_2)+(x-x')\tan^{-1}\left(\frac{y-mx'-c}{x-x'}\right)-\right. \quad \text{.A10}$$
$$\left.(y-mx')\ln\sqrt{(y-mx')^2+(x-x')^2}-(x-x')\tan^{-1}\left(\frac{y-mx'}{x-x'}\right)\right)dx'$$

Eq. A10 is broken into five parts so that the integral is manageable. Two parts contain the log term and the other two contain the arctan term and the fifth term is simple and its integral reduces to $(y_1-y_2)(x_1-x_2)$.

$$\varphi_1=\int_{x_2}^{x_1}(y-mx'-c)\ln\sqrt{(y-mx'-c)^2+(x-x')^2}\,dx' \quad \text{.....A11}$$

$$\varphi_1=\left[\begin{array}{l}\left(\frac{1}{2}(y-c)\left(\frac{1}{1+m^2}\right)-\frac{1}{2}\frac{m}{(1+m^2)}x\right)\left(\begin{array}{l}\left(x'-\frac{m}{1+m^2}(y-c)\right)\left(-2+\ln(1+m^2)\right)-\left(\frac{-2+\ln(1+m^2)}{1+m^2}\right)x+\\ \left(x'-\frac{m}{1+m^2}(y-c)-\frac{x}{1+m^2}\right)\left(\ln\left(\frac{(y-mx'-c)^2+(x-x')^2}{1+m^2}\right)\right)\end{array}\right)\\ +2\left(\frac{mx-y+c}{1+m^2}\right)\tan^{-1}\left(\frac{2(1+m^2)x'-2m(y-c)-2x}{mx-y+c}\right)-\frac{m}{4}\ln(1+m^2)\left(\left(x'-\frac{m}{1+m^2}(y-c)-\frac{x}{1+m^2}\right)^2\right)\\ -\frac{m}{4}\left(\frac{(y-mx'-c)^2+(x-x')^2}{1+m^2}\right)\ln\left(\frac{(y-mx'-c)^2+(x-x')^2}{1+m^2}\right)+\frac{m}{4}\left(x'-\frac{m}{1+m^2}(y-c)-\frac{x}{1+m^2}\right)^2\end{array}\right]_{x_2}^{x_1} \quad \text{A12}$$

In equation A10 there was a second term similar to Eq.A11 but with c=0. The integral need not be solved again; instead we will substitute c=0 in Eq.A12.

$$\varphi_2=\int_{x_2}^{x_1}(y-mx')\ln\sqrt{(y-mx')^2+(x-x')^2}\,dx' \quad \text{.....A13}$$

$$\varphi_2 = \left[\begin{array}{l} \left(\frac{1}{2}(y)\left(\frac{1}{1+m^2}\right) - \frac{1}{2}\frac{m}{(1+m^2)}x\right)\left(\begin{array}{l} \left(x' - \frac{m}{1+m^2}(y)\right)\left(-2+\ln(1+m^2)\right) - \left(\frac{-2+\ln(1+m^2)}{1+m^2}\right)x + \\ \left(x' - \frac{m}{1+m^2}(y) - \frac{x}{1+m^2}\right)\left(\ln\left(\frac{(y-mx')^2+(x-x')^2}{1+m^2}\right)\right) \end{array} \right) \\ +2\left(\frac{mx-y}{1+m^2}\right)\tan^{-1}\left(\frac{2(1+m^2)x' - 2m(y) - 2x}{mx-y}\right) - \frac{m}{4}\ln(1+m^2)\left(\left(x' - \frac{m}{1+m^2}(y) - \frac{x}{1+m^2}\right)^2\right) \\ -\frac{m}{4}\left(\frac{(y-mx')^2+(x-x')^2}{1+m^2}\right)\ln\left(\frac{(y-mx')^2+(x-x')^2}{1+m^2}\right) + \frac{m}{4}\left(x' - \frac{m}{1+m^2}(y) - \frac{x}{1+m^2}\right)^2 \end{array} \right]_{x_2}^{x_1} \quad \text{A14}$$

The other term in eq. A10 is one containing arctan,

$$\varphi_3 = \int_{x_2}^{x_1} (x - x')\tan^{-1}\left(\frac{y - mx' - c}{x - x'}\right)dx' \quad \text{A15}$$

$$\varphi_3 = \left[\begin{array}{l} \left(xx' - \frac{x'^2}{2}\right)\tan^{-1}\left(\frac{y-c-mx'}{x-x'}\right) + \frac{x(y-c-mx')}{2(1+m^2)} \\ +\left(\frac{x-ym+cm}{(1+m^2)^2} - \frac{x}{(1+m^2)}\right)\frac{(y-c-mx)}{2}\ln\left((x-x')^2+(y-c-mx')^2\right) \\ -\frac{1}{2}\left(\frac{-2x^2(1+m^2)-(y-c)^2-m^2x^2-2xm^3(y-c)}{(1+m^2)^2}\right)\tan^{-1}\left(\frac{(1+m^2)x'-x-(y-c)m}{mx-y+c}\right) \end{array} \right]_{x_2}^{x_1} \quad \text{A16}$$

The fourth term in the integral in A10 is similar to Eq.A15 but with c=0.

$$\varphi_4 = \int_{x_2}^{x_1} (x - x')\tan^{-1}\left(\frac{y - mx' - c}{x - x'}\right)dx' \quad \text{A17}$$

Substituting c=0 in eq. A16 gives the solution for the fourth term,

$$\varphi_4 = \left[\begin{array}{l} \left(xx' - \frac{x'^2}{2}\right)\tan^{-1}\left(\frac{y-mx'}{x-x'}\right) + \frac{x(y-mx')}{2(1+m^2)} \\ +\left(\frac{x-ym}{(1+m^2)^2} - \frac{x}{(1+m^2)}\right)\frac{(y-mx)}{2}\ln\left((x-x')^2+(y-mx')^2\right) \\ -\frac{1}{2}\left(\frac{-2x^2(1+m^2)-(y)^2-m^2x^2-2xm^3(y)}{(1+m^2)^2}\right)\tan^{-1}\left(\frac{(1+m^2)x'-x-(y)m}{mx-y}\right) \end{array} \right]_{x_2}^{x_1} \quad \text{A18}$$

The potential for a rhombohedral shape would be given as

$$\varphi = \varphi_1 - \varphi_2 + \varphi_3 - \varphi_4 + (y_1 - y_2)(x_1 - x_2) \quad \text{A19}$$

To obtain the value of σ_{xx} we need to differentiate Eq.A19 twice with respect to x. Hence we need to differentiate each term in Eq. A19 i.e. Eqs. A12, A14, A16, and A18 twice with respect to x. For Eq.A12 we get

$$\frac{\partial^2\varphi_1}{\partial x^2}=\left[\begin{array}{l}\left(\frac{m}{(1+m^2)^2}-\frac{m}{2(1+m^2)}\right)\ln\left((y-mx'-c)^2+(x-x')^2\right)+\left(-\frac{3m}{2(1+m^2)^2}-\frac{m}{2(1+m^2)^2}\ln(1+m^2)+\frac{m}{2(1+m^2)}\ln(1+m^2)\right)\\ +\left(-\frac{2m}{(1+m^2)}\left(x'-\frac{m}{1+m^2}(y-c)-\frac{x}{1+m^2}\right)-\frac{m}{1+m^2}(x-x')-\frac{2(y-c-mx)}{(1+m^2)^2}\right)\left(\frac{x-x'}{(x-x')^2+(y-mx'-c)^2}\right)\\ +\left(\frac{(y-c)}{2(1+m^2)}-\frac{mx}{2(1+m^2)}\right)\left(x'-\frac{m(y-c)}{1+m^2}-\frac{x}{1+m^2}\right)\left(\frac{2}{(x-x')^2+(y-mx'-c)^2}-\frac{4(x-x')^2}{\left((x-x')^2+(y-mx'-c)^2\right)^2}\right)\\ +\frac{4m}{1+m^2}\left(\frac{2(mx-y+c)-2m((1+m^2)x'-m(y-c)-x)}{(mx-y+c)^2+4((1+m^2)x'-m(y-c)-x)^2}\right)\\ -2\left(\frac{mx-y+c}{1+m^2}\right)\left(\frac{\left(2(mx-y+c)-2m((1+m^2)x'-m(y-c)-x\right)\left(2(mx-y+c)m-8((1+m^2)x'-m(y-c)-x)\right)}{\left((mx-y+c)^2+4((1+m^2)x'-m(y-c)-x)^2\right)^2}\right)\end{array}\right] \quad \text{.A20}$$

Similarly for Eq. A14,

$$\frac{\partial^2\varphi_2}{\partial x^2}=\left[\begin{array}{l}\left(\frac{m}{(1+m^2)^2}-\frac{m}{2(1+m^2)}\right)\ln\left((y-mx')^2+(x-x')^2\right)+\left(-\frac{3m}{2(1+m^2)^2}-\frac{m}{2(1+m^2)^2}\ln(1+m^2)+\frac{m}{2(1+m^2)}\ln(1+m^2)\right)\\ +\left(-\frac{2m}{(1+m^2)}\left(x'-\frac{m}{1+m^2}(y)-\frac{x}{1+m^2}\right)-\frac{m}{1+m^2}(x-x')-\frac{2(y-mx)}{(1+m^2)^2}\right)\left(\frac{x-x'}{(x-x')^2+(y-mx')^2}\right)\\ +\left(\frac{(y)}{2(1+m^2)}-\frac{mx}{2(1+m^2)}\right)\left(x'-\frac{m(y)}{1+m^2}-\frac{x}{1+m^2}\right)\left(\frac{2}{(x-x')^2+(y-mx')^2}-\frac{4(x-x')^2}{\left((x-x')^2+(y-mx')^2\right)^2}\right)\\ +\frac{4m}{1+m^2}\left(\frac{2(mx-y)-2m((1+m^2)x'-m(y)-x)}{(mx-y)^2+4((1+m^2)x'-m(y)-x)^2}\right)\\ -2\left(\frac{mx-y}{1+m^2}\right)\left(\frac{\left(2(mx-y)-2m((1+m^2)x'-m(y)-x\right)\left(2(mx-y)m-8((1+m^2)x'-m(y)-x)\right)}{\left((mx-y)^2+4((1+m^2)x'-m(y)-x)^2\right)^2}\right)\end{array}\right] \quad \text{.A21}$$

For Eq. A16

$$\frac{\partial^2\varphi_3}{\partial x^2}=\left[\begin{array}{l}\frac{2x'(mx'-y+c)}{(x-x')^2+(y-c-mx')^2}-\left(xx'-\frac{x'^2}{2}\right)\left(\frac{2(x-x')(mx'-y+c)}{\left((x-x')^2+(y-c-mx')^2\right)^2}\right)-\frac{m}{1+m^2}\\ -\left(\frac{m}{(1+m^2)^2}-\frac{m}{1+m^2}\right)\ln\left((x-x')^2+(y-c-mx')^2\right)+2\left(\frac{1}{(1+m^2)^2}-\frac{1}{1+m^2}\right)\frac{(x-x')(y-c-mx)}{(x-x')^2+(y-c-mx')^2}\\ -2\left(\frac{x-ym+cm}{(1+m^2)^2}-\frac{x}{1+m^2}\right)\frac{m(x-x')}{(x-x')^2+(y-c-mx')^2}+\left(\frac{2(1+m^2)+m^2}{(1+m^2)^2}\right)\tan^{-1}\left(\frac{x'(1+m^2)-x-(y-c)m}{mx-y+c}\right)\\ +\left(\frac{x-ym+cm}{(1+m^2)^2}-\frac{x}{1+m^2}\right)(y-c-mx)\left(\frac{3(x-x')^2+(y-c-mx')^2}{\left((x-x')^2+(y-c-mx')^2\right)^2}\right)\\ +2\left(\frac{2x(1+m^2)+m^2x+m^3(y-c)}{(1+m^2)^2}\right)\left(\frac{y-c-m(1+m^2)x'+m^2(y-c)}{(mx-y+c)^2+\left((1+m^2)x'-x-(y-c)m\right)^2}\right)\\ -\left(\frac{2x^2(1+m^2)+(y+c)^2+m^2x^2+2xm^3(y-c)}{(1+m^2)^2}\right)\left(\frac{\left(y-c-m(1+m^2)x'+m^2(y-c)\right)\left(2(mx-y+c)m+2\left((1+m^2)x'-x-(y-c)m\right)\right)}{\left((mx-y+c)^2+\left((1+m^2)x'-x-(y-c)m\right)^2\right)^2}\right)\end{array}\right] \quad \text{..A22}$$

Similarly for Φ_4 ,

$$\frac{\partial^2\varphi_4}{\partial x^2}=\left[\begin{array}{l}
\dfrac{2x'(mx'-y)}{(x-x')^2+(y-mx')^2}-\left(xx'-\dfrac{x'^2}{2}\right)\left(\dfrac{2(x-x')(mx'-y)}{\left((x-x')^2+(y-mx')^2\right)^2}\right)-\dfrac{m}{1+m^2}\\
-\left(\dfrac{m}{(1+m^2)^2}-\dfrac{m}{1+m^2}\right)\ln\left((x-x')^2+(y-mx')^2\right)+2\left(\dfrac{1}{(1+m^2)^2}-\dfrac{1}{1+m^2}\right)\dfrac{(x-x')(y-mx)}{(x-x')^2+(y-mx')^2}\\
-2\left(\dfrac{x-ym}{(1+m^2)^2}-\dfrac{x}{1+m^2}\right)\dfrac{m(x-x')}{(x-x')^2+(y-mx')^2}+\left(\dfrac{2(1+m^2)+m^2}{(1+m^2)^2}\right)\tan^{-1}\left(\dfrac{x'(1+m^2)-x-(y)m}{mx-y}\right)\\
+\left(\dfrac{x-ym}{(1+m^2)^2}-\dfrac{x}{1+m^2}\right)(y-mx)\left(\dfrac{3(x-x')^2+(y-mx')^2}{\left((x-x')^2+(y-mx')^2\right)^2}\right)\\
+2\left(\dfrac{2x(1+m^2)+m^2x+m^3(y)}{(1+m^2)^2}\right)\left(\dfrac{y-m(1+m^2)x'+m^2(y)}{(mx-y)^2+\left((1+m^2)x'-x-(y)m\right)^2}\right)\\
-\left(\dfrac{2x^2(1+m^2)+(y)^2+m^2x^2+2xm^3(y)}{(1+m^2)^2}\right)\left(\dfrac{\left(y-m(1+m^2)x'+m^2(y)\right)\left(2(mx-y)m+2\left((1+m^2)x'-x-(y)m\right)\right)}{\left((mx-y)^2+\left((1+m^2)x'-x-(y)m\right)^2\right)^2}\right)
\end{array}\right] \quad \text{.....A23}$$

The final expression for the solution of Eq.A10 is given by the sum of Eq. A20, A21, A22, A23.

$$\frac{\partial^2\varphi}{\partial x^2}=\frac{\partial^2\varphi_1}{\partial x^2}-\frac{\partial^2\varphi_2}{\partial x^2}+\frac{\partial^2\varphi_3}{\partial x^2}-\frac{\partial^2\varphi_4}{\partial x^2} \quad \text{.....A24}$$

Eq. A24 applies only to one part of the groove. We need three other expressions, one for the other side of the groove and two for the top planar parts on either side of the groove(see fig. A1). The expressions would be same except the parameters defining the slope, intercept and boundaries are different.

The final expression for the stress would be ,

$$\sigma_{xx}^{c}=-\frac{1}{12\pi}\frac{1+\upsilon}{1-\upsilon}e^{T}E\frac{\partial^2\varphi}{\partial x^2}$$

where e^T is the dilatational strain given by,

$$e^{T}=e_{ii}^{T}=3\frac{(a_l-a_s)}{a_s}$$

a_l and a_s are the lattice parameters of the layer and substrate respectively and E is the elastic constant.

9.2 APPENDIX B: FINITE ELEMENT ANALYSIS (FEA)

Finite element method (FEM) is a numerical technique for solving problems involving complex geometries. The main assumption in this method is that the properties of a continuum body can be represented as a discrete body. Once the system is divided into a set of elements, then the boundary conditions and forces are put into the program to give the required solution.

The mathematical details of the finite element method can be found in the book by Zienkiewicz (1971). Since a continuum body is being approximated by a set of discrete elements, the shape and size of these elements becomes a very important consideration. In a 3D problem the element shape can be a prism or cuboid. To simplify the problem it is better to start out with a coarse mesh and gradually refine it till further mesh refinement does not change the values of the output. The mesh size must be kept fine in areas where there is a rapid change in the stress.

In the present work, a commercial software package called ABAQUS, was used for solving the 3D geometry. This program has a large selection of elements. The geometry of the problem at hand has been defined to be a 3D semi-infinite substrate of material one, on which a thin layer of material two has been deposited. The mesh size in the two materials is chosen such that a single set of interface nodes belongs to both the substrate and the layer. This condition has to be met because it is assumed that the system remains coherent throughout the deformation. In the problem of strained layers, the strain in the system arises due to a lattice mismatch between the layer and the substrate. To simulate this we have assumed a thermal mismatch between the substrate and the layer.

Since the substrate is semi-infinite, the deformation in the bulk of the substrate is zero. Thus it is assumed that the thermal expansion coefficient of the substrate is zero. To

simulate a layer in compression, a positive thermal expansion coefficient in the layer is assumed.

To solve the problem of a strained layer in a V-groove cubic elements with 8 (linear) nodes were used (Fig. B1). This choice was made because there were no bending forces in the system. Also the system was assumed to be elastic. The layer and the substrate were given the same elastic constants.

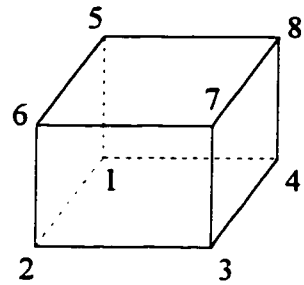

Fig.B1: 3D cubic element used in the problem.

The next step was to define the boundary conditions. These boundary conditions should reflect the experimental conditions. In case of DOP the sample which is used for the experiment is about 1mm thick, whereas in TEM the sample is around 1000Å thick. Hence in a TEM sample the stresses at the surfaces of the cross-sectional samples are relaxed and the contrast that we see arises completely from this relaxation process. In a DOP experiment the data is collected from a depth of about a micron, so the data mainly reflects the bulk stresses. To simulate the DOP results we will use boundary condition I (BC I)defined below. For the TEM results we will use boundary condition two (BC II). Since the groove is symmetrical, only half of the groove need be considered in the analysis (see Fig. B2).

B.C.I: The front and back surfaces perpendicular to the z-direction (A) in both the substrate and the layer are constrained in the z-direction. The bottommost xz plane (B) is

constrained in the y direction. The left hand yz plane of symmetry (C) and the rightmost yz plane (D) are constrained in the x-direction.

B.C.II: The front and back surfaces perpendicular to the z-direction (A) in both the substrate and the layer are free to relax. Planes B, C, and D are constrained as in BC I.

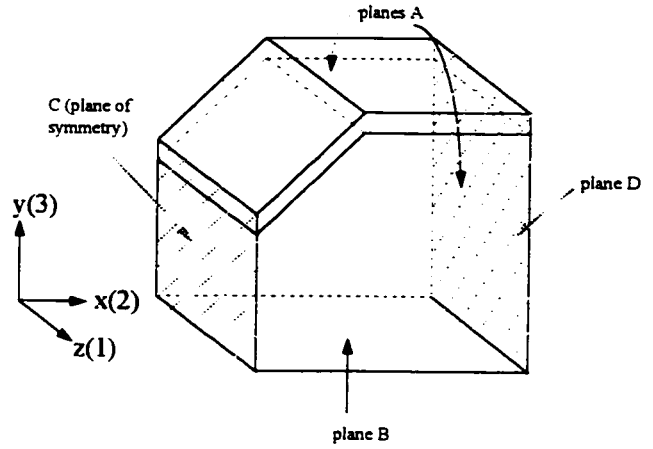

Fig.B2: Shows the planes on which boundary conditions are applied (xyz correspond to the universal axes used in this thesis and 123 correspond to the axes used in ABAQUS).

As shown in Fig. B2 only half of the groove was considered for solution because of the symmetry of the problem.

Elastic constants used for solving the problem were those of InP with E= 1.E12 dyne/cm^2 and ν= 0.28. The Thermal expansion coefficient of the layer and substrate were taken to be α_{layer}= 2.0 E-4 /°C and $\alpha_{substrate}$= 0 /°C, while ΔT, the change in temperature, was 3.0°C. This leads to a strain of -6E-4 (-0.06%) between the layer and the substrate.

The original undeformed mesh is shown in Fig. B3 and the deformed mesh after applying B.C.I is shown in Fig. B5 for $\alpha\Delta T$= -0.06% and layer thickness to groove size ratio of 0.28. The deformed mesh after applying B.C.II is shown in Fig. B4. Note that in both these figures the deformations are magnified by a considerable factor to illustrate the change of shape of the V-groove at the free surface.

```
INPUT USED IN THE FINITE ELEMENT PROGRAM 'ABAQUS'
*HEADING
MISMATCH REAL
**ratio of thickness of the layer to groove size=0.28
**strain=-0.061%
**bulk boundary conditions
*NODE
1,0.,0.,3.
241,0.,1.,3.72
15001,0.,0.,-2.
15141,0.,8.,-2.
15241,0.,8.,3.72
40001,0.,0.,3.2
40241,0.,1.,3.92
55241,0.,8.,3.92
20000001,-1.0,0.,3.
20000241,-1.0,1.,3.72
20015241,-1.0,8.,3.72
20015001,-1.0,0.,-2.
20015141,-1.0,8.,-2.
20040001,-1.0,0.0,3.2
20040241,-1.0,1.,3.92
20055241,-1.0,8.,3.92
*PREPRINT,CONTACT=NO,ECHO=NO,HISTORY=NO,MODEL=NO
*NGEN,NSET=TIP1
1,241,10
*NGEN,NSET=RIGHT1
15141,15241,10
*NGEN,NSET=BOTTOM1
15001,15141,10
*NSET,NSET=GROOVE1
TIP1
*NSET,NSET=CONNECT1
BOTTOM1,RIGHT1
*NFILL,NSET=FRONT1,BIAS=0.8
GROOVE1,CONNECT1,15,1000
*NGEN,NSET=TIP11
40001,40241,10
*NFILL,NSET=TIP111
TIP1,TIP11,2,20000
*NGEN,NSET=TOP100
241,40241,20000
*NGEN,NSET=TOP200
15241,55241,20000
*NFILL,NSET=TOP11,BIAS=0.8
TOP100,TOP200,15,1000
*NSET,NSET=LAYER2
TIP111,TOP11
*NSET,NSET=FRONT
LAYER2,FRONT1
*NGEN,NSET=TIP2
20000001,20000241,10
*NGEN,NSET=RIGHT2
20015141,20015241,10
*NGEN,NSET=BOTTOM2
```

```
20015001,20015141,10
*NSET,NSET=GROOVE2
TIP2
*NSET,NSET=CONNECT2
BOTTOM2,RIGHT2
*NFILL,NSET=BACK1,BIAS=0.8
GROOVE2,CONNECT2,15,1000
*NGEN,NSET=TIP22
20040001,20040241,10
*NFILL,NSET=TIP222
TIP2,TIP22,2,20000
*NGEN,NSET=TOP300
20000241,20040241,20000
*NGEN,NSET=TOP400
20015241,20055241,20000
*NFILL,NSET=TOP22,BIAS=0.8
TOP300,TOP400,15,1000
*NSET,NSET=LAYER4
TIP222,TOP22
*NSET,NSET=BACK
LAYER4,BACK1
*NFILL,NSET=COMPLETE
FRONT,BACK,10,2000000
*NFILL,NSET=FACET
BOTTOM1,BOTTOM2,10,2000000
*NGEN,NSET=LINE1
1,40001,20000
*NGEN,NSET=LINE2
20000001,20040001,20000
*NFILL,NSET=MID1
LINE1,LINE2,10,2000000
*NGEN,NSET=LINE3
1,20000001,2000000
*NGEN,NSET=LINE4
15001,20015001,2000000
*NFILL,NSET=MID2,BIAS=0.8
LINE3,LINE4,15,1000
*NSET,NSET=MID
MID1,MID2
*NGEN,NSET=LINE5
15241,55241,20000
*NGEN,NSET=LINE6
20015241,20055241,20000
*NFILL,NSET=SIDED1
LINE5,LINE6,10,2000000
*NGEN,NSET=LINE7
15141,15241,10
*NGEN,NSET=LINE8
20015141,20015241,10
*NFILL,NSET=SIDED2
LINE7,LINE8,10,2000000
*NSET,NSET=SIDED
SIDED1,SIDED2
*ELEMENT,TYPE=C3D8
1,1001,1011,2001011,2001001,1,11,2000011,2000001
```

```
20001,1,11,2000011,2000001,20001,20011,2020011,2020001
20241,241,1241,2001241,2000241,20241,21241,2021241,2020241
*ELGEN,ELSET=LAYER
20001,10,2000000,2000000,24,10,10,2,20000,20000
20241,10,2000000,2000000,15,1000,1000,2,20000,20000
*ELGEN,ELSET=SUBS
1,10,2000000,2000000,24,10,10,15,1000,1000
*SOLID SECTION,ELSET=LAYER,MATERIAL=ONE
*MATERIAL,NAME=ONE
*ELASTIC
1.E12,0.28
*EXPANSION
2.E-4
*SOLID SECTION,ELSET=SUBS,MATERIAL=TWO
*MATERIAL,NAME=TWO
*ELASTIC
1.E12,0.28
*EXPANSION
0.0
*BOUNDARY
FACET,1,6
MID,YSYMM
SIDED,YSYMM
FRONT,1
BACK,1
*INITIAL CONDITIONS,TYPE=TEMPERATURE
COMPLETE,20.
*STEP
*STATIC
*TEMPERATURE
COMPLETE,23.o
*EL PRINT
COORD,S22,S33
*RESTART,WRITE
*END STEP
```

ABAQUS

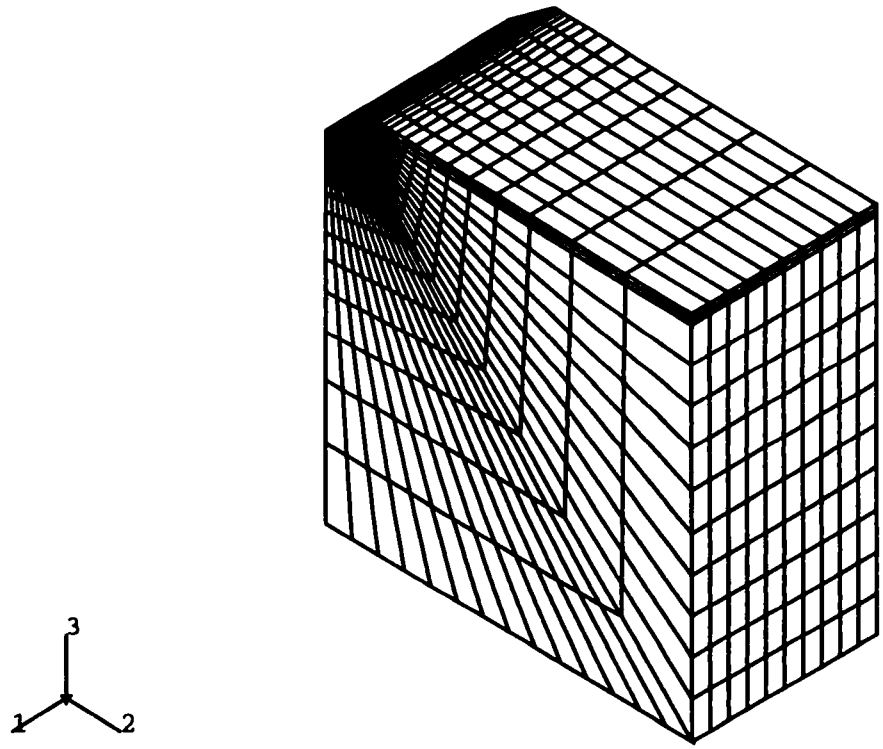

Fig. B3 Original mesh in case of bulk analysis. Axes 1,2, and 3 in case of FEM correspond to z, x, and y respectively , used in the thesis.

ABAQUS

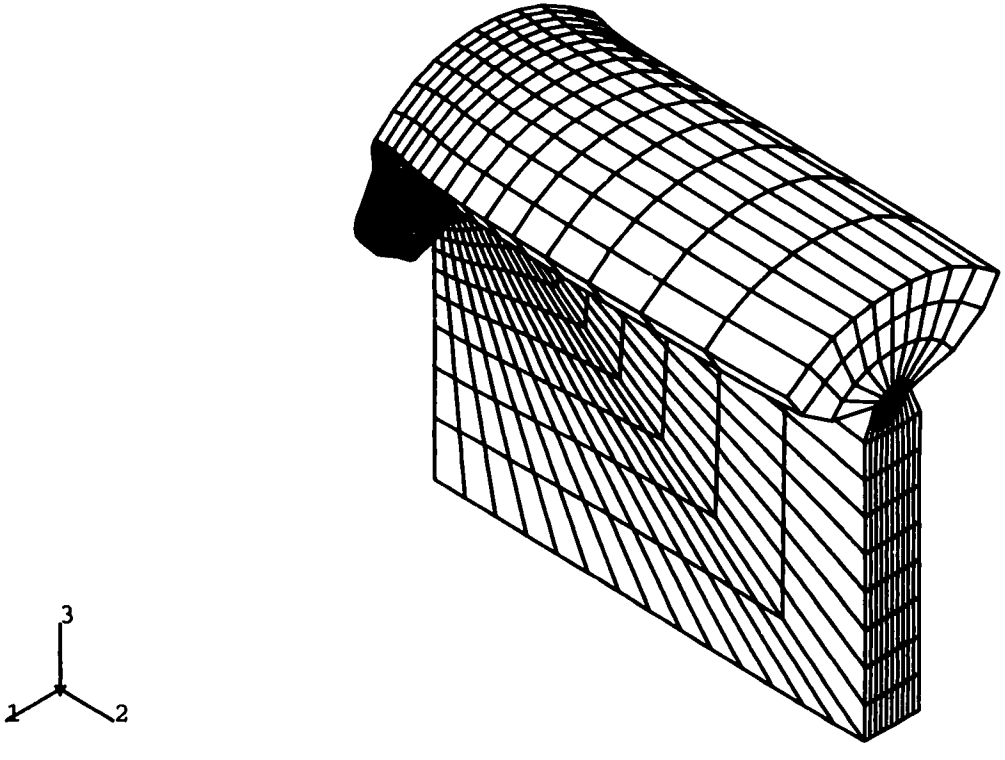

Fig. B4 3DDeformed mesh in the case of analysis with boundary conditions corresponding to a thin sample.

ABAQUS

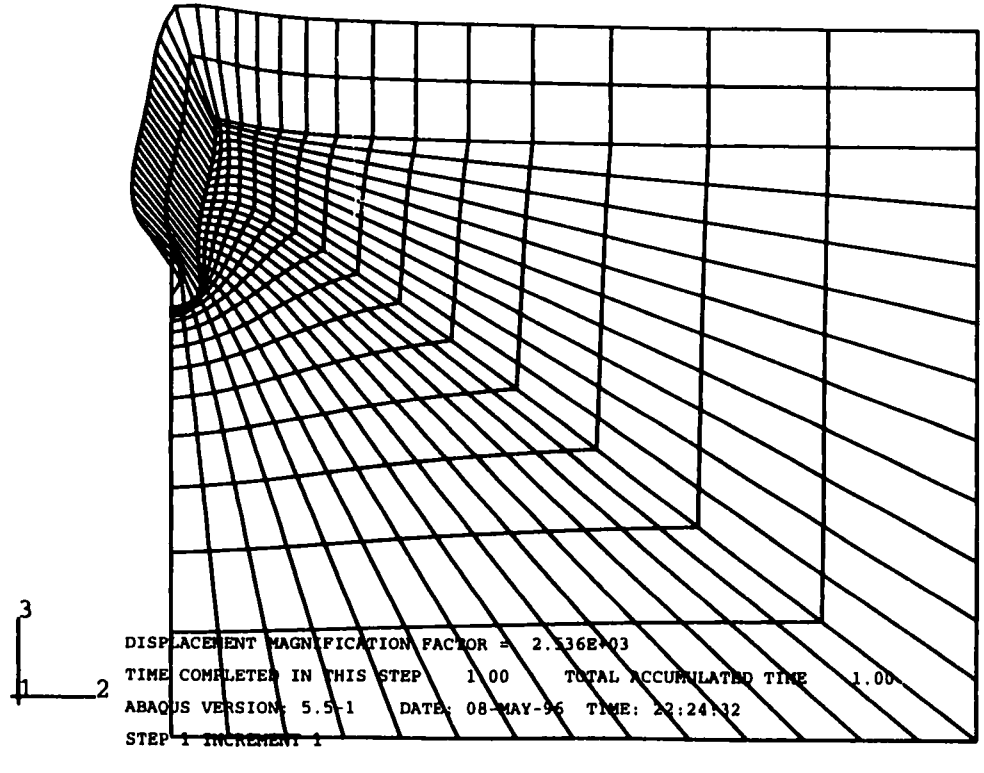

Fig. B5 2D deformed mesh in the case of analysis with boundary conditions corresponding to a thick sample.

9.3 APPENDIX C: COMPOSITION ANALYSIS USING EDX ON STEM

Table C1 Composition analysis at different points in the InGaAs layer deposited on planar InP substrate.

P	Ga	As	In	In-P	Rev In%	Rev Ga%	Rev As%
2.03	25.2	47.13	25.64	23.61	24.61%	26.27%	49.12%
7.91	20.9	41.22	29.98	22.07	26.21%	24.82%	48.96%
1.15	24.87	49.1	24.88	23.73	24.29%	25.46%	50.26%
1.09	25.44	48.25	25.22	24.13	24.67%	26.01%	49.33%
0.47	25.36	49.08	25.08	24.61	24.85%	25.60%	49.55%
1.14	25.93	47.86	25.06	23.92	24.48%	26.54%	48.98%
0	25.99	50.25	23.81	23.81	23.80%	25.98%	50.22%
0.28	27.03	48.72	23.97	23.69	23.82%	27.18%	48.99%
2.71	24.31	47.65	25.34	22.63	23.92%	25.70%	50.38%
0.82	25.1	49.83	24.25	23.43	23.82%	25.52%	50.66%
9.52	20.53	40.03	29.92	20.4	25.20%	25.36%	49.44%
2.75	24.73	47.58	24.94	22.19	23.48%	26.17%	50.35%
0.91	25.16	49.79	24.14	23.23	23.66%	25.63%	50.71%
5.25	22.88	44.76	27.1	21.85	24.42%	25.57%	50.02%
0.73	25.24	49.78	24.25	23.52	23.87%	25.61%	50.52%
0.91	25.17	49.55	24.36	23.45	23.89%	25.64%	50.47%
10.67	19.23	37.81	32.29	21.62	27.49%	24.45%	48.07%
0.69	25.27	49.68	24.36	23.67	24.00%	25.62%	50.38%
0.66	25.75	50.1	23.5	22.84	23.14%	26.09%	50.77%
8.19	20.4	41.43	29.99	21.8	26.07%	24.39%	49.54%
0.97	25.33	49.86	23.84	22.87	23.32%	25.83%	50.85%
0.64	25.08	50.1	24.17	23.53	23.84%	25.41%	50.75%
0.99	25.36	49.56	24.09	23.1	23.57%	25.87%	50.56%
2.43	24.22	47.06	26.29	23.86	25.08%	25.46%	49.46%
1.02	25.69	48.49	24.79	23.77	24.27%	26.23%	49.50%
2.98	23.64	46.54	26.84	23.86	25.37%	25.14%	49.49%
3.19	23.85	46.37	26.58	23.39	24.99%	25.48%	49.54%
3.72	24.14	46.52	25.62	21.9	23.66%	26.08%	50.26%
				Mean	***24.13%***	***26.17%***	***49.69%***
				Dev.	***0.67%***	***0.13%***	***0.80%***

First four columns correspond to the compositions calculated by the program from the net integrals of intensities. The column corresponding to (In-P) is obtained by subtracting the P from the In atomic percent. Last three columns correspond to the revised composition after subtracting the P and taking the net In amount (In-P) and recalculating the percentages. The mean corresponds to the average of all the values measured in that particular region and Dev. corresponds to the standard deviation of the mean. The rest of the tables in this chapter follow the same procedure.

Table C2(a) Composition of the layer deposited on (211)A facet of sample 560A (Columns defined in Table C1)

P	Ga	As	In	In-P	Rev In%	Rev Ga%	Rev As%
2.45	21.74	47.44	28.38	25.93	27.26%	22.86%	49.88%
3.26	23.76	44.94	28.03	24.77	26.50%	25.42%	48.08%
2.47	21.14	47.77	28.62	26.15	27.51%	22.24%	50.25%
3.34	19.26	48.06	29.35	26.01	27.87%	20.64%	51.49%
2.02	22.7	50.26	25.02	23	23.97%	23.66%	52.38%
2.06	23.68	49.83	24.43	22.37	23.33%	24.70%	51.97%
3.11	20.96	46.43	29.5	26.39	28.14%	22.35%	49.51%
0.53	21.72	51.56	26.19	25.66	25.93%	21.95%	52.11%
0.01	20.15	52.62	27.21	27.2	27.21%	20.16%	52.64%
2.64	26.4	44.41	26.55	23.91	25.24%	27.87%	46.89%
2.89	22.8	49.46	24.85	21.96	23.31%	24.20%	52.49%
4.81	23.7	46.79	24.7	19.89	22.01%	26.22%	51.77%
2.01	25.23	49.81	22.95	20.94	21.82%	26.29%	51.90%
3.58	20.98	46.39	29.04	25.46	27.43%	22.60%	49.97%
2.63	20.24	50.32	26.81	24.18	25.52%	21.36%	53.11%
3.21	20.49	49.24	27.06	23.85	25.49%	21.90%	52.62%
1.59	19.95	51.13	27.32	25.73	26.58%	20.61%	52.81%
				Mean	***25.59%***	***23.24%***	***51.17%***
				Dev	***2.03%***	***2.24%***	***1.79%***

Table C2 (b) Composition of the layer deposited on (311)A facet of sample 560A (Columns defined in Table C1).

P	Ga	As	In	In-P	Rev In%	Rev Ga%	Rev As%
1.34	21.59	53.86	23.22	21.88	22.48%	22.18%	55.34%
3.1	20.42	50.91	25.58	22.48	23.96%	21.77%	54.27%
2.76	19.37	49.71	28.16	25.4	26.88%	20.50%	52.61%
2.26	21.51	49.24	27	24.74	25.91%	22.53%	51.57%
2.76	19.59	49.4	28.25	25.49	26.98%	20.73%	52.29%
2.4	20.05	50.22	27.33	24.93	26.19%	21.06%	52.75%
1.47	22.35	50.82	25.36	23.89	24.61%	23.03%	52.36%
2.24	18.67	51.71	27.39	25.15	26.33%	19.54%	54.13%
2.65	18.68	50.79	27.88	25.23	26.64%	19.73%	53.63%
2.31	19.13	53.6	24.97	22.66	23.76%	20.05%	56.19%
1.61	20	52.1	26.29	24.68	25.50%	20.67%	53.83%
1.47	22.35	50.82	25.36	23.89	24.61%	23.03%	52.36%
				Mean	***25.32%***	***21.23%***	***53.44%***
				Dev.	***1.43%***	***1.24%***	***1.38%***

Table C2 (c) Composition of the layers deposited on top (100) facet of sample 560A (columns defined in Table C1).

P	Ga	As	In	In-P	Rev In%	Rev Ga%	Rev As%
1.26	24.21	50.01	24.52	23.26	23.86%	24.84%	51.30%
1.67	22.38	47.26	28.69	27.02	27.95%	23.15%	48.89%
1.48	22.78	47.87	27.87	26.39	27.19%	23.47%	49.33%
2.22	24.11	48.98	24.69	22.47	23.51%	25.23%	51.26%
1.26	24.21	50.01	24.52	23.26	23.86%	24.84%	51.30%
0.6	21.54	53.83	24.04	23.44	23.72%	21.80%	54.48%
3.39	23.02	48.6	24.98	21.59	23.16%	24.70%	52.14%
3.1	21.09	51.63	24.17	21.07	22.47%	22.49%	55.05%
5.5	20.41	44.84	29.25	23.75	26.69%	22.93%	50.38%
5.91	19.08	43.2	31.82	25.91	29.38%	21.64%	48.99%
				Mean	***25.18%***	***23.51%***	***51.31%***
				Dev.	***2.39%***	***1.33%***	***2.13%***

Table C3 (a) Analysis in region 1 on the top (100) plane of sample 570 (111)B.

P	Ga	As	In	In-P	Rev In%	Rev Ga%	Rev As%
1.52	21.16	51.69	25.64	24.12	24.87%	21.82%	53.31%
1.79	20.53	51.01	26.67	24.88	25.80%	21.29%	52.90%
1.52	21.16	51.69	25.64	24.12	24.87%	21.82%	53.31%
1.68	19.45	51.23	27.64	25.96	26.86%	20.13%	53.01%
2.08	19.15	51.99	26.78	24.7	25.77%	19.98%	54.25%
2.32	19.86	50.14	27.69	25.37	26.60%	20.82%	52.57%
1.3	20.58	52.32	25.8	24.5	25.15%	21.13%	53.72%
2.01	19.73	51.33	26.93	24.92	25.96%	20.56%	53.48%
2.21	19.38	50.97	27.44	25.23	26.40%	20.28%	53.33%
2.41	19.02	50.73	27.84	25.43	26.72%	19.98%	53.30%
2.81	19.11	50.17	27.91	25.1	26.59%	20.25%	53.16%
2.73	18.67	50.43	28.18	25.45	26.92%	19.75%	53.34%
2.86	18.75	50.01	28.38	25.52	27.07%	19.89%	53.04%
1.93	21.03	51.13	25.92	23.99	24.95%	21.87%	53.18%
2.04	19.03	50.85	28.08	26.04	27.15%	19.84%	53.01%
2.65	18.97	50.82	27.56	24.91	26.30%	20.03%	53.66%
2.84	18.7	49.63	28.83	25.99	27.56%	19.83%	52.62%
3.35	19	48.51	29.14	25.79	27.64%	20.36%	51.99%
1.76	21.06	51.41	25.77	24.01	24.89%	21.83%	53.29%
3.95	18.21	48.53	29.31	25.36	27.54%	19.77%	52.69%
3.2	18.04	48.78	29.97	26.77	28.60%	19.28%	52.12%
5.42	17.37	46.61	30.61	25.19	28.25%	19.48%	52.27%
4.66	17.6	47.7	30.04	25.38	27.99%	19.41%	52.60%
				Mean	***26.54%***	***20.41%***	***53.05%***
				Dev.	***1.12%***	***0.83%***	***0.53%***

Table C3 (b) Analysis in region 2 in the defective region on (111)B facet of sample 570(111)B.

P	Ga	As	In	In-P	Rev In%	Rev Ga%	Rev As%
9.03	20.37	40.31	30.29	21.26	25.95%	24.86%	49.19%
11.74	17.95	38.04	32.27	20.53	26.83%	23.46%	49.71%
9.13	21.96	40.98	27.94	18.81	23.01%	26.86%	50.13%
11.29	21.93	38.87	27.91	16.62	21.47%	28.33%	50.21%
7.31	22.93	43.6	26.15	18.84	22.07%	26.86%	51.07%
10.55	20.49	39.69	29.26	18.71	23.72%	25.97%	50.31%
10.4	21.05	39.22	29.33	18.93	23.90%	26.58%	49.52%
8.17	22.63	41.55	27.65	19.48	23.28%	27.05%	49.67%
7.99	23.27	42.04	26.7	18.71	22.27%	27.70%	50.04%
4.22	26.04	47.4	22.34	18.12	19.79%	28.44%	51.77%
				Mean	***23.23%***	***26.61%***	***50.16%***
				Dev.	***2.06%***	***1.53%***	***0.76%***

Table C3 (c) Analysis in region 3 on the upper portion of (n11)B plane of sample 570(111)B.

P	Ga	As	In	In-P	Rev In%	Rev Ga%	Rev As%
4.58	19.02	46.04	30.36	25.78	28.38%	20.94%	50.68%
8.74	15.81	40.42	35.03	26.29	31.86%	19.16%	48.98%
9.16	15.34	39.28	36.23	27.07	33.14%	18.78%	48.08%
8.62	15.84	40.94	34.6	25.98	31.39%	19.14%	49.47%
4.58	19.02	46.04	30.36	25.78	28.38%	20.94%	50.68%
3.38	18.03	48.57	30.02	26.64	28.57%	19.34%	52.09%
8.56	15.98	40.98	34.48	25.92	31.27%	19.28%	49.44%
3.77	18.51	47.1	30.62	26.85	29.04%	20.02%	50.94%
2.75	18.37	49.09	29.8	27.05	28.62%	19.44%	51.94%
11.35	13.08	37.74	37.84	26.49	34.26%	16.92%	48.82%
18.09	10.64	30.7	40.57	22.48	35.22%	16.67%	48.10%
7.35	15.78	43.1	33.77	26.42	30.97%	18.50%	50.53%
17.45	11.38	30.76	40.41	22.96	35.27%	17.48%	47.25%
12.93	13.7	35.91	37.46	24.53	33.09%	18.48%	48.44%
16.5	11.51	32.77	39.22	22.72	33.91%	17.18%	48.91%
8.55	15.25	41.21	34.98	26.43	31.89%	18.40%	49.72%
10.19	14.89	39.28	35.64	25.45	31.96%	18.70%	49.33%
10.9	14.25	38.54	36.31	25.41	32.49%	18.22%	49.28%
8.48	15.23	40.85	35.44	26.96	32.47%	18.34%	49.19%
10.4	14.65	38.7	36.25	25.85	32.64%	18.50%	48.86%
10.19	14.89	39.28	35.64	25.45	31.96%	18.70%	49.33%
3.1	18.82	51.35	26.72	23.62	25.18%	20.07%	54.75%
6.93	16.6	45.67	30.79	23.86	27.70%	19.27%	53.02%
5.2	17.16	48.66	28.98	23.78	26.54%	19.15%	54.31%
3.1	18.82	51.35	26.72	23.62	25.18%	20.07%	54.75%
				Mean	***30.86%***	***18.87%***	***50.28%***
				Dev.	***2.90%***	***1.09%***	***2.10%***

Table C3 (d) Analysis in region 4 near the bottom of the groove of sample 570(111)B.

2.61	17.46	50.5	29.43	26.82	28.30%	18.42%	53.28%
3.62	11.52	49.55	35.3	31.68	34.16%	12.42%	53.42%
3.89	9.76	49.95	36.4	32.51	35.25%	10.58%	54.16%
3.75	17.52	49.03	29.7	25.95	28.05%	18.94%	53.01%
3.05	18.66	48.63	29.66	26.61	28.34%	19.87%	51.79%
4.13	17.7	47.57	30.59	26.46	28.85%	19.30%	51.86%
4.2	17.69	46.97	31.14	26.94	29.41%	19.31%	51.28%
2.65	17.58	50.22	29.55	26.9	28.41%	18.56%	53.03%
2.88	12.92	50.48	33.72	30.84	32.72%	13.71%	53.57%
4 34	9.04	49.27	37.36	33.02	36.15%	9.90%	53.95%
4.33	4.45	49.18	42.04	37.71	41.29%	4.87%	53.84%
2.78	13.53	50.08	33.61	30.83	32.65%	14.33%	53.03%
4.84	16.85	46.68	31.63	26.79	29.66%	18.66%	51.68%
3.67	18.05	48.76	29.52	25.85	27.90%	19.48%	52.62%
4.76	14.65	47.24	33.36	28.6	31.61%	16.19%	52.20%
4.57	9.25	49.4	36.78	32.21	35.45%	10.18%	54.37%
5.56	12.41	46.6	35.43	29.87	33.61%	13.96%	52.43%
5.79	15.78	45.23	33.2	27.41	31.00%	17.85%	51.15%
16.57	10	30.69	42.73	26.16	39.13%	14.96%	45.91%
19.06	10.27	27.96	42.71	23.65	38.22%	16.60%	45.18%
11.12	12.6	38.8	37.49	26.37	33.91%	16.20%	49.89%
11.91	14.3	37.42	36.37	24.46	32.11%	18.77%	49.12%
14.98	13.11	33.19	38.71	23.73	33.89%	18.72%	47.39%
19.82	10.56	27.89	41.74	21.92	36.31%	17.49%	46.20%
				Mean	***32.76%***	***15.80%***	***51.43%***
				Dev.	***3.79%***	***3.89%***	***2.74%***

Table C3 (e) Analysis in region 5 at the bottom of the groove of sample 570(111)B.

5.75	6.78	45.73	41.74	35.99	40.67%	7.66%	51.67%
5.44	9.06	47.72	37.78	32.34	36.29%	10.17%	53.55%
4.96	9.77	47.2	38.07	33.11	36.76%	10.85%	52.40%
5.75	6.78	45.73	41.74	35.99	40.67%	7.66%	51.67%
3.1	11.43	51.03	34.43	31.33	33.40%	12.19%	54.41%
4.07	10.31	49.7	35.92	31.85	34.67%	11.22%	54.10%
5.66	7.05	46.74	40.55	34.89	39.34%	7.95%	52.71%
2.56	10.7	51.52	35.22	32.66	34.42%	11.28%	54.30%
4.61	10.3	49.95	35.14	30.53	33.63%	11.35%	55.02%
10.22	9.18	40.76	39.83	29.61	37.22%	11.54%	51.24%
2.48	11.38	50.15	35.99	33.51	35.26%	11.97%	52.77%
5.41	11.06	46.83	36.71	31.3	35.09%	12.40%	52.51%
2.74	10.62	49.7	36.94	34.2	36.18%	11.24%	52.58%
2.54	8.23	50.84	38.39	35.85	37.77%	8.67%	53.56%
4.63	9.93	46.29	39.15	34.52	38.04%	10.94%	51.01%
16.33	9.95	30.2	43.53	27.2	40.39%	14.77%	44.84%
4.77	11.42	47.37	36.44	31.67	35.01%	12.62%	52.37%
3.66	10.95	49.57	35.83	32.17	34.71%	11.81%	53.48%
5.2	13.18	46.06	35.56	30.36	33.88%	14.71%	51.41%
2.68	12.76	51.14	33.42	30.74	32.48%	13.48%	54.04%
2.63	9.57	52	35.8	33.17	35.01%	10.10%	54.89%
4.83	8.79	48.32	38.06	33.23	36.78%	9.73%	53.49%
				Mean	***36.26%***	***11.11%***	***52.64%***
				Dev.	***2.40%***	***1.98%***	***2.10%***

IMAGE EVALUATION
TEST TARGET (QA-3)

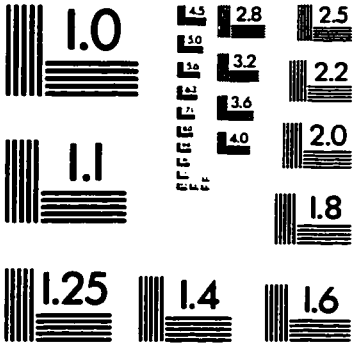

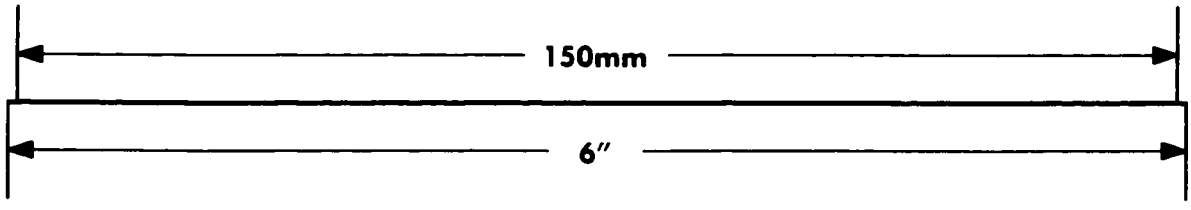

APPLIED IMAGE . Inc
1653 East Main Street
Rochester, NY 14609 USA
Phone: 716/482-0300
Fax: 716/288-5989